UNIVERSIDAD POLITÉCNICA DE MADRID
Escuela Técnica Superior de Ingeniería Aeronáutica y del Espacio



Mission Analysis of Formation Flying in L2

DOCTORAL THESIS

Submitted for the degree of Doctor by:

Juan Bermejo Ballesteros
Máster Universitario en Sistemas Espaciales

Madrid, 2023



UNIVERSIDAD POLITÉCNICA DE MADRID
Escuela Técnica Superior de Ingeniería Aeronáutica y del Espacio

Doctoral Degree in Aerospace Engineering

Mission Analysis of Formation Flying in L2

DOCTORAL THESIS

Submitted for the degree of Doctor by:

Juan Bermejo Ballesteros
Máster Universitario en Sistemas Espaciales

Under the supervision of:
Dr. Javier Cubas Cano (Supervisor)

Madrid, 2023

Title: Mission Analysis of Formation Flying in L2

Author: Juan Bermejo Ballesteros

Doctoral Programme: Aerospace Engineering

Thesis Supervision:

Dr. Javier Cubas Cano, Doctor en Ingeniería Aeronáutica, Universidad Politécnica de Madrid (Supervisor)

External Reviewers:

Thesis Defense Committee:

Thesis Defense Date:

This thesis has been partially supported by the project 478 Y2020/NMT-6427 OAPES of the program “Sinérgicos 2020” from Comunidad de Madrid (Spain).

A Lidia

Agradecimientos

La vida y las personas que conoces a lo largo de la misma tienen una similitud curiosa con la trayectoria de una nave en el espacio y las fuerzas que sobre ella se ejercen. Algunas están presentes toda la vida, aunque a veces estés más cerca y otras más lejos, como el Sol en el Sistema Solar. Otras las encuentras una vez en vida y te quedas para para siempre en su órbita. Todas ellas pueden ejercer un pequeño pero continuo efecto en ti, y llevarte más lejos de lo que jamás llegarías tú solo.

Detrás de este documento hay mucho trabajo y ayuda de personas sin las cuales no podría haberse realizado.

En primer lugar, agradezco a mi director, Javier Cubas, toda la ayuda que me ha proporcionado a lo largo del doctorado. Quiero dar las gracias especialmente a los alumnos de la 4ª promoción del MUSE, que colaboraron en la sesión CDF de la que partió el diseño del CalSat, y a la gente del Instituto de Física de Cantabria, quienes trajeron dicho proyecto a mis manos. Gracias también a David Pérez, que contribuyó a los primeros pasos del GNC del CalSat, a Ismael Embarek, que tanto ha colaborado conmigo en el análisis de colisión, a Juan Luis Cano, Álvaro Leyva, Leonardo Ruo y José María Vergara, sin cuyo trabajo mubody no existiría. A Alexandra Elbakyan, cuya contribución a la ciencia no puede cuantificarse. A Thibault, Andrea, Simon y toda la gente de SUPAERO, por su amabilidad y hospitalidad en Toulouse. A Álvaro Flores, cuyos consejos me permitieron empezar a escribir. A Rafa, de cuyos férreos principios he aprendido mucho. A Josemi, Miki y Sergio, por tantas risas en un despacho y soportar mis malos días. A David, por estar siempre dispuesto a echarme una mano y contar conmigo. A Ángel, quien me ha ayudado enormemente a recuperar el ánimo este año. A Alejandro, por saber escuchar y ser siempre generoso con su tiempo. A David Santos, en quien encontré a un compañero para aprender y no solo estudiar. Gracias a todos los profesores que me han inspirado desde pequeño, en especial a Iván, Matilde, Joaquín, Emilio y Esteban.

A mis tíos, que son como mis segundos padres. A Susana, que me inspiró y animó a ser ingeniero. A mis padres y mi hermana, que nunca han dejado de apoyarme y siempre han estado ahí. Y, por último, a la persona más importante de mi vida, Lidia. Tú me has animado en los momentos más bajos, me has ayudado en cada paso y has arrojado una luz que me ha permitido entenderme mejor a mi y a los demás.

Vámonos, los astros no esperan a nadie.

Contents

Agradecimientos **III**

Abstract **XI**

Resumen **XIII**

List of Figures **XXII**

List of Tables **XXV**

Nomenclature **XXVI**

1 Introduction **1**

1.1 Mission analysis definition 1

1.2 Motivation 2

1.3 Problem statement 3

1.4 Thesis objectives 5

1.5 Methodology 6

1.6 Literature production 6

1.7 Document structure 7

2 Dynamics at libration points **9**

2.1 CRTBP model 10

2.1.1 Equations of motion 12
2.1.2 Jacobi constant 13
2.1.3 Location of libration points 13
2.1.4 Zero velocity surfaces 15
2.1.5 Linearization of equations of motion at libration points . . . 16
2.1.6 Stability 17
2.2 Libration point orbits 18
2.2.1 Periodic and quasi-periodic orbits 18
2.2.2 State transition matrix 20
2.2.3 Stability of periodic orbits 20
2.2.4 Orbit generation 21
2.2.5 Station-keeping 23
2.3 Manifolds and low-energy transfers 24
2.4 Ephemeris model 26
2.4.1 Solar radiation pressure 27
2.4.2 Coordinate transformation 28
2.5 Other models 29
2.5.1 Elliptical model 29
2.5.2 Bicircular Restricted Four-Body Problem 30

3 Control of formations **33**
3.1 GNC system 34
3.1.1 Local coordinate frame 35
3.1.2 Inputs 35
3.1.3 On-board GNC 36
3.1.4 Plant 36
3.2 Linear relative motion model 38
3.3 Relative state estimation: Kalman filter 40
3.4 Control strategy design 42
3.4.1 Control laws 43
3.4.2 Control modes 48
3.5 Simulations in High-Fidelity Dynamics 48
3.5.1 Reference mission scenario 48

3.5.2 Figures of merit 50
3.5.3 Implementation 50
3.5.4 Simulations results 51

4 Collision risk assesment 69
4.1 Collision risk probability 70
4.1.1 Triple-integral 71
4.1.2 Integral simplification 73
4.1.3 Propagation of covariance matrix 77
4.2 Numerical validation 79
4.3 Case of study 82
4.4 Discussion of results 86

5 Visibility analysis 87
5.1 Scanning strategy and relative position 88
5.1.1 Numerical modelling 92
5.2 Access analysis 94
5.2.1 Total access time 94
5.2.2 Mean access time 98
5.2.3 Maximum access time 102
5.3 Analysis of viewed detectors 110
5.3.1 Detectors and signal polarization models 110
5.3.2 Numerical results of detectors analysis 112
5.4 Application example 113
5.4.1 Discussion of results 118

6 Mission proposal of an ancillary calibration satellite for a CMB satellite located at L_2 121
6.1 Mission concept, objectives, and requirements 121
6.1.1 Objectives 122
6.1.2 Requirements 122
6.2 Mission description 126
6.2.1 Modes of operation 129
6.2.2 Nominal orbit 130

6.3 Environment 131
6.4 Visibility analysis 135
6.5 CS Support System 137
6.5.1 BaseCalsat 138
6.5.2 Deployable solar panel 138
6.5.3 Mechanical interface with the CMB satellite 139
6.5.4 Power 141
6.5.5 Communications 142
6.5.6 Mass budget 142
6.6 CalSat 143
6.6.1 Payload 143
6.6.2 ADCS 145
6.6.3 GNC 146
6.6.4 OBDH 147
6.6.5 Propulsion 148
6.6.6 Power 149
6.6.7 Thermal control 151
6.6.8 Communications 152
6.6.9 Structure and configuration 153
6.7 Collision risk assessment 156
6.8 Cost budget 157

7 Conclusions **161**

Appendices **165**

A Code repositories **167**

B Libration points location **169**
B.1 Collinear points 169
B.2 Triangular points 171

C Linearization of CRTBP equations **173**

D Multiple-shooting scheme **177**

E Coordinate systems **181**

E.1 Spherical coordinate system 181

Bibliography **182**

Abstract

Formation flying (FF) in space missions is receiving increasing attention in recent years due to its potential advantages, making the number of planned and launched missions of this type grow. Moreover, there has been a significant increase in the utilization of micro and nanosatellites which has improved the accessibility to space technology, which benefits the development of new formation flying missions. This mission concept aims to improve the science return, the redundancy of the mission, and its flexibility compared with a single large and complex satellite. The purpose of this thesis is to study the feasibility of employing a calibration ancillary satellite on a chief-deputy formation with a CMB observation mission in L_2. For that purpose, some of the main current challenges of FF will be tackled by developing tools that will help to analyze these problems, especially during the early stages of the mission design process (Phase 0/A). In particular, the following aspects of the mission have been studied: the design and analysis of a GNC subsystem for the ancillary satellite, the collision risk of the formation in the case of critical failure of the deputy, and visibility between the formation satellites, based on the CMB satellite attitude and its instrument characteristics. Then, these methods will be applied to elaborate a mission proposal based on CubeSat architecture, through which the feasibility of such a mission will be analyzed. This calibration satellite could significantly increase the accuracy of the CMB satellite measurements with a limited impact on its architecture.

Resumen

El vuelo en formación en misiones espaciales está recibiendo una atención creciente en los últimos años debido a sus ventajas potenciales, lo que ha llevado al aumento en el número de misiones de este tipo planeadas y lanzadas. Además, ha habido un aumento significativo en la utilización de micro y nanosatélites, lo que ha mejorado la accesibilidad a la tecnología espacial y beneficia el desarrollo de nuevas misiones de formación en vuelo. Este concepto de misión busca mejorar el rendimiento científico, la redundancia y su flexibilidad en comparación con un solo satélite grande y complejo. El propósito de este estudio es evaluar la viabilidad de emplear un satélite auxiliar de calibración en una formación principal-delegada con una misión de observación de la radiación cósmica de fondo (CMB) en el punto L2. Con este fin, se abordarán algunos de los principales desafíos actuales de la formación en vuelo mediante el desarrollo de herramientas que ayudarán a analizar estos problemas, especialmente durante las primeras etapas del proceso de diseño de la misión (Fase 0/A). En particular, se han examinado los siguientes aspectos de la misión: el diseño y análisis de un subsistema de GNC (guiado, navegación y control) para el satélite auxiliar, el riesgo de colisión de la formación en caso de fallo crítico del satélite auxiliar y la visibilidad entre los satélites de la formación, basada en la actitud del satélite CMB y las características de sus instrumentos. Luego, se aplicarán estos métodos para elaborar una propuesta de misión basada en la arquitectura de CubeSat, a través de la cual se analizará la viabilidad de dicha misión. Este satélite de calibración podría aumentar significativamente la precisión de las mediciones del satélite CMB con un impacto limitado en su arquitectura.

List of Figures

1.1 The anisotropies of the Cosmic Microwave Background (CMB) as observed by Planck mission. Image: ESA/PLANCK. 3

1.2 Artist's view of two satellites in formation flying. Nearby to the left, the proposed calibration system hosted by a 6U CubeSat, while to the right and in the distance a satellite for CMB polarization measurements is visible. 4

1.3 Artist's view of formation flying concepts for space missions. Images: ESA. 4

2.1 Synodic reference frame used in the CRTBP model. 11

2.2 Scheme of the libration points location in the synodic frame. 14

2.3 Value of the Jacobi constant for the points of the xy-plane of a system with $\mu = 0.3$. 14

2.4 Zero velocity surface of the Sun-Earth/Moon system. 16

2.5 Examples of periodic (halo) and quasi-periodic (Lissajous) orbits around the second libration point of Sun-Earth system. 19

2.6 The single-shooting differential correction method. 22

2.7 Multiple-shooting applied to a trajectory divided into five segments. 23

2.8 Transference trajectories based on the unstable and stable manifolds of a halo orbit at L_1 of the Earth-Moon system. Extracted from [53]. 24

2.9 Saddle point vector field. Extracted from [53]. 25

2.10 Coordinate transformation scheme. 29

2.11 Bicircular Restricted Four Body Problem in the Earth-Moon rotating frame. Extracted from [69]. 30

3.1 Functional diagram of the GNC system. 35

3.2 Scheme of the local coordinate frame, which is parallel to the synodic frame and centered in the chief. 35

3.3 Scheme of the Kalman filter. 40

3.4 Scheme of the Equitime Trageting Method. 44

3.5 Model Predictive Controller (receding-horizon) scheme. 45

3.6 Chief's nominal orbit around the L_2 point of the Sun-Earth system. 49

3.7 Scheme of the implementation of the GNC system. Green blocks represent the simulator operation, blue blocks correspond to GNC algorithms, red blocks are related to dynamics, yellow blocks represent models of the spacecrafts and their components and the purple block are options from the simulator. 51

3.8 Evolution of the relative position error (e_r) during calibration using the LQR controller. 53

3.9 Evolution of the relative velocity error (e_v) during calibration using the LQR controller. 53

3.10 Control applied during calibration using the LQR controller. 54

3.11 Evolution of the relative position error (e_r) during calibration using the MPC controller. 54

3.12 Evolution of the relative velocity error (e_v) during calibration using the MPC controller. 55

3.13 Control applied during calibration using the MPC controller. 55

3.14 Evolution of the relative position error (e_r) during stand-by using the ETM controller. 58

3.15 Evolution of the relative velocity error (e_v) during stand-by using the ETM controller. 58

3.16 Control applied during stand-by using the ETM controller. 59

3.17 Evolution of the relative position error (e_r) during stand-by using the MPC controller. 59

3.18 Evolution of the relative velocity error (e_v) during stand-by using the MPC controller. 60

3.19 Control applied during stand-by using the MPC controller. 60

3.20 Evolution of the relative position during reconfiguration using the ETM controller. 62

3.21 Evolution of the relative velocity error during reconfiguration using the ETM controller. 63

3.22 Control applied during reconfiguration using the ETM controller. . 63

3.23 Evolution of the relative position during reconfiguration using the MPC controller. 64

3.24 Evolution of the relative velocity during reconfiguration using the MPC controller. 64

3.25 Control applied during reconfiguration using the MPC controller. . 65

3.26 Evolution of the relative distance between chief and deputy during the reconfiguration maneuver for different controllers. 66

4.1 Combined error ellipsoid centered on secondary and safety sphere centered in primary. 71

4.2 Scale of error ellipsoid according to $n\sigma$ value. Extracted from [98]. 72

4.3 Encounter region for the cumulative probability of collision. Extracted from [53]. 73

4.4 Spherical coordinates and the local coordinate frame associated. . . 74

4.5 View of the uv-plane. 74

4.6 Geometry of spheroidal cap. 75

4.7 Scheme showing the geometric interpretation of the integral limits ρ_1 and ρ_2. 76

4.8 Changes in the encounter region according to the geometry of the error ellipsoid compared to the sphere. 76

4.9 Encounter region and integration limits for the cumulative probability of collision. 77

4.10 Example of time evolution of the instantaneous and cumulative probabilities of collision. 78

4.11 Comparison of numerical and analytical approaches for the cumulative probability of collision. 80

4.12 Comparison of numerical and analytical approaches for the instantaneous probability of collision. 80

4.13 Error between analytical and numerical solutions of the cumulative probability of collision for different values of N. 81

4.14 Error between analytical and numerical solutions of the instantaneous probability of collision for different values of N. 81

4.15 Comparison between analytical solution and numerical solutions for different relative orientations. 81

4.16 Comparison between analytical solution and numerical solutions for different relations of area-to-mass ratio of the formation $f = \frac{A_c/m_c}{A_d/m_d}$. 82

4.17 Time evolution of the probability of collision for different formation sizes (d). 83

4.18 Time evolution of the probability of collision for different safety sphere radius (D). 83

4.19 Time evolution of the probability of collision for different values of the longitudinal uncertainty ($\sigma_{\dot{u}}$). 84

4.20 Time evolution of the probability of collision for different values of lateral uncertainty ($\sigma_{\dot{v}}$). 84

4.21 Maximum value of the probability of collision as a function of the formation size (d) and the safety sphere radius (D). 85

4.22 Maximum value of the probability of collision as a function of the longitudinal uncertainty ($\sigma_{\dot{u}}$) and the formation size (d). 85

4.23 Maximum value of the probability of collision as a function of the lateral ($\sigma_{\dot{v}}$) and longitudinal ($\sigma_{\dot{u}}$) uncertainties. 85

5.1 Pseudo-inertial coordinate frame (0) and attitude motion scheme. . 88

5.2 Orthographic projection of the scan pattern for $\alpha = 45°$, $\beta = 50°$, $T_{spin} = 10$ min, and $T_{prec} = 90$ min. 90

5.3 Change of the scan pattern morphology according to the relation between angles α and β. In both cases $T_{spin} = 10$ min and $T_{prec} = 90$ min. 90

5.4 Change in the scan pattern due to the value of the combined motion period. For (a), the resulting period of the combined motions is $T_{comb} = 190$ min while for (b), the resulting period is $T_{comb} = 970$ min. In both cases $\alpha = 45°$ and $\beta = 50°$. 91

5.5 Pseudo-inertial reference frame and definition of φ and θ coordinates. 92

5.6 Discretization of an sphere following HEALPix approach. From [103]. 93

5.7 Geometrical scheme for the simplified case considered. Note that $\boldsymbol{q}^*$ will move vertically as φ_v changes. 95

5.8 Variation of the percentage of access time regarding the total time considered as a function of coordinate φ. Parameters considered: $T_{sim} = 1$ day, $\alpha = 45°$, $\beta = 50°$, $T_{spin} = 10$ min, $T_{prec} = 93$ min, and $\delta = 7.5°$. 97

5.9 Total access time. Parameters considered: $T_{sim} = 1$ day, $\alpha = 45°$, $\beta = 50°$, $T_{spin} = 10$ min, $T_{prec} = 93$ min, and $\delta = 7.5°$. 97

5.10 Comparison (a) and error (b) between the analytical and numerical results for the variation of the total access time as a function of coordinate φ. Parameters considered: $T_{sim} = 1$ day, $\alpha = 45°$, $\beta = 50°$, $T_{spin} = 10$ min, $T_{prec} = 93$ min, and $\delta = 7.5°$. 98

5.11 Geometrical scheme for the mean access time when precession is negligible. 99

5.12 Variation of the mean access time as a function of coordinate φ for negligible Ω. Parameters considered: $T_{sim} = 1$ day, $\alpha = 45°$, $\beta = 50°$, $T_{spin} = 10$ min, and $\delta = 7.5°$. 100

5.13 Geometrical scheme for mean access time when precession speed is significant. Only the trace for half T_{spin} period is shown. 100

5.14 Variation of the mean access time as a function of coordinate φ, with $\Omega < \omega$ but not negligible. Parameters considered: $T_{sim} = 1$ day, $\alpha = 45°$, $\beta = 50°$, $T_{spin} = 10$ min, $T_{prec} = 93$ min, and $\delta = 7.5°$. . . . 101

5.15 Mean access time. Parameters considered: $T_{sim} = 1$ day, $\alpha = 45°$, $\beta = 50°$, $T_{spin} = 10$ min, $T_{prec} = 93$ min, and $\delta = 7.5°$ 102

5.16 Comparison (a) and error (b) between the analytical and numerical results for the mean access time as a function of coordinate φ. Parameters considered: $T_{sim} = 1$ day, $\alpha = 45°$, $\beta = 50°$, $T_{spin} = 10$ min, $T_{prec} = 93$ min, and $\delta = 7.5°$. 102

5.17 New reference system defined. 103

5.18 Trace of the direction vector over the FOV for different φ^* coordinates.104

5.19 Variation of the maximum access time as a function of coordinate φ for Ω negligible. Parameters considered: $T_{sim} = 1$ day, $\alpha = 45°$, $\beta = 50°$, $T_{spin} = 10$ min, and $\delta = 7.5°$. 105

5.20 Scheme of how the precession speed Ω (black) would be added or subtracted to spin speed ω (red) according to whether $\alpha > \beta$ or $\alpha < \beta$.106

5.21 Definition of γ, projecting the precession velocity vector over the spin velocity vector. 107

5.22 Geometrical scheme of the approach followed to obtain γ. 108

5.23 Variation of the maximum access time as a function of coordinate φ for a non-negligible Ω. Parameters considered: $T_{sim} = 1$ day, $\alpha = 45°$, $\beta = 50°$, $T_{spin} = 10$ min, $T_{prec} = 93$ min, and $\delta = 7.5°$. 109

5.24 Maximum access time. Parameters considered: $T_{sim} = 1$ day, $\alpha = 45°$, $\beta = 50°$, $T_{spin} = 10$ min, and $\delta = 7.5°$. 109

5.25 Comparison (a) and error (b) between the analytical and numerical results for the maximum access time as a function of coordinate φ. Parameters considered: $T_{sim} = 1$ day, $\alpha = 45°$, $\beta = 50°$, $T_{spin} = 10$ min, and $\delta = 7.5°$. 110

5.26 Layout of the array of detectors. 111

5.27 Simplified optical model considered. Each possible direction within the FOV maps one unique point in the focal plane. 112

5.28 Numerical results for the percentage of viewed detectors and the $G(\xi)$ parameter. Parameters considered: $T_{sim} = 1$ day, $\alpha = 45°$, $\beta = 50°$, $T_{spin} = 10$ min, $T_{prec} = 93$ min, and $\delta = 7.5°$. 113

5.29 Variation of the total access time as a function of coordinate φ for different values of α parameter. In all cases $\alpha + \beta = 95°$. Parameters considered: $T_{sim} = 1$ day, $T_{spin} = 10$ min, $T_{prec} = 93$ min and $\delta = 7.5°$. 114

5.30 Comparison between the variation of T_{mean} and the variation of T_{max} as functions of coordinate φ. 115

5.31 Variation of T_{mean} and T_{max} as functions of coordinate φ for different values of the T_{spin} parameter. 115

5.32 Variation of T_{mean} and T_{max} as functions of coordinate φ for different values of the T_{prec} parameter. 115

5.33 Variation of T_{mean} and T_{max} as functions of coordinate φ for different values of α. 116

5.34 Comparison between the variation of ρ and the variation of $G(\xi)$ as functions of coordinate φ. 116

5.35 Variation of ρ and $G(\xi)$ as functions of coordinate φ for different values of T_{sim}. 117

5.36 Variation of ρ and $G(\xi)$ as functions of coordinate φ for different values of T_{comb}, which are achieved keeping T_{spin} constant and using a T_{prec} of 90 min, 93 min and 93.1 min for T_{comb} cases of 430 min, 930 min and 93100 min, respectively. 117

5.37 Variation of ρ and $G(\xi)$ as functions of coordinate φ for different values of α. 118

6.1 View of CalSat with its solar panels deployed. 126

6.2 APC (grey platform), BaseCalSat (green box) and CalSat deployer (blue box) attached to the CMB satellite. 127

6.3 Diagram of the relative locations between the CMB satellite and CalSat during the different phases of the mission. 128

6.4 Diagram of the operational modes and their transitions. The mission subphase associated to the operational mode is indicated in bold. . 130

6.5 Representation of the nominal Lissajous orbit around L_2. 131

6.6 Simplified structure of the magnetosphere and its position relative to Earth and L_2 (left) and cross section (right). The magnetic tail is deflected with respect to the anti-Sun direction due to the solar wind. Extracted from [111]. 132

6.7 Ion spectra for 10 years at L_2 for solar and galactic sources. Extracted from [110]. 133

6.8 Detectors layout used for the simulations showing and example of detectors illuminated by the reference signal after the CS crosses 3 times the instrument FOV during calibration. The blue line indicates the limit of the FOV. 135

6.9 Percentage of viewed detectors for different periods of time according to the position of CalSat relative to the CMB satellite. 135

6.10 Total access time according to the position of CalSat relative to the CMB satellite. 136

6.11 Mean access time according to the position of CalSat relative to the CMB satellite. 136

6.12 Total access time according to the position of CalSat relative to the CMB satellite and with a FOV of 120°. 137

6.13 Front view of the deployable solar panel. 138

6.14 Rear view of the deployable solar panel with the patch antennas used for communications and relative positioning. 139

6.15 Auxiliary Payload Carrier attached to Centaur launcher. Extracted from [119]. 140

6.16 ISIS 6U DuoPack Deployer. 141

6.17 ISIS 2U ISIPOD Deployer. 141

6.18 Calibration source diagram. 144

6.19 Calibration source front view. 145

6.20 Scheme of the GNC system of CalSat. 146

6.21 Representation of an analogous thrusters distribution. Extracted from [78]. 149

6.22 Solar panels view. The solar cells are arranged to maximize the occupation factor. 149

6.23 Rear side. 152

6.24 Relative position hardware “Swift RelNav” by Testhers Unlimited. . 153

6.25 3D model of the 6U structure from Endurosat. 153

6.26 Preliminary design configuration. 154

6.27 Exploded view of CalSat subsystems. 154

6.28 Evolution of the collision risk for a nominal distance of 6600 m and a safety sphere with a radius of 5 m. 156

6.29 Maximum probability of collision for different formation distances and safety spheres sizes. 157

6.30 Cost Breakdown Structure for CalSat Mission. 158

B.1 Location of the collinear libration points regarding the closest primary.171

D.1 Multiple-shooting scheme. 177

E.1 Spherical coordinates and the local coordinate frame asociated. . . 182

List of Tables

2.1 Mass ratio and normalization quantities for distance, time, and velocity of different primaries systems of the Solar System. 11

3.1 Thrusters characteristics employed in the simulation. 37

3.2 Sensor noise characteristics. 38

3.3 Parameters used for the W and V covariance matrices. 42

3.4 Parameters of the chief's nominal orbit. 49

3.5 Physical parameters of the chief and deputy required for the SRP perturbation. 50

3.6 Initial condition and target state for Calibration mode. 52

3.7 LQR configuration parameters for the Calibration mode. 52

3.8 MPC configuration parameters for the Calibration mode. 52

3.9 Achieved relative position control accuracy when using LQR and MPC controllers in calibration phase. The results correspond to the RMSE value of e_r components, in cartesian and spherical coordinates. 56

3.10 Achieved relative velocity control accuracy when using LQR and MPC controllers in calibration phase. The results correspond to the RMSE value of e_v components, in cartesian and spherical coordinates. 56

3.11 ΔV results with each of the control laws in the Calibration mode simulations. 56

3.12 Initial condition and target state for Stand-by mode. 57

3.13 ETM configuration parameters. 57

3.14 MPC configuration parameters for the Stand-by mode. 57

3.15 ΔV results with each of the control laws in the Stand-by mode simulations. 61

3.16 Initial condition and relative target state for Reconfiguration mode. 61

3.17 ETM configuration parameters for the Reconfiguration mode. . . . 61

3.18 MPC configuration parameters for the Reconfiguration mode. . . . 62

3.19 ΔV results with each of the control laws in the Reconfiguration mode simulations. 65

4.1 Characteristics of the flight formation mission studied. 79

6.1 System-level requirements for the CalSat mission. 123

6.2 Attitude determination and control system requirements. 124

6.3 Communications system requirements. 124

6.4 Electrical power system requirements. 124

6.5 Guidance navigation and control system requirements. 125

6.6 On-board data handling system requirements. 125

6.7 Propulsion system requirements. 125

6.8 Structure requirements. 126

6.9 Thermal control system requirements. 126

6.10 Components of the calibration system for the CMB mission. 127

6.11 Parameters of the nominal orbit chosen for the CMB satellite. . . . 130

6.12 Specifications of the components of BaseCalSat. 138

6.13 APC specifications. 139

6.14 ISIS 6U DuoPack Deployer specifications. 140

6.15 Breakdown of CS Support System mass. 142

6.16 Summary of characteristics of the Payload. 143

6.17 ADCS components and their specifications. From [122]. 145

6.18 Achieved position and velocity accuracy for the calibration phase. Spherical components. 146

6.19 ΔV in each phase for the whole mission (6 calibrations). 147

6.20 Total ΔV budget. 147

6.21 NanoMind Z7000 GomSpace on-board computer main specifications. 148

6.22 NanoProp GP3 GomSpace propulsion module. 148

6.23 Power generation parameters. 150

6.24 Power generated at the beginning and at the end of the mission. . . 150
6.25 Power consumption for different operational modes. 151
6.26 Battery specifications [117]. 151
6.27 Thermal and optical properties of the model. 152
6.28 Subsystem dimensions 155
6.29 Subsystem masses. 155
6.30 Subsystem masses. 155
6.31 Space Segment Costs. 159
6.32 Project level costs. Element costs in italics are not considered for the computation of the Total project Level without global mission costs. 159
6.33 Mission overall costs. 160
6.34 Distribution of costs among the development phases of the project. 160

Nomenclature

Acronyms/Abbreviations

ADCS	Attitude Determination and Control System
APC	Auxiliary Payload Carrier
AU	Astronomical Unit
BCS	BaseCalSat
BOL	Beginning of Life
BPF	Band-Pass Filter
CAL	Calibration sub-phase
CDF	Concurrent Design Facility
CH	Conical Horns
CMB	Cosmic Microwave Background
COM	Communications Subsystem
COTS	Commercial off-the-shelf
CRTBP	Circular Restricted Three-Body Problem
CS	CalSat
CW	Continuous Wave
DC	Directional Coupler

DE	Design requirement
EKF	Extended Kalman Filter
EOL	End of Life
EPS	Electric Power System
ERTBP	Elliptical Restricted Three-Body Problem
ESA	European Space Agency
ETM	Equitime Targeting Method
FDIR	Fault, Detection, Isolation and Recovery
FF	Formation Flying
FFP	Formation Flying Phase
FM	Frequency Multipliers
FOV	Field of View
FU	Functional requirement
GEO	Geosynchronous Equatorial Orbit
GNC	Guidance, Navigation and Control System
GNSS	Global Navigation Satellite System
GPS	Global Positioning System
GTBP	General Three Body Problem
IFCA	Instituto de Física de Cantabria
LoS	Line-of-sight
LPO	Libration Point Orbit
LQR	Linear Quadratic Regulator
MLI	Multi-layer Insulation
MPC	Model Predictive Controller
NS	Noise Source
OBC	On-Board Computer
OBDH	On-Board Data Handling

OP	Operational requirement
PA	Power Amplification
PAY	Payload
PE	Performance requirement
PIN	P-type, Intrinsic semiconductor, N-type
POS	Positioning sub-phase
PRO	Propulsion Subsystem
RAM	Random Access Memory
RF	Radio Frequency
RH	Rectangular Horns
S/C	Spacecraft
SA	Solar Array
SBO	Stand-by Orbit sub-phase
SEM	Safe Escape Manoeuvre
SEP	Solar Energetic Particles
SNR	Signal-to-Noise Ratio
SRP	Solar Radiation Pressure
STM	State Transition Matrix
STR	Structure
SYS	System
TCS	Thermal Control System
VA	Variable Attenuator
WGP	Wire-Grid Polarisers
ZBD	Zero-Bias-Detector
ZVS	Zero Velocity Surface

Dynamics of Libration Points

$\boldsymbol{r}_{O_f,O_i}$	Position vector of O_i relative to O_f expressed in the coordinate system f

$\boldsymbol{r}_{qi}$	Position vector of body j regarding central body
$\boldsymbol{r}_{sv}$	Relative position of Sun regarding the S/C
$\boldsymbol{v}_{O_f,O_i}$	Velocity vector of O_i relative to O_f expressed in the coordinate system f
$\boldsymbol{X}$	Third body state in the synodic frame
$\dot{R}_{fi}$	Time derivative of R_{if}
λ, ν	Frequencies of the analytical solution for LPO
$\mathcal{M}$	Monodromy matrix
μ	CRTBP mass ratio
μ_s	Nondimensional mass of the Sun
ν	True anomaly of the primaries orbit
ω	Angular velocity of the Sun
Φ	State Transition Matrix
ϕ, ψ	Phase angles of the analytical solution for LPO
ρ_1, ρ_2	Distance from the third body to the primaries
θ	Sun angle
ε	Perturbation factor
$\widetilde{\omega}$	BCR4BP pseudopotential
A	Matrix of linearized system about the trajectory
a	Semi-major axis of the primaries orbit
a_s	Nondimensional distance between B_1 and the Sun
A_y, A_z	Amplitudes of the analytical solution for LPO
A_{L_p}	Matrix of linearized system about the libration point
A_{sc}	Area of the spacecraft
B_1	Earth-Moon barycenter
B_2	Sun-Earth/Moon barycenter
C	Jacobi constant
c	Speed of light

c_R	Reflection coefficient
e	Eccentricity of the primaries orbit
G	Gravitational constant
l^*	Length characteristic quantity
L_1, L_2, L_3	Collinear libration points
L_4, L_5	Triangular libration points
m^*	Mass characteristic quantity
m_1, m_2	Primaries' masses
m_3	Third body mass
m_j	Mass of celestial body j
m_q	Mass of the central body
m_{sc}	Mass of the spacecraft
n_s	Nondimensional mean motion of the Earth-Moon system
$O_{i,j}$	Origin of frames i, j
P	Solar flux
P_0	Solar flux at 1 AU
R	Sun-S/C distance
R_0	Sun-Earth mean distance
r_1, r_2	Primaries's position vectors
R_{if}	Rotation matrix from coordinate system i to coordinate system f
t^*	Time characteristic quantity
U	CRTBP pseudopotential
U^*	ERTBP pseudopotential
v^*	Velocity characteristic quantity
$W_i^{s,u}$	Eigenvectors of the monodromy matrix
x_1, x_2	Primaries' position in synodic frame $x-$axis
x_L	Distance from the collinear libration point to the synodic frame origin

x_s, y_s, z_s Sun position regarding B_1

Mission Proposal

η_{cell} Cell efficiency

A_{cell} Solar cell area

C_{batt} Battery capacity

E Solar irradiance

EOL End of Life

L_d Lifetime degradation index

m_D Dry mass

m_D Propellant mass

n_{cell} Number of solar cells

P_{tot} Excess of power consumed in Calibration mode

t_{on} Amount of time that the payload can be turned on

Visibility

α Precession axis angle

β Instrument axis angle

$\boldsymbol{n}$ Unitary normal to the trace

$\boldsymbol{p}_{\varphi}$ Arbitrary direction

$\boldsymbol{p}_{cd}$ Unit vector of the deputy position relative to the chief

$\boldsymbol{q}$ Instrument pointing direction

$\boldsymbol{q}'$ Derivate of instrument pointing direction

$\boldsymbol{q}^*$ Equivalent vertical motion of the instrument

$\boldsymbol{q}_0$ Starting position of the instrument direction

$\boldsymbol{q}_e$ Exterior curve direction

$\boldsymbol{q}_i$ Interior curve direction

$\boldsymbol{r}_{cd}$ Deputy position relative to the chief

$\boldsymbol{r}_{chief}$ Chief position vector

$\boldsymbol{r}_{deputy}$	Deputy position vector
$\boldsymbol{u}_{spin}$	Spin axis direction
$\boldsymbol{v}_{prec}$	Precession velocity unitary vector
$\boldsymbol{v}_{spin}$	Spin velocity unitary vector
δ	Half-angle of instrument FoV
γ	Projection of $\boldsymbol{v}_{prec}$ over $\boldsymbol{v}_{spin}$
λ	Wavelength of signal
Ω	Precession speed
ω	Spin speed
ϕ	Spin angle
ψ	Precession angle
ρ	Percentage of viewed detectors
τ	Auxiliary angle to describe $\boldsymbol{v}_{prec}$
θ_{φ}	Half-arc angle of directions with the same φ coordinate inside the FoV
θ^*_{φ}	Half-arc angle of a direction trajectory inside the FoV
ε	Angular size
φ, θ	Coordinates in the pseudo-inertial reference frame
φ^*, θ^*	Coordinates in the instrument frame
$\varphi^*_{t_{max}}$	Value of φ^* coordinate to achieve t_{max}
φ_e, θ_e	Coordinates of exterior curve
φ_i, θ_i	Coordinates of interior curve
φ_v	Angle between instrument direction and X_0-axis
ζ	Spatial separation between sequential trace rings
$C_{0,b}$	Satellite attitude matrix
$C_{0,inst}$	Instrument attitude matrix
$C_{b,inst}$	Instrument mounting matrix
D	Distance between satellites

d	Size of emitting source
dT	Time step
f_m	Fraction of directions that have been inside the FoV after one spin period
f_t	Average fraction of directions inside the FoV in one spin period
$G(\xi)$	Angular coverage parameter
N	Number of accesses
$q(t)$	Instrument pointing direction
R	Rotation matrix around the spin axis
t_1, t_2, t_3	Maximum access time according to φ coordinate
T_{access}	Access time
T_{comb}	Period of the combined motion of precession and spin motions
T_{max}	Maximum access time
t_{max}	Optimum access time
T_{mean}	Mean access time
T_{prec}	Precession motion period
T_{sim}	Simulated time
T_{spin}	Spin motion period
T_{total}	Total access time
x_e, y_e, z_e	Cartesian coordinates of exterior curve
x_i, y_i, z_i	Cartesian coordinates of interior curve
Re[x]	Real part of x

CHAPTER 1

Introduction

This chapters provides an introduction to the content of this doctoral dissertation. First, some remarks are made about the meaning and use of the term “mission analysis”. Then, the motivation of this research is treated, followed by the problem statement and the thesis objectives. Afterward, the methodology used during the research is briefly presented. A summary of the literature production and a brief description of the structure of this doctoral dissertation are provided at the end of this chapter.

1.1 Mission analysis definition

As the title of this thesis indicates, the focus of this work is on the “mission analysis of formation flying at L_2”. But what exactly does “mission analysis” mean? This term is used ambiguously in the literature. For example, according to ESA [1], this concept refers to the analysis of satellite orbits to determine how best to achieve the objectives of a space mission. This includes trade-offs for selection of the nominal mission trajectory, definition of maneuvering strategies, optimization of orbital maneuvers, calculation of propellant budget, analysis of launch windows, analysis of orbit perturbations, and navigation. This definition is clearly centered on the orbital trajectory of the spacecraft and how it affects the rest of the mission. On the contrary, Wertz [2] provides a broader definition: “mission analysis is the process of quantifying the system parameters and the resulting performance (...). Ideally, in the mission analysis process, the different parameters and alternatives considered for the mission are varied and the effect of this variation on the parameters that flow from the mission choices (orbit type, its altitude, coverage parameters, etc.) and on the system’s quantitative outputs (which indicate its performance, effectiveness,

cost, and risk) is evaluated to consider different mission alternatives". In this case, mission analysis is not restricted to analyzing the spacecraft trajectory and its impact on the mission, but it covers the whole mission design.

The interpretation followed in this work is the latter. Therefore, the whole mission is studied, deepening in those aspects where required in order to answer the research questions proposed in this investigation.

1.2 Motivation

The scientific instruments on board satellites are becoming increasingly sensitive [3, 4]. To obtain measurements with an accuracy in line with such sensitivity, it is necessary to apply exhaustive calibration processes and error reduction algorithms to mitigate systematic errors [5, 6].

The calibration process is usually performed prior to flight and also during the mission [7]. Each case presents its own limitations. Pre-flight calibration is not always capable of reproducing the mission environment or the signal to be measured due to the laboratory constraints (size, technology, etc.). Furthermore, after calibration, the satellite experiences different environmental conditions during launch, orbital transfer, and eclipses, with subsequent thermal loads and vibrations, which can result in slight calibration drifts. During the mission, the main obstacles are that the signals from natural sources (moons, planets, compact objects, or even galaxies) are not known with the required accuracy and, due to their scanning strategies to cover the whole sky or the orbital position of the satellite, they do not always allow for the calibration of the instrumentation as required [8].

One well-known example of this issue is the case of Cosmic Microwave Background (CMB) space missions. These telescopes measure the microwave signals that arrive from all directions of space and that contain very valuable information about the origins of the universe. The primordial CMB signal (see Figure 1.1) was produced when the universe was about 380.000 years old and has a black-body spectrum that, at present, peaks in the microwave range at about 160 GHz. Its tiny anisotropies in temperature and even dimmer ones in polarization contain a wealth of information about the origin, matter and energy content and the evolution of the universe. However, their measurement represents a very difficult challenge and requires the use of ultra-sensitive telescopes with very accurate calibration procedures and exquisite control of systematic effects [9, 10, 11]. Some telescopes use the signal arriving from Jupiter as a reference for CMB intensity calibration, but it cannot be used for polarization calibration, as it is not polarized. If more precise scientific goals are to be achieved with sufficient success, a more robust in-flight calibration must be addressed for future missions.

In-flight calibration could be largely improved by using an ancillary small satellite which would fly in formation with the main satellite and would emit a precisely characterized reference signal. This concept was initially proposed to calibrate Ground-based CMB telescopes [12] and has been extended for CMB satellites located in Sun-Earth L_2 [13, 14]. This location is commonly used for astronomical missions due to its thermally stable environment (ideal for cryogenic missions),

low acceleration, and the possibility of observing the sky continuously without interference from Earth or the Moon [10, 11, 15]. These CMB telescopes have a given scan strategy, which defines its attitude motion in order to cover all the sky and collect data according to its scientific objectives [16, 17].

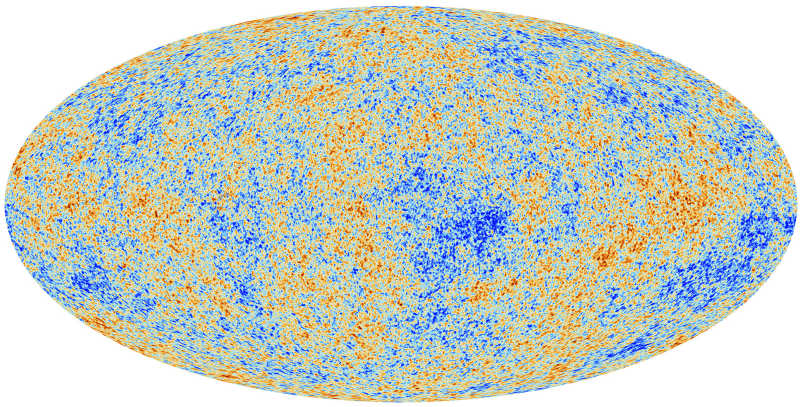


Figure 1.1: The anisotropies of the Cosmic Microwave Background (CMB) as observed by Planck mission. Image: ESA/PLANCK.

1.3 Problem statement

As stated in the previous section, the use of an ancillary small satellite could help address current calibration limitations in deep-space observation satellites. This thesis proposes a chief-deputy formation and examines its feasibility. In this type the formations, the chief (main satellite) moves independently while the deputy (ancillary satellite) locates itself around the chief, keeping the formation. Figure 1.2 provides an illustration of this proposed concept. During the operation, the calibration satellite would remain out of sight, so it does not interfere with the scientific observations. Then, when calibration is required, the deputy would move to a predefined location so that the calibration signal could reach the chief's instrument.

The use of formation flying (FF) in space missions has drawn increasing attention in recent years because of the advantages it offers and the potential for new missions [18]. The distribution of functions among multiple spacecraft that operate coordinately can increase the science return [13, 14, 19], the redundancy of the mission, and its flexibility compared to a single large and complex satellite. Furthermore, it enables new mission concepts that take advantage of techniques such as interferometry and coronagraphy (Figure 1.3) [20, 21, 22], and could help extend the lifetime of the mission [23, 24]. In spite of all the potential uses and advantages of employing FF in libration points and all the proposed missions in this direction, this concept has not yet been tested at such a location. While formation flying can provide the aforementioned advantages, its use brings into the mission new problems to be solved, such as maintaining formation and preventing collision between the satellites.

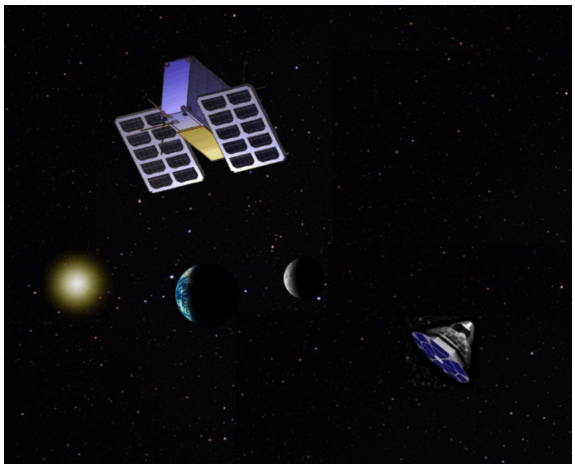
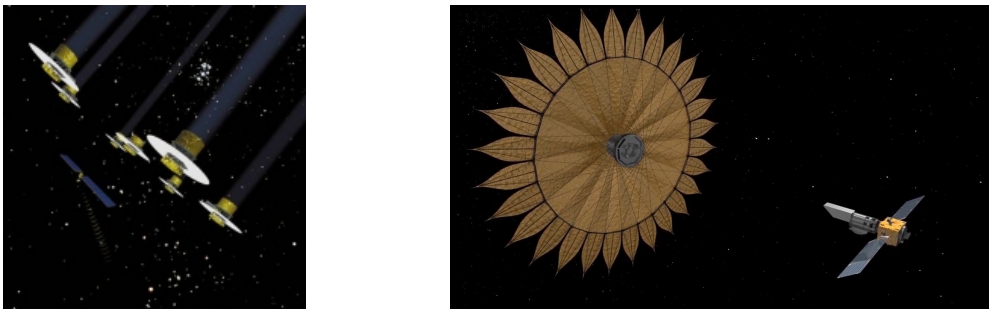


Figure 1.2: Artist's view of two satellites in formation flying. Nearby to the left, the proposed calibration system hosted by a 6U CubeSat, while to the right and in the distance a satellite for CMB polarization measurements is visible.

Small satellites, including CubeSats and nano-satellites, have revolutionized the space sector due to their reduced cost and launch opportunities [25]. They could be very useful for scientific missions [26, 27] and they have already been employed in several missions as ancillary satellites for support activities [28, 29] or as main satellite of the mission [30]. Their use in formation flying is also expanding [18, 31]. Their flexibility allows for scalable and adaptable formation configurations, enabling novel missions and research in formation flying technology. Nevertheless, their limited size imposes constraints on available power, communication, and computing capabilities, restricting the complexity of on-board instruments [32, 33, 34].



(a) Interferometry. **(b)** Coronagraphy.

Figure 1.3: Artist's view of formation flying concepts for space missions. Images: ESA.

One of the main challenges associated with FF is the design of a Guidance, Navigation, and Control (GNC) system that complies with mission requirements, which are becoming more demanding, particularly in science missions [35, 36, 37, 38]. In a chief-deputy formation, the GNC system of the deputy is in charge of keeping the formation, which can be challenging for small satellites [39, 40]. Furthermore, the GNC system for a mission located in a libration point orbit (LPO) has differ-

ent challenges compared to a FF orbiting Earth [41]: GPS unavailable, complex dynamics environment, and low thrust requirements.

Furthermore, the formations are susceptible not only to collisions with foreign objects passing through the formation, but also to collisions of satellites that might drift toward each other. In the case of the collinear libration points, their intrinsic instability keeps these regions clear from most debris, as any uncontrolled object will end up orbiting away from the libration point, into an ordinary heliocentric orbit. Nevertheless, there are situations, as in periodic stable orbits, where an uncontrolled satellite or debris can lead to repeated recontact risk [42] and must be taken into consideration. As for the operative satellites in these regions, they are safely located in orbits that cannot intersect, so there is no risk of collisions in these cases and its disposal is studied in detail prior its completion [43]. Regarding the risk of collision within the formation, the formation control enforced by the GNC subsystem shall prevent that either indirectly by keeping the formation or directly by including some type of collision avoidance system. However, the quantitative evaluation of the collision risk in case of a critical failure of the deputy is a valuable information from the mission design perspective.

For the proposed mission, there is an additional challenge, due to the attitude motion that CMB satellites normally have [44]. The extent of the sky region that is seen by the instrument at a given moment is called Field of View (FOV). Therefore, assuming that the deputy always emits its calibration signal pointing to the main satellite, the calibration will only occur when the deputy is inside the instrument FOV. Due to the chief's scan strategy, this only occurs in certain instants, and it is not intuitive when and how frequently it will happen [45]. This visibility problem must be taken into account, as it will determine how effective the calibration can be.

1.4 Thesis objectives

The main objective of this thesis is to study the feasibility of employing a calibration ancillary satellite for a CMB observation mission. To do so, first, some of the main challenges of FF described in the previous section will be tackled here by developing tools that will help to analyze these problems, especially during the early stages of the mission design process (Phase 0/A) [46]. In particular, the following aspects of the mission will be studied:

- Design and analysis of a GNC system for the deputy to control the formation.
- Collision risk assessment for the formation in case of critical failure of the deputy.
- Visibility analysis between the formation satellites, based on the CMB satellite attitude and its instrument characteristics.

Then, these methods will be applied to develop a mission proposal based on CubeSat architecture [47], through which the feasibility of such a mission will be analyzed.

1.5 Methodology

The methodology section outlines how the research questions and objectives were addressed. The diversity of the thesis objectives, the extended duration of the research, and the inevitable and unforeseen issues that arise as the work progress have resulted in different approaches to each objective, although with some common grounds.

The first step was a comprehensive review of the literature that established the groundwork for the study. This review identified key theories, concepts, and models relevant to the research area, establishing a strong theoretical foundation. The literature review informed the definition of key variables and provides methodological insights from previous studies. By avoiding duplication and ensuring alignment with existing knowledge, this initial step facilitated well-informed and purposeful research of the chosen topic.

The design and analysis of the GNC system were supported by the development of two simulators: an orbital mechanics simulators focused on libration points and a GNC simulator to implement the GNC architecture. On the basis of the latest developments in control of formations, the GNC system proposal was outlined and tested.

The collision risk assessment and the visibility analysis were carried out following the same approach, although they were solved separately. The procedure is as follows. Each particular problem was presented and then simplified by establishing several assumptions. This enabled the derivation of an analytical solution that is dependent on certain parameters of the formation. The analytical solution was then validated against numerical simulations of the whole problem. Finally, the analytical solution, which significantly reduces the computational cost compared to the numerical one, was used to explore the impact of the formation parameters on the problem at hand through a case of study.

Finally, the preliminary design of the ancillary satellite was performed by first defining the mission objectives and requirements and then designing each subsystem. This process has been iterative, with a continuous reformulation and refinement of the requirements and adjusting the design of all the subsystems accordingly.

All code used in this project has been made open source under a MIT license. Further details included in Appendix A.

1.6 Literature production

During the development of this doctoral dissertation, several articles were presented at conferences or published in scientific journals.

- Bermejo Ballesteros, J., García González, S., Cubas Cano, J., Casas Reinares, F., & Martínez González, E. (2019). Development of a calibration satellite for a CMB telescope flying in formation about L2 libration point. In 8th European Conference for Aeronautics and Aerospace Sciences (EUCASS).
- Casas, F. J., Martínez-González, E., Bermejo-Ballesteros, J., García, S., Cubas,

J., Vielva, P., & Sanz, A. (2021). L2-CalSat: A calibration satellite for ultra-sensitive CMB polarization space missions. Sensors, 21(10), 3361.

- Bermejo-Ballesteros, J., Cubas, J., Casas, F., & Martínez-González, E. (2022). Visibility study in a chief-deputy formation for CMB polarization missions. The Journal of the Astronautical Sciences, 69(3), 651-691.
- Bermejo Ballesteros, J., Vergara Pérez, J. M., Fernández Soler, A., & Cubas Cano, J. (2022, April). Mubody, an astrodynamics open-source Python library focused on libration points. In 4th Symposium on Space Educational Activities. Universitat Politècnica de Catalunya.
- Bermejo-Ballesteros, J., Cubas, J., Casas, F., & Martínez-González, E. (2022, November). Alternative analytic method for computing mean observation time in space-telescopes with spin-precession attitude motion. In AIP Conference Proceedings (Vol. 2611, No. 1). AIP Publishing.

1.7 Document structure

This doctoral dissertation has been divided into seven chapters. This first chapter has provided the motivation and objectives of this thesis. The second chapter provides the necessary background on the libration point dynamics for subsequent chapters. In the third chapter, a collision risk analysis of formation flying is performed. In the fourth chapter, the potential GNC system for the calibration satellite is outlined. The fifth chapter is focused on the visibility analysis of the formation, in order to determine the better position to locate the calibration satellite. In the sixth chapter, the overall feasibility of the mission is studied, based on the preliminary design of a 6U CubeSat. Finally, in the seventh chapter, the conclusions of this work are presented, including some potential lines of future work.

CHAPTER 2

Dynamics at libration points

The libration points are 5 points of equilibrium for small-mass objects which are under the gravitational influence of two massive bodies. Three of them (L_1, L_2, and L_3) were discovered by Euler around 1750 and the other two (L_4 and L_5) were discovered by the Italian-French mathematician Joseph Louis Lagrange around 1760, while working on the three-body problem [48]. Despite this, it is common in the literature to refer to all points as "Lagrange points" or "Lagrangian points".

As its name implies, the three-body problem studies the motion of three bodies under the influence of their mutual gravitational fields. In the most general case, when there are no restrictions in terms of the body masses and initial conditions, it is called the general three-body problem (GTBP), in which the motions of the objects may follow three-dimensional trajectories. Except in very special cases, this problem cannot be solved explicitly as with the two-body problem [49]. Although a power series solution for the general problem was found in 1912 [50], its convergence is so slow that it has no practical applications. Nevertheless, various simplifying assumptions lead to interesting cases in which periodic orbits can be found. The most well-known is the so-called circular restricted three-body problem (CRTBP). In this problem, the mass of one of the bodies is negligible compared to that of the other two, which are called primaries and are assumed to have circular orbits around their common barycenter. Is in this particular case in which the libration points appear as equilibrium points.

Although the CRTBP is an ideal model, it closely matches real scenarios that can be found in the Solar System, such as the Sun-Earth, Sun-Jupiter, or Earth-Moon systems. This model constitutes a good starting point for understanding the problem and studying its dynamics. Its use is greatly extended in the study of libration points

orbits (LPO) and interplanetary spacecraft trajectory design. Nevertheless, in order to obtain accurate results, any development based on the CRTBP must be tested against high-fidelity models that include perturbations such as the eccentricity of the primaries orbits, fourth-body perturbations, and the solar radiation pressure (SRP).

The dynamics of the libration points is an important example of non-Keplerian dynamics, which refers to the motion of objects in space that cannot be studied with the classical two-body model. In the case of the libration points, the gravitational influence of the primaries must be considered simultaneously to be able to model accurately the motion of a body in these regions. Non-Keplerian dynamics can also be found when there are non-spherical gravity fields (asteroids) or the magnitude of the perturbations is comparable to the main body attraction.

This chapter presents the dynamics of the libration points based on the CRTBP model, deriving the equations of motion and their equilibrium solutions (the libration points location), the orbits that can be found in these regions and how they are built, and the stability of motion from analyzing the phase space (manifolds). Finally, the ephemeris model, used for high-fidelity simulations, is presented.

2.1 CRTBP model

As stated above, in the circular restricted three-body problem, the primaries (m_1, m_2) have circular orbits. In this approach, the most massive primary is referred to with subscript 1 and the less massive with subscript 2. Thus:

$$m_1 > m_2 >> m_3 \tag{2.1}$$

where m_3 refers to the third body mass. In some cases, one of the primaries may have a natural satellite with a mass significant enough to be taken into account. In such cases, both bodies can be considered as a single combined body, with its center of mass located at their barycenter. A typical example is the Sun-Earth/Moon system.

In order to simplify the equations of motion of the third body, it is convenient to express them in a rotating frame of reference, known as the synodic frame. This frame is depicted in Figure 2.1. The frame axes are defined as follows: the synodic frame rotates at the same angular speed (ω) as the primaries do around their common center of mass. Its origin is located in the barycenter of the primaries, the x-axis is defined as the line that crosses both primaries and with m_2 on the positive side, the y-axis is contained in the orbital plane of the primaries and in the same direction as the orbital velocity of m_2. The right-hand rule completes the coordinate frame.

Further simplification can be achieved by using dimensionless units. This is done by using three normalizing constants, labeled as characteristics quantities: the sum of the primaries' masses, m^*, used to normalize mass quantities, the distance between the primaries, l^*, used to normalize length quantities, and the time unit t^*, which is defined so that the angular velocity has a value of unity (and therefore, the orbit period becomes 2π):

$$m^* = m_1 + m_2 \tag{2.2}$$

$$l^* = ||\boldsymbol{r_2} - \boldsymbol{r_1}|| \tag{2.3}$$

$$t^* = \sqrt{\frac{(l^*)^3}{Gm^*}} \tag{2.4}$$

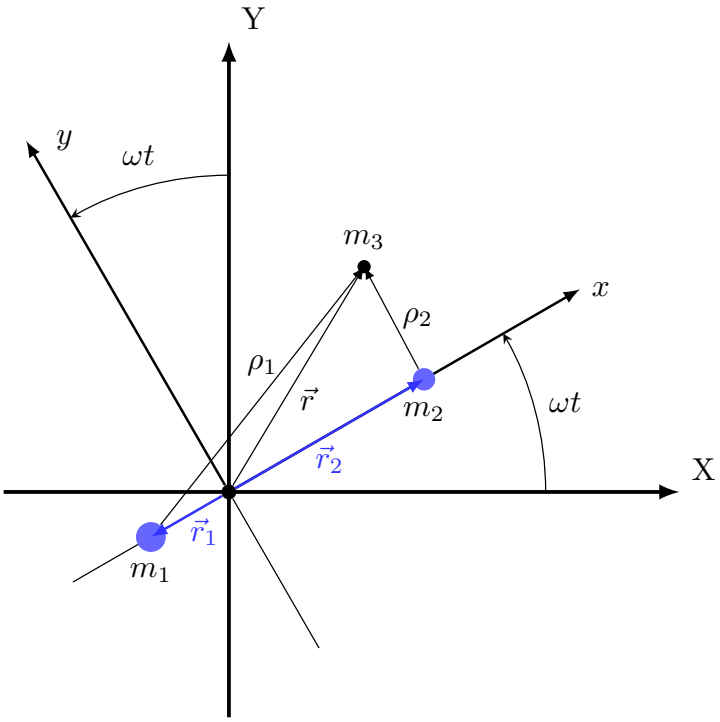


Figure 2.1: Synodic reference frame used in the CRTBP model.

In addition to these normalizing constants, it is useful to also define $v^* = l^*/t^*$ for the velocity quantities. When this normalization is performed, a mass ratio (Eq. (2.5)) is defined with the parameter μ, which must not be mistaken for the standard gravitational parameter. In Table 2.1, the mass ratio and normalization parameters for different primaries systems of the Solar System are listed.

$$\mu = \frac{m_2}{m_1 + m_2} \tag{2.5}$$

Table 2.1: Mass ratio and normalization quantities for distance, time, and velocity of different primaries systems of the Solar System.

System	μ	l^* [km]	t^* [s]	v^* [km/s]
Sun-Jupiter	$9.539 \cdot 10^{-4}$	$7.785 \cdot 10^{8}$	$5.960 \cdot 10^{7}$	13.062
Sun-Earth/Moon	$3.040 \cdot 10^{-6}$	$1.496 \cdot 10^{8}$	$5.023 \cdot 10^{6}$	29.785
Earth-Moon	$1.215 \cdot 10^{-2}$	$3.840 \cdot 10^{3}$	$3.746 \cdot 10^{5}$	1.025

In this approach, the state vector is expressed in nondimensional components defined in the synodic frame as:

$$\boldsymbol{X} = \begin{pmatrix} x & y & z & \dot{x} & \dot{y} & \dot{z} \end{pmatrix}^\top \tag{2.6}$$

For the following part, it is useful to obtain the position of the primaries along the x-axis (x_1 and x_2) of the synodic frame. As in these new dimensionless units $m_1 + m_2 = 1$, Eq. (2.5) is reduced to:

$$m_2 = \mu \tag{2.7}$$

and, therefore:

$$m_1 = 1 - m_2 = 1 - \mu \tag{2.8}$$

In this reference system, the primaries lie on the x-axis and, as the origin is in their barycenter, then:

$$m_1 x_1 + m_2 x_2 = 0 \tag{2.9}$$

Knowing that the distance between the primaries has a value of unit after the normalization:

$$x_2 - x_1 = 1 \tag{2.10}$$

then it is possible to clear the value of x_1 and x_2 substituting Eq. (2.10) into Eq. (2.9) and using μ definition in Eq. (2.5):

$$x_1 = -\mu \tag{2.11}$$

$$x_2 = 1 - \mu \tag{2.12}$$

2.1.1 Equations of motion

Through the assumptions and simplifications presented in the previous section, the equations of motion of the third body are [51]:

$$\ddot{x} = x + 2\dot{y} - (1-\mu)\frac{x+\mu}{\rho_1^3} - \mu\frac{x-(1-\mu)}{\rho_2^3} \tag{2.13a}$$

$$\ddot{y} = y - 2\dot{x} - (1-\mu)\frac{y}{\rho_1^3} - \mu\frac{y}{\rho_2^3} \tag{2.13b}$$

$$\ddot{z} = -(1-\mu)\frac{z}{\rho_1^3} - \mu\frac{z}{\rho_2^3} \tag{2.13c}$$

with ρ_1 and ρ_2 being the distances to the primaries:

$$\rho_1 = \sqrt{(x+\mu)^2 + y^2 + z^2} \tag{2.14a}$$

$$\rho_2 = \sqrt{(x-(1-\mu))^2 + y^2 + z^2} \tag{2.14b}$$

A pseudopotential function U can be defined as:

$$U = \frac{1}{2}(x^2 + y^2) + \frac{1-\mu}{\rho_1} + \frac{\mu}{\rho_2} \tag{2.15}$$

such that Eqs. (2.13) can be written as:

$$\ddot{x} - 2\dot{y} = \frac{\partial U}{\partial x} \tag{2.16a}$$

$$\ddot{y} + 2\dot{x} = \frac{\partial U}{\partial y} \tag{2.16b}$$

$$\ddot{z} = \frac{\partial U}{\partial z} \tag{2.16c}$$

Since U does not depend explicitly on time, the problem, as expressed in Eqs. (2.16) is autonomous. This characteristic enables the identification of an infinite number of periodic and quasi-periodic orbits [50].

2.1.2 Jacobi constant

The CRTBP presents a single integral of motion, called the Jacobi integral. To derive this integral, the equations of motion presented in Eq. (2.16) are multiplied by the corresponding components of the velocity vector, $\dot{x}$, $\dot{y}$, and $\dot{z}$, and their sum is taken, which yields:

$$\dot{x}\ddot{x} + \dot{y}\ddot{y} + \dot{z}\ddot{z} = \dot{x}\frac{\partial U}{\partial x} + \dot{y}\frac{\partial U}{\partial y} + \dot{z}\frac{\partial U}{\partial z} = \frac{dU}{dt} \tag{2.17}$$

Integrating Eq. (2.17) gives the Jacobi integral:

$$\dot{x}^2 + \dot{y}^2 + \dot{z}^2 = V^2 = 2U - C \tag{2.18}$$

where V is the magnitude of the velocity vector in the rotating frame and C is the Jacobi constant, which is determined by the initial conditions. This constant can be regarded as a measure of the relative energy (to the rotating frame), an analogous quantity to the specific energy in the two-body problem, but with opposite sign. Thus, a body can travel further away from a primary with higher two-body energy and lower Jacobi constant values. The integral of motion is used to study which trajectories of the third body are feasible given some initial energy state and as a mean to verify the accuracy of a numerical integration. Any body whose motion is governed by the equations in Eqs. (2.13) must satisfy Eq. (2.18) at any time.

2.1.3 Location of libration points

As previously said, the libration points are equilibrium solutions of the CRTBP and therefore their location can easily be obtained applying its definition to the equations of motion in Eqs. (2.13). Any body (of negligible mass) located at a libration point will be in equilibrium, i.e., its acceleration will be null ($\ddot{x} = \ddot{y} = \ddot{z} = 0$) and, if the body velocity is also zero ($\dot{x} = \dot{y} = \dot{z} = 0$), it will stay in that location indefinitely, making its position to appear invariant or stationary as seen from the rotating frame.

In Figure 2.2, the location of the five libration points in the synodic frame is shown. The set of libration points is contained within the xy-plane and three of the points (L_1, L_2 and L_3) are located on the line passing through the primaries, thus receiving the name of collinear libration points. The position of these points along the line depends on the mass ratio μ. However, as will be shown later (section 2.1.6), they are unstable for any value of μ, so any perturbation to a third body located at one of these points will cause it to drift away. The other two points (L_4 and L_5) form an equilateral triangle with the primaries and are stable for certain values of μ.

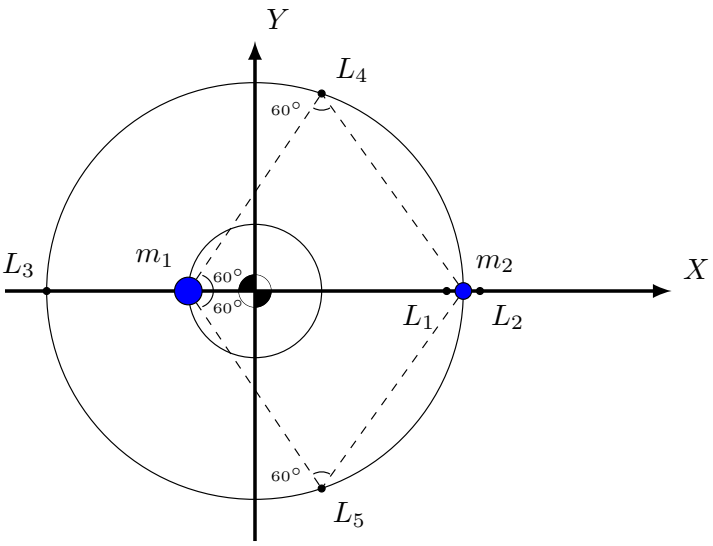


Figure 2.2: Scheme of the libration points location in the synodic frame.

Note that there is no unique naming convention in the literature for the collinear libration points. Szebehely [51] names the collinear points sequentially, thus locating L_2 between the primaries. Here, the convention that sorts the points according to their Jacobi constant [52] is adopted, making L_1 the point located between the primaries. This can be observed in Figure 2.3, where the Jacobi constant value is plotted for the points of the xy-plane in a system with $\mu = 0.3$. The libration point L_1 of this system presents the largest value of C, followed by L_2 and L_3. In the case of the triangular points, the convention is that the one in the upper half-plane is denoted L_4, and the one in the lower half-plane is denoted L_5.

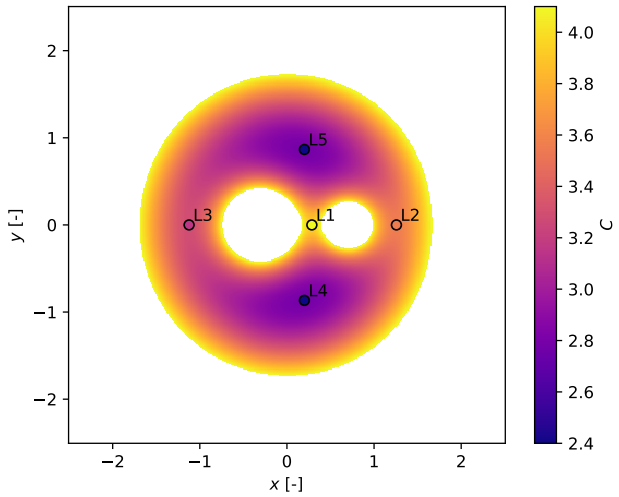


Figure 2.3: Value of the Jacobi constant for the points of the xy-plane of a system with $\mu = 0.3$.

As the focus of this doctoral dissertation is on the L_2 point, the computation of its position coordinates will be addressed now. To solve for the scalar coordinate x of

the collinear libration points, the equilibrium conditions are applied to Eq. (2.13a) as well as setting $y = z = 0$. Thus, Eq. (2.13a) simplifies to:

$$x - (1-\mu)\frac{x+\mu}{|x+\mu|^3} - \mu\frac{x-(1-\mu)}{|x-(1-\mu)|^3} = 0 \tag{2.19}$$

which provides the position of the L_1, L_2, and L_3 points. The absolute value functions in the above equation produce three different equations, one for each collinear point, depending on whether the value of x is higher or lower than x_1 and x_2. For the second Lagrange point, $x_1 < x_2 < x$, so the equation reduces to:

$$x - \frac{1-\mu}{(x+\mu)^2} - \frac{\mu}{(x-1+\mu)^2} = 0 \tag{2.20}$$

The Eq. (2.20) is a quintic equation with five roots, but only one is real. This real root depends on the system (μ) and is the x coordinate of L_2, called x_L here. In the appendix B.1 can be found the polynomial form of Eq. 2.19 particularized for each one of the three collinear points. The expressions to find the distance from the libration point to the closest primary are also included. Regarding the triangular libration points, its location is significantly easier to find, and the required equations have been included in the appendix B.2.

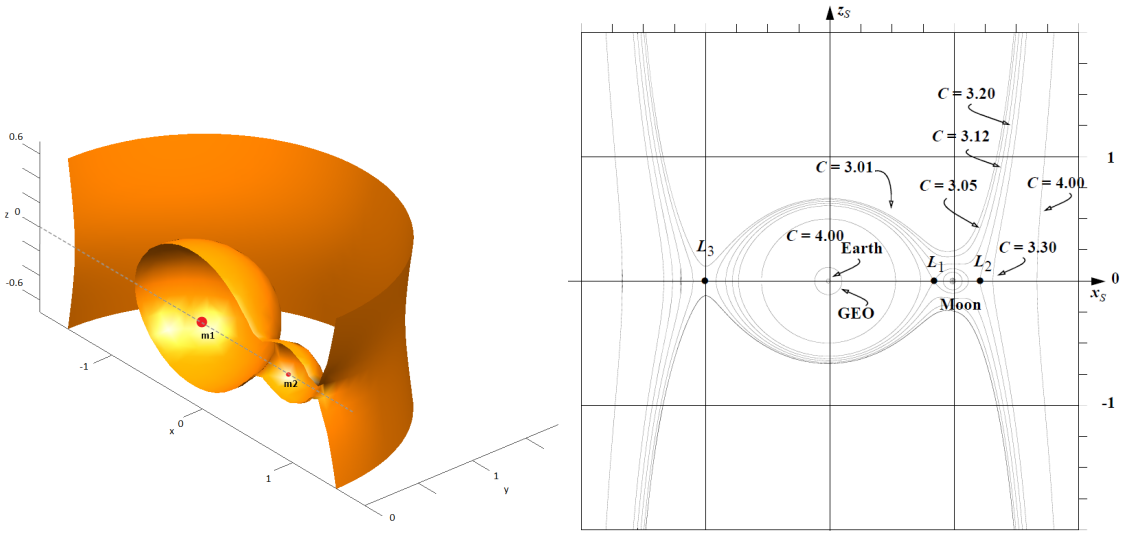
2.1.4 Zero velocity surfaces

As explained in section 2.1.2, Jacobi integral in Eq. (2.18) can be used to study which trajectories of the third body are feasible given some initial energy state. For an unpowered flight, the initial position and velocity vectors determine the resulting trajectory. Furthermore, through the Jacobi integral, the initial state also sets the value of the constant C. Once an energy level is fixed, the magnitude of the velocity at any point is uniquely determined. Although this value does not allow to obtain the specific trajectory of the satellite, it is possible to determine the boundary of permissible motion for the spacecraft by considering setting its velocity to zero in Eq. (2.18), which yields:

$$2U - C = (x^2 + y^2) + 2\left(\frac{1-\mu}{\rho_1} + \frac{\mu}{\rho_2}\right) - C = 0 \tag{2.21}$$

The surfaces described by this equation (called zero velocity surfaces or ZVS) determine the geometric extremes possible for a given energy state. If an orbit begins from a given point with such an energy state, then should it reach the ZVS its velocity must be zero when it arrives. In this way, the Jacobi surfaces determine the allowable regions of motion for fixed energies in the CRTBP. These allowable regions are called Hill's Regions, and they make it easier to determine if it is possible for a body to transit from m_1 to m_2 or beyond. This can be observed in Figure 2.4a, where a three-dimensional cross-section of these zero velocity surfaces for the Earth-Moon system is shown. Note that the missing halves of the surfaces are mirror images of the displayed halves due to the symmetry of the problem. In particular, the ZVS plotted in Figure 2.4a corresponds to an energy level that would allow a spacecraft to travel between the primaries and reach L_1 or L_2. For lower levels of energy (i.e., larger values of C), the spacecraft is limited to orbit around

one of the primaries, as shown in Figure 2.4b, where the zero relative surface contours of the Earth-Moon system in the xz-plane are shown. The value of the Jacobi constant at the different libration points establishes the critical case; if the spacecraft energy is higher (and thus the Jacobi constant is lower), the spacecraft can reach such a point and even move further.



(a) Zero velocity surface.

(b) Zero velocity surface contours in the xz-plane. Extracted from [53].

Figure 2.4: Zero velocity surface of the Sun-Earth/Moon system.

2.1.5 Linearization of equations of motion at libration points

The linearization of the equations of motion enables the derivation of analytical solutions and the study of stability. The approach presented in this section follows the work of Howell and Pernicka [54] and Ardaens [41]. First, the synodic frame origin is translated to one of the collinear libration points, L_i, and new position coordinates x', y', and z' are defined with respect to this point. By linearizing the equations of motion of the CRTBP given in Eqs. (2.13), the following equations are obtained:

$$\ddot{x}' - 2\dot{y}' - (1 + 2\alpha)x' = 0 \tag{2.22a}$$
$$\ddot{y}' + 2\dot{x}' - (1 - \alpha)y' = 0 \tag{2.22b}$$
$$\ddot{z}' + \alpha z' = 0 \tag{2.22c}$$

where α is a positive constant defined in Eq. (2.23) which only depends on the distance from the collinear libration point to the synodic frame origin (x_L) and the parameter μ. The step-by-step derivation process to linearize the equation can be found in appendix C.

$$\alpha = \frac{1-\mu}{|x_L + \mu|^3} + \frac{\mu}{|x_L - 1 + \mu|^3} > 0 \tag{2.23}$$

The system matrix for this linear system can also be defined:

$$\mathrm{A}_{L_p} = \begin{pmatrix} 0 & 0 & 0 & 1 & 0 & 0 \\ 0 & 0 & 0 & 0 & 1 & 0 \\ 0 & 0 & 0 & 0 & 0 & 1 \\ 1+2\alpha & 0 & 0 & 0 & 2 & 0 \\ 0 & 1-\alpha & 0 & -2 & 0 & 0 \\ 0 & 0 & -\alpha & 0 & 0 & 0 \end{pmatrix} \tag{2.24}$$

This matrix is a linear mapping between the state and its derivative:

$$\dot{\boldsymbol{X}}(t) = \mathrm{A}_{L_p}(t)\boldsymbol{X}(t) \tag{2.25}$$

2.1.6 Stability

The linearization of the system near the libration points, i.e., equilibrium points, allows to perform the stability analysis of such a linear system in order to study the possible dynamics near these points.

To determine the stability of a linear system, the eigenvalues and eigenvectors from the system matrix must be found, for which the Eq. (2.26) is used. In the case of the collinear libration points, the system matrix is given by Eq. (2.24). Substituting this equation into Eq. (2.26), the characteristic equation shown in Eq. (2.27) is obtained.

$$\det(\mathrm{A}_{L_p} - \lambda \mathrm{I}_{6\times 6}) = 0 \tag{2.26}$$

$$\lambda^6 + 2\lambda^4 + (1 + 3\alpha - 3\alpha^2)\lambda^2 + \alpha(1 + \alpha - 2\alpha^2) = 0 \tag{2.27}$$

Solving Eq. (2.27) yields the following eigenvalues:

$$\lambda^2_{1,2,3,4} = \frac{\alpha - 2 \pm \sqrt{9\alpha^2 - 8\alpha}}{2} > 0 \quad \forall \mu \text{ in } \left[0, \frac{1}{2}\right] \tag{2.28}$$

$$\lambda^2_{5,6} = -\alpha \tag{2.29}$$

Some of the first four eigenvalues in Eq. (2.28) have a positive real part for all values of μ between 0 and 0.5, making the collinear libration points unstable [52]. Hence, any perturbation over a body situated close to one of these points will cause that body to move away from such a point.

Similarly, if Eqs. (2.13) are linearized about the triangular libration points, the eigenvalues for L_4 and L_5 are [41]:

$$\lambda^2_{1,2,3,4} = \frac{-1 \pm \sqrt{1 - 27\mu(1-\mu)}}{2} > 0 \quad \forall \mu \text{ in } \left[0, \frac{1}{2}\right] \tag{2.30}$$

$$\lambda^2_{5,6} = -1 \tag{2.31}$$

The triangular libration points are thus stable if and only if $0 > 1 - 27\mu(1-\mu) < 1$, which is satisfied as long as $\mu < 1/2 - 1/6\sqrt{23/3} \approx 0.0385$. Using the definition of

μ in Eq. (2.5), the minimum ratio of the primaries masses necessary for the stability of L_4 and L_5 is:

$$\frac{m_1}{m_2} \approx 24.9599 \tag{2.32}$$

It should be noted that these findings are based on linearized theory, and thus only the infinitesimal stability can be inferred. However, second-order effects and perturbations to the CRTBP have a significant impact on the stability and motion around the collinear libration points. For instance, second-order effects, for sufficiently large amplitudes, lead to coupling between the motion in the xy-plane and z-direction, resulting in a three-dimensional orbit of fixed geometry and size about one of the collinear libration points. Such orbits, called halo, would not be possible without non-linear effects.

2.2 Libration point orbits

The inherent instability of the collinear points makes it impractical to locate a spacecraft exactly at those points. Nevertheless, there exist an infinite number of periodic and quasi-periodic orbits around the collinear libration points. Since the late 1800s, numerous periodic orbits were identified in the CRTBP, and since the 1960s, the use of modern computers and numerical techniques has increased the quantity and complexity of the discovered periodic orbits. Although the study of periodic orbits in the CRTBP is beyond the scope of this thesis, the two most important common types of orbits and how they are derived from the Eqs. (2.13) are included here.

2.2.1 Periodic and quasi-periodic orbits

It is possible to find an analytical solution for the linearized equations of motion of the CRTBP (Eqs. (2.22)) [55]. The solution of the out-of-plane z-motion is characterized by a simple harmonic motion. On the contrary, the in-plane xy motion is described by a characteristic equation that yields two real roots and two imaginary roots. These roots correspond to distinct modes of motion, namely divergent and non-divergent. When only the non-divergent mode is excited, then the resulting solution is bounded and can be expressed as:

$$x = (A_y/c_2)\cos(\omega_{xy}t + \phi) \tag{2.33a}$$
$$y = -A_y \sin(\omega_{xy}t + \phi) \tag{2.33b}$$
$$z = A_z \sin(\omega_z t + \psi) \tag{2.33c}$$

$$\omega_{xy} = \frac{1}{\sqrt{2}}(-\alpha + 2 + \sqrt{9\alpha^2 - 8\alpha})^{\frac{1}{2}} \tag{2.34}$$

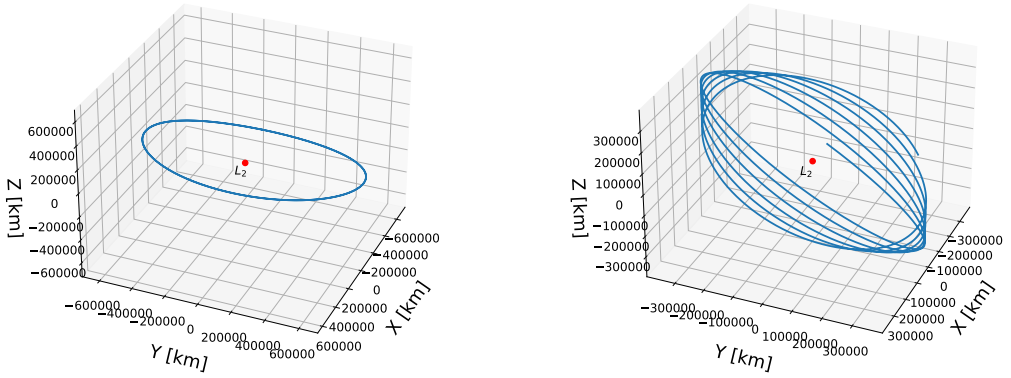
$$\lambda_{xy} = \frac{1}{\sqrt{2}}(\alpha - 2 + \sqrt{9\alpha^2 - 8\alpha})^{\frac{1}{2}} \tag{2.35}$$

$$c_1 = \frac{\lambda_{xy}^2 + 1 + 2\alpha}{2\lambda_{xy}} \tag{2.36}$$

$$c_2 = \frac{\omega_{xy}^2 + 1 + 2\alpha}{2\omega_{xy}} \tag{2.37}$$

$$\omega_z = \sqrt{\alpha} \tag{2.38}$$

The motion given by Eqs. (2.33) is described by six variables: the amplitudes (A_y and A_z), the frequencies (ω_{xy} and ω_z), and the phase angles (ϕ and ψ) of the in-plane and out-of-plane motion. The periodic orbits described by these equations can be characterized by oscillatory motion. If the frequencies (ω_{xy} and ω_z) are either the same or have a common factor, then the resulting motion will be periodic. However, if the frequencies are incommensurate, the resulting motion will be quasi-periodic. Those orbits whose frequencies are equal are known as halo orbits (see Figure 2.5a) while the more general quasi-periodic trajectories are known as Lissajous orbits or quasi-halo orbits (see Figure 2.5b). The analytical derivation of these orbits is possible, since the linearization process around the libration points results in a good approximation of the system dynamics. Nevertheless, other orbits are only possible due to second-order effects, and thus are not well described by linear approximations and require numerical methods to generate them.



(a) Halo orbit.

(b) Lissajous orbit.

Figure 2.5: Examples of periodic (halo) and quasi-periodic (Lissajous) orbits around the second libration point of Sun-Earth system.

Keplerian orbits and a position in such orbits can be uniquely specified in the two-body problem using six parameters, usually the keplerian elements or the Cartesian state (position and velocity with respect to the main body). In the case of the three-body problem, since there are no general analytical solutions, the parameterization of orbits is not so simple.

The halo and Lissajous orbits are the most well-known libration point orbits and they have already been used in real missions [55]. Nevertheless, it is possible to find other periodic orbits in the three-body problem that revolve about all five libration points, the primary, the secondary, and even about the entire system. The variety of available periodic orbits is extensive and with different characteristics: prograde sense, retrograde sense, symmetric, asymmetric, etc. These orbits are

studied because they help to understand the flow of a spacecraft in the system, making it possible to construct a trajectory that takes advantage of the flow, rather than forcing its way through the system.

2.2.2 State transition matrix

The state transition matrix (STM) is a linear mapping between two states of a dynamical system, which allows evaluating the effect of small variations in the initial conditions in the system state at a later instant of time. The state transition matrix (Φ) will be a 6×6 matrix that satisfies the following:

$$\boldsymbol{X}(t) = \Phi(t, t_0)\boldsymbol{X}(t_0) \tag{2.39}$$

The STM is obtained by linearizing the equations of motion of the CRTBP about a nominal trajectory [56, 57]. The A_{L_p} matrix from section 2.1.5 was obtained by linearizing the equations of motion around the libration point. In this case, the A matrix is obtained linearizing the system about the current state of the spacecraft at a time t:

$$\mathrm{A}(t) = \frac{\partial \dot{\boldsymbol{X}}(t)}{\partial \boldsymbol{X}(t)} \tag{2.40}$$

$$\mathrm{A}(t) = \begin{bmatrix} 0_{3\times3} & \mathrm{I}_{3\times3} \\ \mathrm{U}_{XX} & 2\Omega \end{bmatrix}, \quad \text{where} \quad \Omega = \begin{bmatrix} 0 & 1 & 0 \\ -1 & 0 & 0 \\ 0 & 0 & 0 \end{bmatrix} \tag{2.41}$$

and U_{XX} is the symmetric matrix composed of second derivatives of the pseudopotential U in Eq. (2.15) with respect to the third body's position evaluated along the orbit:

$$\mathrm{U}_{XX} = \begin{bmatrix} \frac{\partial \ddot{x}}{\partial x} & \frac{\partial \ddot{x}}{\partial y} & \frac{\partial \ddot{x}}{\partial z} \\ \frac{\partial \ddot{y}}{\partial x} & \frac{\partial \ddot{y}}{\partial y} & \frac{\partial \ddot{y}}{\partial z} \\ \frac{\partial \ddot{z}}{\partial x} & \frac{\partial \ddot{z}}{\partial y} & \frac{\partial \ddot{z}}{\partial z} \end{bmatrix} \tag{2.42}$$

Substituting Eq. (2.39) into Eq. (2.25), which is also valid here, yields an equation for the derivative of the STM:

$$\dot{\Phi}(t, t_0) = \mathrm{A}(t)\Phi(t, t_0) \tag{2.43}$$

which enables the propagation of the STM from the initial condition $\Phi(t_0, t_0) = \mathrm{I}_{6\times6}$. Thus, a system of 42 differential equations is obtained (6 from the equations of motion and 36 from the STM). If the time interval is small compared to the orbital period, $\mathrm{A}(t)$ can be approximated by $\mathrm{A}(t_0)$ [58].

The STM provides important information about the stability and sensitivity of the system and is often used in trajectory optimization and control problems.

2.2.3 Stability of periodic orbits

In order to asses the stability of a periodic orbit, the STM is evaluated stroboscopically, i.e., after a period (T) of the orbit. The STM of a periodic orbit of period T

after one revolution is called monodromy matrix ($\mathcal{M}$). To build this matrix, the STM is propagated along the orbit for a whole period. Thus:

$$\mathcal{M} = \Phi(t_0 + T, t_0) \tag{2.44}$$

As previously said, this requires solving the system of 42 differential equations from the initial conditions $\boldsymbol{X}(t_0) = \boldsymbol{X}_0$ and $\Phi(t_0, t_0) = \mathrm{I}_{6\times6}$. Based on the Floquet theory, the eigenvalues of the monodromy matrix define the stability of the orbit and the behavior of motion in its vicinity [48]. If an orbit is precisely periodic, its monodromy matrix's eigenvalues appear in the following format: (1, 1, λ_1, $1/\lambda_1$, λ_2, $1/\lambda_2$) [57], where λ_i is a complex number. The two eigenvalues equal to 1 are known as the trivial pair. The monodromy matrix is also used to study and build the invariant manifolds associated to periodic orbits, as will be explained in section 2.3.

2.2.4 Orbit generation

The multi-body dynamics are more complex than the classical problem of a single gravitational source. Such complexity manifests itself through the fully numerical nature of the orbital solutions, which have to be searched and developed by means of dedicated algorithms.

There are many methods to identify and construct orbits. There are three main types of techniques typically used to do so: analytical expansion techniques, differential corrections techniques, and the poincaré method. In this work, the second method has been used as it can be used with the ephemeris model.

Differential corrections

Differential correction is a process in which the STM is used to change the initial conditions of a spacecraft trajectory so a criteria is met after a period of time. There are two main types of differential corrections routines, the single-shooting method and the multiple-shooting method.

Single-shooting method: In the single-shooting method, the spacecraft starts at an initial state $\boldsymbol{X}_0$ and follows its natural trajectory, resulting from the integration of the equations of motion, and arrives to its nominal final state $\boldsymbol{X}_f$ after a period of time t_f. The goal is to shift the trajectory so it encounters a desired final state $\hat{\boldsymbol{X}}_f$. Normally, two constraints are added to the problem: first, the spacecraft initial position does not change and second, only the final position vector is fixed, letting the final velocity vary freely. Thus, the initial velocity of the spacecraft may change ($\hat{\boldsymbol{X}}_0$), simulating an impulsive maneuver ($\delta\boldsymbol{v}_0$). In some cases, the final time is also varied. An scheme of how this method works is shown in Figure 2.6.

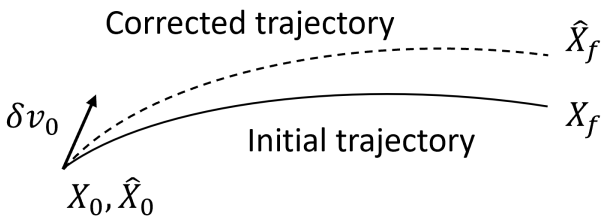


Figure 2.6: The single-shooting differential correction method.

As previously said, the STM is used to estimate what change must be made in the initial velocity of the state in order to achieve the desired position at the end of the trajectory:

$$\delta \boldsymbol{X}_f = \Phi(t_f, t_0)\delta \boldsymbol{X}_0 \tag{2.45}$$

$$\delta \boldsymbol{X}_0 = \hat{\boldsymbol{X}}_0 - \boldsymbol{X}_0 \tag{2.46}$$

$$\delta \boldsymbol{X}_f = \hat{\boldsymbol{X}}_f - \boldsymbol{X}_f \tag{2.47}$$

As the state is composed by the position and the velocity vectors:

$$\delta \boldsymbol{X}_f = \begin{pmatrix} \delta \boldsymbol{r}_f \\ \delta \boldsymbol{v}_f \end{pmatrix} = \begin{bmatrix} \Phi_{rr}(t_f, t_0) & \Phi_{rv}(t_f, t_0) \\ \Phi_{vr}(t_f, t_0) & \Phi_{vv}(t_f, t_0) \end{bmatrix} \begin{pmatrix} \delta \boldsymbol{r}_0 \\ \delta \boldsymbol{v}_0 \end{pmatrix} \tag{2.48}$$

Given the aforementioned constraints, $\delta \boldsymbol{r}_0 = 0$ and $\delta \boldsymbol{v}_0$ can be freely varied, so the previous equation can be simplified and solved for $\delta \boldsymbol{v}_0$:

$$\delta \boldsymbol{v}_0 = [\Phi_{rv}(t_f, t_0)]^{-1} \delta \boldsymbol{r}_f \tag{2.49}$$

As the STM is the result of a linearization process, the algorithm requires several iterations until it reaches convergence. Note that the STM must be updated in each iteration as it depends on the trajectory followed by the spacecraft.

Multiple-shooting method: In the case of multiple-shooting method, instead of correcting a single initial state, the trajectory is divided into several segments and all the initial states of each one are corrected simultaneously to construct a trajectory that satisfies a set of constraints. This method is adequate for complex or long trajectories in unstable dynamical environments, such as libration points, in which the single-shooting method may not work because the trajectory deviation grows too large due to finite numerical precision. The corrections (maneuvers) applied in each segment counteract the build-up of propagated round-off errors, and they can be reduced by shortening the length of the segments. Hence, they are not normally considered as part of the maneuvers of the mission.

The first step of the method is to divide the trajectory into a series of patchpoints (which delimit the segments). Then, an iterative two-level process (see Figure 2.7) is applied:

1. The first level corrects the patchpoints velocities using a single-shooting method. The goal is that the final position of each segments coincides with the following patchpoint and thus obtaining a continuous trajectory with maneuvers applied in each patchpoint.

2. The second level adjust the position and the epochs of every patchpoint. A least-square method is used to reduce the ΔV of all the maneuvers produced from the first level. The resulting trajectory will require less ΔV after the following iteration of the first level is applied.

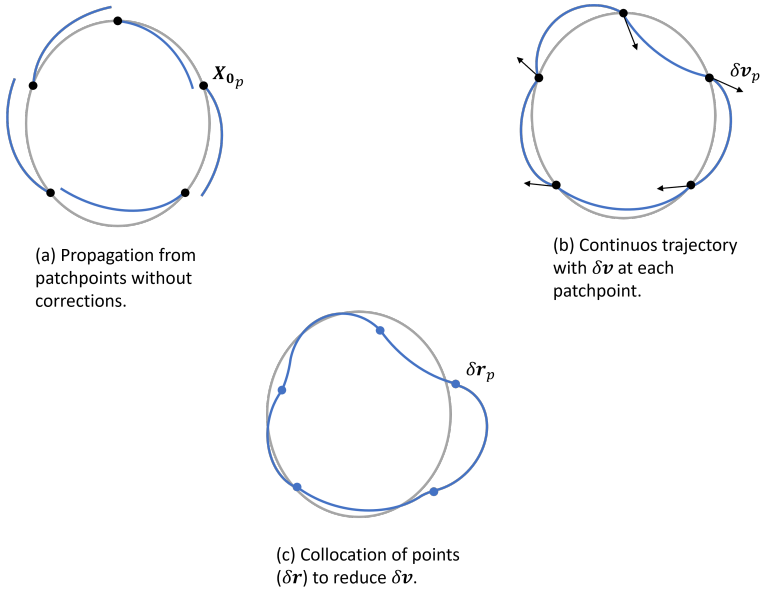


Figure 2.7: Multiple-shooting applied to a trajectory divided into five segments.

This iterative process continues until the discontinuities in the position and the velocity in each patchpoint are below the defined thresholds. As in the first level, the changes in the position and/or times for the second level are computed using a linear approximation.

In this work, a multiple-shooting method has been employed to build the required orbits. The formulation was first applied to LPO by Howell [54] only reduces the ΔV of each interior patchpoint, leaving the start and end points of the trajectory unconstrained. It has been included in appendix D for reference.

2.2.5 Station-keeping

Station-keeping refers to the process of adjusting a spacecraft's trajectory to maintain it closer to the reference orbit, within a given error threshold. In the case of the collinear libration points, due to the inherent instability, the use of a station-keeping strategy is required, as any deviation from the designed trajectory will grow exponentially over time. Nevertheless, the missions located at these regions require very small maneuvers if performed frequently (about weekly for the Earth-Moon system and about monthly for the Earth-Sun system) and accurately enough [53, 57].

Although the CRTBP model is a good starting point in the development of station-keeping strategies, these should always be further developed (along with the nominal trajectory design) in a high-fidelity model. A station-keeping method developed in a low-fidelity model of motion will normally require greater costs in high-fidelity models. One key consideration in developing these models is to

account for orbit determination and thrusting errors, both of which can significantly impact the effectiveness of control strategies. Therefore, it is crucial to simulate these factors to ensure that the control strategies developed are robust and effective in real-world scenarios.

There are numerous station-keeping strategies developed for LPO [59]. While continuous control strategies are still under development, impulsive methods have been extensively tested and have proven effective in certain mission scenarios. There are two fundamentally different approaches that have been implemented when designing the station-keeping strategies of historical missions, namely tight control and loose control. The term tight control describes a strategy in which each station-keeping strategy is designed to bring the spacecraft's trajectory back to a design reference trajectory. Conversely, a loose station-keeping strategy describes one in which a spacecraft may travel anywhere within some wide corridor, and the particular route taken is not important. Transferences will also require correction maneuvers to compensate for injection errors.

2.3 Manifolds and low-energy transfers

As explained in section 2.1.6, the collinear libration points are unstable, and, therefore, any perturbation in these regions will deviate the spacecraft from its nominal path. The collection of trajectories that move away from the libration point defines its unstable manifold ($\boldsymbol{W}^u$). Likewise, the set of trajectories that approach a libration point defines its stable manifold ($\boldsymbol{W}^s$). The manifolds associated with a given orbit can be used as low-energy transfers to place a spacecraft in such an orbit. An example of this is shown in Figure 2.8, where the unstable and stable manifolds of a halo orbit located in the Earth-Moon system L_1 are depicted. The manifolds can be either a 1D manifold associated to a libration point, or a 2D manifolds associated to the periodic orbits around the point.

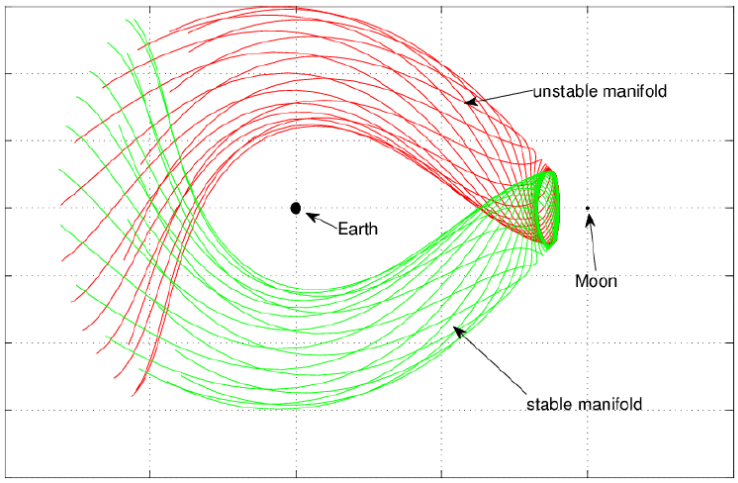


Figure 2.8: Transference trajectories based on the unstable and stable manifolds of a halo orbit at L_1 of the Earth-Moon system. Extracted from [53].

The use of manifolds for low-energy transfers has been studied extensively over the

last few decades [60, 61, 62, 63]. The first step to design a low-energy transfer is to compute the manifolds of the nominal orbit around the libration point. From a mathematical point of view, the collinear libration points are dynamical saddle points, as illustrated in the plot shown in Figure 2.9. When the spacecraft motion is propagated forward in time after a perturbation, it will follow the point's unstable manifold; whereas it will follow the stable manifold when propagated backward in time.

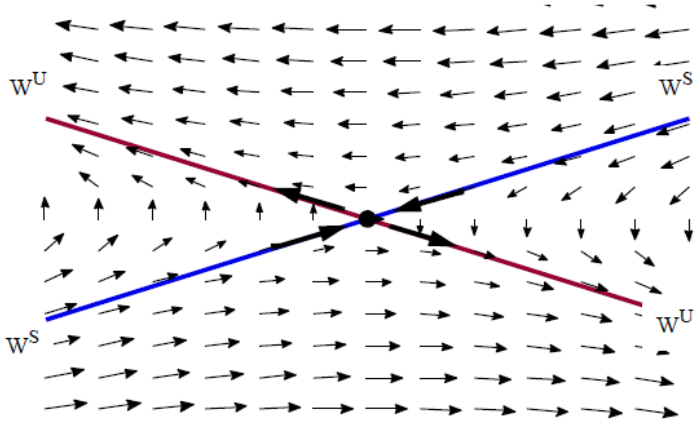


Figure 2.9: Saddle point vector field. Extracted from [53].

If the nominal orbit is periodic, the monodromy matrix can be used to obtain the manifolds. This monodromy matrix has been produced by propagating the STM all the way around the orbit, from time $t = t_0$ to time $t = t_0 + T$. To determine the stable and unstable directions at each point along the orbit, the stable and unstable eigenvectors of the monodromy matrix, $\boldsymbol{\nu}_s$ and $\boldsymbol{\nu}_u$ respectively, can be propagated to time t_i using:

$$\boldsymbol{\nu}_i^{s,u} = \Phi(t_i, t_0)\boldsymbol{\nu}^{s,u} \tag{2.50}$$

Once the eigenvectors are computed, trajectories for both manifolds are generated by perturbing an initial condition ($\boldsymbol{X}_i$) in the direction of the eigenvector (see Eqs. (2.51)), and propagating the equations of motion backward in time (for stable manifold) or forward in time (unstable manifold).

$$\boldsymbol{X}_i^s = \boldsymbol{X}_i \pm \varepsilon \frac{\boldsymbol{\nu}^s}{|\boldsymbol{\nu}^s|} \tag{2.51a}$$

$$\boldsymbol{X}_i^u = \boldsymbol{X}_i \pm \varepsilon \frac{\boldsymbol{\nu}^u}{|\boldsymbol{\nu}^u|} \tag{2.51b}$$

According to the sign used for the perturbation term (ε) in Eqs. (2.51), the interior or exterior manifold will be obtained. By convention, the half of the manifold moving toward the smaller primary is referred to as the interior manifold, since it will stay, at least for a short period, within the smaller body's influence. Likewise, the other half is referred to as the exterior manifold [57].

Although quasi-periodic orbits also have stable and unstable invariant manifolds, the procedure to generate them is slightly different. Since these orbits are not

periodic, they do not have associated monodromy matrices. Nevertheless, there are two alternatives: one is to approximate the manifolds by producing a pseudo-monodromy matrix by propagating the state transition matrix from one plane crossing to the next (half revolution), and the other is propagating directly the eigenvectors of the Jacobian of the states at each point along sample elements of the orbit. The first method is less numerically intensive and was successfully used in the Genesis mission design [57].

Once the manifold has been obtained, a specific trajectory must be chosen from it. The region of space that can be reached with the unstable manifolds of a given orbit is vast; however, the constraints of the mission limit the segment of the manifold that provides an acceptable trajectory for the mission objectives. If the manifold and the parking orbit are nowhere tangent, within the bounds of some specified set of conditions (e.g., time of flight), the problem is redefined as the search for a path between the parking orbit and any point on the manifold.

Due to the stability of the triangular libration points, these do not present interesting associated invariant manifolds. A spacecraft near these points will oscillate about the point, changing its motion due to the perturbations, but without diverging.

2.4 Ephemeris model

The perturbations are deviations from the idealized motion. Actual problems do not conform exactly to the assumptions made for the ideal restricted three-body problem.

Modeling the motion of a spacecraft in high-fidelity involves constructing a dynamical model that approximates the true environment as closely as possible. The elements included in this modelization of the dynamical environment are used to form a second-order vector differential equation from which the spacecraft path is obtained through numerical integration. This differential equation reflects the acceleration that acts on the spacecraft relative to a selected central body.

In this work, the high-fidelity dynamical model is referred to as the ephemeris model and is based on the N-body problem (using the point mass model and real ephemerides) and the solar radiation pressure. The number of celestial bodies taken into account, apart from the primaries, is variable and their position is accessed using the SPICE kernels [64]. In this model, the acceleration on the spacecraft relative to a central body (labeled with the subscript q) due to the gravitational influence of such a central body and $N-1$ additional celestial bodies can be expressed as:

$$\ddot{\boldsymbol{r}} = -G\frac{m_q}{r_{sc}^3}\boldsymbol{r} + G\sum_{k=1}^{N-1} m_k \left(\frac{\boldsymbol{r}_k - \boldsymbol{r}}{||\boldsymbol{r}_k - \boldsymbol{r}||^3} - \frac{\boldsymbol{r}_k}{||\boldsymbol{r}_k||^3} \right) \tag{2.52}$$

where G is the gravitational constant, m_k is the mass of every celestial body taken into account (besides the central body), $\boldsymbol{r}_k$ the position of such a body and $\boldsymbol{r}$ is the position of the spacecraft. The Eq. (2.52) is propagated in the J2000 inertial frame (centered in the central body) and includes Earth, Moon, and Sun as celestial bodies of influence. The acceleration of this equation can be broken down into

three categories: the first term is the acceleration of the spacecraft due to the central body, the second term accounts for the acceleration of the k^{th} body on the spacecraft, and the third term accounts for the force of the k^{th} body on the central body. This dynamical environment has been implemented in a Python library called Mubody [65].

2.4.1 Solar radiation pressure

The solar radiation pressure (SRP) is the force produced by the impact of sunlight photons on the surface of the spacecraft. The exchange of momentum between these particles and the spacecraft produces an acceleration in the latter. Despite being a small perturbation, SRP can have a significant impact in missions with a high surface-mass ratio or placed in low-acceleration environments, which is the case for libration point missions, where SRP is the fourth most relevant force after the gravitational attraction of Earth, Sun, and Moon. Therefore, this perturbation must be taken into account in a high-fidelity environment.

The level of accuracy of SRP modeling has a direct impact on trajectory design and orbit determination. The magnitude and direction of the acceleration due to SRP will depend on the solar activity, the satellite attitude, its geometry, and the optical properties of its surface materials, making its modeling a challenging task. An accurate prediction of the SRP perturbation involves determining the Sun's location, the satellite attitude, the exact value of the solar radiation pressure, the exposed area to the incoming radiation, and the usually time-varying coefficients that model the satellite's reflectivity.

Nevertheless, there are simpler models available for rough estimations, such as the cannonball model [53], in which the satellite is assumed to have a constant attitude perpendicular to the Sun, and the reflection coefficient is also assumed to be constant and uniform for all the satellite surface. These assumptions lead to the following expression of the SRP acceleration:

$$\boldsymbol{a}_{SRP} = P_s \frac{c_R A_{sc}}{m_{sc}} \frac{\boldsymbol{r}_{sun,sc}}{||\boldsymbol{r}_{\boldsymbol{sun,sc}}||} \tag{2.53}$$

where A_{sc} is the projected area, m_{sc} is the spacecraft mass, $r_{sun,sc}$ the Sun position vector (with respect to the spacecraft), c_R is the reflection coefficient and P_s is the solar radiation pressure, which depends on the distance from the Sun and is given by:

$$P_s = \frac{P_0}{c} \left(\frac{R_0}{||\boldsymbol{r}_{\boldsymbol{sun,sc}}||} \right)^2 \tag{2.54}$$

where $P_0 = 1367$ W/m^2 is the solar flux at 1 AU, c is the speed of light and R_0 is the mean distance between the Sun and Earth, equivalent to 1 AU. From Eq. (2.53), it can be deduced that the effect of SRP can be comparable in satellites with similar values of c_R and A_{sc}/m_{sc}. This is relevant in formations of satellites located at the libration points, where the SRP can represent the main source of relative acceleration.

2.4.2 Coordinate transformation

The CRTBP and the ephemeris model use different reference frames, the former is based on a synodic coordinate system defined using the motion of two massive bodes (which results in a rotating frame) and the latter is formulated in an inertial reference frame. In order to be able to compare the trajectories of both models or translate the results from one model to the other for further calculations, the transformation between both frames must be defined. Furthermore, the states along the orbit in the CRTBP have to be converted into dimensional states. This particular operation requires assumptions that may result in slight differences between the results obtained with different implementations.

To transform the position and velocity vectors of a body p from an initial coordinate system (i) centered in O_i to another coordinate system (f) centered in O_f, the following general expressions are used:

$$\boldsymbol{r}^f_{O_f,p} = R_{fi}(t)\boldsymbol{r}^i_{O_i,p} + \boldsymbol{r}^f_{O_f,O_i} \tag{2.55}$$

$$\boldsymbol{v}^f_{O_f,p} = R_{fi}(t)\boldsymbol{v}^i_{O_i,p} + \dot{R}_{fi}(t)\boldsymbol{r}^i_{O_i,p} + \boldsymbol{v}^f_{O_f,O_i} \tag{2.56}$$

where $R_{fi}(t)$ is the rotation matrix from coordinate system i to coordinate system f and $\dot{R}_{fi}(t)$ is its time derivative. Then, $\boldsymbol{r}_{O_f,O_i}$ and $\boldsymbol{v}_{O_f,O_i}$ are the position and velocity vectors of O_i relative to O_f expressed in the coordinate system f. These expressions correspond to the more general case, which involves a rotation and a translation of the frame's origin.

The main two frames used in this work are the aforementioned synodic frame (defined in section 2.1 and an inertial reference frame (based on the J2000 frame of SPICE[1] [66]). As the CRTBP, and therefore, its synodic frame, are based on simplifications that are no longer true in the inertial frame, the transformation between both frames must also make certain assumptions. In particular, the primaries have eccentric orbits, so the libration point distances to the origin will not be constant over time. To minimize the impact of the transformation on the shape of the orbit regarding the libration point, an auxiliary rotating frame centered on the libration point and parallel to the synodic frame is used. This frame is called the Rotating Libration Point (RLP) frame. Thus, any transformation between the synodic and inertial frames will involve an intermediate transformation to this RLP frame. In Figure 2.10 a scheme of these transformation steps is shown.

The derivation of the rotation matrix between J2000 and the RLP frame, its time derivative, and the relative position and velocity vectors between all the frames' origins can be found in [67].

[1] J2000 frame coincides almost exactly with the ICRF frame and in fact, any SPICE data said to be referenced to the J2000 frame are actually referenced to the ICRF frame. The same is valid for this work.

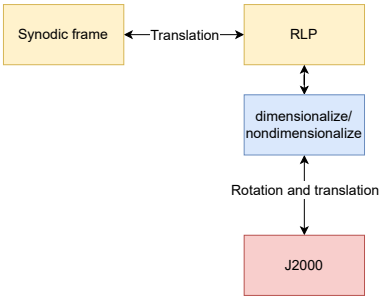


Figure 2.10: Coordinate transformation scheme.

2.5 Other models

2.5.1 Elliptical model

The Elliptical Restricted Three-Body Problem (ERTBP) is a modified version of the CRTBP, where a non-zero eccentricity for the primaries orbits is allowed. The equations and formulas presented in this work have been taken from [68]. In the CRTBP, the synodic frame presents a uniform rotation speed, where the primaries are fixed. However, in the case of the elliptic problem, the equations of motion are presented in a non-uniformly rotating and pulsating coordinate system. In such a frame, the primaries also have fixed positions, even though the distance separating them varies due to the ellipticity of their orbits. This pulsating coordinate system is introduced by using the variable distance between the primaries as the basic length of the system by which distances are divided.

To convert from nondimensional units to dimensional units, the following factors are used, which depend on the orbital position of the primaries and are analogous to those of the CRTBP:

$$l^* = \frac{a(1-e^2)}{1+e\cos(\nu)} \tag{2.57}$$

$$t^* = \sqrt{\frac{a^3(1-e^2)^3}{G(m_1+m_2)(1+e\cos(\nu))^4}} \tag{2.58}$$

where a, e and ν are the semi-major axis, the eccentricity, and the true anomaly of the primaries orbits. Contrary to the CRTBP, the normalized units are not constants in the ERTBP, due to the eccentricity of the primaries. The equations of motion for the ERTBP can be written as:

$$\ddot{x} - 2\dot{y} = (1+e\cos(\nu))^{-1}\left(x - \frac{1-\mu}{\rho_1^3}(x+\mu) - \frac{\mu}{\rho_2^3}(x+\mu-1)\right) \tag{2.59a}$$

$$\ddot{y} + 2\dot{x} = (1+e\cos(\nu))^{-1}\left(y - \frac{1-\mu}{\rho_1^3}y - \frac{\mu}{\rho_2^3}y\right) \tag{2.59b}$$

$$\ddot{z} + z = (1+e\cos(\nu))^{-1}\left(z - \frac{1-\mu}{\rho_1^3}z - \frac{\mu}{\rho_2^3}z\right) \tag{2.59c}$$

Both ρ_1 and ρ_2 are still defined by Eq. (2.10). It is also possible to define a

pseudopotential function (U^*), which provides a more concise notation:

$$\ddot{x} - 2\dot{y} = \frac{\partial U^*}{\partial x} \tag{2.60a}$$

$$\ddot{y} + 2\dot{x} = \frac{\partial U^*}{\partial x} \tag{2.60b}$$

$$\ddot{z} + z = \frac{\partial U^*}{\partial x} \tag{2.60c}$$

with

$$U^* = (1 + e\cos(\nu))^{-1}\left[\frac{1}{2}(x^2 + y^2 + z^2) + \frac{1-\mu}{\rho_1} + \frac{\mu}{\rho_2}\right] \tag{2.61}$$

In the case of zero eccentricity, the Eqs. (2.59) reduces to Eqs. (2.13), i.e. the CRTBP. The location of the libration points in the non-dimensional coordinates is the same for both problems, but not their dimensional coordinates. For the ERTBP there is not an integral of motion, as the Jacobi integral of the CRTBP.

2.5.2 Bicircular Restricted Four-Body Problem

The Bicircular Restricted Four-Body Problem (BCR4BP) is a time-dependant periodic model that includes an additional gravity source to the CRTBP [69]. It is adequate for libration points of planet-moon systems where the influence of the Sun is non-negligible. The BCR4BP is an intermediate step between the CRTBP and a high-fidelity ephemeris model. In this model, the Earth and the Moon are assumed to have circular orbits around their barycenter (B_1), while the Sun and B_1 move in circular orbits with respect to the Earth-Moon-Sun barycenter, labeled B_2. A scheme of the frame is shown in Figure 2.11. The three bodies are in the same plane of motion although versions of this model with different orbital planes for the primaries exist. The period of the orbit of the Sun in this frame is equal to the synodic month (roughly 29.5 days). This model is also useful for including the SRP perturbation and eclipses in the CRTBP.

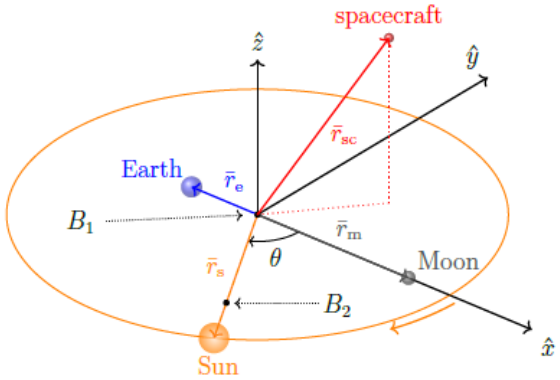


Figure 2.11: Bicircular Restricted Four Body Problem in the Earth-Moon rotating frame. Extracted from [69].

The equations of motion for the BCR4BP are obtained by extending Eqs. (2.13):

$$\ddot{x} - 2\dot{y} = \frac{\partial \widetilde{\omega}}{\partial x} \tag{2.62a}$$

$$\ddot{y} + 2\dot{x} = \frac{\partial \widetilde{\omega}}{\partial y} \tag{2.62b}$$

$$\ddot{z} = \frac{\partial \widetilde{\omega}}{\partial z} \tag{2.62c}$$

where $\widetilde{\omega}$ is the pseudopotential function in the BCR4BP:

$$\widetilde{\omega} = U + \frac{\mu_s}{r_{sun,sc}} - \frac{\mu_s}{a_s^3}(x_s x + y_s y + z_s z) \tag{2.63}$$

with:

$$\mu_s = \frac{m_s}{m_e + m_m} \tag{2.64}$$

$$a_s = \frac{r_s}{r_{e,m}} \tag{2.65}$$

where U is the CRTBP pseudopotential for the Earth-Moon system, μ_s is the nondimensional mass of the Sun, $r_{sun,sc}$ is the distance between the Sun and the spacecraft, and m_s, m_e, and m_m are the masses of the Sun, the Earth and the Moon respectively. The parameters a_s and r_s are the nondimensional and dimensional distances between the Earth-Moon barycenter and the Sun, and $r_{e,m}$ is the distance between the Earth and the Moon. The variables x_s, y_s, and z_s are the position components of the Sun with respect to B_1, and are expressed in terms of the Earth-Moon rotating frame:

$$\begin{pmatrix} x_s \\ y_s \\ z_s \end{pmatrix} = a_s \begin{pmatrix} \cos(\theta) \\ \sin(\theta) \\ 0 \end{pmatrix} = \begin{pmatrix} a_s \cos(\omega t + \theta_0) \\ a_s \sin(\omega t + \theta_0) \\ 0 \end{pmatrix} \tag{2.66}$$

where the Sun angle θ is measured from the rotating x-axis to the Sun position vector as shown in Figure 2.11, and $\omega = -0.9253$ is the nondimensional angular velocity of the Sun as viewed in the Earth-Moon rotating frame. The time variable, t, is expressed in Earth-Moon nondimensional units. The angular velocity is computed as the difference between the nondimensional mean motion of the Sun in the inertial frame centered at the Earth-Moon barycenter, that is, $n_s = \sqrt{(1+\mu_s)/a_s^3}$, and the nondimensional mean motion of the Earth-Moon system with respect to the same observer, n, that is, the value one. Since the nondimensional mean motion of the Sun is less than nondimensional mean motion of the Earth-Moon system, ω is negative and the Sun appears to move clockwise in the Earth-Moon rotating frame. As the time variable, t, appears explicitly in the pseudopotential expression, this problem does not admit an integral of motion.

CHAPTER 3

Control of formations

The first aspect studied of the formation flying mission is its control. Spacecraft formation flying is defined by NASA's Goddard Space Flight Center (GSFC) as: *The tracking or maintenance of a desired relative separation, orientation, or position between or among spacecraft* [73]. Therefore, the fundamental requirement of any formation flying mission is to ensure that the involved spacecrafts do not separate (fly apart). During the mission, there will be different scenarios or modes of operation that will require varying levels of precision in formation control and/or reconfiguration maneuvers.

There are multiple coordination strategies for formation flying, the one followed here is known as chief-deputy (or leader-follower). In this approach, one spacecraft, the chief, is controlled to a reference orbit, and the other spacecraft, the deputy, controls its relative state to the chief [74]. This approach has the advantage that the chief follows the natural dynamics of its orbit, unaffected by the deputy control, which limits the impact in the chief design.

As described in chapter 1, the mission under study is a chief-deputy formation in which the chief is a CMB telescope that needs to be calibrated periodically. The deputy is a CubeSat that will be deployed from the chief once it has reached its nominal orbit. The deputy has three main modes of operation: calibration, stand-by, and reconfiguration; each one with different target states and accuracy requirements. In the Calibration mode, the chief moves to a predefined position in the observation zone, where it emits a well-known reference signal to be received by the chief's instrument. In this mode, the formation must be held more tightly, with a margin error of cm or m (depending on the size of the formation). In the Stand-by mode, the deputy stays out of the observation zone of the chief, loosely keeping the

formation. As for the Reconfiguration mode, in this mode the deputy moves from the calibration position to the standby position and vice versa. Therefore, three control modes are required for this mission, one for each of the operational modes and named after them: Calibration mode, Stand-by mode, and Reconfiguration mode.

The present chapter aims to provide a preliminary scheme of the deputy GNC system, with emphasis on the controller design, for the mission described above. This GNC system and its analysis under a high-fidelity dynamical simulator will help obtain an initial assessment of the feasible GNC performance and the ΔV budget in chapter 6.

The proposed GNC design consists of a single controller, based on the Model Predictive Control (MPC) algorithm [75], which will have a different configuration for each control mode. In order to have a baseline reference to compare and assess the performance and cost of the proposed GNC system, alternative controllers are defined for each control mode to be used as a baseline reference. Such controllers are the Linear Quadratic Regulator (LQR) [76], for the Calibration control mode, and the Equitime Targeting Method (ETM) [77], for the Reconfiguration and Stand-by control modes. These controllers are widely used, and its implementation is simple and straightforward.

The chapter is organized as follows. Section 3.1 describes the GNC system, including details of its implementation. In section 3.2 a linear relative motion model is derived from the CRTBP equations. Sections 3.3 and 3.4 focus on the navigation filter and the controllers design, respectively. Finally, in section 3.5 the results of the analysis of the GNC system in a high-fidelity dynamics simulator are presented.

3.1 GNC system

The formation control is exerted by the the guidance, navigation and control (GNC) system of the deputy spacecraft. Overall, the on-board GNC system is responsible of the following tasks:

- Guidance: defines the desired state in order to follow the nominal path.
- Navigation: determines the current state of the spacecraft.
- Control: produces the required forces to achieve the desired state.

A functional diagram of the GNC system is depicted in Figure 3.1, showing the typical data flow within the GNC system and the closed-loop control system. The main block comprises the on-board GNC, *Inputs* block includes the reference relative state commanded to the deputy, and the *Plant* block incorporates the dynamics that governs the spacecraft motion, and the actuators and sensors.

This GNC is designed as a semi-autonomous GNC, which would operate with the minimum interaction from the chief, in order to minimize the impact in the architecture of the latter spacecraft. Furthermore, it is intended for a microsatellite which, due to its small size and limited resources, faces several restrictions, one being the limited onboard computing capabilities. These two conditions set constraints on

the complexity of GNC algorithms. Although the assessment of the computational cost of GNC algorithms is out of the scope of this work, simplicity is taken into account as a design driver.

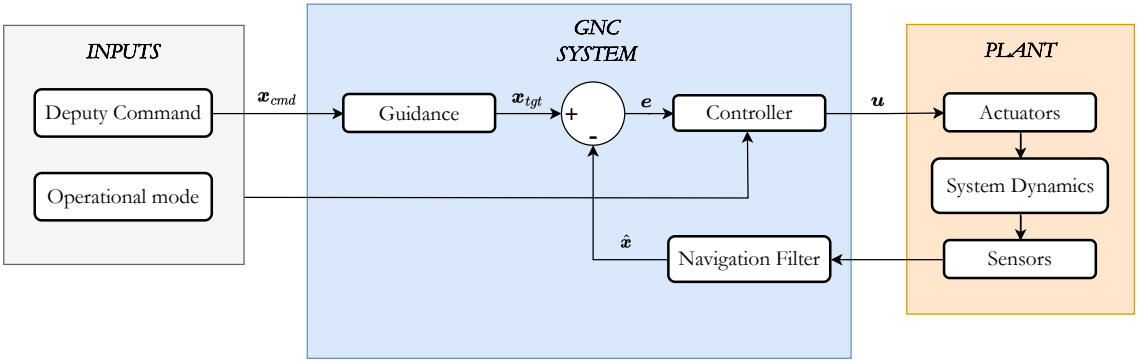


Figure 3.1: Functional diagram of the GNC system.

3.1.1 Local coordinate frame

In order to work with the relative position and velocity of the deputy with respect to the chief, a local coordinate frame centered in the chief is defined here (see Figure 3.2). The axes of this frame are parallel to the synodic frame defined in section 2.1.

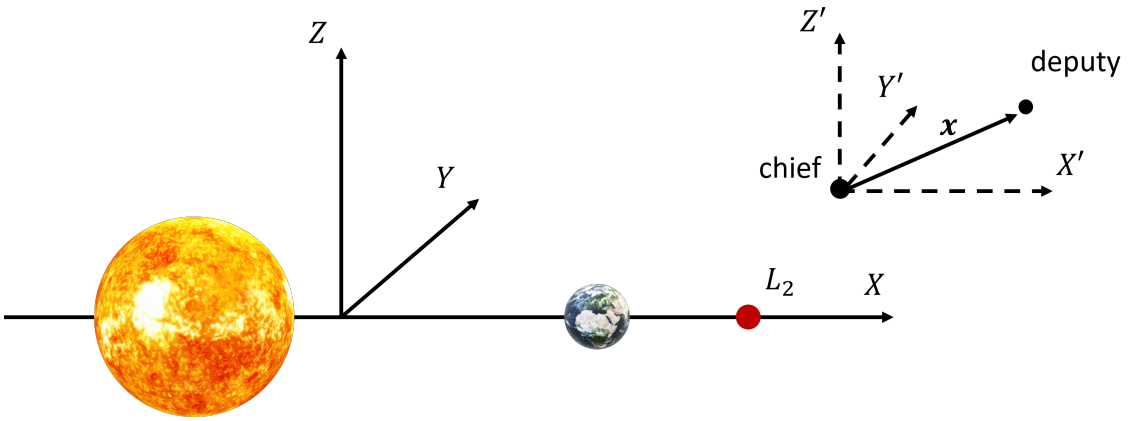


Figure 3.2: Scheme of the local coordinate frame, which is parallel to the synodic frame and centered in the chief.

3.1.2 Inputs

As shown in Figure 3.1, the GNC has two main inputs, the deputy command ($\boldsymbol{x}_{cmd}$) and the operational mode. The latter determines which controller is activated and its configuration. According to such a configuration, the level of precision and flexibility of the controller will vary. For a tight control, the allowable error will be lower, and it can be expected to have a larger control effort while for a loose control, the constraints are less strict, with higher variations of relative position and velocity and lower control effort.

3.1.3 On-board GNC

Guidance

The guidance function chosen for the GNC is straightforward and no guidance algorithm is implemented. The target relative state ($\boldsymbol{x}_{tgt}$) for the deputy with respect to the chief is set manually as input (deputy command).

Navigation

The main goal of the navigation function is to provide the necessary parameters to the guidance and control functions, typically the current state of the spacecraft. Normally, filters are used to estimate the state from a combination of sensor measurements and a mathematical model. The navigation filter processes the different types of measurement to provide an estimate of the current state of the spacecraft. In this case a discrete Kalman Filter (KF) is employed, which allows to perform data fusion from the sensors outputs, obtaining an estimation of the full state of the system even though not all the state variables are directly observable by the sensors. The KF is explained in detail in section 3.3.

Control

The controller provides the control signal ($\boldsymbol{u}$) based on the difference (error $\boldsymbol{e}$) between the desired state and the actual state of the spacecraft. Three different control laws are considered, namely the Linear Quadratic Regulator (LQR), the Equitime Targeting Method (ETM), and the Model Predictive Controller (MPC).

The LQR control law, a well-established technique in control theory, provides a systematic approach to designing optimal feedback controllers. It leverages mathematical models of the spacecraft dynamics and objectives to determine control inputs that minimize a predefined cost function.

The ETM method uses impulsive maneuvers at constant time intervals in order to keep the relative position in a spacecraft formation within a certain error tolerance.

The MPC relies on mathematical models to predict the future behavior of the system, optimizing control inputs over a defined time horizon to achieve specific objectives while adhering to constraints.

The configuration of the LQR and ETM control laws with the weighting matrices in the former case and through the maneuver period and allowable error, in the latter, allows to tailor the controller behavior to different formation flying scenarios. The MPC requires similar weight matrices to the LQR, the horizon size, maneuver period, and, if implemented, collision constraints.

3.1.4 Plant

The *Plant* block describes the dynamics of the formation of both spacecraft at the libration point, taking into account the forces exerted by the actuators and providing data for the sensor models.

Actuators

The spacecraft typically maneuver by using thrusters. These actuators are activated during a time period (burn time or t_b) in which they produce a thrust force. These thruster burns are commonly specified by the spacecraft's desired change in velocity (ΔV). The error in the implementation of the ΔV affects the performance of the formation control and must be taken into account. Each time the controller is executed, it returns a ΔV command from which the burn time is obtained following the Eq. (3.1).

$$t_b = \frac{m\Delta V}{T_n} \tag{3.1}$$

where m is the mass of the spacecraft (assumed to be constant during the maneuver) and T_n is the nominal force provided by the thruster. The actual thrust delivered, T_a will be slightly different (due to unpredictable fluctuations in the engine or slow spinning of the spacecraft during the maneuver) and can be modeled as:

$$T_a = T_n(1 + w) \tag{3.2}$$

where w is a small random variable that accounts for errors during the maneuver. The characteristics of the thrusters are outlined in Table 3.1 and are based on the specifications of a COTS propulsion module for CubeSats [78].

Table 3.1: Thrusters characteristics employed in the simulation.

Parameter	Value
Nominal thrust	1 mN
Thrust resolution	10 μN
I_{sp}	100 s
Thrust error	$\mathcal{N}(0, 0.005)$

In the case of continuous controllers as LQR, the control signal is directly the acceleration to be applied to the system. As the controllers operate in a discrete system (the OBC running at a fixed frequency), this control signal is discretized by accounting for the total ΔV that such acceleration would produce in the system during the duration of a step, and then it is used as input to compute t_b.

Sensors

The measurements are a fundamental element for the navigation function, as the navigation filter performance is strongly dependent on the type of measurement, their frequency and their quality. In this case, a RF based metrology system [79] is considered to provide the deputy with the range and line of sight (LOS) at which the chief is located.

Noise is an inherent characteristic of any physical measurement system and thus must be included in the model to be able to asses the performance and robustness of the GNC system. Sensor noise is modeled as random Gaussian noise added to each component of the relative position. According to the sensor considered, two distinct

sources of error are identified: the range measurement error and the angular error in the direction measurement. In order to add the noise to the measurements, the Cartesian relative position is first converted into spherical coordinates, then, the noise is incorporated into the radial distance, zenith angle, and azimuth angle and finally the spherical coordinates are converted back into Cartesian coordinates. The noise characteristics for the sensors are described in Table 3.2 and are based on the results obtained in the PRISMA mission [80], which implemented a similar metrology system.

Table 3.2: Sensor noise characteristics.

Parameter	Value (σ)
Range error [mm]	10
Angular error [°]	1

Dynamics

The on-board dynamics model is based on the linearized equations of the CRTBP, which is, in turn, an idealized model of the libration point dynamics. The use of approximate linear models is useful due to its computational simplicity and ease of implementation. Nevertheless, the simplification or exclusion of perturbations and nonlinear effects adds uncertainty (process noise) to the dynamical model, which can degrade the control performance in real-world operations. Therefore, in order to test the robustness and accuracy of the proposed on-board GNC system, it will be analyzed using a high-fidelity dynamics model based on ephemeris and SRP perturbation.

3.2 Linear relative motion model

In order to model the dynamics of the relative motion of the deputy with respect to the chief, the equations of motion of a body in the CRTBP can also be written in vector form, which provides a compact representation of the dynamics of the third body and will also facilitate its manipulation. By denoting the position of the third body as $\boldsymbol{r} = (x \quad y \quad z)^\top$ and the positions of the primaries as $\boldsymbol{r}_2 = (-\mu \quad 0 \quad 0)^\top$ and $\boldsymbol{r}_2 = (1-\mu \quad 0 \quad 0)^\top$ respectively, Eq. (2.13) becomes:

$$\ddot{\boldsymbol{r}} = \mathrm{M}_1 \boldsymbol{r} + \mathrm{M}_2 \dot{\boldsymbol{r}} + \boldsymbol{f}(\boldsymbol{r}) \tag{3.3}$$

$$\mathrm{M}_1 = \begin{pmatrix} 1 & 0 & 0 \\ 0 & 1 & 0 \\ 0 & 0 & 0 \end{pmatrix} \tag{3.4}$$

$$\mathrm{M}_2 = \begin{pmatrix} 0 & 2 & 0 \\ -2 & 0 & 0 \\ 0 & 0 & 0 \end{pmatrix} \tag{3.5}$$

$$\boldsymbol{f}(\boldsymbol{r}) = -\frac{1-\mu}{\rho_1^3}(\boldsymbol{r} - \boldsymbol{r}_1) - \frac{\mu}{\rho_2^3}(\boldsymbol{r} - \boldsymbol{r}_2) \tag{3.6}$$

The equations of motion for the chief ($\boldsymbol{r}_c$) and the deputy ($\boldsymbol{r}_d$) are then:

$$\ddot{\boldsymbol{r}}_c = \mathrm{M}_1 \boldsymbol{r}_c + \mathrm{M}_2 \dot{\boldsymbol{r}}_c + \boldsymbol{f}(\boldsymbol{r}_c) \tag{3.7}$$

$$\ddot{\boldsymbol{r}}_d = \mathrm{M}_1 \boldsymbol{r}_d + \mathrm{M}_2 \dot{\boldsymbol{r}}_d + \boldsymbol{f}(\boldsymbol{r}_d) \tag{3.8}$$

Subtracting Equation (3.7) from Equation (3.8), the differential equation of the relative motion is obtained, as shown in Equation (3.9). This equation describes the relative acceleration, denoted by $\delta\ddot{\boldsymbol{r}}$, as a function of the relative position, denoted by $\delta\boldsymbol{r} = \boldsymbol{r}_d - \boldsymbol{r}_c$, and the relative velocity, denoted by $\delta\dot{\boldsymbol{r}}$, between the two spacecrafts. The nonlinear vector function $\boldsymbol{f}(\boldsymbol{r}_d) - \boldsymbol{f}(\boldsymbol{r}_c)$ describes the perturbations that affect the relative motion.

$$\delta\ddot{\boldsymbol{r}} = \ddot{\boldsymbol{r}}_d - \ddot{\boldsymbol{r}}_c = \mathrm{M}_1 \delta\boldsymbol{r} + \mathrm{M}_2 \delta\dot{\boldsymbol{r}} + \boldsymbol{f}(\boldsymbol{r}_d) - \boldsymbol{f}(\boldsymbol{r}_c) \tag{3.9}$$

By linearizing Equation (3.9) about the L_2 libration point, the relative motion can be approximated by Equation (3.10), which is expressed in terms of the relative displacement $\delta\boldsymbol{r}$ and the velocity $\delta\dot{\boldsymbol{r}}$.

$$\delta\ddot{\boldsymbol{r}} \approx \mathrm{M}_1 \delta\boldsymbol{r} + \mathrm{M}_2 \delta\dot{\boldsymbol{r}} + \left.\frac{\partial \boldsymbol{f}}{\partial \boldsymbol{r}}\right|_{\boldsymbol{r}_{L_2}} \delta\boldsymbol{r} \tag{3.10}$$

Defining the relative state vector as $\boldsymbol{x} = (\delta\boldsymbol{r} \quad \delta\dot{\boldsymbol{r}})^\top$, Eq. (3.10) can be expressed as:

$$\dot{\boldsymbol{x}} \approx \begin{pmatrix} 0_{3x3} & \mathrm{I}_{3x3} \\ \left.\frac{\partial \boldsymbol{f}}{\partial \boldsymbol{r}}\right|_{\boldsymbol{r}_{L_2}} + \mathrm{M}_1 & \mathrm{M}_2 \end{pmatrix} \boldsymbol{x} = \mathrm{A}\boldsymbol{x} \tag{3.11}$$

with:

$$\mathrm{A} = \begin{pmatrix} 0 & 0 & 0 & 1 & 0 & 0 \\ 0 & 0 & 0 & 0 & 1 & 0 \\ 0 & 0 & 0 & 0 & 0 & 1 \\ 1+2\alpha & 0 & 0 & 0 & 2 & 0 \\ 0 & 1-\alpha & 0 & -2 & 0 & 0 \\ 0 & 0 & -\alpha & 0 & 0 & 0 \end{pmatrix} \tag{3.12}$$

The system matrix A given in Equation (3.12) describes the linear dynamics of the relative motion (note that it is the same matrix as in the linear motion of a single spacecraft around a libration point (see Eq. 2.25)). Therefore, the state transition matrix Φ for the relative motion can be expressed as:

$$\boldsymbol{x} = \Phi(t, t_0)\boldsymbol{x}_0 \tag{3.13}$$

$$\dot{\Phi}(t, t_0) = \mathrm{A}\Phi(t, t_0) \tag{3.14}$$

where $\boldsymbol{x}_0$ represents the initial difference between the chief and deputy states. As the system matrix A is constant, the solution to the Eq. (3.14) is [58]:

$$\Phi(t_f, t_0) = \Phi(t_0, t_0) + \mathrm{A}(t_f - t_0) \tag{3.15}$$

with the initial condition $\Phi(t_0, t_0) = \mathrm{I}_{6\times6}$.

3.3 Relative state estimation: Kalman filter

The Kalman filter (KF) was originally developed in 1960 by Robert Kalman as a new approach to linear filtering and prediction problems. There are multiple variants of this filter, each one developed to address specific requirements; some examples are the Unscented Kalman Filter (UKF), the Particle Finder (PF) or the Extended Kalman Filter (EFK). In this case, a discrete Kalman filter [81] based on the linear relative dynamic model has been implemented for the deputy relative state estimation.

This section provides a brief introduction to the principle of the KF. This filter has a recursive predictor-corrector structure, as shown in Figure 3.3. First, the system state is predicted by propagating forward in time the previous state estimate using a dynamic model. Then, the new information provided by the sensors is incorporated by correcting the propagated estimation with a gain matrix. One of the main advantages of the Kalman filter is that it enables the computation of the covariance matrix (P) associated with the state estimate ($\hat{\boldsymbol{x}}$), providing with a measure of the confidence (or uncertainty) in such estimation.

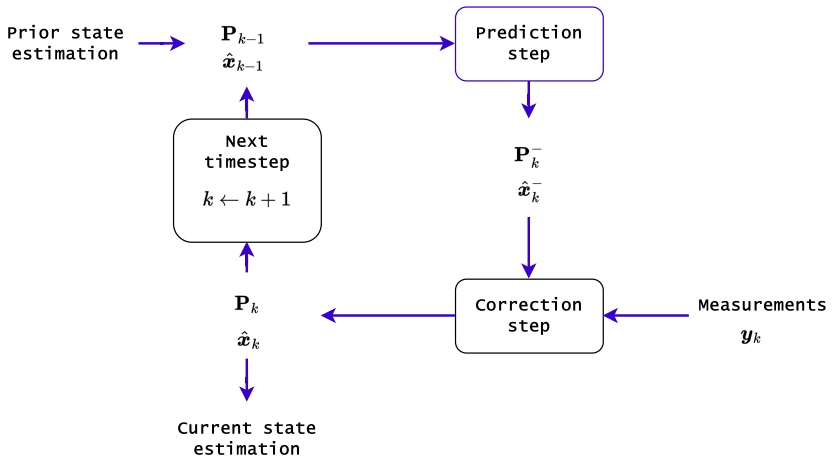


Figure 3.3: Scheme of the Kalman filter.

Prediction step

As previously said, in this step, the previous state estimate (or the initial estimation in the starting step), $\hat{\boldsymbol{x}}_{k-1}$, is propagated using the following model:

$$\hat{\boldsymbol{x}}_k^- = \boldsymbol{f}(\hat{\boldsymbol{x}}_{k-1}) + \mathrm{B}\boldsymbol{u}_{k-1} \tag{3.16}$$

where $\boldsymbol{f}(\hat{\boldsymbol{x}}_{k-1})$ is the function that maps the state in the time step $k-1$ with the state in the time step k and B represents the influence of the control $\boldsymbol{u}_{k-1}$ on the

state:

$$\mathrm{B} = \begin{pmatrix} 0 & 0 & 0 \\ 0 & 0 & 0 \\ 0 & 0 & 0 \\ 1 & 0 & 0 \\ 0 & 1 & 0 \\ 0 & 0 & 1 \end{pmatrix} \tag{3.17}$$

The function $\boldsymbol{f}$ can represent the integration of the nonlinear dynamics between those time steps or a linear approximation of the dynamics. In this case, the linearized relative motion model presented in the previous section is used. Thus, incorporating Eq. (3.13), the Eq. (3.16) becomes:

$$\hat{\boldsymbol{x}}_k^- = \Phi_{k-1}\hat{\boldsymbol{x}}_{k-1} + \mathrm{B}\boldsymbol{u}_{k-1} \tag{3.18}$$

where Φ_{k-1} is the state transition matrix between time steps $k-1$ and k, that is, $\Phi(t_k, t_{k-1})$. Note that in this case, if the time step is constant, Φ will remain also constant (see Eq. (3.15)). The resulting predicted state estimate $\hat{\boldsymbol{x}}_k^-$ is also called *a priori* state estimate. The covariance matrix P is also propagated by using the following equation:

$$\mathrm{P}_k^- = \Phi_{k-1}\mathrm{P}_{k-1}\Phi_{k-1}^\top + \mathrm{W} \tag{3.19}$$

where W represents the process noise covariance matrix, which is constructed using the values from Table 3.3:

$$\mathrm{W} = \begin{pmatrix} \sigma_r^2 & 0 & 0 & 0 & 0 & 0 \\ 0 & \sigma_r^2 & 0 & 0 & 0 & 0 \\ 0 & 0 & \sigma_r^2 & 0 & 0 & 0 \\ 0 & 0 & 0 & \sigma_v^2 & 0 & 0 \\ 0 & 0 & 0 & 0 & \sigma_v^2 & 0 \\ 0 & 0 & 0 & 0 & 0 & \sigma_v^2 \end{pmatrix} \tag{3.20}$$

Correction step

The availability of measurements $\boldsymbol{y}_k$ enables the refinement of the state estimate by comparing such measurements with those that would be obtained if the spacecraft were in the *a priori* state. To do so, a linear correction equation is defined:

$$\hat{\boldsymbol{x}}_k = \hat{\boldsymbol{x}}_k^- + \mathrm{K}_k(\boldsymbol{y}_k - \hat{\boldsymbol{y}}_k) \tag{3.21}$$

$$\hat{\boldsymbol{y}}_k = \mathrm{C}\hat{\boldsymbol{x}}_k^- \tag{3.22}$$

where C is the matrix that relates the system state to the sensors measurements:

$$\mathrm{C} = \begin{pmatrix} 1 & 0 & 0 \\ 0 & 1 & 0 \\ 0 & 0 & 1 \end{pmatrix} \tag{3.23}$$

and K_k is the Kalman gain, computed using Eq. (3.24). The Kalman gain K_k determines the extent to which the calculated *a priori* state will be corrected, based on the confidence in the sensor measurements compared to the propagated measurements. A detailed explanation of how the Eq. (3.24) is derived can be found in [81].

$$K_k = P_k^- C^T (C P_k^- C^\top + V)^{-1} \tag{3.24}$$

The matrix V contains the variance of the measurement errors, providing information about their quality. This matrix is constructed using the values from Table 3.3:

$$V = \sigma_{sensor}^2 I_{3\times 3} \tag{3.25}$$

Since the estimated state has been corrected with a measurement, the uncertainty associated with the state will also be corrected, decreasing more as the sensor's precision increases. Therefore, the covariance matrix also needs to be updated, resulting in the *a posteriori* covariance matrix P_k.

$$P_k = (I_{6\times 6} - K_k C) P_k^- \tag{3.26}$$

The estimation of the state will have a direct impact on the control performance. First, when computing the error in the control loop and second, when applying maneuvers (i.e., thrusting in an unintended direction). In addition to thrusting errors, the uncertainty in the dynamical model used for the propagation will impact the state estimation.

As indicated previously, the Table 3.3 contains the parameters used for the W and V covariance matrices. These matrices balance the uncertainty in the measurements with the uncertainty in the dynamics model. The parameters have been selected based on the sensor model noise and those used in [82] for the system covariance matrix.

Table 3.3: Parameters used for the W and V covariance matrices.

Parameter	Value
σ_r	0
σ_v	$1 \cdot 10^{-6}$
σ_{sensor}	$1 \cdot 10^{-2}$

3.4 Control strategy design

In this section, the theory behind the three control laws used is discussed, followed by an explanation of the control modes in which these control laws are applied.

3.4.1 Control laws

LQR

LQR, which stands for Linear Quadratic Regulator, is a well-known control technique in the field of control systems engineering. It is used to design optimal feedback controllers for linear time-invariant (LTI) systems:

$$\dot{\boldsymbol{x}} = \mathrm{A}\boldsymbol{x} + \mathrm{B}\boldsymbol{u} \tag{3.27}$$

$$\boldsymbol{y} = \mathrm{C}\boldsymbol{x} \tag{3.28}$$

The main objective of LQR is to minimize a cost function that represents the trade-off between the control effort and the performance of the system. This cost function typically includes terms related to the state error and the control effort. The LQR controller determines the control input that minimizes this cost function over a specified time horizon. In order to simplify the problem, an infinite time window is considered. Typically, this cost function takes the form:

$$J(\boldsymbol{u}) = \int_0^\infty (\boldsymbol{x}^\top \mathrm{Q}\boldsymbol{x} + \boldsymbol{u}^\top \mathrm{R}\boldsymbol{u})dt \tag{3.29}$$

where Q and R are the weight matrices for the state error and the control effort, respectively. These weighting matrices define the relative importance of the state error and the control effort in the cost function. More details about these matrices and how they are built are included at the end of this section.

The LQR control design process involves solving a mathematical optimization problem known as the algebraic Riccati equation. By solving this equation, the optimal state-feedback gain matrix K_{lqr}, which determines the control law for the system, is obtained. The LQR controller applies a linear feedback of the state variables, where the feedback gain is computed based on the system model and weighting matrices.

The LQR control law is defined as:

$$\boldsymbol{u} = -\mathrm{K}_{lqr}\boldsymbol{x} + \mathrm{K}_{eq}\boldsymbol{x}_{tgt} \tag{3.30}$$

where $\boldsymbol{x}_{tgt}$ is the target relative state. Substituting Eq. (3.30) into Eq. (3.27) and considering that K_{eq} matrix is used to fix the equilibrium position, then:

$$0 = (\mathrm{A} - \mathrm{B}\mathrm{K}_{lqr})\boldsymbol{x} + \mathrm{B}\mathrm{K}_{eq}\boldsymbol{x}_{tgt} \tag{3.31}$$

$$\boldsymbol{y} = \mathrm{C}\boldsymbol{x} \tag{3.32}$$

and therefore:

$$\mathrm{K}_{eq} = -(\mathrm{C}(\mathrm{A} - \mathrm{B}\mathrm{K})^{-1}\mathrm{B})^{-1} \tag{3.33}$$

The gain matrix can be obtained as:

$$\mathrm{K} = \mathrm{R}^{-1}\mathrm{B}\mathrm{P}_{lqr} \tag{3.34}$$

where P_{lqr} results from solving the Ricatti equation:

$$\dot{\mathrm{P}}_{lqr} = \mathrm{A}^\top \mathrm{P} + \mathrm{P}_{lqr}\mathrm{A} - (\mathrm{P}_{lqr}\mathrm{B})\mathrm{R}^{-1}(\mathrm{B}^\top \mathrm{P}_{lqr}) + \mathrm{Q} \tag{3.35}$$

In the case of optimizing the cost function with an infinite superior limit, $\dot{P}_{lqr} = 0$.

ETM

The Equitime Targeting Method (ETM) is an approach used in spacecraft formation flying to maintain a desired relative position within a specified tolerance [77]. This technique involves employing impulsive maneuvers at fixed time intervals. Figure 3.4 provides an illustration of the ETM method.

In this method, the deputy spacecraft follows a nominal orbit that deviates from the chief spacecraft's natural orbit by a constant offset, denoted $\boldsymbol{s}$. Consequently, the deputy's orbit is generally considered unnatural. To ensure that the deputy spacecraft remains on this unnatural orbit, the orbit is divided into equal time segments. At the beginning of each segment, the deputy spacecraft executes an impulsive maneuver, denoted as ΔV_i, in order to intersect with the nominal orbit at the end of that particular segment. The subscripts in Figure 3.4 indicate the corresponding segments, and the relative velocities of the deputy spacecraft are represented by δV_i, where the superscripts $-$ and $+$ denote the state before and after the impulsive maneuver, respectively. It is important to note that the determination of the required ΔV is achieved by using a single shooting differential correction method (see section 2.2.4).

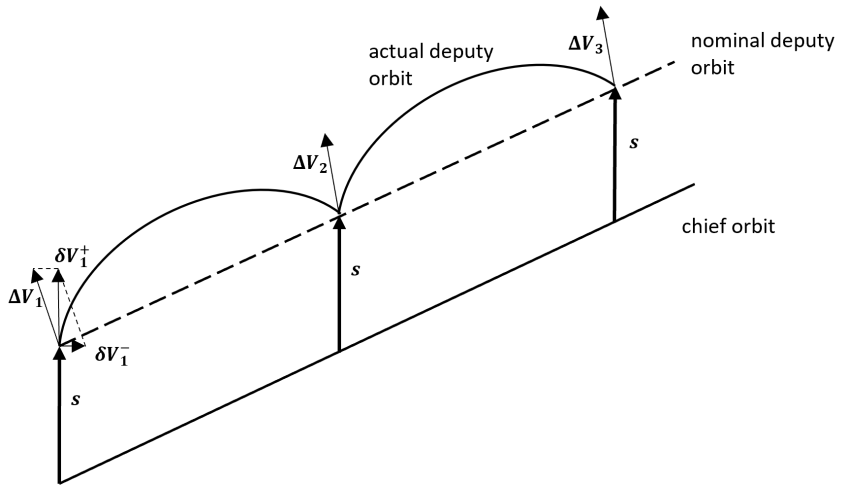


Figure 3.4: Scheme of the Equitime Trageting Method.

MPC

Model Predictive Controller (MPC) is a control strategy that uses a dynamic model of the system to predict its behavior over a future time horizon (see Figure 3.5). By leveraging these predictions, MPC determines an optimal control sequence that minimizes a defined cost functions while satisfying a set of constraints. Each time the control algorithm is executed, the current state of the system is used as initial condition of the optimization and then the control input is applied to the system until a new computation is completed, providing an updated control input. The horizon (n_p) can have a fixed size (receding-horizon) or extend until a given final time (shrinking-horizon). Here, the former approach is followed, as it is more adequate for the problem on hand. This is because long horizons increase the computational cost and are prone to accumulate large errors in highly nonlinear dynamics.

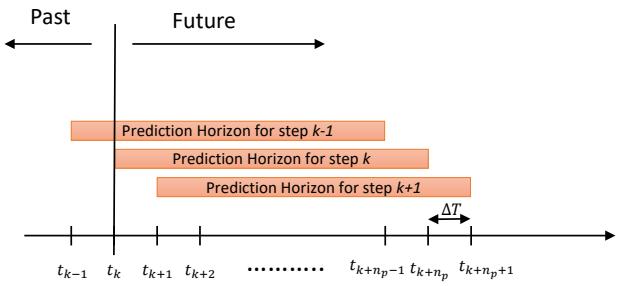


Figure 3.5: Model Predictive Controller (receding-horizon) scheme.

Similarly to the LQR problem, MPC aims to compute the control input by minimizing a cost function that quantifies the control performance. Unlike in LQR, in this case the cost function is discretized within a time frame, and solved through a numerical optimization scheme. Therefore, the cost function from Eq. (3.29) can be written as:

$$J(\Delta \boldsymbol{x}_{k,\dots,k+n_p}, \boldsymbol{u}_{k,\dots,k+n_p}) = \sum_{i=1}^{n_p} \Delta \boldsymbol{x}_{k+i}^\top \mathrm{Q} \Delta \boldsymbol{x}_{k+i} + \sum_{i=0}^{n_p-1} \boldsymbol{u}_{k+i}^\top \mathrm{R} \boldsymbol{u}_{k+i} \tag{3.36}$$

where $\Delta \boldsymbol{x}_k = \boldsymbol{x}_{tgt} - \boldsymbol{x}_k$ represents the deviation of the state at the instant t_k from the target state and $\boldsymbol{u}_k$ the control input at such an instant. The period of time between maneuvers is constant ΔT. The matrices R and Q are, as in the LQR controller, the weight matrices. Following the approach presented in [83], it is possible to express the cost function in matrix form, since the evolution of the system is completely defined by the initial conditions and a given sequence of control actions ($\boldsymbol{u}_k$, $\boldsymbol{u}_{k+1}$,..., $\boldsymbol{u}_{k+n_p}$):

$$J(\mathbb{U}_k) = \frac{1}{2} \mathbb{U}_k^\top \mathbb{H}_k \mathbb{U}_k + \boldsymbol{l}^\top \mathbb{U}_k \tag{3.37}$$

$$\mathbb{H}_k = \mathbb{B}_k^\top \hat{\mathrm{Q}} \mathbb{B}_k + \hat{\mathrm{R}} \tag{3.38}$$

$$\boldsymbol{l} = (\Delta \boldsymbol{x}_k^\top \mathbb{A}_k^\top \hat{\mathrm{Q}} \mathbb{B}_k)^\top \tag{3.39}$$

where $\mathbb{A}_k \in \mathbb{R}^{6n_p \times 6}$ and $\mathbb{B}_k \in \mathbb{R}^{6n_p \times 3n_p}$ are the stack matrices of the state transition matrix and the input matrix of the system and are constructed as in Eqs. (3.40) and (3.41). The matrices $\hat{\mathrm{Q}}$ and $\hat{\mathrm{R}}$ are the stacked weight matrices. A detailed explanation of how they are build is included at the end of this section.

$$\mathbb{A}_k = \begin{bmatrix} \mathrm{A}_k^{k+1} \\ \mathrm{A}_{k+1}^{k+2} \mathrm{A}_k^{k+1} \\ \prod_{i=2}^{0} \mathrm{A}_{k+i}^{k+i+1} \\ \dots \\ \prod_{i=n_p-1}^{0} \mathrm{A}_{k+i}^{k+i+1} \end{bmatrix} \tag{3.40}$$

$$\mathbb{B}_k = \begin{bmatrix} \mathrm{B}_k^{k+1} & 0 & 0 & \dots & 0 \\ \mathrm{A}_{k+1}^{k+2}\mathrm{B}_k^{k+1} & \mathrm{B}_{k+1}^{k+2} & 0 & & 0 \\ \mathrm{A}_{k+2}^{k+3}\mathrm{A}_{k+1}^{k+2}\mathrm{B}_k^{k+1} & \mathrm{A}_{k+2}^{k+3}\mathrm{B}_{k+1}^{k+2} & \mathrm{B}_{k+2}^{k+3} & & 0 \\ \vdots & \vdots & \vdots & \ddots & \\ (\prod_{i=n_p-1}^{1}\mathrm{A}_{k+i}^{k+i+1})\mathrm{B}_k^{k+1} & (\prod_{i=n_p-1}^{2}\mathrm{A}_{k+i}^{k+i+1})\mathrm{B}_{k+1}^{k+2} & \dots & \mathrm{A}_{k+n_p-1}^{k+n_p}\mathrm{B}_{k+n_p-2}^{k+n_p-1} & \mathrm{B}_{k+n_p-1}^{k+n_p} \end{bmatrix} \tag{3.41}$$

Thus, it is possible to write:

$$\mathbb{X}_{k+1} = \mathbb{A}_k \Delta \boldsymbol{x}_k + \mathbb{B}_k \mathbb{U}_k \tag{3.42}$$

$$\mathbb{X}_{k+1} = [\Delta \boldsymbol{x}_{k+1}^\top \, \Delta \boldsymbol{x}_{k+2}^\top \, \dots \, \Delta \boldsymbol{x}_{k+n_p}^\top]^\top \tag{3.43}$$

One of the advantages of the MPC is that it is possible to add a collision avoidance constraint to the optimization problem. Following the approach from [83, 84], the collision avoidance constraint is implemented into the present problem. In order to exploit the quadratic programming formulation, such constraint needs to be expressed in linear form. The distance constraint, which is nonlinear (Eq. (3.44)), establishes a sphere around the chief that the deputy must not enter, the so called *Keep Out Zone* (KOZ) sphere, of radius R_{KOZ}.

$$\|\mathrm{C}\Delta \boldsymbol{x}_{t,k+i}\|_2^2 = \Delta \boldsymbol{x}_{t,k+i}^\top \mathrm{C}^\top \mathrm{C} \Delta \boldsymbol{x}_{t,k+i} > R_{KOZ}^2 \tag{3.44}$$

By approximating the aforementioned sphere by a plane tangent to such sphere and normal to the $\Delta \boldsymbol{x}_{t,k+i}$ vector, the constraint can be expressed in a convex form (Eq. (3.45)). The sign of both sides of the equation is inverted, so the constraint is expressed as an upper boundary inequality.

$$-\Delta \boldsymbol{x}_{t,k+i}^\top \mathrm{C}^\top \mathrm{C} \Delta \boldsymbol{x}_{t,k+i} < -R_{KOZ} \|\mathrm{C}\Delta \boldsymbol{x}_{t,k}\|_2 \tag{3.45}$$

As Eq. (3.45) is applied to each step of the time window, it is possible to rearrange the constraint to be expressed as a stacked matrix:

$$\mathrm{A}_{ineq} \mathbb{U}_k < \boldsymbol{b}_{ineq} \tag{3.46}$$

$$\mathrm{A}_{ineq} = -\mathrm{I}_{n_p \times n_p} \otimes \Delta \boldsymbol{x}_{t,k+i}^\top \mathrm{C}^\top \mathrm{C} \mathbb{B}_k \tag{3.47}$$

$$\boldsymbol{b}_{ineq} = -R_{KOZ} \|\mathrm{C}\Delta \boldsymbol{x}_{t,k}\|_2 \mathbf{1}_{n_p \times 1} + \mathrm{I}_{n_p \times n_p} \otimes \mathbb{A}_k \Delta \boldsymbol{x}_{t,k+i} \tag{3.48}$$

which only depends on the current deviation from the target state $\Delta \boldsymbol{x}_{t,k}$. Finally, the complete control problem, with the addition of the collision avoidance constraint, is expressed as:

$$\min_{\mathbb{U}_k} \quad J(\mathbb{U}_k) = \frac{1}{2} \mathbb{U}_k^\top \mathbb{H}_k \mathbb{U}_k + \boldsymbol{l}^\top \mathbb{U}_k \tag{3.49}$$

$$\text{s.t.} \quad \mathrm{A}_{ineq} \mathbb{U}_k < \boldsymbol{b}_{ineq} \tag{3.50}$$

Weight matrices

When choosing matrices Q and R to ensure proper functioning of the LQR and MPC control laws, the following conditions must be satisfied:

- The matrix Q must be positive semidefinite. This will be true if $\boldsymbol{x}^\top \mathrm{Q}\boldsymbol{x} \geq 0$ for all $\boldsymbol{x}$. This is equivalent to having all its eigenvalues non-negative. This premise ensures that regardless of the value of the error $\boldsymbol{x}$, the term $\boldsymbol{x}^\top \mathrm{Q}\boldsymbol{x}$ in the cost function will never be negative. Otherwise, there could exist some error value that reduces the cost. Minimizing the cost function would then tend towards that error instead of a null error.
- The matrix R must be positive definite. This will be true if $\boldsymbol{u}^\top \mathrm{R}\boldsymbol{u} > 0$ for all $\boldsymbol{u} \neq 0$. This is equivalent to having all of its eigenvalues positive. This premise ensures that if a control $\boldsymbol{u} \neq 0$ is applied, there will be a non-zero associated cost since the term $\boldsymbol{u}^\top \mathrm{R}\boldsymbol{u}$ will always be positive.

The choice of coefficients characterizing the cost function is what influences the controller design, and in the literature, numerous proposals can be found. The matrices Q and R selected for this work are those used in [41], which adopts the technique of maximum magnitude. This configuration is based on setting boundary values ($\bar{x}_i$ and $\bar{u}_i$) for each component of the state (x_i) and control (u_j).

$$|x_i| < \bar{x}_i \qquad |u_j| < \bar{u}_j \tag{3.51}$$

where $i \in \{1, \ldots, 6\}$ and $j \in \{1, \ldots, 3\}$.

The matrices Q and R are given by:

$$\mathrm{Q} = \begin{bmatrix} \frac{1}{\bar{x}_1^2} & \frac{1}{2\bar{x}_1\bar{x}_2} & 0 & \frac{1}{2\bar{x}_1\bar{x}_4} & \frac{1}{2\bar{x}_1\bar{x}_5} & 0 \\ \frac{1}{2\bar{x}_2\bar{x}_1} & \frac{1}{\bar{x}_2^2} & 0 & \frac{1}{2\bar{x}_2\bar{x}_4} & \frac{1}{2\bar{x}_2\bar{x}_5} & 0 \\ 0 & 0 & \frac{1}{\bar{x}_3^2} & 0 & 0 & \frac{1}{2\bar{x}_3\bar{x}_6} \\ \frac{1}{2\bar{x}_4\bar{x}_1} & \frac{1}{2\bar{x}_4\bar{x}_2} & 0 & \frac{1}{\bar{x}_4^2} & \frac{1}{2\bar{x}_4\bar{x}_5} & 0 \\ \frac{1}{2\bar{x}_5\bar{x}_1} & \frac{1}{2\bar{x}_5\bar{x}_2} & 0 & \frac{1}{2\bar{x}_5\bar{x}_4} & \frac{1}{\bar{x}_5^2} & 0 \\ 0 & 0 & \frac{1}{2\bar{x}_3\bar{x}_6} & 0 & 0 & \frac{1}{\bar{x}_6^2} \end{bmatrix} \tag{3.52}$$

$$\mathrm{R} = \begin{bmatrix} \frac{1}{\bar{u}_1^2} & \frac{1}{2\bar{u}_1\bar{u}_2} & 0 \\ \frac{1}{2\bar{u}_2\bar{u}_1} & \frac{1}{\bar{u}_2^2} & 0 \\ 0 & 0 & \frac{1}{\bar{u}_3^2} \end{bmatrix} \tag{3.53}$$

Examining the terms along the diagonal of both matrices reveals the intention behind this configuration. The closer the variables are to their maximum values, the greater their respective coefficients, and therefore, their assigned cost will be higher. Off the diagonal, all terms relating the relative motion in the xy-plane to the normal motion outside that plane are canceled out. This approach ensures that the controller does not couple terms that are originally independent in the equations of motion for the problem.

For the MPC, the matrices $\hat{\mathrm{Q}}$ and $\hat{\mathrm{R}}$ have $6n_p \times 6n_p$ and $3n_p \times 3n_p$ size respectively and are build stacking the Q and R matrices from Eqs. (3.52) and (3.53):

$$\hat{\mathrm{Q}} = \begin{bmatrix} \mathrm{Q} & 0_{6\times6} & \cdots & 0_{6\times6} \\ 0_{6\times6} & \mathrm{Q} & \cdots & 0_{6\times6} \\ \vdots & & \cdots & \\ 0_{6\times6} & 0_{6\times6} & \cdots & \mathrm{Q} \end{bmatrix} \tag{3.54}$$

$$\hat{\mathrm{R}} = \begin{bmatrix} \mathrm{R} & 0_{3\times3} & \cdots & 0_{3\times3} \\ 0_{6\times3} & \mathrm{R} & \cdots & 0_{3\times3} \\ \vdots & & \cdots & \\ 0_{3\times3} & 0_{3\times3} & \cdots & \mathrm{R} \end{bmatrix} \tag{3.55}$$

3.4.2 Control modes

As explained in the introduction of the chapter, three control modes are defined for the GNC:

- **Calibration mode**: This mode is used to maintain a tight formation, with low permissible errors and keeping a close distance between both satellites during the calibration phase.
- **Stand-by mode**: In this mode, the formation is controlled loosely, allowing the deputy to get further from the chief compared to the Calibration mode.
- **Reconfiguration mode**: This mode is exclusively used to relocate the satellite from the calibration position to the stand-by position, and vice-versa. The main constraints in this mode are to maintain the minimum safe distance and the maneuvering time.

3.5 Simulations in High-Fidelity Dynamics

As mentioned above, each mission phase (Calibration, Stand-by, and Reconfiguration) has its own control mode, named after the associated phase. The proposed GNC design implements the same MPC controller with different configurations for each control mode. The performance of this GNC system is assessed by comparing it with a baseline design that implements the already discussed LQR (for the Calibration control mode) and ETM (for the Stand-by and Reconfiguration control modes) control laws. In this section, the simulation environment and the results of simulations carried out to assess the GNC system performance are presented.

3.5.1 Reference mission scenario

In order to perform the simulations, it is necessary to define a reference orbit (along with its primary system and the libration point at which it is located) for the chief. This choice does not affect the validity of the proposed control laws as the applied simplifications do not depend on either the primary system or the reference orbit.

However, the control performance may differ, as the disturbances to which the formation is subjected will vary.

The chosen orbit is of Lissajous type (see section 2.2.1) and is situated at the L_2 point of the Sun-Earth/Moon system. The parameters defining this orbit have been collected in Table 3.4 and are similar to those of other observation missions located at L_2 [85]. This orbit has been obtained using a differential corrections process (see section 2.2.4) and the ephemeris model (including SRP perturbation). The resulting orbit, which has been obtained for a period of 3 years, is shown in Figure 3.6.

Table 3.4: Parameters of the chief's nominal orbit.

Parameter	Value
A_x [km]	$300 \cdot 10^3$
A_z [km]	$300 \cdot 10^3$
ψ [°]	90
ϕ [°]	0

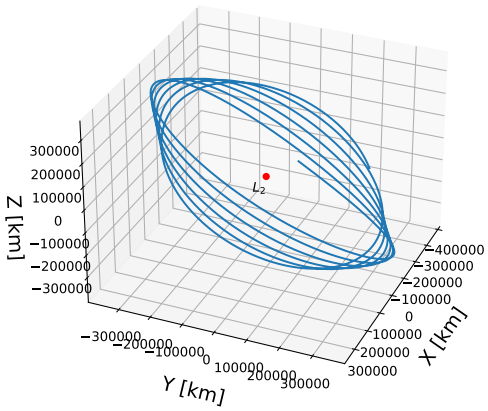


Figure 3.6: Chief's nominal orbit around the L_2 point of the Sun-Earth system.

To incorporate the solar pressure perturbation, it is necessary to define the masses (m), areas (A), and reflectivity coefficients (c_R) of both spacecraft, which are listed in Table 3.5. These values provided for the chief are on the same order of magnitude of similar missions [86, 87], and for the deputy, a 6U CubeSat with deployable panels is considered.

Table 3.5: Physical parameters of the chief and deputy required for the SRP perturbation.

Parameter	Value
A_{chief} [m^2]	10 m^2
A_{deputy} [m^2]	0.15 m^2
m_{chief} [kg]	1000 kg
m_{deputy} [kg]	10 kg
$c_{R_{chief}}$ [-]	1
$c_{R_{deputy}}$ [-]	1

3.5.2 Figures of merit

To assess the effectiveness of the control modes, three different performance metrics have been employed:

- Control accuracy: Precision with which the deputy maintains its desired relative state.

$$\boldsymbol{e} = \begin{pmatrix} \boldsymbol{e}_r \\ \boldsymbol{e}_v \end{pmatrix} = \begin{pmatrix} \boldsymbol{r} - \boldsymbol{r}_{target} \\ \boldsymbol{v} - \boldsymbol{v}_{target} \end{pmatrix} \tag{3.56}$$

  This quantity is computed at each instant and averaged over a period to assess the overall accuracy of the control. Its also expressed in spherical components (see Appendix E.1).

- Control effort: Total ΔV consumed by each control strategy.

- Convergence time (T_{conv}): The time required for each control mode to complete the specified target position. This metric is only employed for the maneuver mode.

3.5.3 Implementation

In order to be able to perform all simulations repeatedly and to facilitate the comparison of the results, a GNC simulator has been implemented (see Figure 3.7). This simulator performs two main operations during the simulation: propagating the satellites trajectories and running the predefined tasks associated with each satellite (primarily the GNC closed-loop of the deputy). The structure of the simulator is modular and allows to easily add new models for each of the components.

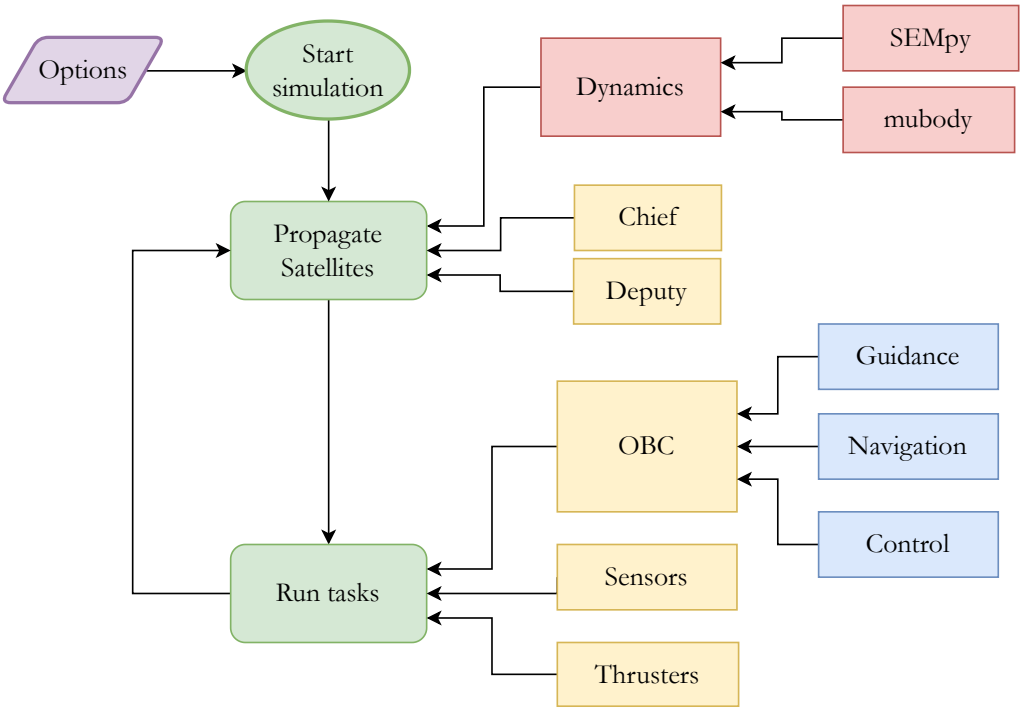


Figure 3.7: Scheme of the implementation of the GNC system. Green blocks represent the simulator operation, blue blocks correspond to GNC algorithms, red blocks are related to dynamics, yellow blocks represent models of the spacecrafts and their components and the purple block are options from the simulator.

The first task is performed by calling an external library that provides the propagation functionality. This enables the use and comparison of different astrodynamics libraries. In this case, access to two different libraries has been implemented, SEMpy [88] and mubody [65] although only the latter is used for the simulations included here.

The second task involves three operations: sensor measurements, OBC execution, and thruster actuation. The structure of the simulator enables the addition of new tasks to the OBC, different control algorithms, estimation algorithms, alternative models for the sensors and thrusters, and the execution of predefined and time-stamped commands during the simulation.

3.5.4 Simulations results

In this section, the results of the simulations are presented. Each control mode has been analyzed separately, setting initial conditions and a target state representative of the expected scenario in the corresponding mission phase. Then, the scenario has been simulated with the proposed controller and the baseline controller.

Calibration mode

The calibration control mode requires the tightest control to ensure that the reference signal produced from the calibration satellite reaches the main satellite steadily. This control mode is used to keep the deputy in its operational relative

position, where it has been relocated using the reconfiguration maneuver. In Table 3.6, the initial state (x_0) and the target state (x_{tgt}), both equal, used in the simulations are shown.

Table 3.6: Initial condition and target state for Calibration mode.

Parameter	Value [m, m/s]
$\boldsymbol{x}_0$	$[100, 100, 100, 0, 0, 0]^\top$
$\boldsymbol{x}_{tgt}$	$[100, 100, 100, 0, 0, 0]^\top$

In Table 3.7 and Table 3.8, the parameters used to configure the LQR and MPC controllers are listed. The coefficients for the weight matrices are the same for both controllers, and a horizon of size 10 with a period of 60 s has been chosen for the MPC. The simulation time is 2 h.

Table 3.7: LQR configuration parameters for the Calibration mode.

Parameter	Value
$\bar{x}_{1,2,3}$	$5 \cdot 10^{-2}$ m
$\bar{x}_{4,5,6}$	$1 \cdot 10^{-3}$ m/s
$\bar{u}_{1,2,3}$	$1.5 \cdot 10^{-4}$ m/s

Table 3.8: MPC configuration parameters for the Calibration mode.

Parameter	Value
$\bar{x}_{1,2,3}$	$5 \cdot 10^{-2}$ m
$\bar{x}_{4,5,6}$	$1 \cdot 10^{-3}$ m/s
$\bar{u}_{1,2,3}$	$1.5 \cdot 10^{-4}$ m/s^2
n_p	10
ΔT	60 s

In Figure 3.8 and Figure 3.9, the evolution of the position and velocity errors with the LQR controller is shown. As the initial state is the same as the target state, there is no transient phase. Although the controller is continuous, the OBC runs at a frequency of 1 Hz, so the control is applied every second. This makes the controller act fast on any disturbance, allowing to control the satellite very tightly but making it more susceptible to the noise from the state estimation.

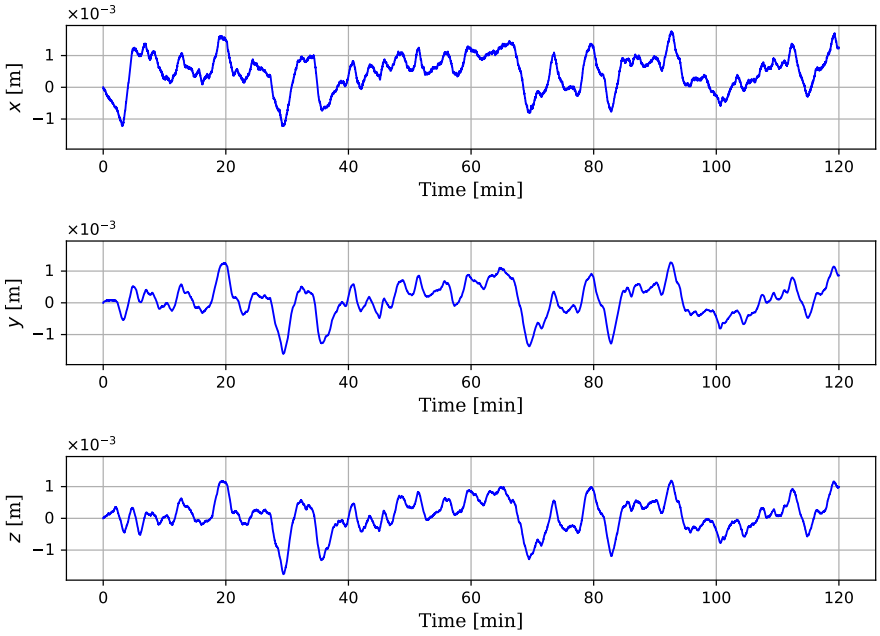


Figure 3.8: Evolution of the relative position error (e_r) during calibration using the LQR controller.

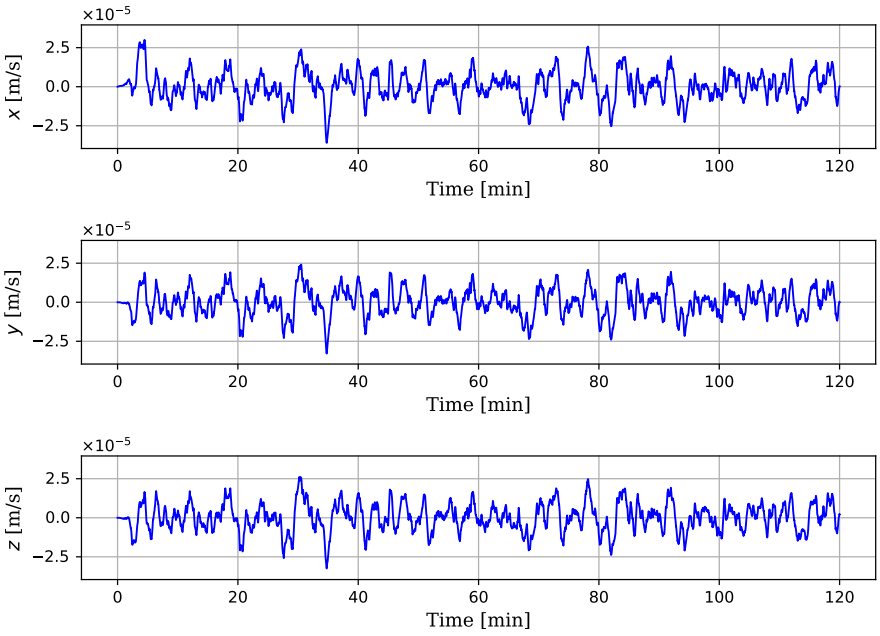


Figure 3.9: Evolution of the relative velocity error (e_v) during calibration using the LQR controller.

In Figure 3.10, the control applied by the LQR controller in the simulation is shown. The magnitude of the impulses is in the range of µm/s which is roughly the same as the thruster resolution, given the mass considered for the deputy. This can reduce the effectiveness of the controller, as the applied impulse may not precisely match the commanded one.

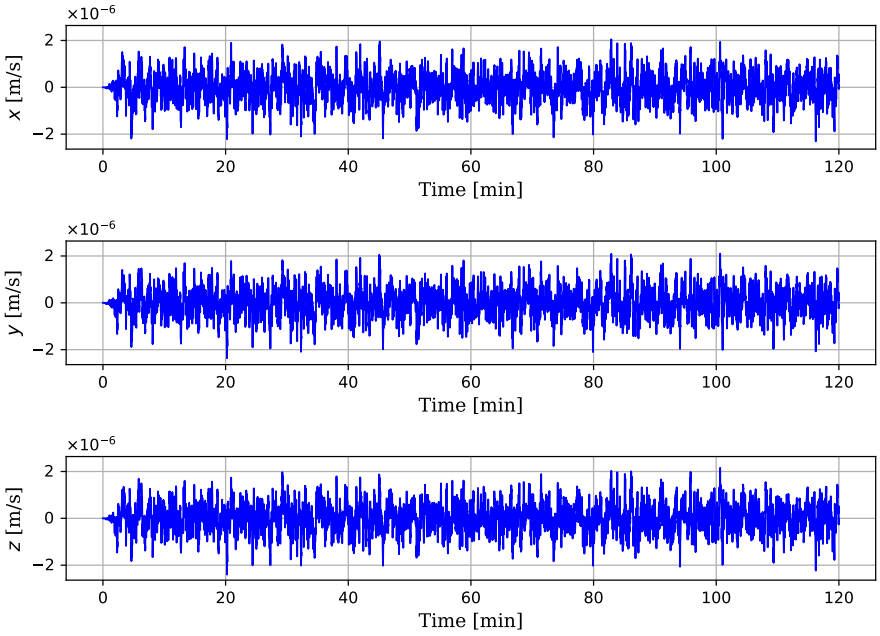


Figure 3.10: Control applied during calibration using the LQR controller.

In Figure 3.11 and Figure 3.12, the position and velocity error for the MPC controller are shown. As in the LQR case, there is no transient phase. The position error is slightly higher than with LQR and presents slower variations, which result from the discrete maneuvers every 60 s.

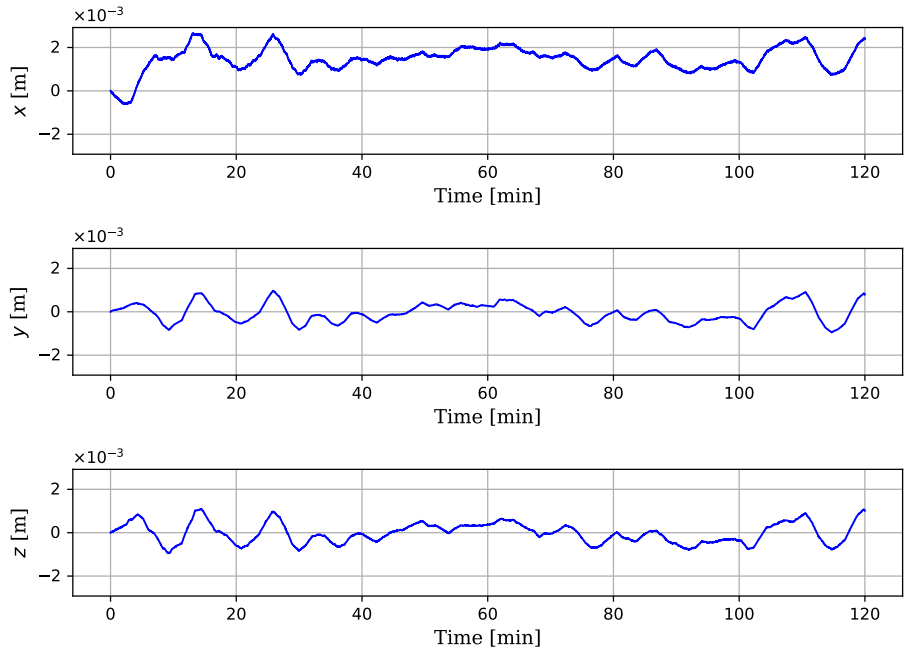


Figure 3.11: Evolution of the relative position error (e_r) during calibration using the MPC controller.

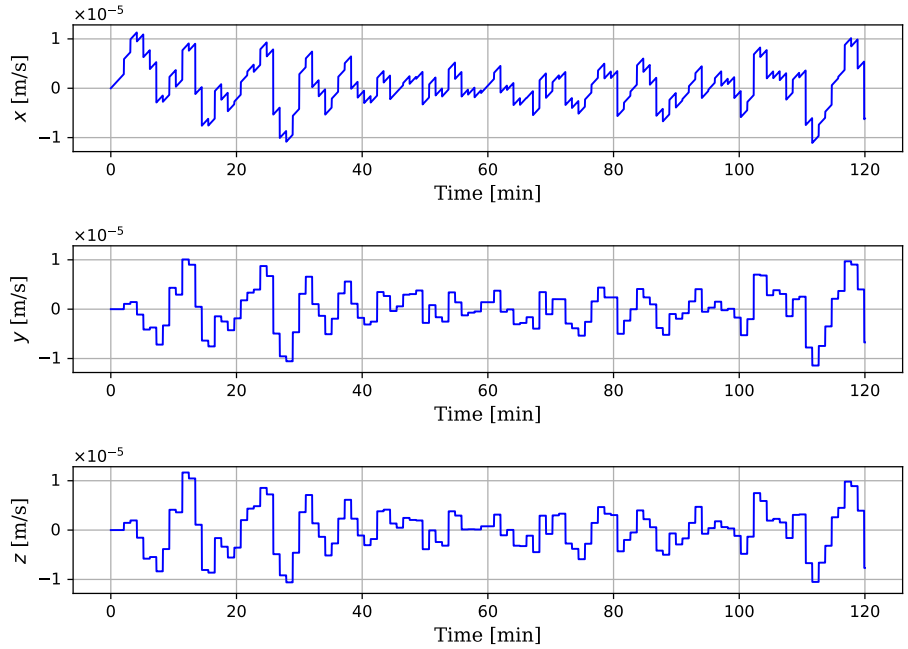


Figure 3.12: Evolution of the relative velocity error (e_v) during calibration using the MPC controller.

In Figure 3.13, the control applied by the MPC controller during the simulation is shown. The magnitude of the impulse is 10 times greater than with LQR, which enables more efficient control, as the impulses can be applied more accurately.

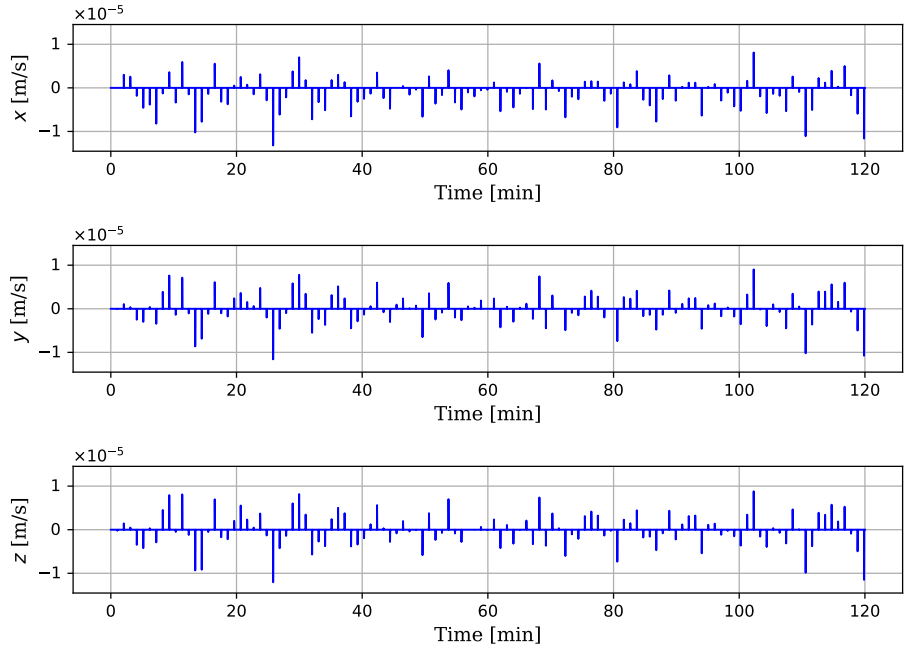


Figure 3.13: Control applied during calibration using the MPC controller.

Table 3.9 and Table 3.10 summarize the relative control performance of both controllers during the calibration phase. Although both controllers achieve similar accuracy in velocity control, LQR presents a better performance in position control than the MPC. However, the MPC controller has a ΔV cost much lower than the LQR (see Table 3.11). Furthermore, the position accuracy achieved by the MPC is in the same order as the threshold selected for the Q weight matrix, so it could be reduced by changing such a threshold (at the expense of an increase in the ΔV cost).

Table 3.9: Achieved relative position control accuracy when using LQR and MPC controllers in calibration phase. The results correspond to the RMSE value of e_r components, in cartesian and spherical coordinates.

Control Law	Cartesian [m]			Spherical [m]		
	$\boldsymbol{e}_x$	$\boldsymbol{e}_y$	$\boldsymbol{e}_z$	$\boldsymbol{e}_\rho$	$\boldsymbol{e}_\theta$	$\boldsymbol{e}_\phi$
LQR	6.34e-02	4.57e-02	4.43e-02	8.34e-02	1.85e-02	2.78e-02
MPC	1.33e-01	3.63e-02	3.92e-02	9.28e-02	5.37e-02	9.48e-02

Table 3.10: Achieved relative velocity control accuracy when using LQR and MPC controllers in calibration phase. The results correspond to the RMSE value of e_v components, in cartesian and spherical coordinates.

Control Law	Cartesian [m/s]			Spherical [m/s]		
	$\boldsymbol{e}_{v_x}$	$\boldsymbol{e}_{v_y}$	$\boldsymbol{e}_{v_z}$	$\boldsymbol{e}_{v_\rho}$	$\boldsymbol{e}_{v_\theta}$	$\boldsymbol{e}_{v_\phi}$
LQR	7.86e-04	7.46e-04	7.55e-04	1.30e-03	1.62e-04	1.67e-04
MPC	3.66e-04	3.53e-04	3.70e-04	6.07e-04	9.98e-05	1.31e-04

Table 3.11: ΔV results with each of the control laws in the Calibration mode simulations.

Control Law	$\boldsymbol{\Delta V}$ [m/s]
LQR	0.00608
MPC	0.00067

Stand-by mode

For the stand-by control mode, the ETM controller is compared with the MPC controller. In this phase, the control is looser than in the calibration phase, and the time period between control maneuvers (ΔT) is longer (6 h). In Table 3.12, the initial conditions and the target state are listed. As in the calibration phase, both are equal, but in this case the distance to the chief is larger and the deputy is situated between the Sun and the chief. The simulation time is 10 days.

Table 3.12: Initial condition and target state for Stand-by mode.

Parameter	Value [m, m/s]
$\boldsymbol{x}_0$	[-500, -500, -500, 0, 0, 0]$^\top$
$\boldsymbol{x}_{tgt}$	[-500, -500, -500, 0, 0, 0]$^\top$

In Table 3.13, the parameters used to configure the ETM controller are listed, while the configuration parameters used for the MPC controller are in Table 3.14.

Table 3.13: ETM configuration parameters.

Parameter	Value
ΔT	6 h
e_{max}	1 m

Table 3.14: MPC configuration parameters for the Stand-by mode.

Parameter	Value
$\bar{x}_{1,2,3}$	1 m
$\bar{x}_{4,5,6}$	$1 \cdot 10^{-5}$ m/s
$\bar{u}_{1,2,3}$	$1.5 \cdot 10^{-3}$ m/s^2
n_p	10
ΔT	6 h

In this case, the error in position is especially high on the x-axis (see Figure 3.14). This behavior is due to the dynamics model employed by the ETM controller, which does not include the SRP perturbation, and hence, it is not properly compensated, producing a constant bias in the direction of the perturbation (x-axis). The magnitude of this steady error increases proportionally to the period between maneuvers. Meanwhile, the y and z components of the position error are much lower and within the error threshold considered for this control mode.

This impact is also observable in the error of the relative velocity in Figure 3.15. The y and z components of the velocity error are near zero and barely grow between maneuvers. Meanwhile, the x component grows constantly over time, and the controller reduces in each maneuver approximately the same amount it has grown from the previous maneuver. The control applied (see Figure 3.16) corresponds to these changes in velocity.

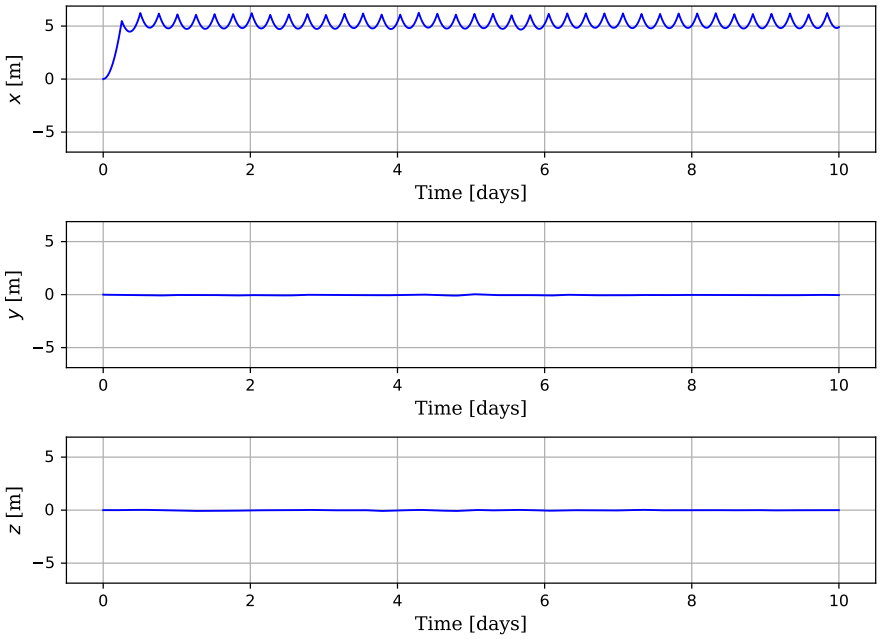


Figure 3.14: Evolution of the relative position error (e_r) during stand-by using the ETM controller.

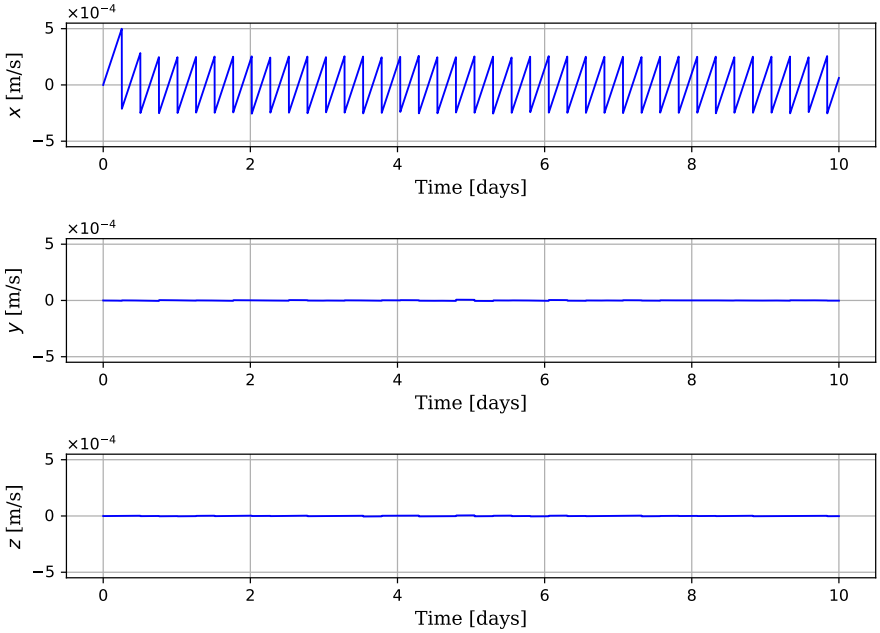


Figure 3.15: Evolution of the relative velocity error (e_v) during stand-by using the ETM controller.

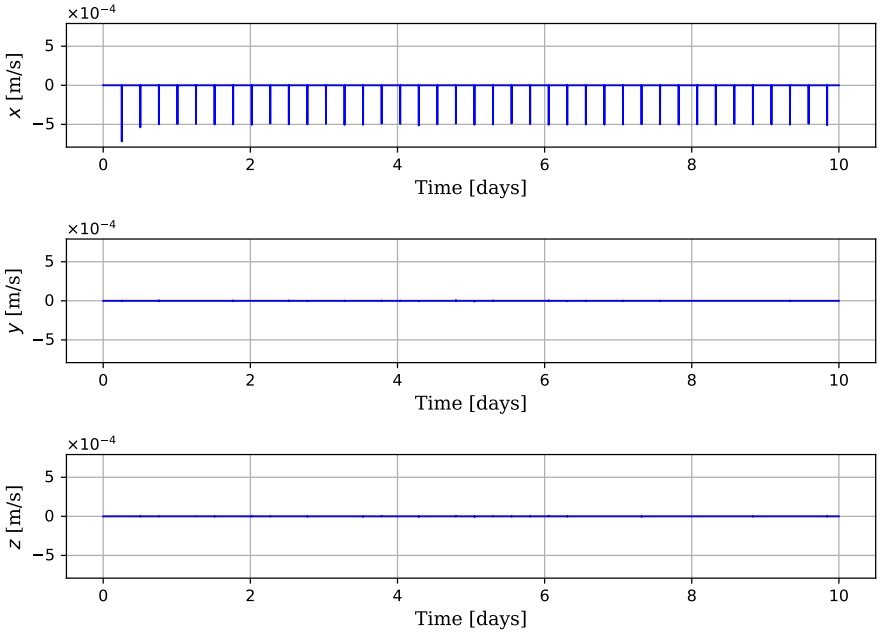


Figure 3.16: Control applied during stand-by using the ETM controller.

Similarly to the ETM, for the MPC controller the error in x-axis is higher than in the other two axes (see Figure 3.17). As said before, this is because the controller is not able to compensate the SRP perturbation, as it does not expect it, making the position error to grow. The bias can be compensated partially ajusting the corresponding value in the weight matrix Q, but it will increase the ΔV cost.

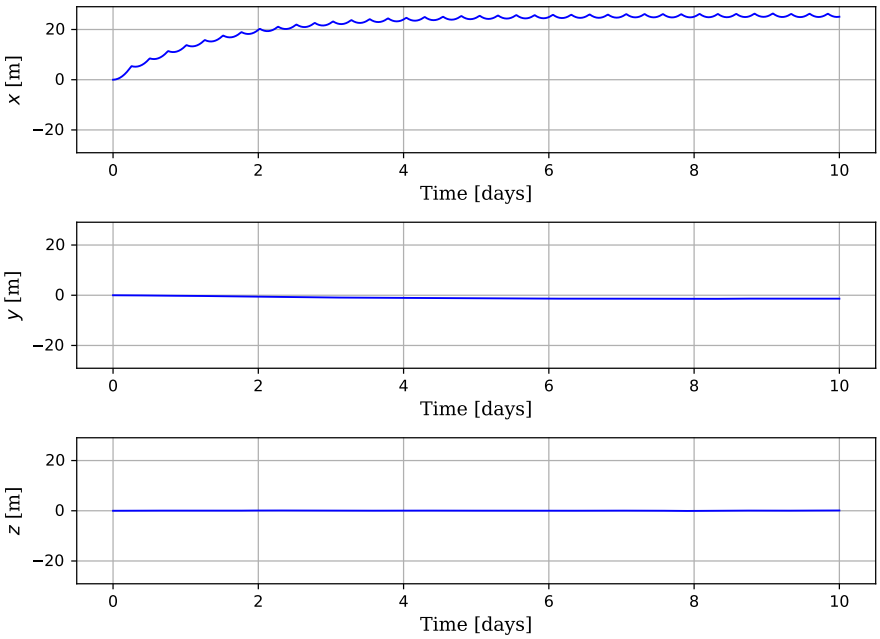


Figure 3.17: Evolution of the relative position error (e_r) during stand-by using the MPC controller.

As for the velocity error (Figure 3.18) and the control (Figure 3.19) with the MPC controller, they behave similarly to the ETM case.

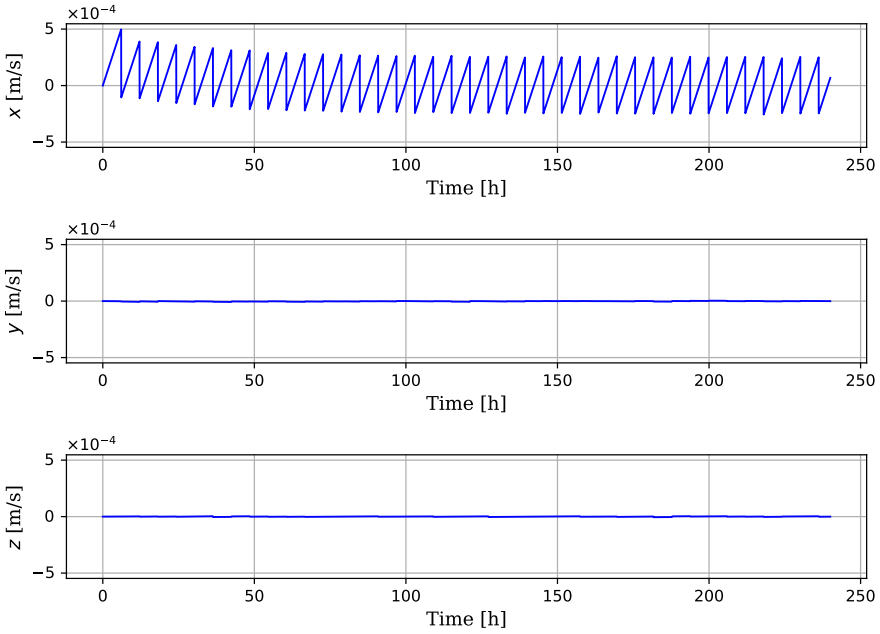


Figure 3.18: Evolution of the relative velocity error (e_v) during stand-by using the MPC controller.

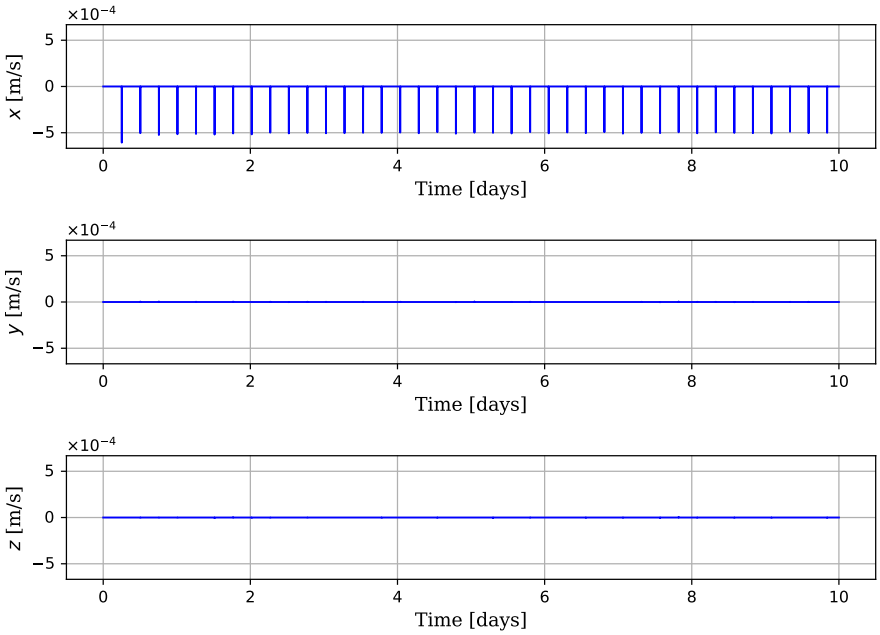


Figure 3.19: Control applied during stand-by using the MPC controller.

In Table 3.15, the ΔV consumed for each controller is shown. Both values are similar as the main contribution to them is the compensation of the SRP perturbation,

so it is reasonable to expect that they remain comparable for longer simulations. This can be checked using Eq. (2.53) with the data from Table 3.5, which gives $\Delta V \approx 0.0196\,\mathrm{m/s}$. This value will decrease as the area-to-mass ratios of both satellites become closer.

Table 3.15: ΔV results with each of the control laws in the Stand-by mode simulations.

Control Law	ΔV [m/s]
ETM	0.0196
MPC	0.0197

Reconfiguration

The Reconfiguration mode is intended to relocate the deputy from the calibration position to the stand-by position and vice versa. The initial condition and the target state are listed in Table 3.16 and are based on the nominal states from the Calibration mode and Stand-by mode. In Table 3.17, the parameters used to configure the ETM controller are shown, while the parameters for the MPC controller can be found in Table 3.18. The ETM controller is set to perform a maneuver every 6 h, which will set the duration of the reconfiguration for this controller. Meanwhile, the MPC controller will perform maneuvers every 30 min and the duration of the reconfiguration will depend on the values chosen for the Q and R matrices. The collision avoidance constraint of the MPC controller is activated with a minimum distance (R_{KOZ}) of 50 m.

Table 3.16: Initial condition and relative target state for Reconfiguration mode.

Parameter	Value [m, m/s]
$\boldsymbol{x}_0$	[100, 100, 100, 0, 0, 0]$^\top$
$\boldsymbol{x}_{tgt}$	[-500, -500, -500, 0, 0, 0]$^\top$

Table 3.17: ETM configuration parameters for the Reconfiguration mode.

Parameter	Value
ΔT	6 h
e_{max}	0.3 m

Table 3.18: MPC configuration parameters for the Reconfiguration mode.

Parameter	Value
$\bar{x}_{1,2,3}$	0.3 m
$\bar{x}_{4,5,6}$	$1 \cdot 10^{-4}$ m/s
$\bar{u}_{1,2,3}$	$7 \cdot 10^{-3}$ m/s^2
n_p	10
ΔT	30 min
Collision avoidance	True
R_{KOZ}	50 m

For the Reconfiguration mode simulations, instead of the position and velocity errors, the relative position and velocity of the deputy regarding the chief have been used in the plots. For the ETM case, the relative position and velocity are shown in Figure 3.20 and Figure 3.23. The time of convergence of the ETM controller for this particular maneuver is close 6 h, as set in its configuration. In this simulation, this controller only performs two impulses, one to gain velocity and another to stop the satellite when it reaches its target position. This produces a straight trajectory that, in this particular case, crosses the chief position. This situation has been intentionally chosen to demonstrate the importance of implementing a collision avoidance system (which the MPC controller does) if maneuvers are to be computed and performed autonomously.

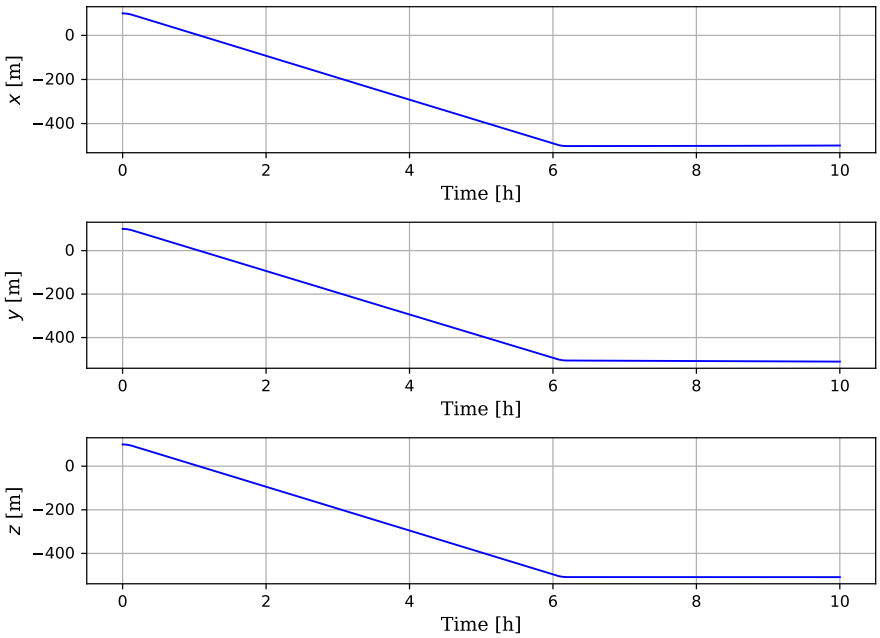


Figure 3.20: Evolution of the relative position during reconfiguration using the ETM controller.

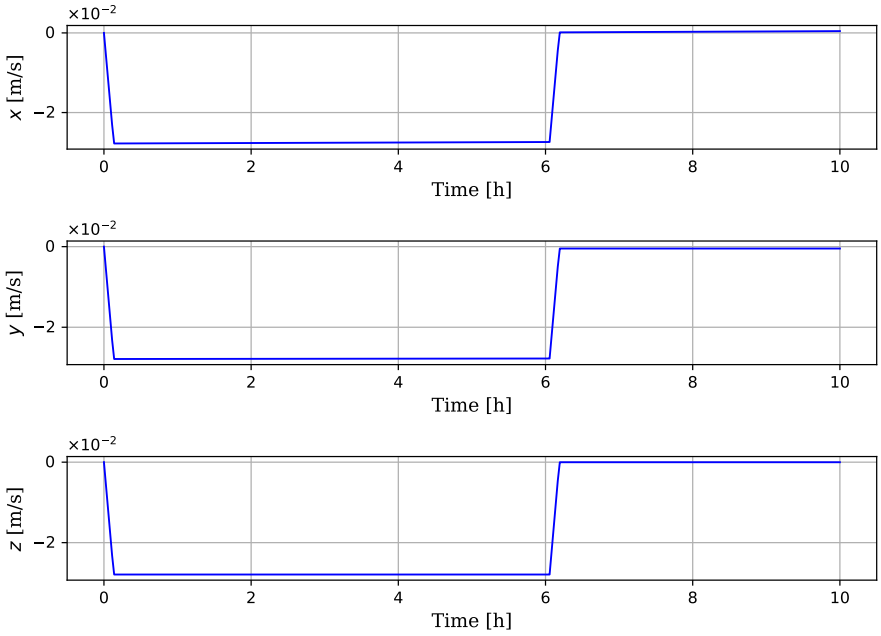


Figure 3.21: Evolution of the relative velocity error during reconfiguration using the ETM controller.

The control applied by ETM is shown in Figure 3.22, where the start and stop impulses can be clearly observed. The magnitude of these impulses depends directly on the selected ΔT for the ETM controller.

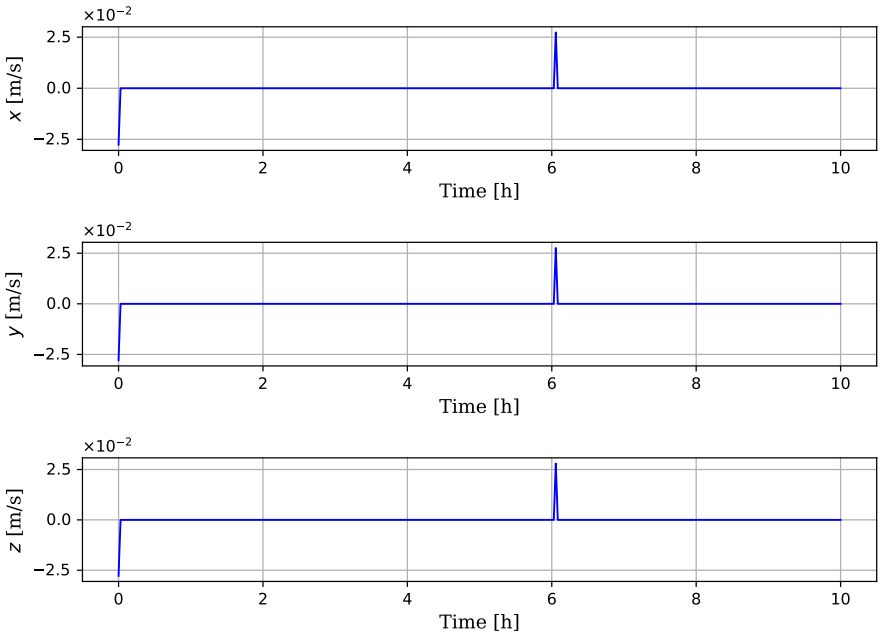


Figure 3.22: Control applied during reconfiguration using the ETM controller.

In the case of the MPC controller, the convergence time is around 10 h. The collision

avoidance constraint is activated in this simulation, and its effect can be noticed in the z component of the relative position in Figure 3.23, which takes longer to start changing compared to the x and y components. This prevents the total distance from the chief from falling below the established minimum distance (50 m).

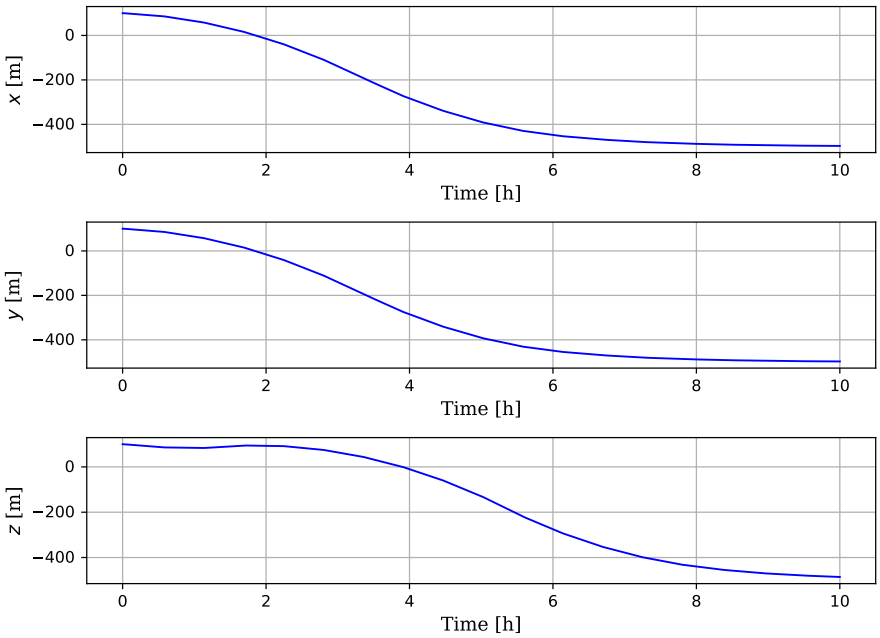


Figure 3.23: Evolution of the relative position during reconfiguration using the MPC controller.

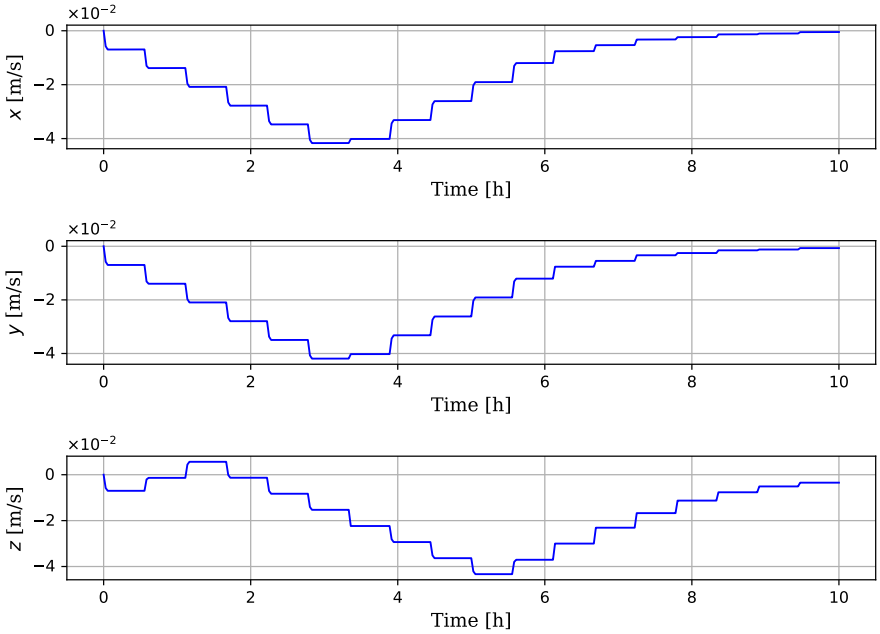


Figure 3.24: Evolution of the relative velocity during reconfiguration using the MPC controller.

The velocity and control of the MPC are shown in Figure 3.24 and Figure 3.25 respectively. With this controller, the changes in the deputy velocity are gradual, which results in a smoother maneuver.

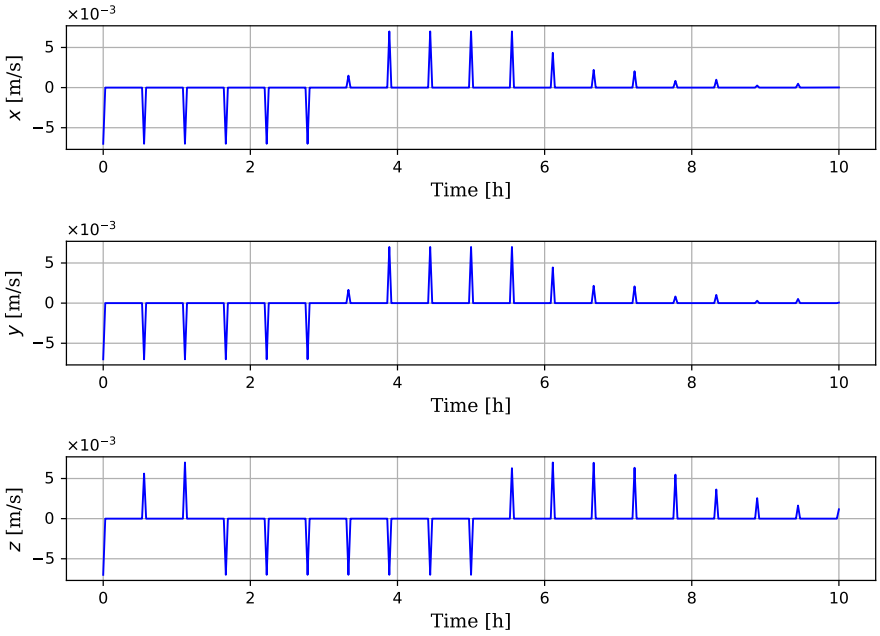


Figure 3.25: Control applied during reconfiguration using the MPC controller.

In Table 3.19, the ΔV consumed for each controller is shown. In this case, the ETM performs better than the MPC. This is because the MPC controller spends an additional amount of ΔV to maintain the minimum distance and also performs a smoother maneuver than the ETM controller, gradually accelerating and decelerating, resulting in lower efficiency.

Table 3.19: ΔV results with each of the control laws in the Reconfiguration mode simulations.

Control Law	**ΔV [m/s]**
ETM	0.096
MPC	0.167

Finally, in Figure 3.26, the evolution of the distance during maneuvering is shown for different scenarios. In the case of using the ETM controller, the distance between both satellites is close to zero at the beginning of the maneuver as the deputy's trajectory passes close to the chief position. This would not always occur, and the initial condition and the target position have been chosen so this issue arises. Nevertheless, such situation could happen and the ETM controller is not capable of detecting it nor avoiding it. For the MPC case, the results with the collision avoidance constraint activated (MPC+CA) and not activated (MPC) have also been

included in the figure. If the collision avoidance constraint is not included, the deputy gets too close to the chief. However, if the constraint is included, the MPC controller successfully respects the minimum distance set.

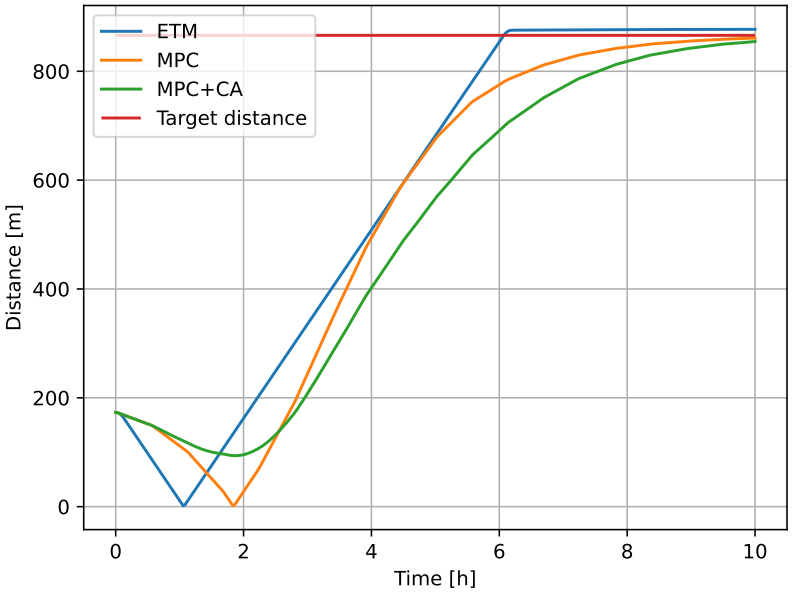


Figure 3.26: Evolution of the relative distance between chief and deputy during the reconfiguration maneuver for different controllers.

Discussion of results

The analyses presented in the previous sections show that the proposed GNC system is a feasible option for a chief-deputy mission on L_2. The MPC controller is able to meet the objective of each control mode.

Regarding the Calibration mode, although the position error is higher with MPC than with LQR, it is in accordance with the weights used in the Q matrix and the ΔV cost is considerably lower in the MPC case. Therefore, the performance of the MPC could be improved at the expense of ΔV.

While the MPC controller does not provide the same improvements in ΔV when compared to the ETM controller in the Stand-by and Reconfiguration modes, it enables the addition of the collision avoidance constraint. The implementation of this feature adds safety to the maneuvering system and would also help avoid unexpected and undesired close approaches in the Stand-by mode. Although the MPC controller consumes more ΔV than the ETM controller in the Reconfiguration mode, it also allows for smoother maneuvers and lower impulses.

The SRP perturbation has been included in the simulations, but it is not considered in the dynamics model of any of the controllers. This affects performance, particularly for long periods between maneuvers. Its inclusion in the MPC controller would help extend the time between maneuvers, reduce the ΔV in some scenarios (such as maneuvering) and make the collision avoidance system more robust. However,

SRP perturbation is the main contributor to ΔV during the Stand-by mode, and this depends solely on the relation between the area-to-mass ratio of both satellites. The more similar these ratios are, the less differential acceleration to be compensated by the controller in the formation.

These analyzes (accuracy and ΔV) will be repeated in chapter 6 to help define the preliminary design of a CubeSat as a deputy of a similar formation.

CHAPTER 4

Collision risk assesment

Internal collisions in a satellite formation can be motivated by inaccuracy in knowledge of the individual spacecraft state, failure of one of the satellites, or both. In chief-deputy formations, the formation control is exerted by the deputy, which will avoid potential collisions by keeping the formation geometry or by applying some type of collision avoidance system. Active spacecraft formation flight collision avoidance systems monitor collision risk with indicators such as the closest distance and collision probability. Although the probability of a spacecraft colliding with another spacecraft of the same formation has long been a topic of concern [89], recent work to look at formations located in libration point orbits has caused increased emphasis in this area [90, 91].

This chapter is focused on assessing the collision risk in a chief-deputy flight formation at a collinear libration point. Specifically, the collision risk in the event of a critical failure of the deputy, which would leave the satellite uncontrolled and the inherent instability of this region would lead it outside the libration point vicinity. Nevertheless, due to the low acceleration environment, the relative motion is initially dominated by the relative velocity between the satellites of the formation. Therefore, although the formation may have been subjected to a tight formation control until the deputy failure, once it occurs, the deputy would follow a path defined by any residual relative velocity.

The probability of collision (P_c) is one of the most common metrics used to assess the risk of collision between two satellites or objects (often referred to as primary and secondary) when they become closer than a predefined threshold. Although there are numerous methods to compute it, most of them are based on the integration of the three-dimensional probability density function (PDF) that arises from

the uncertainty associated with the orbit determination of both satellites. This approach can be computationally intensive, which limits its application in practice. To overcome this limitation, many approximation methods have been developed over the past three decades [92]. These methods rely on simplifying assumptions, mainly that satellites have "short encounters" due to their high relative velocities and that the covariance matrices which express the position uncertainty are constant. This does not adjust to the scenario of a formation flying at a libration point, in which the satellites will stay close for long periods of time and the uncertainty associated with the relative velocity will make the position covariance matrix grow. Although not focused on formation on libration points, there have been advances regarding long encounters [93, 94, 95] and the inclusion of velocity uncertainty [96] in the computation of the collision risk.

Building upon these advancements, this work presents a semi-analytical method to compute the collision risk in this scenario based on the relative velocity uncertainty and the distance between the satellites. By considering that the error ellipsoid from the position covariance matrix is aligned with the line of sight between both satellites, the collision probability integral is expressed as a single variable integral that can be integrated numerically. Then, a relative motion model of the formation is used to propagate the position covariance matrix, which allows to compute the evolution of the probability over time. This method enables the study of the impact of different parameters (formation distance, control performance, and safety distances) on the probability of collision.

The proposed method will allow to find out how well must the relative state be controlled, so in case of critical failure, the risk of collision is below a predefined threshold. This information will help define the requirements for the navigation and orbit control systems of the deputy and also assess the collision risk during flight. Furthermore, this method could be used by a collision avoidance system that uses the collision probability as a metric to compute it. The method has been validated using Monte Carlo simulations in the high-fidelity environment described in chapter 3, which is based on ephemeris and includes the solar radiation pressure (SRP) perturbation.

The chapter is organized as follows: first, the calculation of collision probability using probability density functions is reviewed, the approach followed to simplify this integral is described, and then the propagation of covariance is presented. Next, numerical validation of the method is conducted, and finally, a case study is presented to demonstrate its utility.

4.1 Collision risk probability

The exact state of a satellite cannot be known as a result of the inevitable errors in orbit determination. Such an uncertainty is usually described using a three-dimensional probability density function (PDF). The PDF is typically assumed to follow a Gaussian distribution and is defined by the nominal state of the satellite and a covariance matrix. Typically, velocity uncertainty is assumed to be negligible, which results in constant position covariances for both satellites. These covariances can be merged under the assumption that they are uncorrelated. The resulting com-

bined covariance is then associated to one of the satellites (typically the secondary) and can be represented as an error ellipsoid (see Figure 4.1).

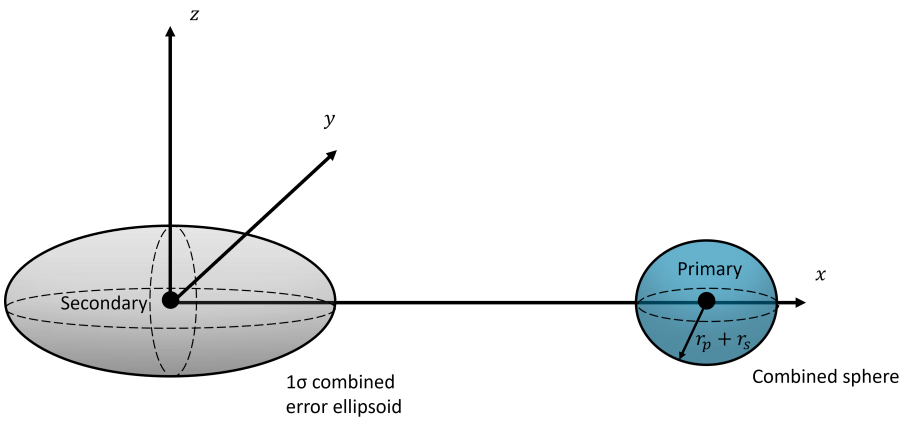


Figure 4.1: Combined error ellipsoid centered on secondary and safety sphere centered in primary.

Satellites are usually modeled as spheres (r_p for the primary and r_s for the secondary) for simplicity. Then, if the secondary satellite comes within a sphere with radius $r = r_p + r_s$ centered on the primary satellite (see Figure 4.1), there will be a collision. This sphere is known as the combined, safety, or hardbody sphere.

In general, collision probabilities are divided into two types: instantaneous collision probability and cumulative collision probability. The instantaneous collision probability is the collision probability at a single instant. It is computed by integrating the PDF over the volume of the combined sphere. Meanwhile, the cumulative collision probability is the overall collision probability for a period of time. It is obtained by integrating the PDF over the volume swept out by the motion of the combined sphere.

To evaluate this risk, a three-dimensional integral is often used. This integral accounts for several factors, such as the location of satellites, their trajectories, and the volume of space they occupy.

The three-dimensional integral for collision risk is essentially a mathematical representation of the probability of a collision occurring within a specific volume of space over a given time interval.

4.1.1 Triple-integral

Integrating the PDF involves solving a triple integral [97] over the defined integration volume, also called encounter region, Ω:

$$p_c = \frac{1}{\sqrt{8\pi^3}\sigma_x\sigma_y\sigma_z} \iiint_{\Omega} e^{-\left(\frac{x^2}{2\sigma_x^2}+\frac{y^2}{2\sigma_y^2}+\frac{z^2}{2\sigma_z^2}\right)} dxdydz \tag{4.1}$$

where σ_x, σ_y, and σ_z are the standard deviations from the position covariance:

$$P_r = \begin{pmatrix} \sigma_x^2 & 0 & 0 \\ 0 & \sigma_y^2 & 0 \\ 0 & 0 & \sigma_z^2 \end{pmatrix} \tag{4.2}$$

For instantaneous probability of collision, the encounter region can be seen as the volume resulting from the intersection between the $n\sigma$ error ellipsoid, centered on the secondary satellite, and the combined sphere, centered on the primary. The factor n scales the size of the error ellipsoid and is typically in the range of 3 to 8 to accommodate conjunction probabilities that range from 97.070911% to 99.999999% (see Figure 4.2). This calculation will yield the instantaneous probability of collision. To determine the cumulative probability of collision (i.e., the likelihood that a collision has occurred at some point during the encounter), the encounter region will encompass the volume swept by the sphere as the encounter occurs, as shown in Figure 4.3.

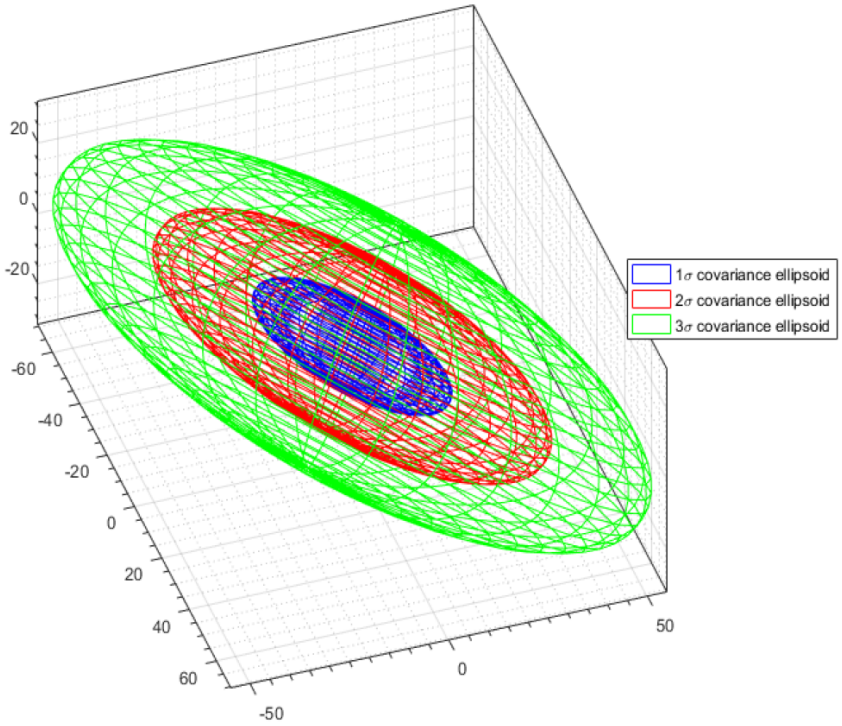


Figure 4.2: Scale of error ellipsoid according to $n\sigma$ value. Extracted from [98].

The computation of the three-dimensional integral can be time consuming. Because of this, some simplifying assumptions are usually applied. The most common is to consider the encounters as short-encounters due to the high relative velocity between the satellites, which leads to the assumption of linear relative motion and constant covariances. Nevertheless, this does not occur in flight formations, where the relative velocities are low and the satellites can stay at short distances for long periods of time.

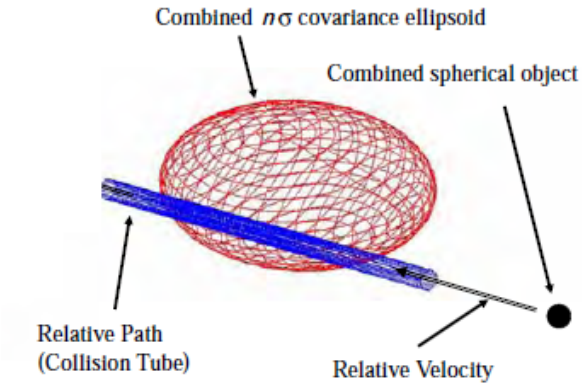


Figure 4.3: Encounter region for the cumulative probability of collision. Extracted from [53].

In the chief-deputy formation under study, the deputy is able to maintain a fixed position relative to the chief by controlling its trajectory. Thus, the relative state (position and velocity) of the deputy with respect to the chief can be expressed as a probability density function, which is assumed to be Gaussian and describes the deviation from the nominal state that the control aims to maintain. Once failure occurs, the PDF of the deputy can be propagated using a relative motion model, enabling the calculation of the evolution of the collision risk over time.

4.1.2 Integral simplification

In this section, the triple integral from Eq. (4.1) will be reduced, through a series of simplifications, to a single-variable integral over a defined interval. This integral will be expressed in terms of the parameters of the problem, that is, the distance between the satellites of the formation (d), the radius of the safety sphere (D), and the position covariance (P_{rr}). The goal is to leverage the geometry of the proposed problem to easily define the volume of encounter.

In general, the deputy will be placed at the coordinates (x, y, z) relative to the chief (expressed in the same coordinate presented in section 3.1.1 of previous chapter). It is useful to work in an auxiliary reference system, the local spherical frame based on the spherical coordinates of the deputy (see Figure 4.4). Any position referred to this local frame will be expressed in the coordinates u, v, w. The equations required to transform between Cartesian and spherical frame are included in the appendix E.1. As shown in the previous chapter, if the control error in these local components is considered, it exhibits a similar level of error in its lateral components (v, w) when the Calibration mode is operating. Therefore, it is reasonable to assume that the covariance matrix will exhibit such symmetry ($\sigma_v = \sigma_w$), and hence the error ellipsoid (which thus becomes a spheroid) will be aligned with the chief-deputy line and symmetric with respect to such an axis (see Figure 4.5). Note that while the covariance matrix is diagonal in this frame, it will not be so in Cartesian coordinates.

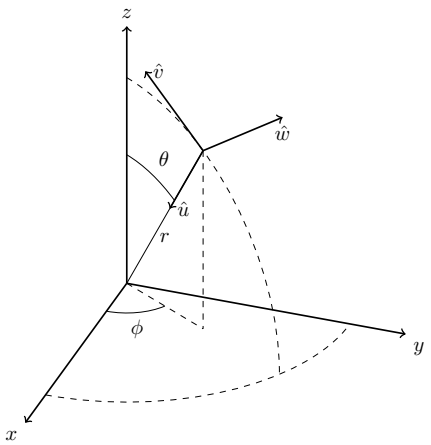


Figure 4.4: Spherical coordinates and the local coordinate frame associated.

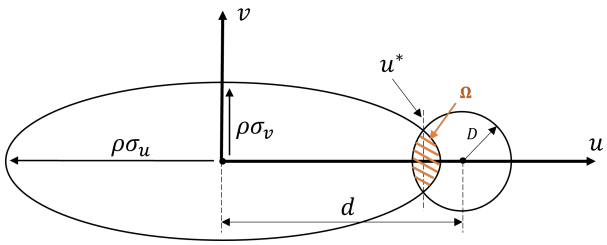


Figure 4.5: View of the uv-plane.

The probability of collision can be calculated by integrating the probability density function in the region intersected between the sphere and the ellipsoid (the encounter region, Ω). To do so, consider the equations of a variable size spheroid ($\sigma_v = \sigma_w$), defined by the parameter ρ and centered at the origin:

$$\frac{u^2}{\sigma_u^2} + \frac{v^2}{\sigma_v^2} + \frac{w^2}{\sigma_v^2} = \rho^2 \tag{4.3}$$

and the safety sphere, located at a distance d in the u-axis:

$$(u-d)^2 + v^2 + w^2 = D^2 \tag{4.4}$$

Then, the intersection of both surfaces can be found substituting Eq. (4.3) into Eq. (4.4):

$$(u-d)^2 + \sigma_v^2(\rho^2 - \frac{u^2}{\sigma_u^2}) = D^2 \tag{4.5}$$

which results in a second-degree equation for u:

$$(1-k^2)u^2 - 2du + d^2 - D^2 + (k\sigma_u\rho)^2 = 0 \tag{4.6}$$

where $k = \sigma_v/\sigma_u$. The roots (u^*) of this equation are:

$$u^*(\rho) = \frac{d \pm \sqrt{d^2 - (1-k^2)(d^2 - D^2 + k\sigma_u\rho)^2}}{(1-k^2)} \tag{4.7}$$

For a given value of ρ, Eq. (4.7) determines the u coordinate of the intersection between both surfaces. The solution of this equation exists only if the surfaces intersect, but it will provide two solutions regardless of whether the surfaces intersect just once. Thus, it is important to choose the valid solution in each case. As can be observed in the equation, one of the solutions is greater than d and the other is smaller. In the particular case of a sphere ($\sigma_u = \sigma_v = \sigma_w$), $k = 1$ and the Eq. (4.6) is reduced to:

$$u^*(\rho) = \frac{d^2 - D^2 + (\sigma_u \rho)^2}{2d} \tag{4.8}$$

The coordinate u^* delimits a spheroidal cap on the surface of the ellipsoid, whose general geometry is shown in Figure 4.6. The volume of such a cap is:

$$V(\rho) = \frac{\pi a^2}{3c^2} h^2 (3c - h) = \frac{\pi k^2 h^2}{3} (3\sigma_u \rho - h) \tag{4.9}$$

where $a = \rho\sigma_v$, $c = \rho\sigma_u$, and $h = \rho\sigma_u - u^*$. This formula allows to compute the differential volume ($d\Omega$) of a cap with a differential thickness ($d\rho$):

$$d\Omega = V(\rho + d\rho) - V(\rho) = 2\pi k^2 \rho \sigma_u^2 h(\rho) d\rho \tag{4.10}$$

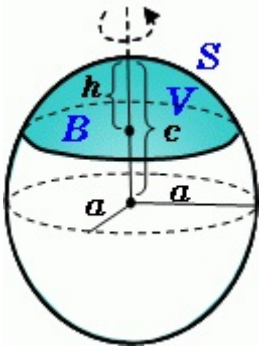


Figure 4.6: Geometry of spheroidal cap.

If Eq. (4.1) is expressed in spherical coordinates and taking into account Eq. (4.3), it can be observed that the integrand of Eq. (4.1) is constant over the surface of an ellipsoid with ρ constant:

$$p_c = \frac{1}{\sqrt{8\pi^3}\sigma_u\sigma_v\sigma_w} \iiint_\Omega e^{\frac{-\rho}{2}} d\Omega \tag{4.11}$$

Furthermore, the triple integral can be converted to a single variable integral (over ρ) by considering the differential volume defined in Eq. (4.10):

$$p_c = \frac{1}{\sqrt{2\pi}\sigma_u} \int_{\rho_1}^{\rho_2} h(\rho) \rho e^{\frac{-\rho}{2}} d\rho \tag{4.12}$$

The limits of the integral (ρ_1 and ρ_2) depend on how the error ellipsoid and the safety sphere intersect, which changes with the problem parameters (k, σ_u, n, d and D) and according to whether the probability of collision is instantaneous or

cumulative. The basic case is depicted in Figure 4.7, which is valid for ellipsoids of error that meet $d - D < \sigma_u n < d + D$. This constraint ensures that both volumes have only one intersection. In this case, $\rho_1 = \frac{d-D}{\sigma_u}$ and $\rho_2 = n$.

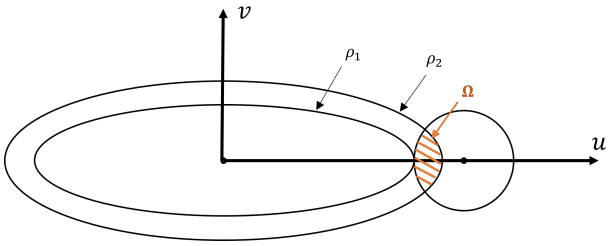
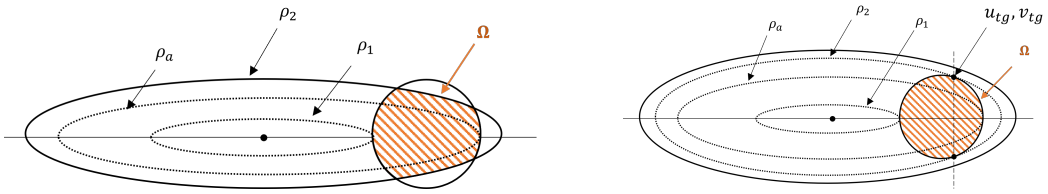


Figure 4.7: Scheme showing the geometric interpretation of the integral limits ρ_1 and ρ_2.

For error ellipsoids where $\sigma_u n \geq d + D$, the ellipsoid overgrows the sphere and the integral of Eq. (4.12) is divided into two parts:

$$p_c = \frac{1}{\sqrt{2\pi}\sigma_u} \int_{\rho_1}^{\rho_a} h(\rho)\rho e^{\frac{-\rho}{2}} d\rho + \frac{1}{\sqrt{2\pi}\sigma_u} \int_{\rho_a}^{\rho_2} (h(\rho) - h'(\rho))\rho e^{\frac{-\rho}{2}} d\rho \tag{4.13}$$

where $h' = d - u_2^*$, with u_2^* being the second solution of the Eq. (4.7), and $\rho_a = \frac{d+D}{\sigma_u}$. A negative term is added to compensate for the extra volume outside the sphere. There are two possible scenarios, according to the proportion and size of the ellipsoid compared to the sphere, as shown in Figure 4.8, which will define the value of ρ_2. In the first case, depicted in Figure 4.8a, the second integration limit is still $\rho_2 = n$.



(a) $D > k\sigma_v^2 n$ **(b)** $D < k\sigma_v^2 n$

Figure 4.8: Changes in the encounter region according to the geometry of the error ellipsoid compared to the sphere.

For the second case (see Figure 4.8b), the limit ρ_2 is obtained from the condition of tangency between the sphere and the ellipsoid:

$$\rho_2 = \sqrt{\frac{u_{tg}^2}{\sigma_u^2} + \frac{v_{tg}^2}{\sigma_v^2}} \tag{4.14}$$

$$u_{tg} = u^*(\rho_a) \tag{4.15}$$

$$v_{tg} = \sqrt{D^2 - (u_{tg} - d)^2} \tag{4.16}$$

where u_{tg} and v_{tg} are the coordinates of one of the points of tangency between the sphere and the ellipsoid of size ρ_a.

The encounter volumes (Ω) defined until now correspond to the instantaneous probability of collision. To calculate the cumulative probability, the encounter region must be extended, taking into account all the trajectories that would have crossed the safety sphere. As will be shown in the following section, the motion is linear, so the encounter region can be defined with lines from the center of the ellipsoid and tangent to the sphere as shown in Figure 4.9. In this case, $\rho_1 = (d - D)/\sigma_u$ and $\rho_2 = n$, but now the height of the cap will depend on the value of u_{tg}, the u coordinate of the tangency points:

$$h = \rho\sigma_u - u_{tg} \tag{4.17}$$

$$u_{tg} = \sqrt{\frac{\rho^2\sigma_v^2}{k^2 + \tan(\arcsin(D/d))^2}} \tag{4.18}$$

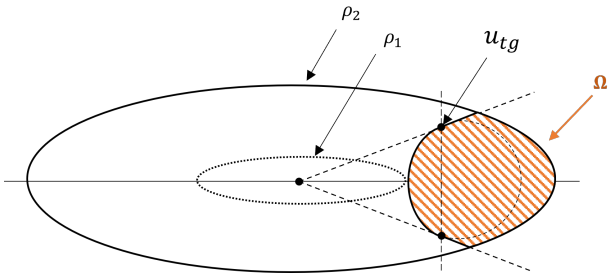


Figure 4.9: Encounter region and integration limits for the cumulative probability of collision.

4.1.3 Propagation of covariance matrix

In the previous section, expressions to calculate the instantaneous probability of collision and the cumulative probability of collision for a given position covariance were derived. Now, through the relative motion model presented in section 3.2, the position covariance will be propagated as a function of the uncertainty associated with the deputy's velocity. First, the covariance matrix of the deputy's state is expressed:

$$P = \begin{pmatrix} \sigma_u^2 & 0 & 0 & 0 & 0 & 0 \\ 0 & \sigma_v^2 & 0 & 0 & 0 & 0 \\ 0 & 0 & \sigma_w^2 & 0 & 0 & 0 \\ 0 & 0 & 0 & \sigma_{\dot{u}}^2 & 0 & 0 \\ 0 & 0 & 0 & 0 & \sigma_{\dot{v}}^2 & 0 \\ 0 & 0 & 0 & 0 & 0 & \sigma_{\dot{w}}^2 \end{pmatrix} = \begin{pmatrix} \mathrm{P}_{rr} & \mathrm{P}_{rv} \\ \mathrm{P}_{vr} & \mathrm{P}_{vv} \end{pmatrix} \tag{4.19}$$

where σ_u, σ_v, and σ_w are the uncertainties in the relative position of the deputy expressed in the longitudinal and lateral components and $\sigma_{\dot{v}}$, $\sigma_{\dot{v}}$ and $\sigma_{\dot{w}}$ are the uncertainties associated to the relative velocity. Here, these uncertainties are defined by the formation control accuracy, which can also be expressed as a Gaussian distribution.

This covariance matrix, as with the satellite state, can be propagated using the state transition matrix (Eq. (3.15)). Since the covariance matrix is expressed in the

spherical reference system, it is necessary to transform the state transition matrix into this system:

$$\Phi_2(t,t_0) = \mathrm{R}_{E_{21}}^{\top}\Phi_1(t,t_0)\mathrm{R}_{E_{21}} \tag{4.20}$$

with:

$$\mathrm{R}_{E_{21}} = \begin{pmatrix} \mathrm{R}_{21} & 0_{3x3} \\ 0_{3x3} & \mathrm{R}_{21} \end{pmatrix} \tag{4.21}$$

where the subscript 2 indicates the spherical reference frame and the subscript 1 the Cartesian frame. Thus, the covariance matrix for a given instant t would be:

$$\mathrm{P}(t) = \Phi_2(t,t_0)\mathrm{P}(t_0)\Phi_2^{\top}(t,t_0) \tag{4.22}$$

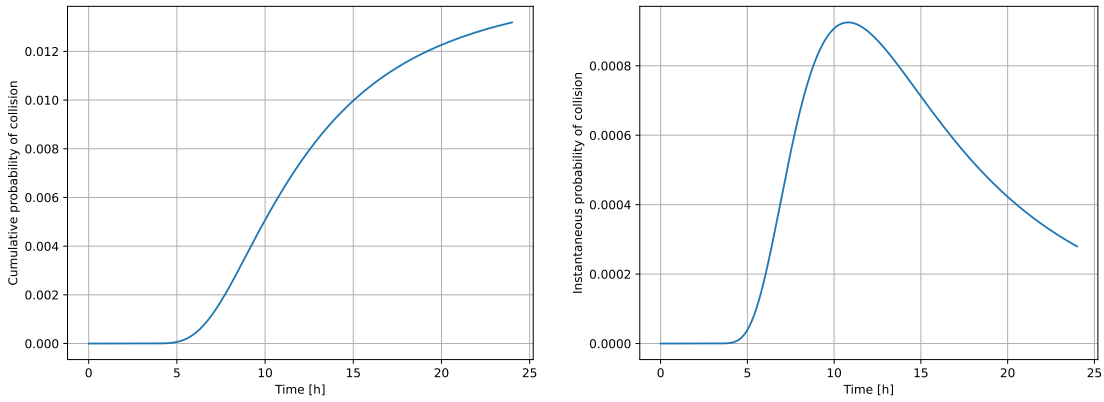
Consequently, the position covariance for a given instant would be:

$$\mathrm{P}_{rr}(t) = \begin{pmatrix} \sigma_{\dot{u}}^2\Delta t^2+\sigma_{u_0}^2 & 0 & 0 \\ 0 & \sigma_{\dot{v}}^2\Delta t^2+\sigma_{v_0}^2 & 0 \\ 0 & 0 & \sigma_{\dot{w}}^2\Delta t^2+\sigma_{w_0}^2 \end{pmatrix} = \begin{pmatrix} \sigma_u^2(t) & 0 & 0 \\ 0 & \sigma_v^2(t) & 0 \\ 0 & 0 & \sigma_w^2(t) \end{pmatrix} \tag{4.23}$$

where $\Delta t = t_f - t_0$. The interpretation of such a position covariance matrix is that it is initially defined by σ_{u_0}, σ_{v_0}, and σ_{w_0} and grows over time according to the value of $\sigma_{\dot{v}}$, $\sigma_{\dot{v}}$ and $\sigma_{\dot{w}}$. If the values of the initial position covariance matrix are small, their value over time will be much greater, as they are proportional to Δt, so $\mathrm{P}_{rr}(t,t_0)$ can be approximated as:

$$\mathrm{P}_{rr}(t) \approx \mathrm{P}_{vv}(t_0)\Delta t^2 = \begin{pmatrix} \sigma_{\dot{u}}^2\Delta t^2 & 0 & 0 \\ 0 & \sigma_{\dot{v}}^2\Delta t^2 & 0 \\ 0 & 0 & \sigma_{\dot{w}}^2\Delta t^2 \end{pmatrix} \tag{4.24}$$

In this manner, the evolution over time of the cumulative collision probability and the instantaneous collision probability is obtained. An example of both outcomes is depicted in Figure 4.10.



(a) Cumulative probability of collision **(b)** Instantaneous probability of collision

Figure 4.10: Example of time evolution of the instantaneous and cumulative probabilities of collision.

4.2 Numerical validation

In order to validate the analytical solution presented in this work, a Monte Carlo analysis has been performed. An initial fixed relative position and null relative velocity are assumed between the chief and deputy. From this particular state, a set of initial conditions is generated using normal distributions to represent the error in relative velocity control between the spacecrafts (Eq. (4.25)):

$$X_0 = \begin{pmatrix} \boldsymbol{r}_0 \\ \boldsymbol{v}_0 \end{pmatrix} = \begin{pmatrix} \boldsymbol{r}_0 \\ \mathcal{N}(0, \mathrm{P}_{vv}) \end{pmatrix} \tag{4.25}$$

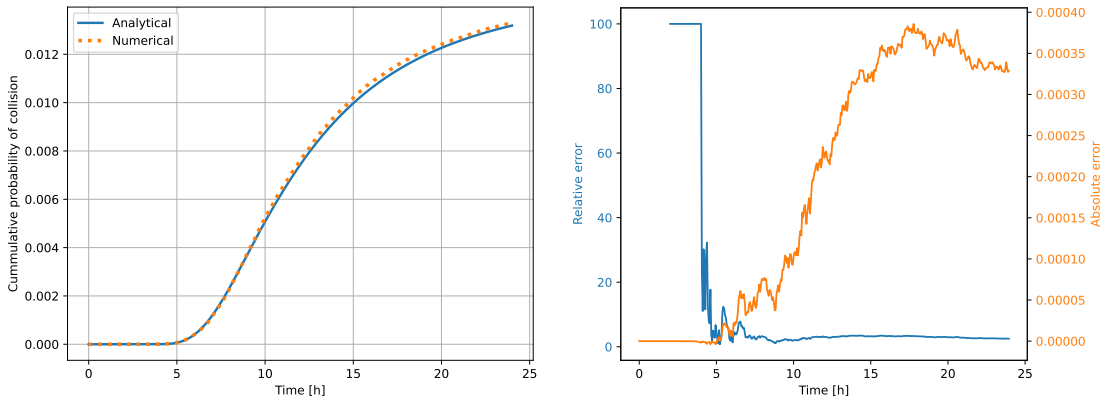
The set of initial conditions is generated in spherical coordinates and then transformed to Cartesian. The trajectories have been propagated using the open-source astrodynamics Python library mubody [65], which provides the dynamical environment for both the CRTBP model and the ephemeris model (with SRP perturbation included). After propagation of the trajectories, a collision is considered to have occurred when the relative distance is below a threshold value D. After propagation of the trajectories, a collision is considered to have occurred when the relative distance is below a threshold value D.

The characteristics of the formation used for this analysis are included in Table 4.1. These characteristics are similar to those employed in chapter 3, but the deputy area has been modified so that the area-to-mass ratio of both satellites is equal to decouple the effect of the SRP on the results, which is evaluated separately.

Table 4.1: Characteristics of the flight formation mission studied.

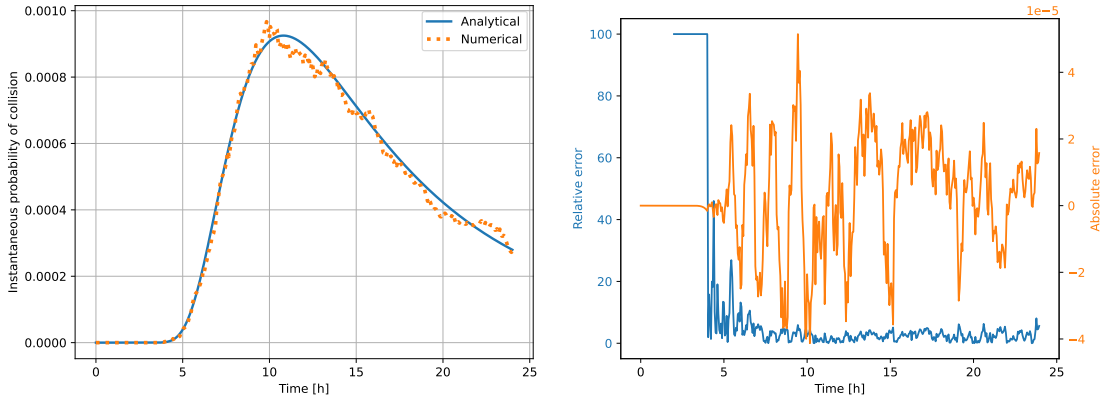
Parameter	Value
Chief area (A_c)	10 m^2
Deputy area (A_d)	0.1 m^2
Chief mass (m_c)	1000 kg
Chief mass (m_d)	10 kg
Formation size (d)	100 m
Safety sphere radius (D)	5 m
Longitudinal uncertainty (velocity) ($\sigma_{\dot{u}}$)	1.5 mm/s
Lateral uncertainty (velocity) ($\sigma_{\dot{v}}$)	$3 \cdot 10^{-1}$ mm/s

In Figure 4.11, the numerical and analytical results of the collision are compared for the cumulative probability. In Figure 4.11a both curves are shown, and in Figure 4.11b the absolute and relative errors of both curves are plotted. Although the absolute error has roughly the same order of magnitude over time, the relative error present high levels at the start. This is due to the near-zero values of the probability at the beginning. Once the probability increases its magnitude, the relative error is roughly constant and low. The same behavior can be observed in Figure 4.12b, in which the instantaneous probability of collision is shown.



(a) **(b)**

Figure 4.11: Comparison of numerical and analytical approaches for the cumulative probability of collision.

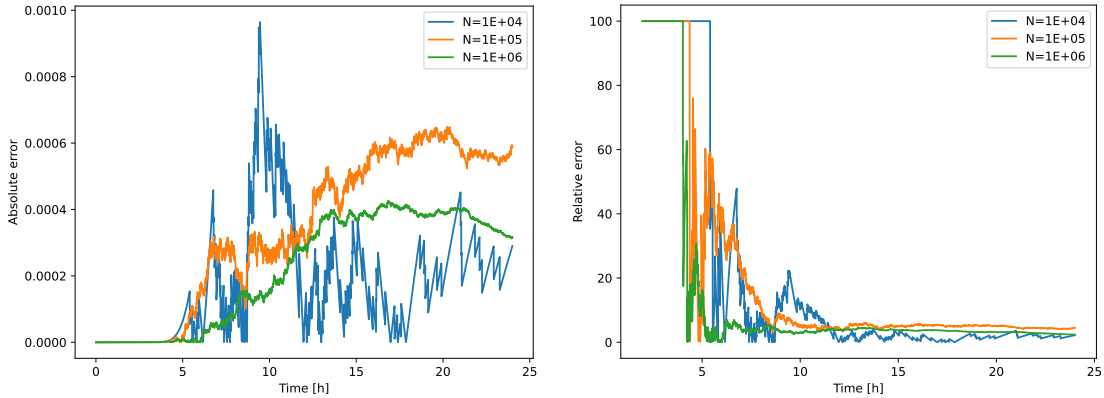


(a) **(b)**

Figure 4.12: Comparison of numerical and analytical approaches for the instantaneous probability of collision.

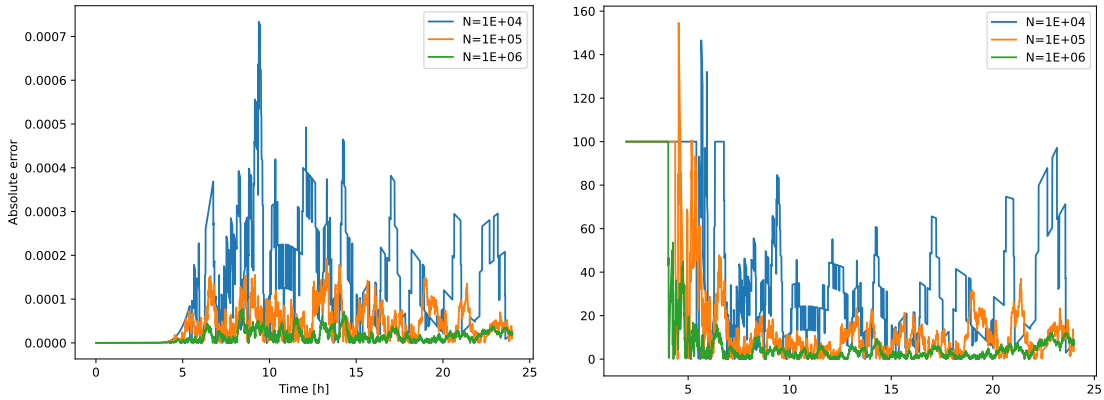
The main factor contributing to the error is the sample size (N) used in the Monte Carlo method used to obtain the numerical results. This parameter determines the accuracy achieved and increases the computational time proportionally. In Figure 4.13 and Figure 4.14, the evolution of the absolute and relative errors when using different sample sizes is shown for the cumulative probability of collision and the instantaneous probability of collision, respectively. As can be observed in these figures, the error is reduced overall as N increases.

The analytical solution proposed does not depend on the formation orientation, so in order to validate it, numerical simulations with different formation orientations have been carried out. The results are plotted in Figure 4.15, where it can be seen that there are no significant deviations from the analytical solution. The small variations are in accordance with the value of N used in the numerical simulations.



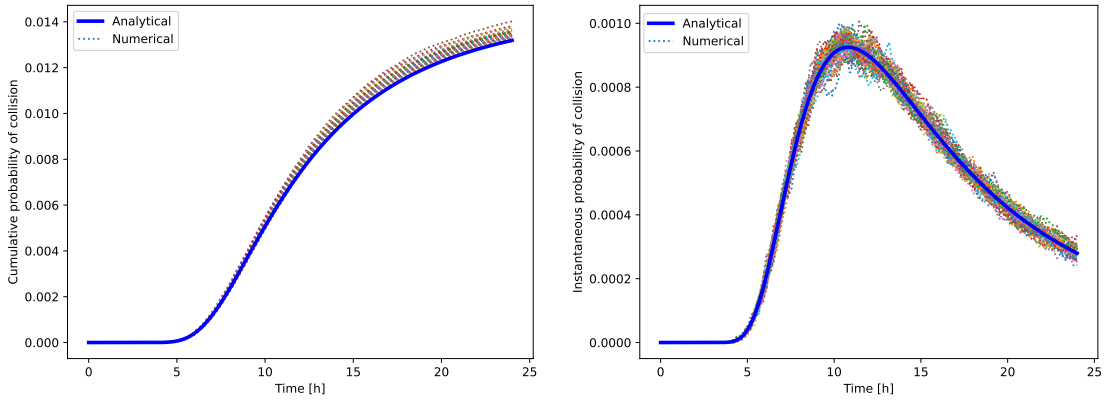
(a) Absolute error. **(b)** Relative error.

Figure 4.13: Error between analytical and numerical solutions of the cumulative probability of collision for different values of N.



(a) Absolute error. **(b)** Relative error.

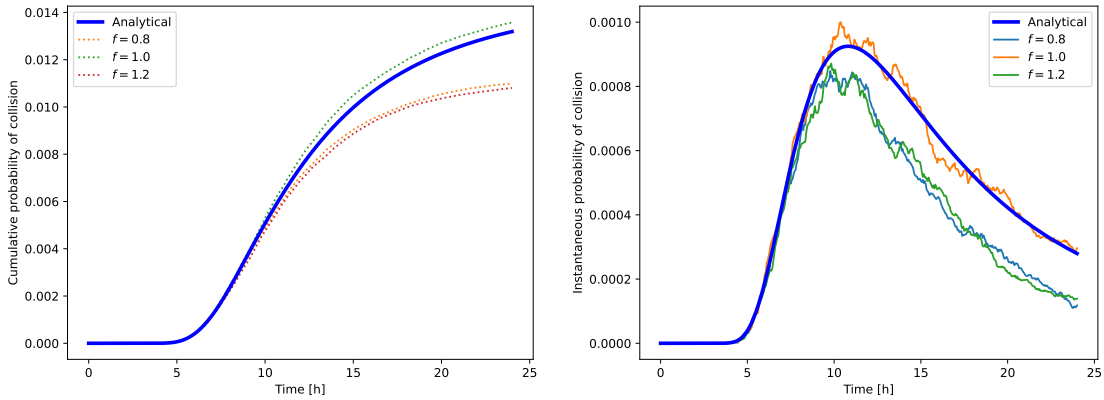
Figure 4.14: Error between analytical and numerical solutions of the instantaneous probability of collision for different values of N.



(a) Cumulative probability of collision. **(b)** Instantaneous probability of collision.

Figure 4.15: Comparison between analytical solution and numerical solutions for different relative orientations.

The main limitation of this method is the SRP perturbation. The STM matrix used to propagate the position covariance matrix does not include such perturbation and, therefore, the analytical method proposed will deviate from reality in accordance to the relevance of such perturbation in the formation dynamics. This deviation can be observed in Figure 4.16, where three cases with different relations of area-to-mass ratio ($f = \frac{A_c/m_c}{A_d/m_d}$) between the formation satellites are numerically simulated and compared with the analytical solution. As can be observed, if the relation is 1, the numerical and analytical results are almost the same. As the relation moves away from the unit, the numerical results deviate from the analytical results. This deviation will grow larger over time, as the perturbation effect builds up.



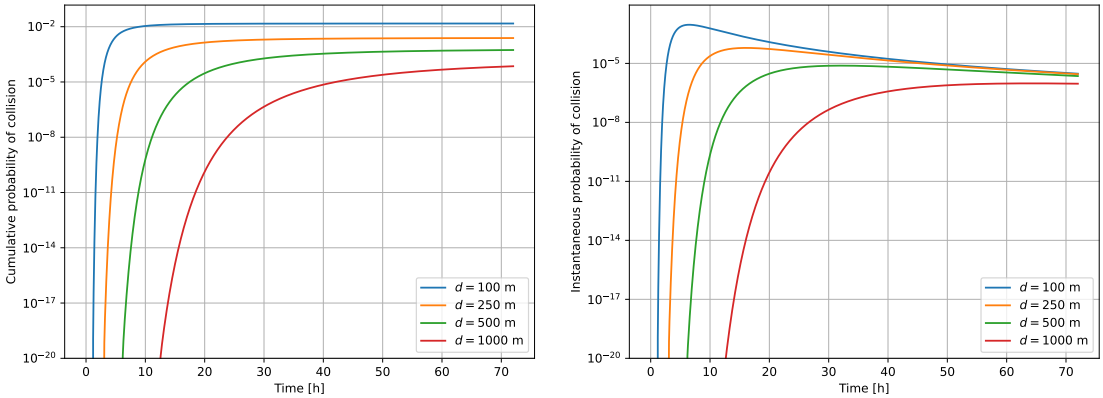
(a) Cumulative probability of collision. **(b)** Instantaneous probability of collision.

Figure 4.16: Comparison between analytical solution and numerical solutions for different relations of area-to-mass ratio of the formation $f = \frac{A_c/m_c}{A_d/m_d}$.

4.3 Case of study

In this section, the above methodology is applied to an example mission, showing how it can be used to assess the impact of the formation size and the formation control accuracy (expressed as uncertainty) on the probability of collision. The baseline characteristics of the formation mission studied are the same as those used in the Monte Carlo simulations (Table 4.1). Unless otherwise stated, the simulation is carried out using the baseline characteristics. To facilitate the comparison of the probability of collision for different cases, the results have been presented on a logarithmic scale.

The main parameter that defines the formation is its nominal distance (d). In Figure 4.17, the probability of collision for different nominal distances is plotted.

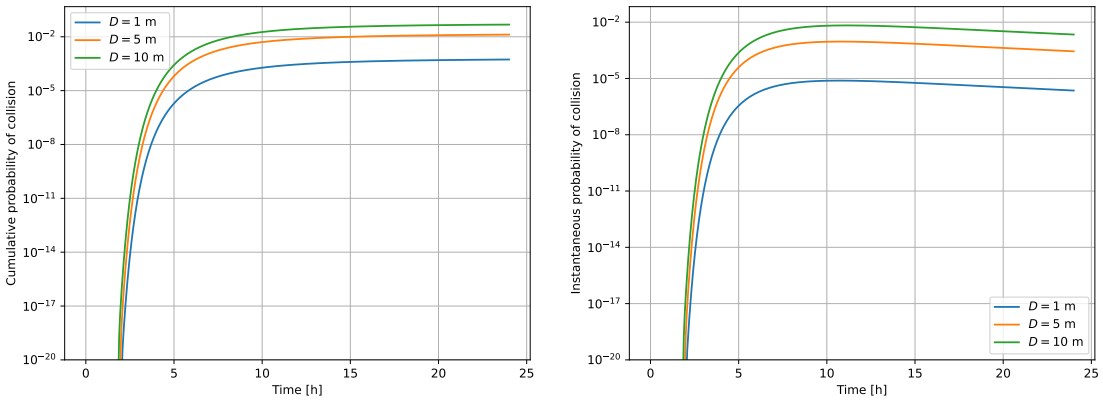


(a) Cumulative probability of collision. **(b)** Instantaneous probability of collision.

Figure 4.17: Time evolution of the probability of collision for different formation sizes (d).

As can be expected, the larger the nominal distance, the lower the probability of collision. Furthermore, these parameters also affect the time when the probability of collision starts to grow, delaying it. If the distance is large enough, the probability of collision will never reach a significant level.

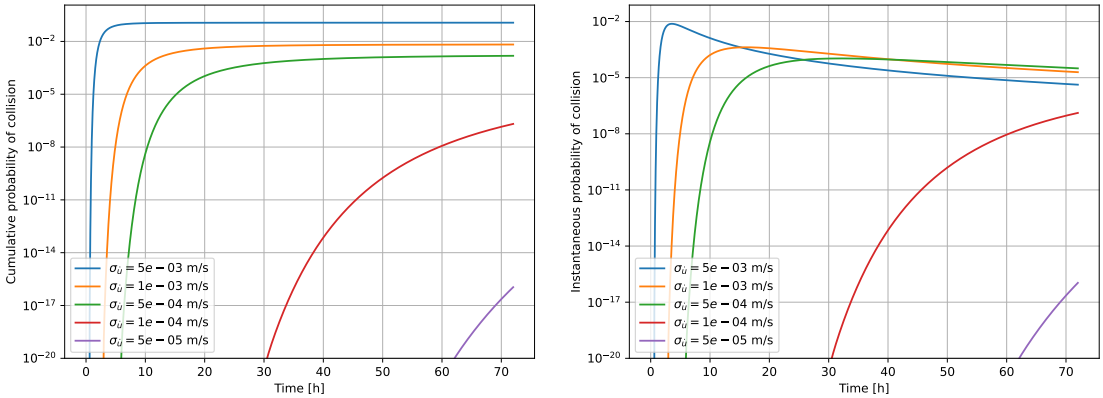
Another relevant parameter is the radius of the safety sphere (D). As it has been said, this distance is obtained adding the hard-radius of both satellites. As shown in Figure 4.18, the probability of collision increases with the size of this sphere.



(a) Cumulative probability of collision. **(b)** Instantaneous probability of collision.

Figure 4.18: Time evolution of the probability of collision for different safety sphere radius (D).

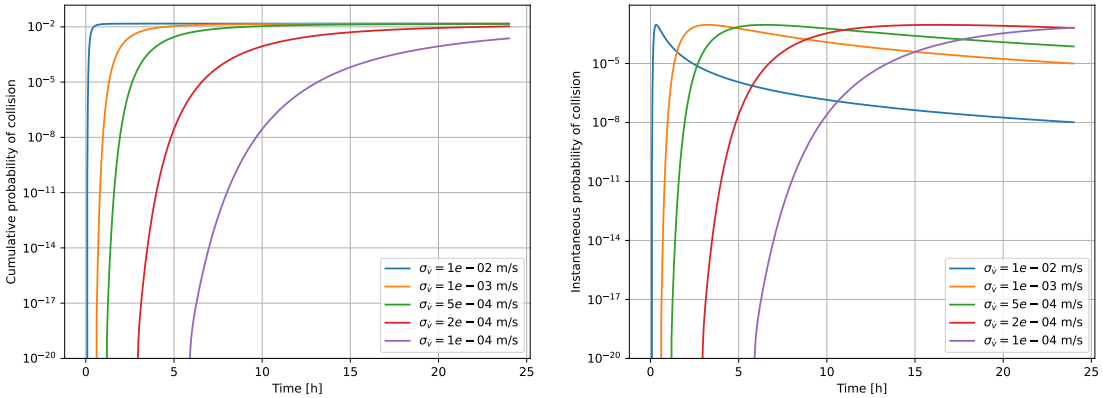
The other two parameters analyzed are the longitudinal ($\sigma_{\dot{u}}$) and lateral ($\sigma_{\dot{v}}$) uncertainties, which are plotted in Figure 4.19 and Figure 4.20. Their impact on the probability of collision is different in each case. The longitudinal uncertainty significantly increases the collision probability and it forwards the instant in which the probability starts increasing. Thus, the maximum instantaneous probability is reached (Figure 4.19b reached earlier). If the longitudinal uncertainty is low enough, the collision probability will not reach a significant level.



(a) Cumulative probability of collision. **(b)** Instantaneous probability of collision.

Figure 4.19: Time evolution of the probability of collision for different values of the longitudinal uncertainty ($\sigma_{\dot{u}}$).

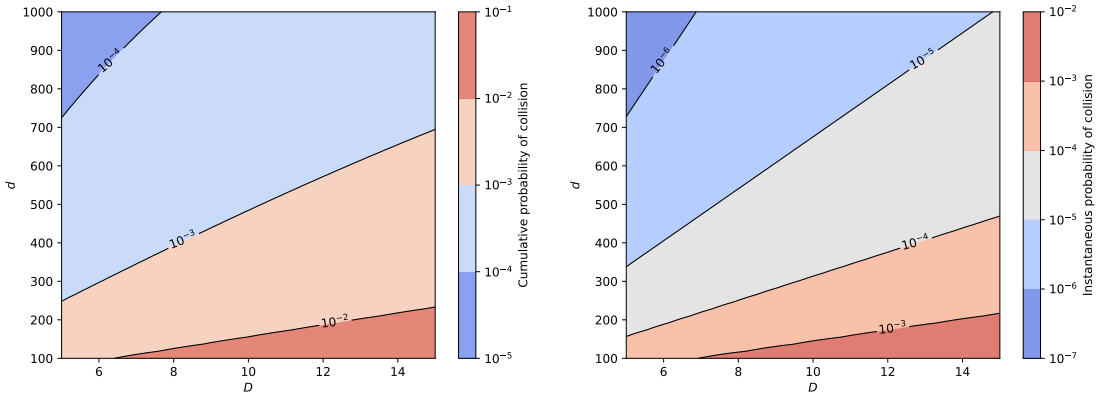
For the lateral uncertainty, the impact is less remarkable. It barely affects the cumulative probability of collision (Figure 4.20a) nor the maximum instant probability of collision (Figure 4.20b). Nevertheless, it slightly delays the growth of the probability and it extends the period of time in which the instant probability collision is at its maximum.



(a) Cumulative probability of collision. **(b)** Instantaneous probability of collision.

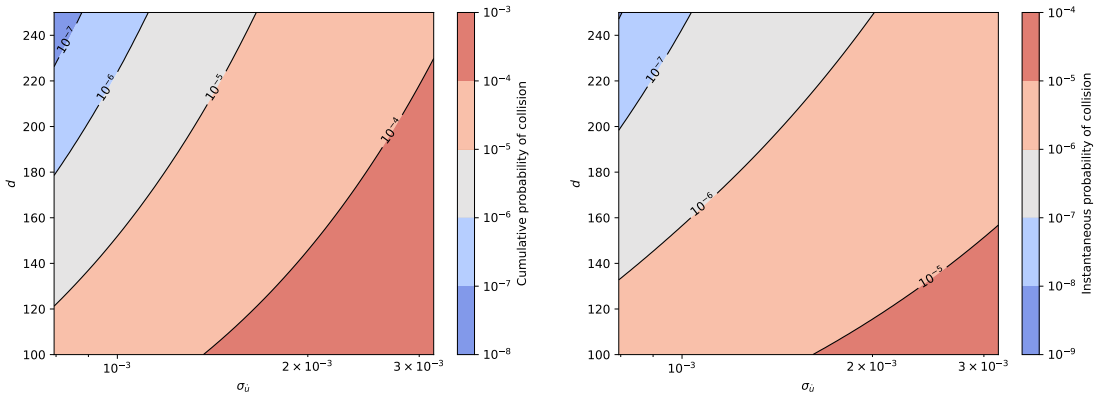
Figure 4.20: Time evolution of the probability of collision for different values of lateral uncertainty ($\sigma_{\dot{v}}$).

In Figure 4.21, the maximum probability of collision is plotted as a function of the size of the formation and the radius of the safety sphere. The same is done for the longitudinal uncertainty and the formation size in Figure 4.22 and for the lateral and longitudinal uncertainties in Figure 4.23. Note that the axes representing the uncertainties are on logarithmic scale.



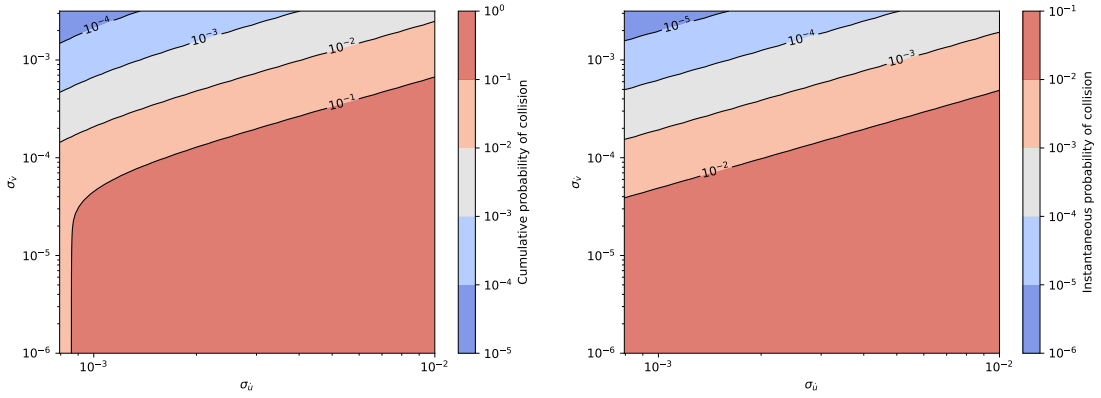
(a) Cumulative probability of collision. **(b)** Instantaneous probability of collision.

Figure 4.21: Maximum value of the probability of collision as a function of the formation size (d) and the safety sphere radius (D).



(a) Cumulative probability of collision. **(b)** Instantaneous probability of collision.

Figure 4.22: Maximum value of the probability of collision as a function of the longitudinal uncertainty ($\sigma_{\dot{u}}$) and the formation size (d).



(a) Cumulative probability of collision. **(b)** Instantaneous probability of collision.

Figure 4.23: Maximum value of the probability of collision as a function of the lateral ($\sigma_{\dot{v}}$) and longitudinal ($\sigma_{\dot{u}}$) uncertainties.

These results allow to asses how the probability of collision evolves over time and how the formation parameters affect this evolution and the maximum value that the probability can reach.

4.4 Discussion of results

The results calculated above can be used to assess the collision risk in a given formation and to evaluate alternatives in its configuration and control to comply with the requirements in this regard. In some formations, the collision risk cannot be eliminated, but it may be possible to mitigate it.

The main options to reduce this risk are to increase the formation distance d or control performance in the longitudinal direction (reducing $\sigma_{\dot{u}}$). The impact of the control performance in the lateral direction ($\sigma_{\dot{v}}$) has a low impact on the magnitude of the risk, although it delays the moment when the maximum collision risk occurs, leaving more time to the chief to perform an evasion maneuver.

The size of the radius of the safety sphere (D) also affects the magnitude of the risk, but depends on the geometry of the satellites and is not easy to modify. Nevertheless, this parameter allows to assess the risk of causing an interference (like getting too close to the chief and saturating its sensors) and could also be used for collision avoidance techniques.

CHAPTER 5

Visibility analysis

As mention in the introduction of this work, the proposed formation would be a chief-deputy formation, in which the deputy (calibration satellite) would relocate itself, whenever necessary, to a predefined location so the calibration signal could reach the chief's instrument. The extent of the sky region that is seen by the instrument at a given moment is called Field of View (FOV). Therefore, assuming that the deputy emits its calibration signal pointing always to the main satellite, the calibration will only occur when the deputy is inside the instrument FOV. Due to the chief's scan strategy, this only occurs in certain instants, and it is not intuitive when and how frequently it will happen. Such an event will be called here an "access" and it can be characterized by its frequency, duration, and how effective it can be for calibration. These features depend mainly on the relative position of the deputy and the scan strategy followed by the chief.

The main goal of this chapter is to study the available time for calibration and its characteristics in terms of maximum and mean duration. This study will enable us to know which regions of space are more suitable to place the calibration satellite relative to the main satellite during the calibration phase.

To carry out the analysis, the direction at which the instrument is pointing over time has been modelled (section 5.1) as well as the detectors geometrical disposition in the focal plane and the trajectory of the calibration signal through it (section 5.3). In order to quantify the performance of a certain relative position, a set of parameters have been defined based on the access features. These parameters describe two main aspects of the accesses: their temporal characteristics and how effective they can be for calibration. The former aspect is assessed in section 5.2 through an analytical and numerical analysis that reports the number, frequency, and duration

of the accesses. For the later aspect, analysed in section 5.3, the signal received by the main satellite instrument is evaluated regarding the percentage of detectors that receive the signal and whether they are calibrated at different polarization angles. The complexity added by the instrument model implies the use of numerical methods for this aspect. The methodology described has been applied in section 5.4 to an example mission, assessing the evolution of the parameters according to the variation of the scan strategy parameters and identifying suitable regions where the deputy can be placed.

5.1 Scanning strategy and relative position

The first step has been the modelling of the main satellite attitude motion to determine the instrument attitude and its pointing over time. The model used to describe the main satellite attitude is based on a simplified version of the one presented in [44]. In this case, only four parameters are used: the spin motion period (T_{spin}), the precession motion period (T_{prec}), the precession axis angle (α), and the instrument axis angle (β). The satellite spins around its main axis (spin axis) with a time period of T_{spin}. Simultaneously, the spin axis, which is separated by angle α from the precession axis, rotates around it with a time period of T_{prec}. The instrument line-of-sight (LoS) is separated by angle β from the spin axis and has a circular FOV with a half-angle of δ.

The attitude of the satellite is defined with respect to a pseudo-inertial frame of reference (0) centered in the main satellite. Although this frame would not be inertial due to the satellite orbital motion, it can be considered as such for shorts period of time. The frame is shown along an scheme of the attitude motion in Figure 5.1.

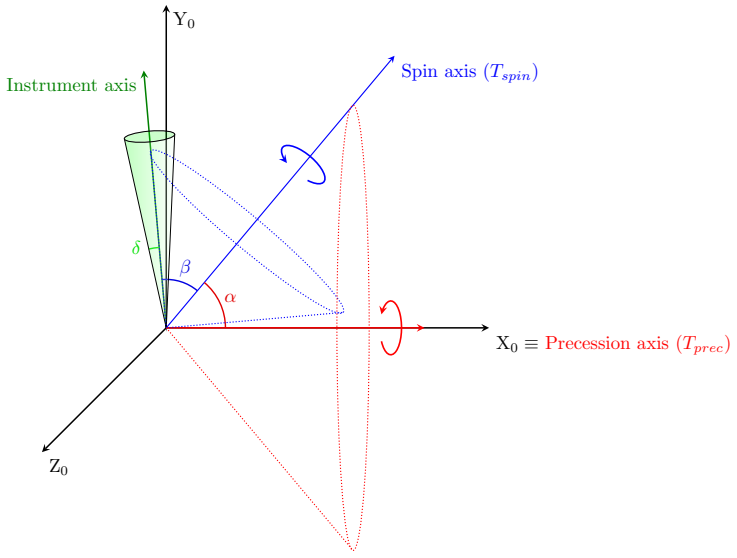


Figure 5.1: Pseudo-inertial coordinate frame (0) and attitude motion scheme.

The X_0-axis of the pseudo-inertial frame, which coincides with the precession axis,

is parallel the Sun direction and it is positive towards deep space. The Y_0 and Z_0 axes complete the right-handed frame and their direction can be chosen arbitrarily.

The attitude of the satellite can be described with an Euler angle sequence (1-3-1) in which the three angles (ψ, α, ϕ) are directly related to the scan strategy parameters, with ϕ being the angle rotated due to spin and ψ the angle rotated due to precession as expressed in Eqs. (5.2) and (5.3). These equations also define the spin speed (ω) and the precession speed (Ω). Then, the attitude matrix, as a function of three of the scan strategy parameters (T_{spin}, T_{prec} and α), is [99]:

$$C_{0,b} = \begin{bmatrix} c_\alpha & c_\phi s_\alpha & s_\phi s_\alpha \\ -c_\psi s_\alpha & c_\psi c_\alpha c_\phi - s_\psi s_\phi & c_\psi c_\alpha s_\phi + s_\psi c_\phi \\ s_\psi s_\alpha & -s_\psi c_\alpha c_\phi - c_\psi s_\phi & -s_\psi c_\alpha s_\phi + c_\psi c_\phi \end{bmatrix} \tag{5.1}$$

where

$$\phi = \omega t = \frac{2\pi}{T_{spin}} t \tag{5.2}$$

$$\psi = \Omega t = \frac{2\pi}{T_{prec}} t \tag{5.3}$$

The attitude matrix $C_{0,b}$ relates the orientation of the satellite body frame (*b*) and the pseudo-inertial reference frame (0). The instrument frame (*inst*) is defined as follows: its X_{inst}-axis is the instrument line of sight and the $Y_{inst}Z_{inst}$-plane corresponds to the plane where the detectors are located. The orientation of the instrument frame with regard to the satellite body frame is expressed by the mounting matrix:

$$C_{b,inst} = \begin{bmatrix} c_\beta & s_\beta & 0 \\ -s_\beta & c_\beta & 0 \\ 0 & 0 & 1 \end{bmatrix} \tag{5.4}$$

which consist of a rotation of angle β around satellite Z_b-axis. Thus, the attitude of the instrument is obtained by combining the satellite attitude matrix $C_{0,b}$ and the mounting matrix $C_{b,inst}$ like:

$$C_{0,inst} = C_{0,b} C_{b,inst} \tag{5.5}$$

The instrument pointing direction can be obtained directly from the orientation of the instrument X_{inst}–axis as:

$$\boldsymbol{q}(t) = C_{0i} \begin{pmatrix} 1 \\ 0 \\ 0 \end{pmatrix} \tag{5.6}$$

As time passes, the line of sight of the instrument creates a pattern of observation over the celestial sphere. The morphology of this trace depends on the four parameters of the scan strategy. The orthographic projection of the instrument axis on the reference frame Y_0Z_0-plane is shown in Figure 5.2 as an example of scan pattern. Note that the area swept by the FOV is not plotted. The scan

strategy parameters choice is subjected to some constraints to ensure a complete and adequate observation of the sky [44]. For example, the sum of α and β defines the extent of the celestial sphere observed for a fixed direction of the precession axis. For a satellite orbiting L_2, where the precession axis usually points towards anti-Sun direction, it is necessary that $\alpha + \beta > 90°$ to observe the entire sky after six months. However, this sum should not be much higher to avoid pointing towards the Sun. Other constraints are the ratio between T_{spin} and T_{prec}, which defines the spatial separation between the sequential rings that are mapped in each spin turn and can be related to the FOV size, or the value of the sampling frequency, that must be high enough to sample the sky with the required accuracy and thus establishes a lower limit on T_{spin}. The scan strategy parameters used in the following examples are similar to to those used in previous and future CMB missions [9, 10, 15, 100, 101].

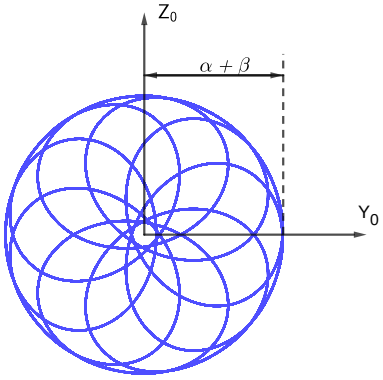
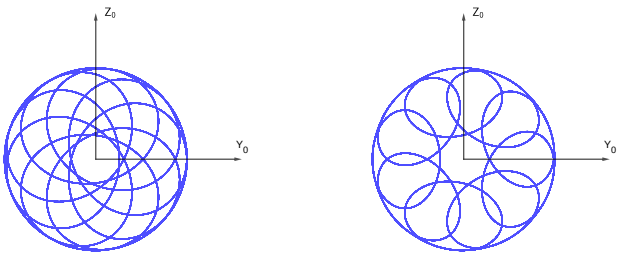


Figure 5.2: Orthographic projection of the scan pattern for $\alpha = 45°$, $\beta = 50°$, $T_{spin} = 10$ min, and $T_{prec} = 90$ min.

Once the sum constraint of α and β is set, the trace geometry will differ according to whether $\alpha > \beta$ or the contrary, as shown in Figure 5.3. In the former case, the instrument line of sight encircles the precession axis in each spin rotation; while in the latter case it does not. In both cases, the minimum angle that the line of sight forms with the precession axis (the origin) is $|\alpha - \beta|$. Due to this, if the difference between both angles is high, the trace does not pass close to the precession axis, leaving a circular region without any crossover.



(a) $\alpha < \beta$ ($\alpha = 40°$ and $\beta = 55°$).

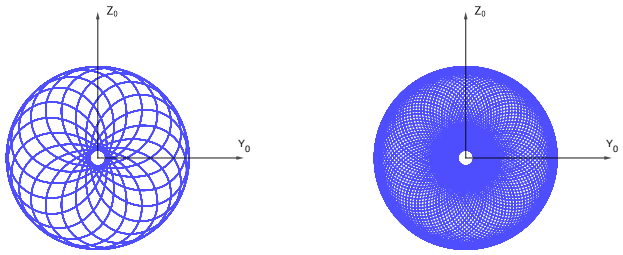
(b) $\alpha > \beta$ ($\alpha = 55°$ and $\beta = 40°$).

Figure 5.3: Change of the scan pattern morphology according to the relation between angles α and β. In both cases $T_{spin} = 10$ min and $T_{prec} = 90$ min.

The relation between the periods of the spin and precession motions will also influence the geometry of the trace and is chosen carefully to avoid undesired effects and to ensure adequate coverage of the sky [44, 102]. As previously said, the ratio between the period of both motions defines the spatial separation ζ between the sequential rings of the trace:

$$\frac{T_{spin}}{T_{prec}} = \frac{\zeta}{2\pi \sin \alpha} \tag{5.7}$$

This separation can be chosen to be less than the FOV size (δ) to allow continuous mapping of the sky. Additionally, as both motions are periodic, their combined motion will also be periodic as long as the periods are related by a rational number (i.e., they are commensurable), in which case the pattern will repeat itself. In general, a higher period of the combined movement will produce a finer pattern, providing a more uniform coverage of the sky, since it will be necessary a larger amount of time until the trace starts repeating itself. Thus, the access duration of those points in the sky at the same angular distance from the precession axis will become more uniform. The combined period (T_{comb}) can be calculated as the least common multiple of both periods. This behaviour can be observed in Figure 5.4, where a slight variation of the parameter T_{prec} changes the coverage considerably as the combined motion period rises. In Figure 5.4(a), the combined period is $T_{comb} = 190$ min while in Figure 5.4(b) the resulting period is $T_{comb} = 970$ min. In the first case, for points separated by 45° from the precession axis and $\delta = 7.5°$, the variations of the mean duration of the accesses is much higher, reaching a difference of 14 s, than in the second case, where the maximum differences is roughly 3 s.



(a) $T_{spin} = 10$ min, $T_{prec} = 95$ min. (b) $T_{spin} = 10$ min, $T_{prec} = 97$ min.

Figure 5.4: Change in the scan pattern due to the value of the combined motion period. For (a), the resulting period of the combined motions is $T_{comb} = 190$ min while for (b), the resulting period is $T_{comb} = 970$ min. In both cases $\alpha = 45°$ and $\beta = 50°$.

As shown in Figure 5.4, the pattern of the trace becomes increasingly uniform as the combined period of the two motions grows. Ideally, if such a period is infinite, this distribution will be fully axial-symmetric around the precession axis. Under this condition, the results of the visibility parameters can also be expected to have axial-symmetry around the precession axis. This simplification will be assumed in the analytical study.

Once the scan strategy is fixed, the access features will vary according to the relative positioning between deputy and chief. The deputy position relative to that of the chief is defined by the vector connecting both satellites:

$$\boldsymbol{r}_{cd} = \boldsymbol{r}_{deputy} - \boldsymbol{r}_{chief} \tag{5.8}$$

In this analysis, the distance separating the satellites is not relevant. For clarity the unit vector, defined as:

$$\boldsymbol{p}_{cd} = \frac{\boldsymbol{r}_{cd}}{||\boldsymbol{r}_{cd}||} \tag{5.9}$$

is used instead. This unit vector represents the direction of the deputy on the sky as seen from the chief's perspective (5.5). This direction can be expressed in terms of two coordinates (φ, θ) as:

$$\boldsymbol{p}_{cd} = \begin{pmatrix} \cos\varphi \\ \sin\varphi\sin\theta \\ \sin\varphi\cos\theta \end{pmatrix} \tag{5.10}$$

with φ being the angular separation with X_0-axis, which here coincides with the precession axis, and θ the angle between the Z_0-axis and the projection of $\boldsymbol{p}_{cd}$ on Y_0Z_0-plane. The use of these coordinates will help to derive the analytical expressions and facilitate the interpretation of the results. Axial-symmetry is equivalent to being independent of the θ coordinate; and the φ coordinate represents the angular separation from the precession axis. The defined vectors and the coordinates definition are shown in Figure 5.5.

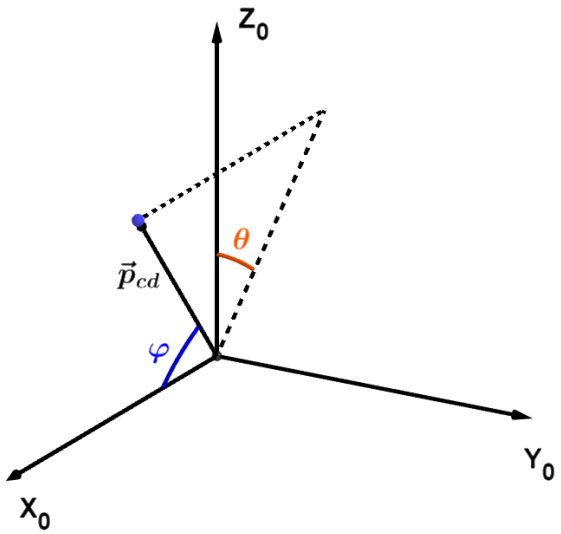


Figure 5.5: Pseudo-inertial reference frame and definition of φ and θ coordinates.

5.1.1 Numerical modelling

For the numerical analysis, the space of possible directions has been discretized and used to detect when accesses will occur in each position. The results obtained

are processed to calculate the parameters of interest. Every orientation vector obtained from the discretization represents a different relative position of the deputy regarding the chief i.e., a point in the sky. Furthermore, this orientation vector defines the line of sight between both satellites, which is used to detect when an access is happening.

For the analysis of a time period, the attitude of the satellite and the instrument is generated with a fixed sample time and stored for subsequent analysis. The time step used in such discretization ($dT = 0.1$ s in this work) establishes the precision of the results.

As has been said previously, the relative orientation between the satellites can be defined by a unitary vector centered in the origin and parallel to the relative position vector. To obtain a set of directions covering all the possible orientations, the HEALPix [103] scheme for tessellating the sky has been used, specifically, an implementation called astropy-healpix, an Astropy [104] coordinated package. This equal area scheme is based on the discretization of a sphere surface (see Figure 5.6), providing a nearly regular grid which avoids distortions that appear when the coordinates φ and θ are discretized with equispaced points. HEALPix also allows to interpolate results in any point in the sphere using bilinear interpolation.

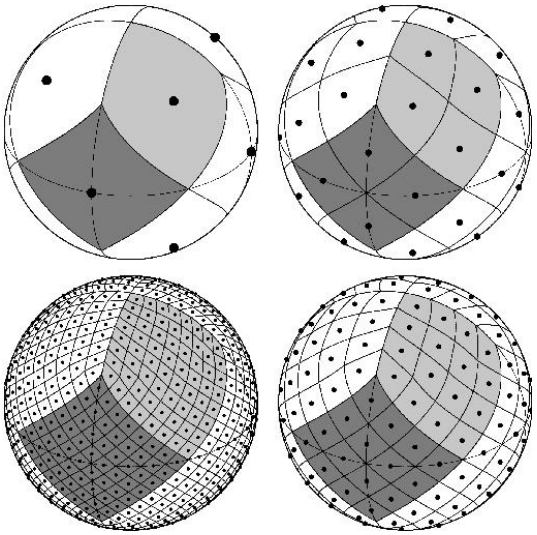


Figure 5.6: Discretization of an sphere following HEALPix approach. From [103].

The numerical algorithm is focused on detecting the access to permit the later analysis of each one. The access event occurs when the line of sight between both satellites is inside the FOV of the chief instrument, which can be verified with the dot product between the orientation vector and the pointing direction of the instrument. This is done at every step time for each orientation obtained from the discretization, computing the number of accesses and its duration. The simulations were performed using SciPy [105].

5.2 Access analysis

In the following subsections, a set of parameters that describe the access features are studied.

5.2.1 Total access time

The first parameter to be analysed is the total access time (T_{total}) of an inertial direction in the sky. As mentioned in (5.10) this direction can be defined with its φ and θ coordinates. The total access time is defined as the total amount of time that the deputy, i.e., the direction that defines its relative position, stays inside the instrument FOV. It is a feature of a given scan strategy.

Analytical approach for total access time

As explained before, if the rotation times (T_{spin} and T_{prec}) are properly selected and the analysis time is long enough, it can be assumed that the results will be axial-symmetric. This implies that T_{total} will not depend on θ and only its variation with the φ coordinate of the direction is relevant. Thus, since T_{total} does not depend on θ, it will be equal for all the points in the sky with the same φ. Furthermore, the precession speed does not influence the fraction of time that each point of the sky is seen as any increase in the speed will shorten the access duration but it will also make the number of accesses grow proportionally. Therefore, an arbitrary precession speed case can be analysed and the conclusions about T_{total} will be applicable to other velocities as long as the high combined period condition is met.

The instrument direction over the time, $\boldsymbol{q}(t)$, can also be expressed in terms of φ and θ coordinates, however, as the final value of T_{total} does not depend on θ, only the variation of the angle between the direction of the instrument and the X_0-axis is relevant. This angle, called here φ_v, only depends on the spin motion and its variation is periodic every spin cycle, thus, the value of T_{total} obtained with the motion of the instrument, $\boldsymbol{q}(t)$, will be equivalent to the one obtained by a vertical periodic motion $\boldsymbol{q}^*(t)$ in the X_0Y_0-plane. Therefore, the analysis of this motion during one spin period will provide all the required information about T_{total}.

Based on these considerations, let us study how much time the directions with the same φ coordinate are inside the instrument FOV for the simplest possible case: the one with almost zero precession ($T_{prec} \longrightarrow \infty$). Furthermore, it is only necessary to study one spin cycle, which, as previously said, can be represented as a vertical periodic motion with $\varphi_v = f(t)$. A scheme of this analysis is shown in Figure 5.7. It should be noticed that, although these schemes do not provide a rigorous projection of the trace, it helps to facilitate the understanding of the process. The angles regarding the precession axis are represented as in an azimuthal equidistant projection, i.e., directions with the same φ coordinate are displayed as a circumference with a radius proportional to φ.

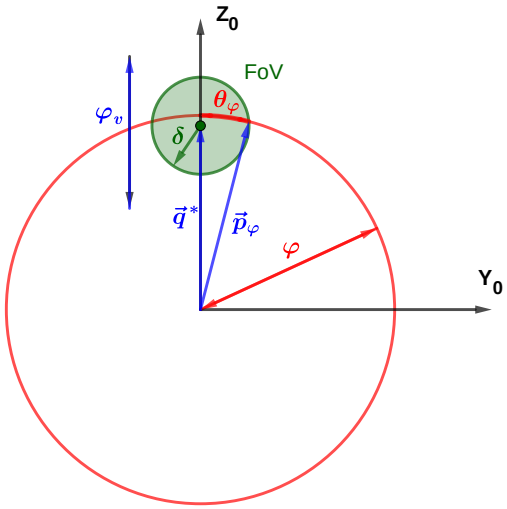


Figure 5.7: Geometrical scheme for the simplified case considered. Note that $\boldsymbol{q}^*$ will move vertically as φ_v changes.

In order to calculate $\varphi_v = f(t)$ it is necessary to define the direction of the instrument $\boldsymbol{q}$. This direction can be expressed as a rotation around spin axis $\boldsymbol{u}_{spin}$, which in this analysis is fixed and contained in X_0Z_0-plane, as follows:

$$\boldsymbol{u}_{spin} = \begin{pmatrix} \cos(\alpha) \\ 0 \\ \sin(\alpha) \end{pmatrix} \tag{5.11}$$

The rotation matrix around the direction defined by this vector is:

$$R = \begin{bmatrix} c_\phi + c_\alpha^2(1-c_\phi) & -s_\alpha s_\phi & c_\alpha s_\alpha(1-c_\phi) \\ s_\alpha s_\phi & c_\phi & -c_\alpha s_\phi \\ c_\alpha s_\alpha(1-c_\phi) & c_\alpha s_\phi & c_\phi + s_\alpha^2(1-c_\phi) \end{bmatrix} \tag{5.12}$$

where ϕ is the rotated angle. If the starting position of $\boldsymbol{q}$ is:

$$\boldsymbol{q}_0 = \begin{pmatrix} \cos(\alpha+\beta) \\ 0 \\ \sin(\alpha+\beta) \end{pmatrix} \tag{5.13}$$

also contained in X_0Z_0-plane, the value of $\boldsymbol{q}$ depending on the spin angle would be:

$$\boldsymbol{q}(\phi) = R \cdot \boldsymbol{q}_0 = \begin{pmatrix} \cos(\alpha)\cos(\beta) - \sin(\alpha)\sin(\beta)\cos(\phi) \\ -\sin(\beta)\sin(\phi) \\ \cos(\alpha)\sin(\beta)\cos(\phi) + \sin(\alpha)\cos(\beta) \end{pmatrix} \tag{5.14}$$

The angle between the instrument direction and the precession axis, φ_v, is then obtained from the dot product between $\boldsymbol{q}$ and X_0-axis direction as:

$$\varphi_v = \arccos(\cos(\alpha)\cos(\beta) - \sin(\alpha)\sin(\beta)\cos(\phi)) \tag{5.15}$$

Then, the equivalent vertical motion of the instrument, $\boldsymbol{q}^*$, is given by:

$$\boldsymbol{q}^* = \begin{pmatrix} \cos(\varphi_v) \\ 0 \\ \sin(\varphi_v) \end{pmatrix} \tag{5.16}$$

where $\varphi_v(t)$ can be calculated using Eq. (5.15).

Once the motion of the instrument has been characterised, the next step is to calculate the fraction of the circumference inside the FOV in each instant. A generic point of the circumference, $\boldsymbol{p}$, is given by Eq. (5.10). The one where the access starts in a certain instant can be written as:

$$\boldsymbol{p}_\varphi = \begin{pmatrix} \cos(\varphi) \\ \sin(\varphi)\sin(\theta_\varphi) \\ \sin(\varphi)\cos(\theta_\varphi) \end{pmatrix} \tag{5.17}$$

For a given position $\boldsymbol{q}^*$ of an instrument with FOV half-angle δ, the vector of the instrument $\boldsymbol{q}^*$ will form an angle δ with $\boldsymbol{p}_\varphi$. Therefore:

$$\boldsymbol{q}^* \cdot \boldsymbol{p}_\varphi = \cos(\delta) \tag{5.18}$$

From this equation, the half-arc angle θ_φ of points with the same φ that are inside the FOV (see Figure 5.7) can be obtained:

$$\cos(\theta_\varphi) = \frac{\cos(\delta) - \cos(\varphi_v)\cos(\varphi)}{\sin(\varphi_v)\sin(\varphi)} \tag{5.19}$$

Therefore, the fraction of points inside the FOV is $2\theta_\varphi/2\pi$.

Averaging this fraction over a half spin period, the fraction of time that directions with the same φ spend inside the FOV during one period can be obtained. This averaged fraction is:

$$f_t(\varphi) = \frac{1}{\pi}\int_0^\pi \frac{1}{\pi}\mathrm{Re}\left(\arccos\left(\frac{\cos(\delta) - \cos(\varphi_v)\cos(\varphi)}{\sin(\varphi_v)\sin(\varphi)}\right) d\phi\right) \tag{5.20}$$

as the second half of the period is symmetric to the first one.

The total access time for a point with angle φ can be calculated multiplying this fraction by the total time of analysis, T_{sim}:

$$T_{total}(\varphi) = f_t(\varphi) \cdot T_{sim} \tag{5.21}$$

As can be deduced from Eqs. (5.15) and (5.20), f_t depends solely on φ, with α, β and δ as parameters while the spin and precession speeds do not appear. An example of the solution of $f_t(\varphi)$ is shown in Figure 5.8.

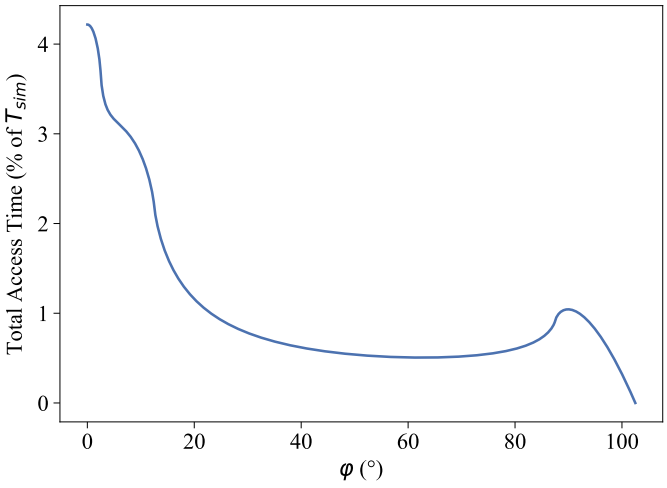


Figure 5.8: Variation of the percentage of access time regarding the total time considered as a function of coordinate φ. Parameters considered: $T_{sim} = 1$ day, $\alpha = 45°$, $\beta = 50°$, $T_{spin} = 10$ min, $T_{prec} = 93$ min, and $\delta = 7.5°$.

Numerical results for total access time

The total access time has been calculated following the methodology explained in section 5.1.1. To represent the numerical results, a Hammer projection [106] of the whole sphere has been chosen to depict them. The center of the image corresponds to the observation direction of the precession axis, while the lateral regions represent the opposite direction. The result for the same example on Figure 5.8 is presented in Figure 5.9, where the axial-symmetry is clear.

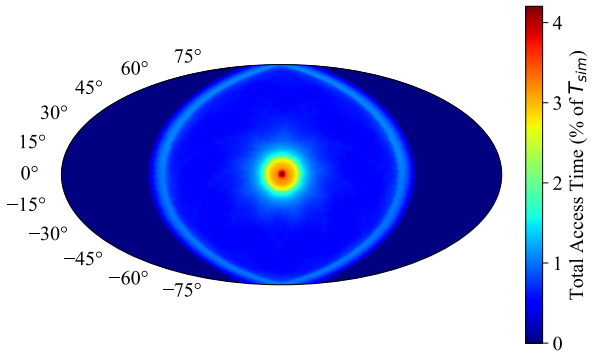
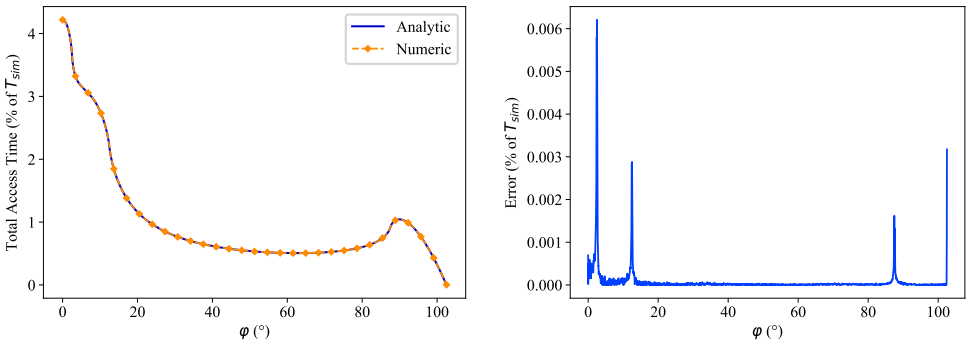


Figure 5.9: Total access time. Parameters considered: $T_{sim} = 1$ day, $\alpha = 45°$, $\beta = 50°$, $T_{spin} = 10$ min, $T_{prec} = 93$ min, and $\delta = 7.5°$.

The main disadvantage of this approach is its computational cost, which grows proportionally with the simulation time and both the temporal and spatial discretization (nevertheless, more than one parameter can be calculated in the same simulation with small additional effort). For this reason, the analytical approach can be useful for validation of the numerical method. In Figure 5.10 the analytical and numerical results for total access time are compared. The numerical results have been averaged over θ. Overall, the error is low except in the deep slope

zones of the curve, due to the limited precision of the bilinear interpolation. The criterion to consider that both results coincide has been established in an RMSE (root-mean-square error) that is lower than 1E-3% of T_{sim}. This is fulfilled for all the scan strategies tested.



(a) Comparison. (b) Error.

Figure 5.10: Comparison (a) and error (b) between the analytical and numerical results for the variation of the total access time as a function of coordinate φ. Parameters considered: $T_{sim} = 1$ day, $\alpha = 45°$, $\beta = 50°$, $T_{spin} = 10$ min, $T_{prec} = 93$ min, and $\delta = 7.5°$.

5.2.2 Mean access time

The mean access time, T_{mean}, can be defined as the total access time over a period of time divided by the number of accesses. As before, for a direction $\boldsymbol{p}$, if spin and precession are chosen properly, it is possible to assure that this parameter does not depend on θ.

Analytical approach for mean access time

In the previous section, the total access time has been obtained, and now the number of accesses is calculated following a similar approach. Although, for calculating the total access time the precession motion can be omitted, it will influence the number of accesses for a certain φ and it has to be taken into account if precession speed Ω is not negligible.

In order to calculate the number of accesses, it is not relevant how much time one given direction stays inside the FOV, but whether after one spin period it has been seen or not. Thus, the approach to solve the problem is to calculate the proportion of directions, f_m, with the same φ coordinate that have been inside the FOV after one spin period . As before, the motion is symmetrical with regard to the axis of rotation after a period, therefore, this proportion must remain constant for subsequent periods. If accesses are equally distributed along all the points with the same φ, the total number of accesses during a given period can be obtained by multiplying the number of spin cycles by the aforementioned proportion:

$$N(\varphi) = f_m(\varphi)\frac{T_{sim}}{T_{spin}} \tag{5.22}$$

First, the case for Ω negligible is presented and then it will be extended to the general case that takes into account the precession speed. A geometrical scheme of half spin period when Ω is negligible is shown in Figure 5.11.

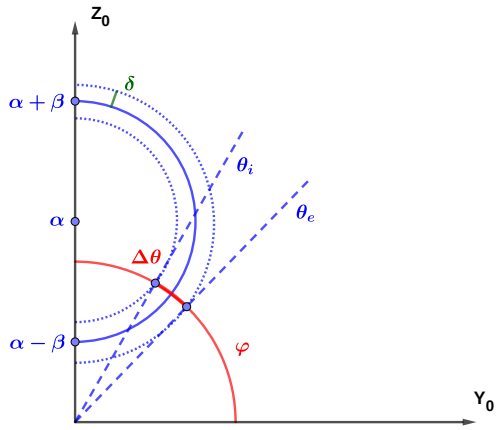


Figure 5.11: Geometrical scheme for the mean access time when precession is negligible.

Every half spin period, an arc of $\Delta\theta$ is seen from the instrument. Over one spin, this makes a proportion of:

$$f_m = \frac{2\Delta\theta}{2\pi} \tag{5.23}$$

which is equal to the mean number of accesses for all the directions with the same φ coordinate. The value of $\Delta\theta$ can be obtained as:

$$\Delta\theta = \theta_e - \theta_i, \tag{5.24}$$

where θ_e and θ_i are the limits of the highlighted arc in Figure 5.11. If Ω is negligible, this arc is limited by the two circles of radius $\beta + \delta$ and $\beta - \delta$. Therefore, following the same approach that in (5.19), the limit values are:

$$\theta_i|_\varphi = \mathrm{Re}\left(\arccos\left(\frac{\cos(\beta-\delta) - \cos(\alpha)\cos(\varphi)}{\sin(\alpha)\sin(\varphi)}\right)\right) \tag{5.25}$$

and

$$\theta_e|_\varphi = \mathrm{Re}\left(\arccos\left(\frac{\cos(\beta+\delta) - \cos(\alpha)\cos(\varphi)}{\sin(\alpha)\sin(\varphi)}\right)\right) \tag{5.26}$$

Once θ_e and θ_i are obtained, the distance $2\Delta\theta$ can be calculated and substituting Eq. (5.23) into Eq. (5.22), the number of accesses will be:

$$N(\varphi) = \frac{2\Delta\theta}{2\pi}\frac{T_{sim}}{T_{spin}} \tag{5.27}$$

Retrieving the total access time from Eq. (5.21), the mean access time is:

$$T_{mean}(\varphi) = \frac{T_{total}(\varphi)}{N(\varphi)} = T_{spin}\frac{f_t(\varphi)}{f_m(\varphi)} \tag{5.28}$$

The mean access time profile for the case of negligible Ω is shown in Figure 5.12.

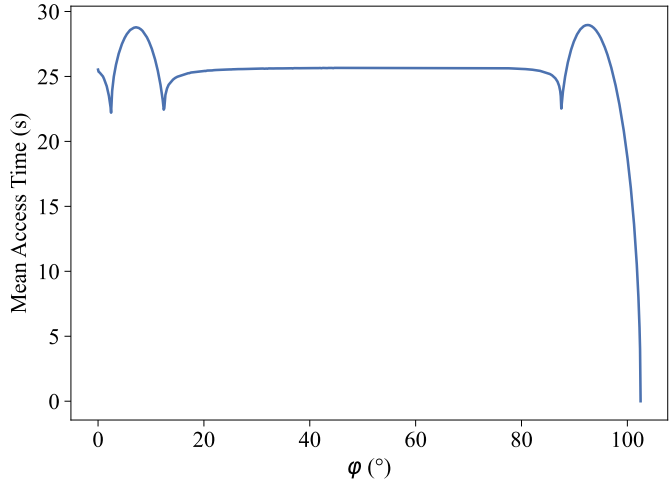


Figure 5.12: Variation of the mean access time as a function of coordinate φ for negligible Ω. Parameters considered: $T_{sim} = 1$ day, $\alpha = 45°$, $\beta = 50°$, $T_{spin} = 10$ min, and $\delta = 7.5°$.

However, if $\Omega < \omega$ but not negligible, the trace cannot be simplified as a circle. An example of how the scheme can look is shown in Figure 5.13.

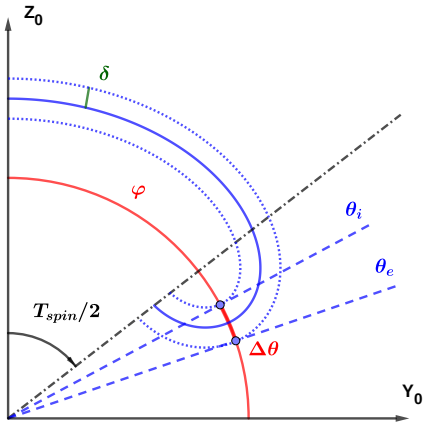


Figure 5.13: Geometrical scheme for mean access time when precession speed is significant. Only the trace for half T_{spin} period is shown.

In this case, in order to calculate the value of θ_i and θ_e it is necessary to obtain the side curves of the trace. These curves are separated by a 2δ distance in the perpendicular direction to the trace. If the trace expression is $\boldsymbol{q}(t)$ from Eq. (5.6), the equations of the exterior and interior curves are respectively:

$$\boldsymbol{q}_e(t) = \boldsymbol{q}\cos(\delta) + \boldsymbol{n}\sin(\delta) = \begin{pmatrix} x_e(t) \\ y_e(t) \\ z_e(t) \end{pmatrix} \tag{5.29}$$

and

$$\boldsymbol{q}_i(t) = \boldsymbol{q}\cos(\delta) - \boldsymbol{n}\sin(\delta) = \begin{pmatrix} x_i(t) \\ y_i(t) \\ z_i(t) \end{pmatrix} \tag{5.30}$$

with $\boldsymbol{n}$ being the unitary normal to the trace, whose expression is:

$$\boldsymbol{n} = \frac{\boldsymbol{q}'(t) \wedge \boldsymbol{q}(t)}{|\boldsymbol{q}'(t)|} \tag{5.31}$$

It is more useful to express the external and internal curves in terms of its φ and θ components. These can be calculated from the Cartesian coordinates from Eqs. (5.29) and (5.30) as:

$$\varphi_e(t) = \mathrm{Re}(\arccos(y_e(t))) \tag{5.32}$$

$$\theta_e(t) = \mathrm{Re}\left(\arccos\left(\frac{z_e(t)}{\sin(\varphi_e(t))}\right)\right) \tag{5.33}$$

and

$$\varphi_i(t) = \mathrm{Re}(\arccos y_i(t)) \tag{5.34}$$

$$\theta_i(t) = \mathrm{Re}\left(\arccos\left(\frac{z_i(t)}{\sin(\varphi_i(t))}\right)\right) \tag{5.35}$$

With the equations of the external and internal curve, the procedure to calculate the $2\Delta\theta$ for a given φ is as follows: first, using equations (5.32) and (5.34) the instants t_i and t_e when the traces have respectively $\varphi_i = \varphi$ and $\varphi_e = \varphi$ are calculated. Second, these instants are used to calculate θ_e and θ_i with equations (5.33) and (5.35). Once these angles are obtained, the distance $2\Delta\theta$ can be determined and the number of accesses is obtained through Eq. (5.28). An example of the resulting profile obtained from Eq. (5.28) is shown in Figure 5.14.

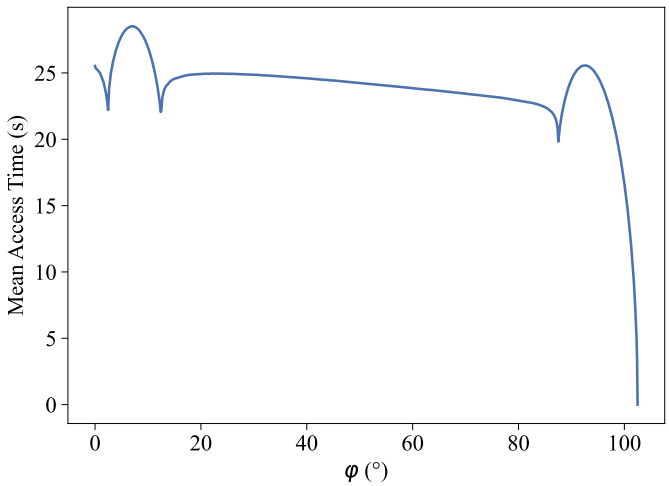


Figure 5.14: Variation of the mean access time as a function of coordinate φ, with $\Omega < \omega$ but not negligible. Parameters considered: $T_{sim} = 1$ day, $\alpha = 45°$, $\beta = 50°$, $T_{spin} = 10$ min, $T_{prec} = 93$ min, and $\delta = 7.5°$.

Numerical results for the mean access time

The numerical results for the mean access time for the same example on Figure 5.14 are presented in Figure 5.15). As can be seen, the mean access time also presents axial-symmetry.

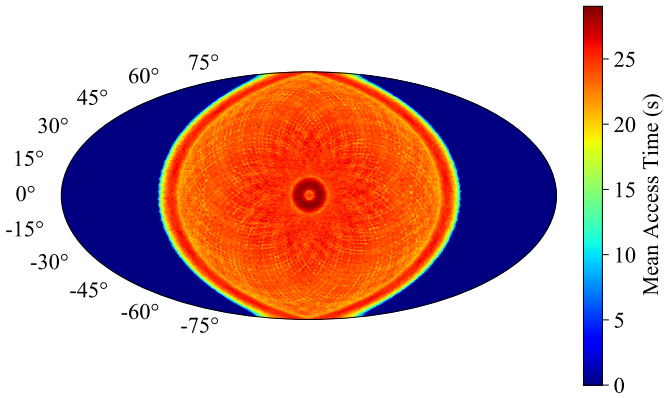
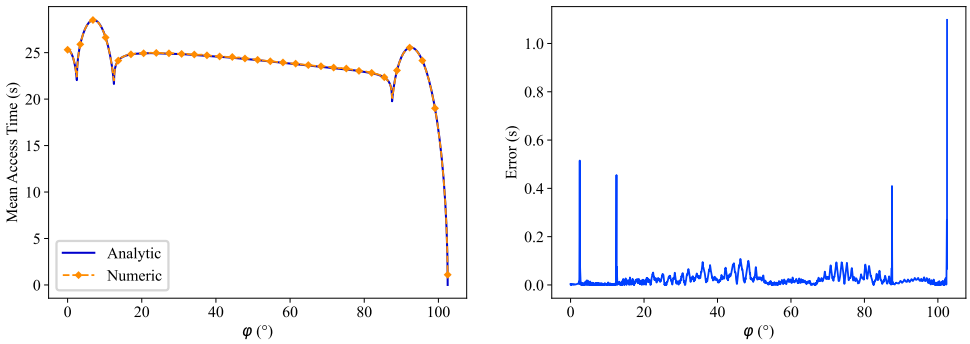


Figure 5.15: Mean access time. Parameters considered: $T_{sim} = 1$ day, $\alpha = 45°$, $\beta = 50°$, $T_{spin} = 10$ min, $T_{prec} = 93$ min, and $\delta = 7.5°$

In Figure 5.16 the analytical and numerical results for mean access time are compared. The numerical results have been averaged over θ. In this case, the criterion to validate the results is that the RMSE is lower than the time step used for the numerical analysis. This is fulfilled for all the scan strategies tested.



(a) Comparison.

(b) Error.

Figure 5.16: Comparison (a) and error (b) between the analytical and numerical results for the mean access time as a function of coordinate φ. Parameters considered: $T_{sim} = 1$ day, $\alpha = 45°$, $\beta = 50°$, $T_{spin} = 10$ min, $T_{prec} = 93$ min, and $\delta = 7.5°$.

5.2.3 Maximum access time

The maximum access time (T_{max}) is the maximum time that a direction $p = f(\varphi, \theta)$ can be inside the FOV of the instrument. This time also depends on the scan strategy and will not depend on θ if the rotation and precession are chosen properly.

Analytical approach for maximum access time

For the maximum access time, the procedure followed is similar to the mean access time section. First, the expression for the duration of an access with no precession motion is obtained. But now, the maximum access time is studied instead of the mean access time. Then, the precession motion is added, distinguishing two cases according to whether the precession speed is negligible or not, like in the mean access time section.

First, the case without precession will be analyzed. As there is only rotation around the spin axis, the motion will be analyzed centered in that axis, the new coordinates being θ^* and φ^*. Furthermore, in order to obtain the access time for this pure spin motion, it is advantageous to consider that the instrument remains fixed and it is the direction vector the one that rotates around the spin axis (X^* in the new coordinates). Without loss of generality, it is assumed that the instrument is located on the X^*Z^*-plane, separated by an angle β from the spin axis, as shown in Figure 5.17, thus:

$$\boldsymbol{q} = \begin{pmatrix} \cos\beta \\ 0 \\ \sin\beta \end{pmatrix} \tag{5.36}$$

In this new frame, the direction vector $\boldsymbol{p}$ is separated an angle φ^* from the spin axis, and its projection over the Y^*Z^*-plane form an angle θ^* with the Z^*-axis, so it can be expressed as:

$$\boldsymbol{p} = \begin{pmatrix} \cos(\varphi^*) \\ \sin(\varphi^*)\sin(\theta^*) \\ \sin(\varphi^*)\cos(\theta^*) \end{pmatrix} \tag{5.37}$$

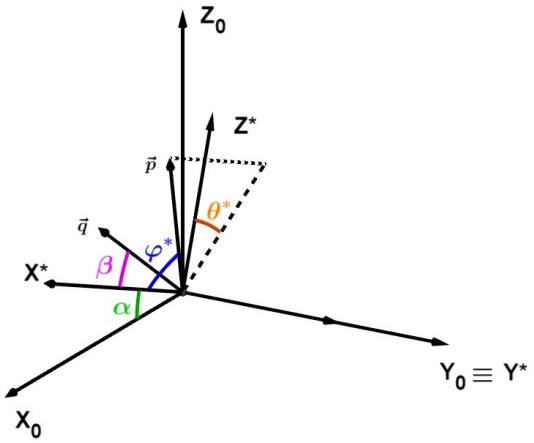


Figure 5.17: New reference system defined.

The starting condition of an access, expressed in Eq. (5.18), establishes that the relation between β, θ^*, φ^* and δ for a given instant is:

$$\cos(\theta^*_\varphi) = \frac{\cos(\delta) - \cos(\varphi_v)\cos(\varphi^*)}{\sin(\varphi_v)\sin(\varphi^*)} \tag{5.38}$$

This equation is similar to Eq. (5.19). Due to how the direction vector is expressed, the angle θ^*_φ is the half-arc of its trajectory inside the FOV. Therefore, if the trajectory in one spin period has a length of 2π, the proportion of time inside the FOV is $2\theta^*_\varphi/2\pi$ and the access time is:

$$T_{access} = \frac{T_{spin}}{\pi}\mathrm{Re}\left(\arccos\left(\frac{\cos(\delta)-\cos(\beta)\cos(\varphi^*)}{\sin(\beta)\sin(\varphi^*)}\right)\right) \tag{5.39}$$

The maximum access time can be obtained deriving Eq. (5.39) with regard to φ^* and equating to zero, which gives:

$$t_{max} = \frac{T_{spin}}{\pi}\mathrm{Re}\left(\arccos\left(\frac{\sqrt{\cos^2(\delta)-\cos^2(\beta)}}{\sin(\beta)}\right)\right) \tag{5.40}$$

This maximum access time, called here optimum access time, is achieved for the directions whose φ^* coordinate is equal to $\varphi^*_{t_{max}}$, whose value is:

$$\varphi^*_{t_{max}} = \arctan\left(\frac{\sqrt{\cos^2(\delta)-\cos^2(\beta)}}{\cos(\beta)}\right) \tag{5.41}$$

For any higher or lower value of φ^*, the access time will be lower than the optimum access time. In Figure 5.18 it is shown a scheme of this behaviour.

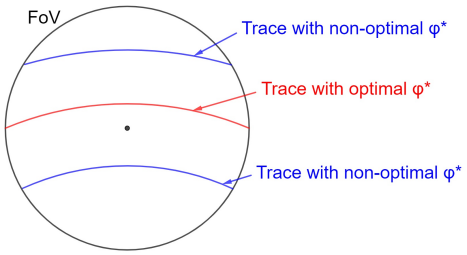


Figure 5.18: Trace of the direction vector over the FOV for different φ^* coordinates.

As mentioned before, to add the effect of precession, two cases have been considered. For the case where $\Omega << \omega$, i.e., the precession motion is much slower than the spin motion, it can be assumed that the trace of the instrument over the sky is nearly a circumference and therefore the previous results can be used directly. As the spin axis rotates around the precession axis, those points in the sky which, at any time, are at an angular distance of $\varphi^*_{t_{max}}$ will have an optimum access time. For any point with $\varphi < \alpha + \varphi^*_{t_{max}}$ and $\varphi > |\alpha - \varphi^*_{t_{max}}|$ there will be an instant in which the trace is at the right point. Therefore, its maximum access time will be the optimum access time.

For those directions whose φ coordinate is out of the aforementioned range, the maximum access time will not be the optimum. However, Eq. (5.39) is still valid

assuming that $\varphi^* = \alpha - \varphi \cdot \text{sgn}(\alpha - \varphi^*_{t_{max}})$ for $\varphi < |\alpha - \varphi^*_{t_{max}}|$ and $\varphi^* = \varphi - \alpha$ for $\varphi > \alpha + \varphi^*_{t_{max}}$. Taking all of this into account, according to the value of φ, its maximum access time is

for $0 < \varphi < |\alpha - \varphi^*_{t_{max}}|$:

$$t_1 = \frac{T_{spin}}{\pi} \text{Re}\left(\arccos\left(\frac{\cos(\delta) - \cos(\beta)\cos(\alpha - \varphi \cdot \text{sgn}(\varphi^*_{t_{max}}))}{\sin(\beta)\sin(\alpha - \varphi \cdot \text{sgn}(\varphi^*_{t_{max}}))}\right)\right) \tag{5.42}$$

for $|\alpha - \varphi^*_{t_{max}}| < \varphi < \alpha + \varphi^*_{t_{max}}$:

$$t_2 = t_{max} = \frac{T_{spin}}{\pi} \text{Re}\left(\arccos\left(\frac{\sqrt{\cos^2(\delta) - \cos^2(\beta)}}{\sin(\beta)}\right)\right) \tag{5.43}$$

for $\alpha + \varphi^*_{t_{max}} < \varphi < \pi$:

$$t_3 = \frac{T_{spin}}{\pi} \text{Re}\left(\arccos\left(\frac{\cos(\delta) - \cos(\beta)\cos(\varphi - \alpha)}{\sin(\beta)\sin(\varphi - \alpha)}\right)\right) \tag{5.44}$$

An example of the maximum access time profile in the case of negligible Ω is shown in Figure 5.19. The three regions can be clearly identified. For the central region, the maximum access time is the highest and is constant.

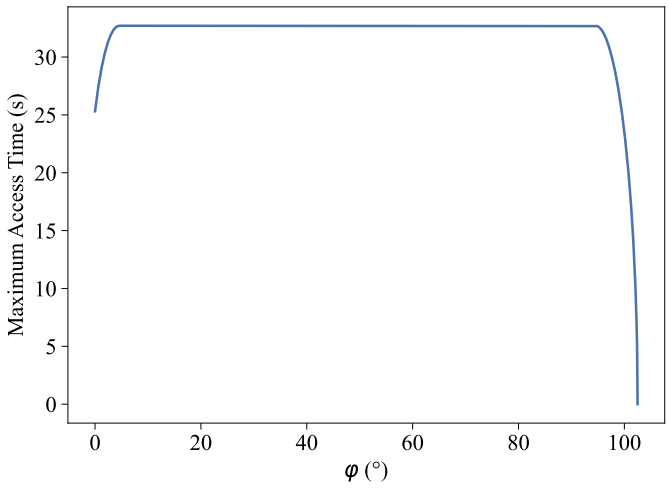
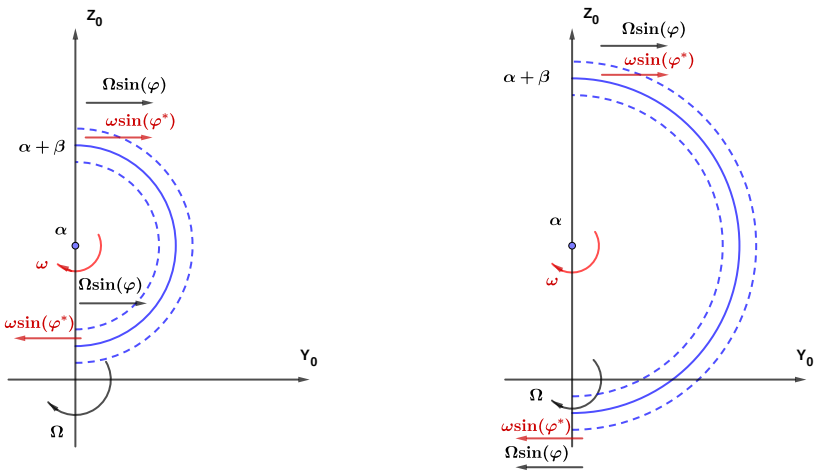


Figure 5.19: Variation of the maximum access time as a function of coordinate φ for Ω negligible. Parameters considered: $T_{sim} = 1$ day, $\alpha = 45°$, $\beta = 50°$, $T_{spin} = 10$ min, and $\delta = 7.5°$.

For the case of a significant precession speed, no analytical solution has been found. However, its effect can be approximated by modifying the maximum access times from Eqs. (5.42), (5.43) and (5.44).

First, let's analyze the points that do not reach $\varphi^*_{t_{max}}$ and therefore, t_{max}. These points have their own optimum access time when they reach the minimum angular

distance from the spin axis. If the precession motion is taken as a rotation of the sky instead of the instrument, it can be assumed that the access time will increase or decrease, according to whether such rotation has the opposite or the same direction as the spin rotation. A scheme explaining this behavior is shown in Figure 5.20. When $\alpha > \beta$, as the speed grows the maximum access time decreases for large values of φ and increases for small values of φ. In the other case, $\alpha < \beta$, the maximum access time will be smaller for any value of φ, as the speed with which the direction travels across the FOV is always increased by the precession motion.



(a) $\alpha > \beta$. (b) $\alpha < \beta$.

Figure 5.20: Scheme of how the precession speed Ω (black) would be added or subtracted to spin speed ω (red) according to whether $\alpha > \beta$ or $\alpha < \beta$.

Therefore, it is possible to approximate how the maximum access time changes introducing a scaling factor for t_1 and t_3 as follows:

for $0 < \varphi < |\alpha - \varphi^*_{t_{max}}|$:

$$t_1^* = t_1 \frac{\omega \sin(\alpha - \varphi k)}{\omega \sin(\alpha - \varphi k) - \Omega \sin(\varphi k)} \tag{5.45}$$

for $\alpha + \varphi^*_{t_{max}} < \varphi < \pi$:

$$t_3^* = t_3 \frac{\omega \sin(\varphi - \alpha)}{\omega \sin(\varphi - \alpha) + \Omega \sin(\varphi)} \tag{5.46}$$

with $k = \text{sgn}(\alpha - \beta)$. The smaller the values of δ and Ω are, the more accurate these approximations will be.

For t_2, the proposed approach is as follows. Taking into account that the instrument sweep speed is produced both by spin and precession, assuming that δ is small and the precession motion slow, it is reasonable to expect that the component of the

precession motion parallel to the spin speed component will be the more significant one in changing the access time. Thus, t_2 can be scaled similarly to t_1 and t_3 but this time with the component of precession speed parallel to spin speed:

for $|\alpha - \varphi^*_{t_{max}}| < \varphi < \alpha + \varphi^*_{t_{max}}$:

$$t_2^* = t_2 \frac{\omega \sin(\varphi^*_{t_{max}})}{\omega \sin(\varphi^*_{t_{max}}) + \Omega \sin(\varphi)\gamma} \tag{5.47}$$

where γ is the projection of the precession velocity unitary vector (Figure 5.21), $\boldsymbol{v}_{prec}$, over the spin velocity unitary vector, $\boldsymbol{v}_{spin}$. To obtain this value, first the vector $\boldsymbol{v}_{spin}$ is calculated, tangent to the spin velocity. In order to do that, Eq. (5.14) is derived with regard to ϕ:

$$\frac{d\boldsymbol{q}}{d\phi} = \begin{pmatrix} \sin(\alpha)\sin(\beta)\sin(\phi) \\ \sin(\beta)\cos(\phi) \\ -\cos(\alpha)\sin(\beta)\sin(\phi) \end{pmatrix} \tag{5.48}$$

and then normalized

$$\boldsymbol{v}_{spin} = \frac{d\boldsymbol{q}/d\phi}{|d\boldsymbol{q}/d\phi|} = \begin{pmatrix} \sin(\alpha)\sin(\phi) \\ \cos(\phi) \\ -\cos(\alpha)\sin(\phi) \end{pmatrix} \tag{5.49}$$

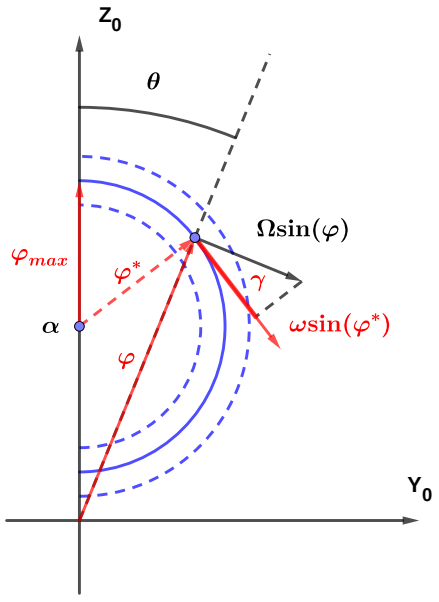


Figure 5.21: Definition of γ, projecting the precession velocity vector over the spin velocity vector.

The vector tangent to the precession velocity, $\boldsymbol{v}_{prec}$, can be easily expressed as a

function of the τ angle, which is defined in Figure 5.22:

$$\boldsymbol{v}_{prec} = \begin{pmatrix} \cos(\tau) \\ 0 \\ -\sin(\tau) \end{pmatrix} \tag{5.50}$$

The relation between both angles is:

$$\tau = \arctan\left(\frac{\sin(\varphi^*_{t_{max}})\sin(\phi)}{\cos(\alpha)\sin(\varphi^*_{t_{max}})\cos(\phi) + \sin(\alpha)\cos(\varphi^*_{t_{max}})}\right) \tag{5.51}$$

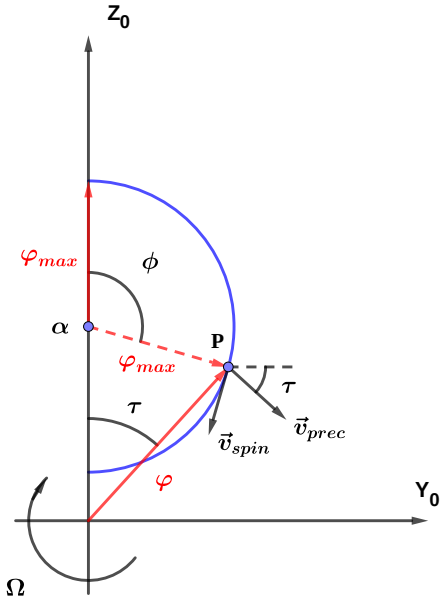


Figure 5.22: Geometrical scheme of the approach followed to obtain γ.

Then, projecting $\boldsymbol{v}_{prec}$ over $\boldsymbol{v}_{spin}$, γ is obtained:

$$\gamma = \cos(\phi)\cos(\tau) + \cos(\alpha)\sin(\phi)\sin(\tau) \tag{5.52}$$

where ϕ can be expressed as a function of φ, $\varphi^*_{t_{max}}$, and α, as follows:

$$\phi = \arccos\left(\frac{\cos(\alpha)\cos(\varphi^*_{t_{max}}) - \cos(\varphi)}{\sin(\alpha)\sin(\varphi^*_{t_{max}})}\right) \tag{5.53}$$

In Figure 5.23 an example of the resulting profile obtained from Eqs. (5.45), (5.46) and (5.47) is shown.

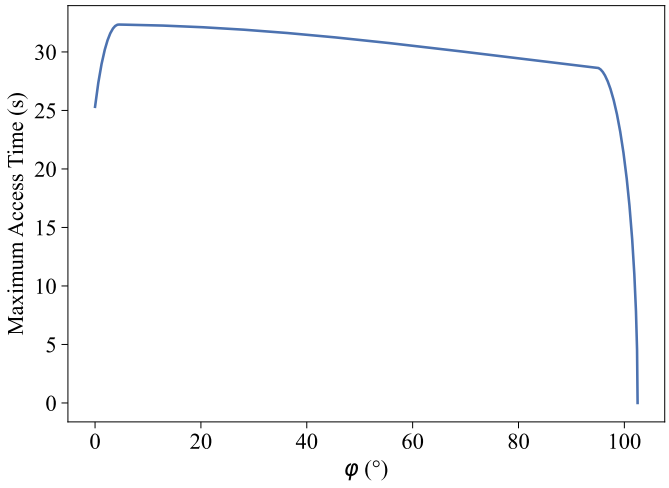


Figure 5.23: Variation of the maximum access time as a function of coordinate φ for a non-negligible Ω. Parameters considered: $T_{sim} = 1$ day, $\alpha = 45°$, $\beta = 50°$, $T_{spin} = 10$ min, $T_{prec} = 93$ min, and $\delta = 7.5°$.

Numerical results for the maximum access time

The numerical results for maximum access time for the same example given in Figure 5.23 are presented in Figure 5.24. As can be seen, this last parameter also presents axial-symmetry.

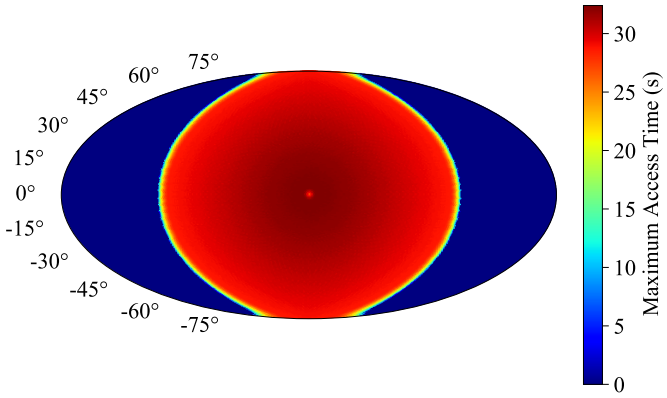
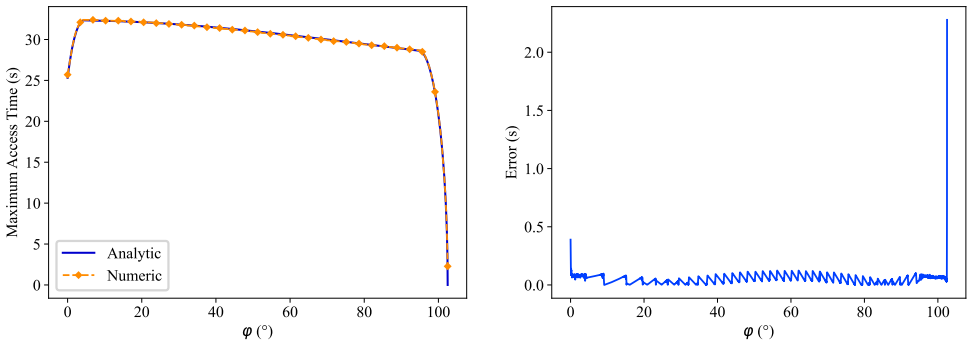


Figure 5.24: Maximum access time. Parameters considered: $T_{sim} = 1$ day, $\alpha = 45°$, $\beta = 50°$, $T_{spin} = 10$ min, and $\delta = 7.5°$.

The analytical and numerical results for maximum access time are compared in Figure 5.25. The numerical results have been averaged over θ. The same RMSE criterion as with T_{mean} has been used and it has been fulfilled for all the scan strategies tested.



(a) Comparison. (b) Error.

Figure 5.25: Comparison (a) and error (b) between the analytical and numerical results for the maximum access time as a function of coordinate φ. Parameters considered: $T_{sim} = 1$ day, $\alpha = 45°$, $\beta = 50°$, $T_{spin} = 10$ min, and $\delta = 7.5°$.

5.3 Analysis of viewed detectors

The previous results have been obtained considering the whole instrument FOV. However, in a real instrument, the calibration signal would be received by the detectors distributed in the instrument focal plane. In the case of CMB telescopes, bolometers are used as detectors. This type of sensor measures the power of incident electromagnetic radiation and can be used in pairs to measure the polarization. In order to evaluate the performance of the calibration at detector level, it is necessary to model the instrument and how the signal arrives at the detectors. Such performance will be evaluated in terms of number of detectors reached by the calibration signal and whether they receive it at different angles.

The obtention of analytical expressions for the quantities characterizing the access time has been based on a set of assumptions that simplify the problem, allowing the analytic treatment of the equations. Conversely, the inclusion of a detector distribution model increases the complexity of the problem and thus the use of numerical methods has been preferred. Two main aspects of the detectors have been analysed: the percentage of viewed detectors (ρ), which is affected by the number, angular size and distribution of the detectors; and the angular coverage parameter ($G(\xi)$), defined in the following section, and which indicates whether the reference signal reaches the detectors with a different polarization orientation during the calibration process.

5.3.1 Detectors and signal polarization models

The instrument model consists of two elements: the instrument frame, whose attitude calculation has been already explained, and the detectors array geometry. The detectors array is a virtual representation of the instrument sensors layout. The sensors are located on the $Y_{inst}Z_{inst}$-plane of the instrument frame and modelled as a rectangular array (26x18) of equally sized circular detectors circumscribed by a circle that represents the resolution of the instrument, as depicted in Figure 5.26.

The total number of detectors is 468, with a half-angle resolution of 0.2° each one. The number of detectors is similar to that of the Low Frequency Telescope of future LiteBIRD mission [10], which has also a rectangular geometry.

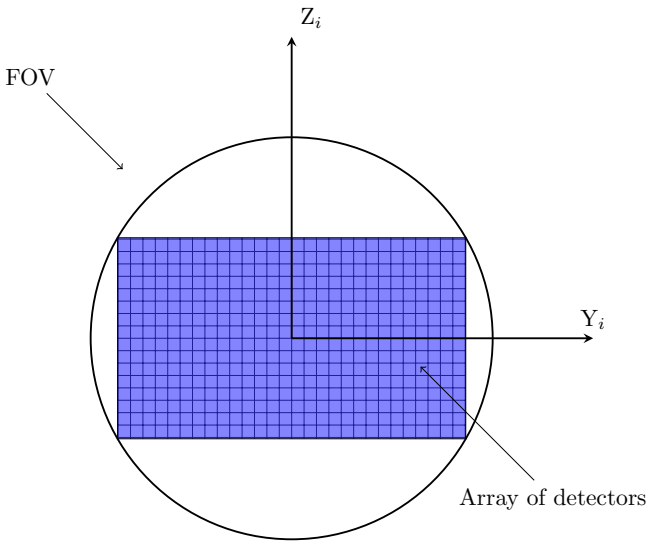


Figure 5.26: Layout of the array of detectors.

The signal source of the calibration satellite is considered to be a point source in the space and the signal is assumed to arrive at the instrument as parallel rays. The assumption of parallel rays will be valid as long as the distance between the source and the observer is larger than the Fraunhofer distance, i.e., the observer is located in the far field of the source:

$$d > \frac{2D}{\lambda} \tag{5.54}$$

where d is the distance between source and observer, D is the instrument aperture and λ the wavelength of the signal. The source of the calibration signals has a size of a few centimeters ($D \sim 10^{-2}$ m) while the frequency is between 40 GHz and 400 GHz for the case considered in this work ($\lambda \sim 1$ mm). Therefore, the minimum distance between the source and the instrument should be roughly tens of meters.

The particularities of the telescope optics are omitted and it has been considered that the signal goes through a simple focusing lens [10, 107], thus, parallel rays arriving at the lens will converge to a unique point in the instrument focal plane, which is considered to be in the $Y_{inst}Z_{inst}$-plane of the instrument frame, where the array of detectors (see Figure 5.27) is situated. Thus, each possible direction in the FOV corresponds unequivocally to a point in the circle where the array of detectors is circumscribed. This mapping is done projecting the orientation vector (equivalent to the incoming direction of the calibration signal) to the $Y_{inst}Z_{inst}$-plane.

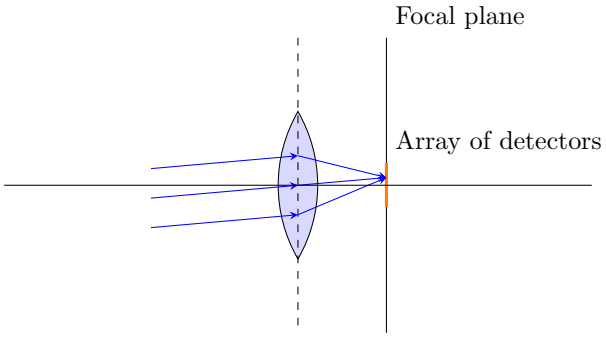


Figure 5.27: Simplified optical model considered. Each possible direction within the FOV maps one unique point in the focal plane.

The linear polarization of the signal can be defined by a vector perpendicular to the direction of propagation. In this case, the direction of propagation coincides with the LoS and the polarization of the calibration signal is chosen as an arbitrary direction perpendicular to the LoS.

During the calibration, it is expected that the reference signal reaches the detectors several times. This will benefit the calibration process, particularly if the relative orientation between the polarization signal and the detectors framework of each measurement is different [14]. In order to assess if the signal arrives with different orientation, the parameter $G(\xi)$, derived from the one used in [16] to asses the angular coverage of each point in the sky, is defined for each of the N detectors which are reached by the reference signal at least once ($k \geq 1$):

$$G_j(\xi) = \left(\frac{1}{k} \sum_{i=1}^{k} \cos(2\xi_i) \right)^2 + \left(\frac{1}{k} \sum_{i=1}^{k} \sin(2\xi_i) \right)^2 \qquad \text{for } j = 1, \ldots, N \tag{5.55}$$

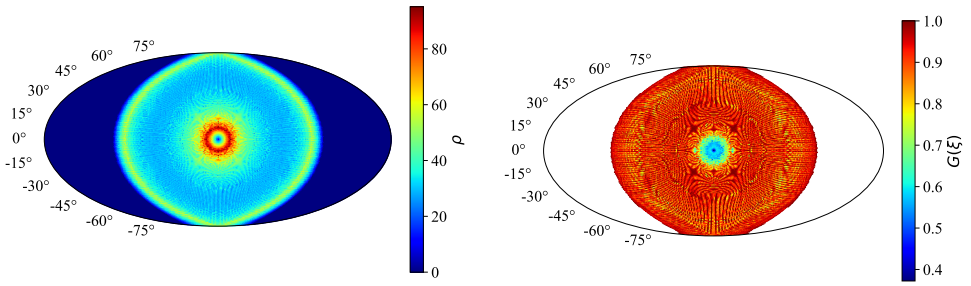
This parameter is computed for each detector using its measurements of the polarization (ξ_i), which is constant during the simulation, and then the mean value between all viewed detectors is calculated. If a detector is reached by the signal only once or several time but with similar orientation (or parallel), the $G(\xi)$ parameter will be equal or close to 1. Conversely, several measures with roughly perpendicular orientations will bring the parameter close to 0.

5.3.2 Numerical results of detectors analysis

Once the events have been detected, they are analyzed in detail. The percentage of viewed detectors (ρ) is obtained similarly to the access detection. For each access, it is checked which detectors receive the signal. These data can be further processed to obtain how many times the detectors are illuminated and for how long. The followed approach assumes that only one detector is illuminated simultaneously.

Additionally, the polarization of the arriving signal is computed and stored. After considering all of the time period, the parameter $G(\xi)$ is computed. This process is done for all the directions obtained in the discretization. In Figure 5.28 the

results for $T_{sim} = 1$ day are shown. As in the accesses analysis, both results present axial-symmetry. It can be observed that for relative angles between 10° and 15° degrees the majority of the detectors (around 80%) are reached and with different polarization orientation ($G(\xi)$ around 0.5). These results will be discussed in more detail in section 5.4.



(a) ρ parameter.

(b) $G(\xi)$ parameter.

Figure 5.28: Numerical results for the percentage of viewed detectors and the $G(\xi)$ parameter. Parameters considered: $T_{sim} = 1$ day, $\alpha = 45°$, $\beta = 50°$, $T_{spin} = 10$ min, $T_{prec} = 93$ min, and $\delta = 7.5°$.

5.4 Application example

In this section, the above methodology is applied to an example mission, showing how it can be used to select the best location to place a calibration satellite or to vary the scan strategy in order to obtain a better calibration performance.

The baseline scan strategy has been chosen to be similar to those employed in previous and future CMB missions [9, 10, 15, 100, 101]: $\alpha = 45°$, $\beta = 50°$, $T_{spin} = 10$ min, $T_{prec} = 93$ min, and $\delta = 7.5°$. The detectors geometrical configuration used is the same as in section 5.3.1. Unless otherwise stated, these results correspond to a simulation period of 1 day. This condition has been selected considering that the calibration process should not last longer to limit interference in the chief's observations.

As shown in Eq. (5.21), the total access time is proportional to the period of time considered (T_{sim}). The total access time will be a fraction of the period that is defined by Eq. (5.20). This will be the fraction of time available for calibration and it is presented in Figure 5.8. The percentage of total access time has significantly higher values in the region near the precession axis, where it reaches roughly 4% and then descends steeply, remaining around 0.5% until it reaches the border, when it increases to 1% before becoming zero. This behaviour is due to the trace geometry. As is shown in Figure 5.2, in the region around the precession axis and the border, the trace overlaps more than in the intermediate regions. This translates into accesses happening more frequently.

This dependency on the trace geometry is shown in Eq. (5.20), where only the scan strategy parameters α and β are present. The instrument FOV half-angle (δ) is also present, as it will affect the length of the accesses. However, it has been assumed as fixed. None of the attitude motion periods are present as their

variations will cause no effect on the total access time. To show the effect of varying α and β, a parametric sweep has been carried out, with the constraint $\alpha + \beta = 95°$. Such constraint is established so that the whole sky is observed, ensuring that the instrument never points at the Sun.

As shown in Figure 5.29, the maximum value is always near $\varphi = |\alpha - \beta|$, reaching its highest value when $\alpha = \beta$, which means that the trace crosses exactly the precession axis in each spin cycle. As α decreases, so does the maximum value until a region with no access time emerges around the precession axis. The effect of decreasing β is symmetrical. That means, from the total access time point of view, a solution with $\alpha = X$ and $\beta = 95° - X$ is equal to a solution with $\beta = X$ and $\alpha = 95° - X$.

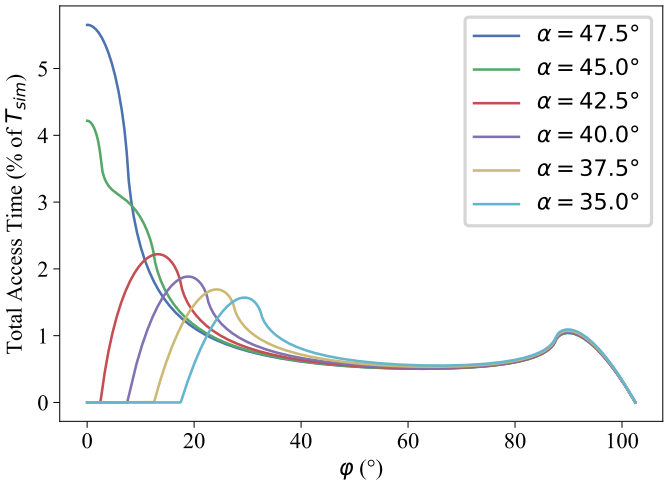


Figure 5.29: Variation of the total access time as a function of coordinate φ for different values of α parameter. In all cases $\alpha+\beta = 95°$. Parameters considered: $T_{sim} = 1$ day, $T_{spin} = 10$ min, $T_{prec} = 93$ min and $\delta = 7.5°$.

In Figure 5.30 the mean access time and the maximum access time are compared. Neither of the two quantities depends on the period of time considered and they are rather uniform along φ coordinate. This can be seen from the mean access time in Equation (5.28), where T_{sim} disappears when dividing T_{total} by $N(\varphi)$. For the maximum access time, T_{sim} is not even considered in the approach followed to obtain its analytical expression. It should be noted that although these parameters do not depend on T_{sim}, it has been assumed that T_{sim} is large enough to achieve axial-symmetry in the results.

The period of spin motion will have a direct effect on both parameters since, as shown in Eqs. (5.28), (5.42), (5.43) and (5.44), they scale proportionally to it, as shown in Figure 5.31. In comparison, the precession period has little effect, being responsible for the slight negative slope as φ increases. As T_{prec} grows, this slope becomes steeper (Figure 5.32).

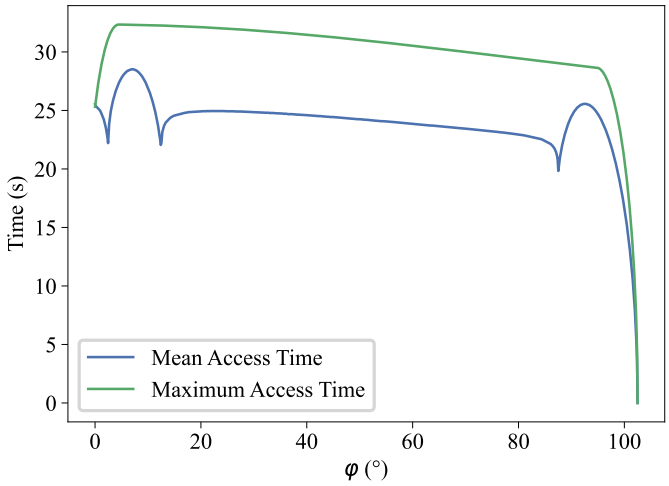
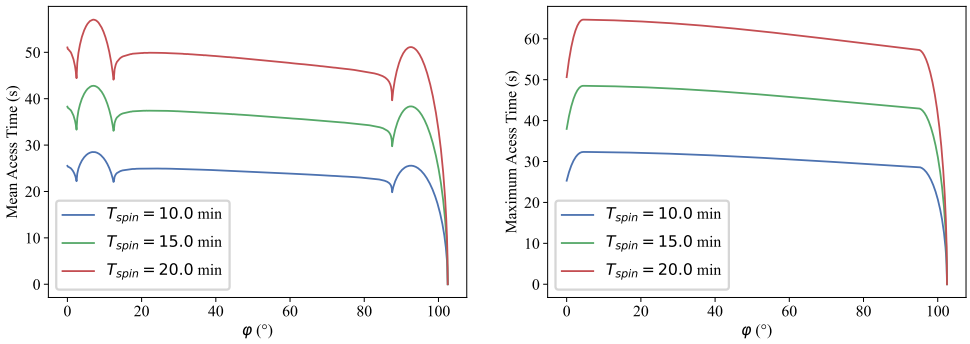


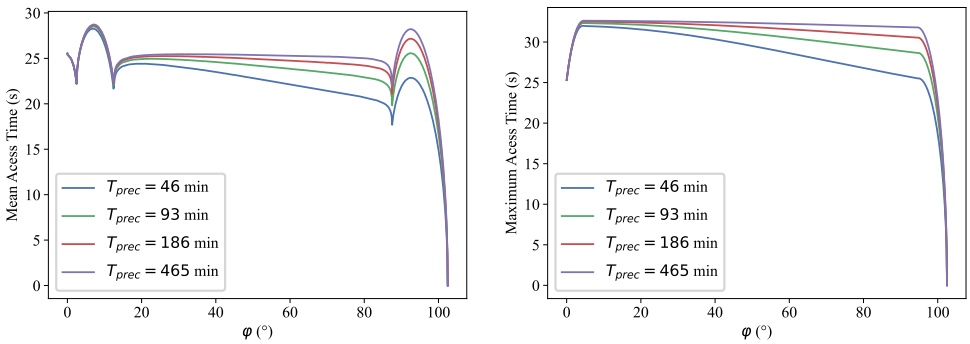
Figure 5.30: Comparison between the variation of T_{mean} and the variation of T_{max} as functions of coordinate φ.



(a) Mean access time.

(b) Maximum access time.

Figure 5.31: Variation of T_{mean} and T_{max} as functions of coordinate φ for different values of the T_{spin} parameter.

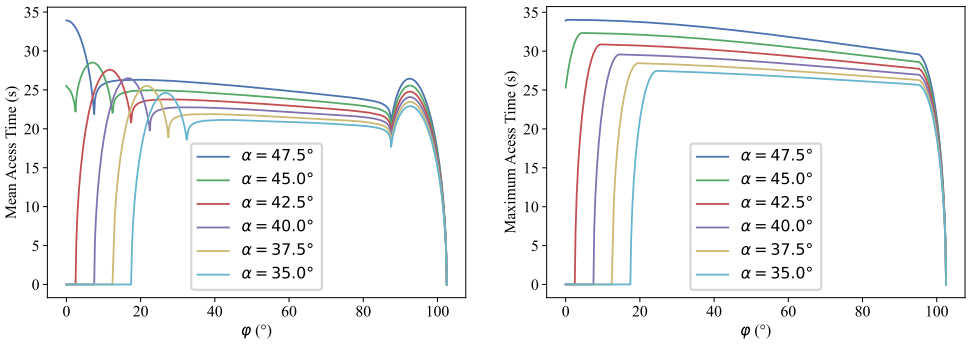


(a) Mean access time.

(b) Maximum access time.

Figure 5.32: Variation of T_{mean} and T_{max} as functions of coordinate φ for different values of the T_{prec} parameter.

As for the effect of varying α and β, the outcome is similar to that experienced by the total access time. Decreasing α reduces the value of the parameters in general and the no-access-zone emerges in the precession axis. This effect is shown in Figure 5.33.



(a) Mean access time.

(b) Maximum access time.

Figure 5.33: Variation of T_{mean} and T_{max} as functions of coordinate φ for different values of α.

The results for ρ and $G(\xi)$ are shown in Figure 5.34. The percentage of viewed detectors presents two maximums, the higher being close to the precession axis and the lower near the border. The $G(\xi)$ parameter has a different behaviour. Its lower point is in the precession axis, from where it raises steeply, staying close to 1. Although the most suitable regions of both parameters are close to the precession axis, they have very different behaviours since the maximum of ρ occurs during the steep change of $G(\xi)$ where a slight variation of φ has a significant effect on this parameter.

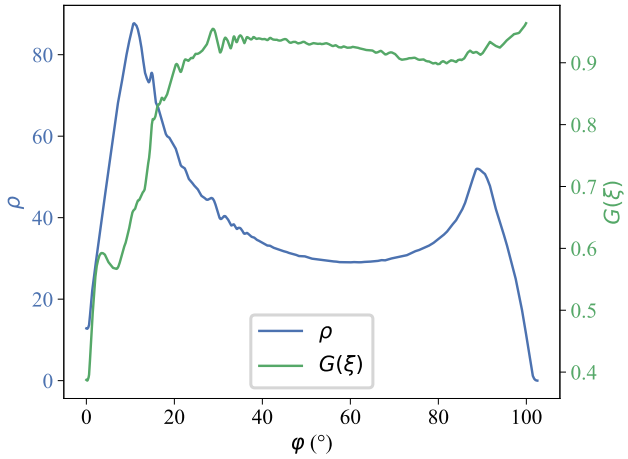
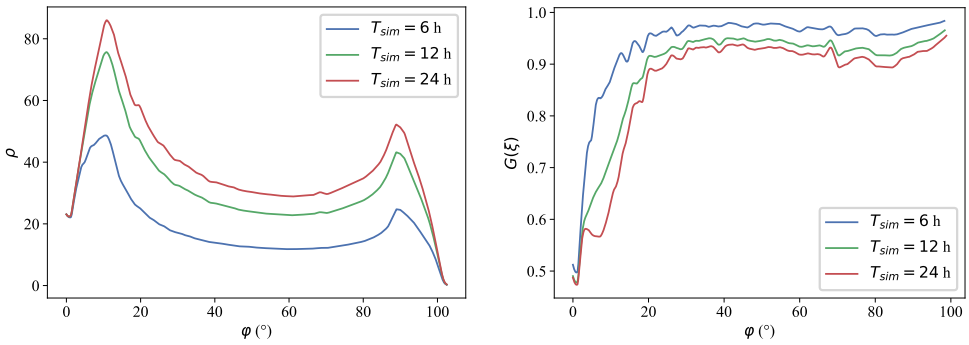


Figure 5.34: Comparison between the variation of ρ and the variation of $G(\xi)$ as functions of coordinate φ.

Both parameters are mainly and similarly affected by T_{sim} and T_{comb}. As shown in Figure 5.35(a), when T_{sim} increases, the percentage of viewed detectors grows for

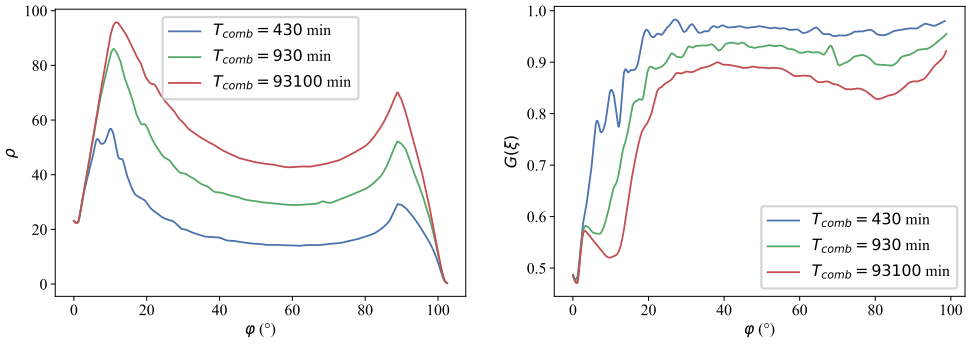
all values except for $\varphi = 0°$, where it remains constant. In this particular position, the trace of the deputy over the instrument is repeated in each access, so the same detectors are viewed each time, causing ρ to stay constant independently of T_{sim}. The same happens with $G(\xi)$ (Figure 5.35(b)), increasing T_{sim} improves its value for all of the interval.



(a) ρ parameter. (b) $G(\xi)$ parameter.

Figure 5.35: Variation of ρ and $G(\xi)$ as functions of coordinate φ for different values of T_{sim}.

The spin and precession periods influence ρ and $G(\xi)$ through how they change T_{comb}. Slight variations in T_{prec} and T_{spin} change radically T_{comb}, which have a significant impact on ρ and $G(\xi)$. This behaviour is shown in Figure 5.36. A variation of roughly 3 minutes in the precession period while keeping T_{spin} fixed causes very different results on both parameters. The higher the value of T_{comb}, the better coverage of all detectors.

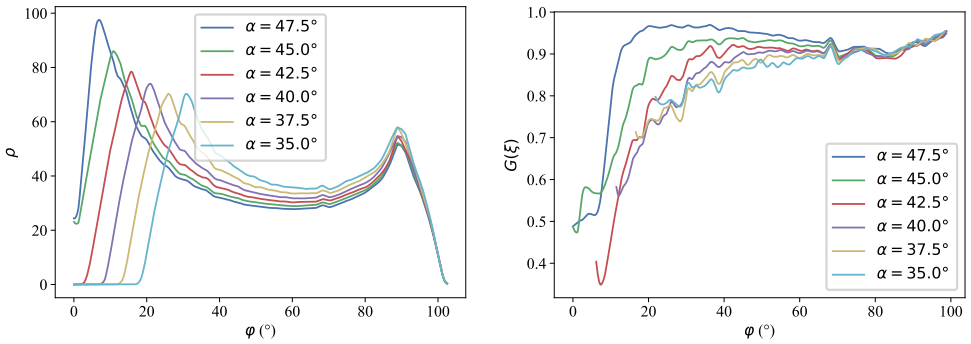


(a) ρ parameter. (b) $G(\xi)$ parameter.

Figure 5.36: Variation of ρ and $G(\xi)$ as functions of coordinate φ for different values of T_{comb}, which are achieved keeping T_{spin} constant and using a T_{prec} of 90 min, 93 min and 93.1 min for T_{comb} cases of 430 min, 930 min and 93100 min, respectively.

Lastly, the variation of α and β also impact ρ and $G(\xi)$ (see Figure 5.37). In the no-access-zone near the precession axis for a low α, the value of ρ drops to zero and $G(\xi)$ is not defined. As for T_{total}, the point of maximum percentage of viewed

detectors is displaced and its value reduced although the value is increased in general. An additional zone with $\rho = 0$ appears at the border. This occurs because for those conditions, the deputy crosses the instrument FOV in the lateral gaps that lie between the detectors array and the FOV border (Figure 5.26). This behaviour is also experienced by $G(\xi)$ although in this case it is reduced in general when α decreases while its minimum value increases.



(a) ρ parameter.

(b) $G(\xi)$ parameter.

Figure 5.37: Variation of ρ and $G(\xi)$ as functions of coordinate φ for different values of α.

5.4.1 Discussion of results

The results calculated above can be used to propose suitable locations for a calibration satellite and to evaluate its performance. Results show that a suitable location of the deputy should provide enough time to calibrate the detectors of the instrument, and that this available time is enough to perform a successful calibration, i.e., reaching a high enough number of detectors and doing so with different relative polarization orientations. This translates into having large values in all the parameters except $G(\xi)$, for which the ideal value is 0.

For the baseline scan strategy studied, the results indicate that the region near the precession axis presents the most advantageous characteristics. This is more noticeable in the case of T_{total}, ρ, and $G(\xi)$ as they experience significant variations along φ. Although T_{mean} and T_{max} remain in a narrower range of values, they also present higher values in this region.

While all the parameters present adequate values near the precession axis, there is not an optimal point where the best value of each parameter is achieved simultaneously. Moreover, a trade-off analysis should be performed according to the characteristics of the calibration process, which will indicate which parameter is more valuable.

The effect of the variation of α and β in the region is mainly the displacement of the parameters curves, with slight variations along φ. This is caused by the trace geometry. The high concentration of the trace lines when it reaches its minimum distance with the precision axis causes the peak values in the parameters. Such lines get as close as $|\alpha - \beta|$ and as this value grows, the region of maximum values is displaced to higher φ.

In comparison, other parameters have a much significant impact. The most important factor for T_{mean} and T_{max} is the value of T_{spin} as they grow proportionally to it. Although not calculated here, the time that a detector receives the signal will also be proportional to T_{spin}. Conversely, it is the T_{comb} of the two motions which mainly drives $G(\xi)$ and ρ. A high value will ensure an elevated percentage of viewed detectors and a region of low $G(\xi)$. It is clear that the higher that T_{sim} is, i.e., the longer the calibration process lasts, better values of T_{total}, $G(\xi)$ and ρ will be achieved, while T_{mean} and T_{max} will not be affected.

Although $G(\xi)$ and ρ results depend on the detectors layout, they will be similar for other layouts as long as the number of detectors is roughly the same and they cover the FOV with axial-symmetry. This condition will keep the effective area of the FOV similar and centered, which will produce analogous results as the trace of the deputy over the FOV is independent of the detectors layout.

CHAPTER 6

Mission proposal of an ancillary calibration satellite for a CMB satellite located at L_2

In this chapter, the concept of an ancillary calibration satellite for a CMB satellite in L_2 is presented and its feasibility is assessed. First, the mission is defined and its objectives and requirements are outlined. Then, the mission is described in detail, including its modes of operation and the nominal orbit. Subsequently, the environmental conditions in L_2 are briefly described and the results of the formation visibility study are presented, followed by the preliminary design of the satellite bus and the required support system for its deployment and operation. Finally, a summary of the mission budgets is provided and the collision risk of the formation is assessed. The mission has been studied under the principle of reducing the impact on the CMB satellite architecture at a minimum.

6.1 Mission concept, objectives, and requirements

For the mission study, the CMB satellite acts as the main satellite and is assumed to orbit around the Sun-Earth L_2 libration point. The ancillary calibration satellite, labeled as CalSat (CS), would be attached to the CMB satellite as a piggyback and deployed directly in the target orbit in L_2, where it would keep the chief-deputy formation acting as deputy itself and the CMB satellite as chief. After CalSat has been detached, part of the piggyback, labeled as CS Support System, stays attached to the CMB satellite, acting as a communications hub between CalSat and the CMB satellite. This support system is mainly composed of an electronic box labeled as BaseCalSat (BCS) and a CubeSat deployer.

Once CalSat has been deployed, the CMB satellite carries out its scientific mission routinely while CalSat stands by in the surroundings, out of sight from the CMB satellite instrument. Periodically, the CMB satellite requires calibration and sends the signal through BaseCalSat to CalSat, which relocates itself so that it can be adequately observed by the CMB satellite instrument. Once calibration has taken place, CalSat returns to its stand-by position until a new calibration is required. The mission is expected to last three years.

The goal of the calibration is to improve the accuracy of the main satellite measurements from the CMB polarization angle and the detectors beam response, meeting the accuracy requirements for the next generation of CMB experiments. Thus, CalSat will carry a perfectly known source capable of emitting a reference signal to reduce the uncertainty of the CMB polarization measurements.

6.1.1 Objectives

The objectives of the mission are derived from the mission description. The primary mission objective is:

- To perform a calibration in the radio frequency (RF) band of the main instrument of the CMB satellite.

The secondary mission objective is the following:

- To demonstrate the feasibility of the proposed mission concept and validate the critical technologies required for formation flying in the libration points.

6.1.2 Requirements

After defining the broad objectives that the space mission is to achieve, these objectives must be transformed into preliminary sets of numerical requirements. These requirements define the overall functionality, performance, and constraints of the mission and serve as a foundation for its design, ensuring that it will meet the desired objectives. Note that in practice, requirements represent a balance between what is aimed to achieve and what is feasible within the constraints of the system [2], so part of this work has been focused on defining and refining the mission concept and its requirements in order to meet the main objective at minimum cost and risk.

Requirement ID

This code uniquely identifies each requirement. The format of the requirement ID is [XXX]-[YY]-[ZZZ], where:

[XXX] System/subsystem requirement: main system/subsystem involved in the requirement, according to the following list:

- **ADC** - Attitude determination and control system
- **EPS** - Electric power system
- **COM** - Communication system

- **GNC** - Guidance, navigation and control system
- **OBD** - On-board data handling system
- **PRO** - Propulsion system
- **STR** - Structure
- **SYS** - System
- **TCS** - Thermal control system

[YY] Requirement nature:

- **FU** - Functional requirement
- **PE** - Performance requirement
- **DE** - Design requirement
- **OP** - Operational requirement

[ZZZ] Unique requirement Identification Number.

System-level requirements

The system-level requirements are listed in Table 6.1.

Table 6.1: System-level requirements for the CalSat mission.

ID	Requirement
SYS-FU-010	CalSat shall enable the calibration of the frequency band 40 to 400 GHz.
SYS-DE-020	CalSat shall be deployed from the CMB satellite directly in the target orbit at L_2.
SYS-DE-030	CalSat shall have a mass of less than 12 kg.
SYS-DE-040	CalSat and BaseCalSat shall withstand the radiation environment at the libration point by incorporating radiation-hardened components and shielding.
SYS-OP-050	CalSat shall provide the capability to calibrate the CMB satellite at least twice per year.
SYS-OP-060	The mission shall have a minimum duration of 3 years from the deployment.
SYS-OP-070	CalSat and BaseCalSat shall not cause any disturbances or interference to the CMB satellite during the processes of deployment or stand-by.

Attitude determination and control system

The requirements related to the attitude determination and control system (ADCS) are listed in Table 6.2.

Table 6.2: Attitude determination and control system requirements.

ID	Requirement
ADC-FU-010	CalSat shall be capable of providing 3-axis control.
ADC-FU-020	CalSat shall be capable of dumping the accumulated moment in the reaction wheels.
ADC-PE-030	CalSat shall be capable of controlling its orientation within an error of less than $3'$.
ADC-PE-040	CalSat shall be capable of determining its orientation with an error of less than $1'$.

Communication system

The requirements related to the communications system are listed in Table 6.3.

Table 6.3: Communications system requirements.

ID	Requirement
COM-FU-010	BaseCalSat shall be capable of communicating with CalSat to exchange telemetry.
COM-FU-020	BaseCalSat shall have a communication link with the CMB satellite.

Electrical power system

The requirements related to the electrical power system (EPS) are listed in Table 6.4.

Table 6.4: Electrical power system requirements.

ID	Requirement
EPS-FU-010	The BaseCalSat EPS shall be self-sufficient and capable of providing energy independently from the CMB satellite.
EPS-PE-020	The CalSat EPS shall be capable of providing sufficient energy to meet the peak consumption of the payload (50 W).
EPS-PE-030	The BaseCalSat EPS shall have the capacity to provide sufficient energy for 12 h of calibration, taking into account the actual payload duty cycle.

Guidance navigation and control system

The requirements of the guidance, navigation and control (GNC) system are listed in Table 6.5.

Table 6.5: Guidance navigation and control system requirements.

ID	Requirement
GNC-FU-010	CalSat shall be capable of determining its relative position (direction and distance) regarding the CMB satellite.
GNC-FU-020	CalSat shall be capable of relocating between the calibration position and the stand-by position.
GNC-OP-030	CalSat shall be capable of maintaining the formation for the mission lifetime.
GNC-OP-040	The distance between CalSat and the CMB satellite shall be within the range of 4620 to 8580 m (±30 % margin of the calibration distance).
GNC-PE-050	CalSat shall be capable of maintaining a distance of 6600 m within an error margin of 66 m (±1 %) during calibration.
GNC-PE-060	The relative position sensors of CalSat shall locate the direction of the CMB satellite with an error less than 10′.
GNC-PE-070	The relative position sensors of CalSat shall locate the distance to the CMB satellite with an error of less than 0.5 %.

On-board data handling system

The requirements related to the On-board data handling system (OBDH) are listed in Table 6.6.

Table 6.6: On-board data handling system requirements.

ID	Requirement
OBD-DE-010	CalSat shall store the history of relative position and attitude, including the corresponding timestamps.

Propulsion system

The requirements of the propulsion system are listed in Table 6.7.

Table 6.7: Propulsion system requirements.

ID	Requirement
PRO-FU-010	The propulsion subsystem shall enable formation control maneuvers.
PRO-DE-020	The propulsion subsystem shall provide three-axis control.

Structure

The requirements related to the structure are listed in Table 6.8.

Table 6.8: Structure requirements.

ID	Requirement
STR-DE-010	The CalSat structure must be compliant with the CubeSat Standard 6U.
STR-DE-020	The BaseCalSat structure must be compliant with the CubeSat Standard 2U.

Thermal control system

The requirements of the thermal control system are listed in Table 6.9.

Table 6.9: Thermal control system requirements.

ID	Requirement
TCS-FU-010	The system shall maintain the payload thermally stable within a range of 0 to 50 °C during calibration.
TCS-DE-020	The thermal flux from CalSat to the detectors of the CMB satellite instrument during calibration shall be inferior to their saturation threshold and stable (less than 5 % variation).

6.2 Mission description

As it has been previously explained, the proposed calibration satellite or CalSat (see Figure 6.1) would travel as a piggyback of the CMB satellite, to be deployed once in the target orbit around the L_2 libration point of the Sun-Earth system.

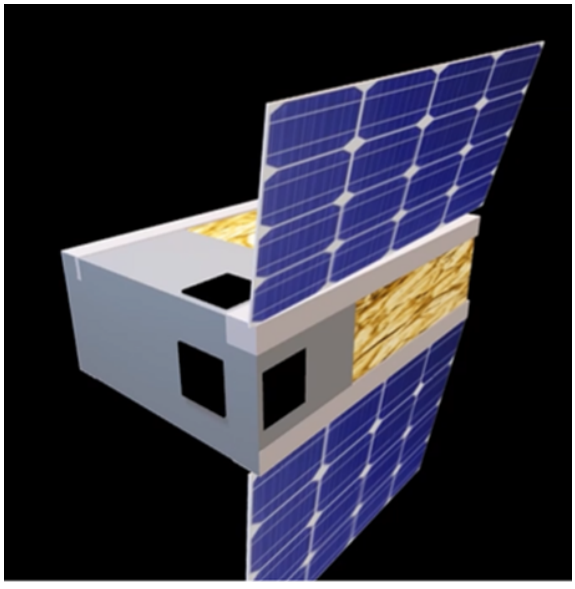


Figure 6.1: View of CalSat with its solar panels deployed.

Once deployed, CS must have some communication capacity with the CMB satellite. Furthermore, it is required that the CMB satellite carries RF antennas to enable the relative positioning system of the CS. These two functionalities are provided by the hardware that remains behind, attached to the CMB satellite, after the CS deployment. This hardware is here referred to as the CS Support System (see Figure 6.2) and comprises the CS deployer, an electronic box (BaseCalSat), and an auxiliary platform for interfacing with the CMB satellite (APC). A summary of the main elements that take part of this calibration system for the CMB mission and their overall size are listed in Table 6.10.

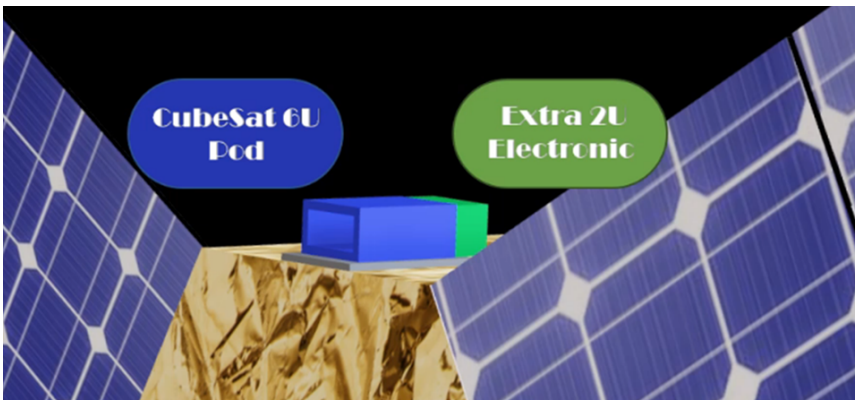


Figure 6.2: APC (grey platform), BaseCalSat (green box) and CalSat deployer (blue box) attached to the CMB satellite.

Table 6.10: Components of the calibration system for the CMB mission.

Element		Description	Dimensions
CalSat		6U CubeSat	$10 \times 20 \times 30$ cm
CS Support System	APC	Auxiliary platform interfacing with the CMB satellite	$10 \times 20 \times 40$ cm
	BCS	2U CubeSat	$10 \times 10 \times 20$ cm
	CS Deployer	6U CubeSat deployer	$10 \times 20 \times 30$ cm

After separation, the CS Support System will be the communication link with CalSat. This communication link is necessary for all CalSat operations. On the one hand, the GNC system of CalSat will need to know the absolute position of the CMB satellite in order to position itself relative to it. On the other hand, it will be necessary to download the position and orientation of CalSat during the calibration process. Although called “calibration process”, the CalSat activity during the mission does not produce an immediate calibration. Error mitigation is done during data analysis back on Earth, after downloading the CMB satellite observation data. Thus, the attitude and position of CalSat during the calibration

process must be sent back to Earth. Furthermore, the communication link will enable the synchronization (start and end) of the calibration tasks. Besides the communication link functionality, the antennas located in the CS Support System will be used for the relative positioning system of CalSat, based on RF signals.

According to requirements, the calibration satellite shall maintain a distance of 6600 ± 66 m during operation. This distance has been established in order to avoid saturation of the CMB mission detectors due to its thermal emission, while being in the far-field of the telescope at the highest frequencies (400 GHz).

In-flight calibration must be performed periodically. During this phase, CalSat has to be relocated and controlled with precision, and a communication link with the CMB satellite has to be maintained. The CMB satellite, which rotates continuously in order to scan the sky, will eventually point to CalSat and will receive the calibration signals. The number, duration, and characteristics of these calibration operations have been analyzed in section 6.4 using the method presented in chapter 5 and the most convenient strategy for the calibration has been chosen.

Three mission phases are considered and constitute the timeline of the mission and its operations. A diagram of the relative locations of the satellites in each phase is shown in Figure 6.3. The main of them is the Formation Flying Phase (FFP), which is active once CalSat is in the vicinity of the CMB satellite, after its deployment from the service platform. As it has been previously noted, the calibration satellite is expected to be equipped with RF ranging sensors, allowing the reconnaissance of the main spacecraft, and also the accurate determination of the relative position between both satellites. In this FFP, three sub-phases are defined. The first of them is the Stand-by orbit (FFP-SBO). During the periods between calibrations, CalSat will be in a waiting orbit, out of the field of view of the CMB satellite. In this phase, the relative position of the satellites will be maintained with loose accuracy. The range of variation of the relative distance will be defined in order to minimize the need of propellant, while ensuring safety of both spacecrafts and a quick transition to the second sub-phase, the Calibration phase (FFP-CAL).

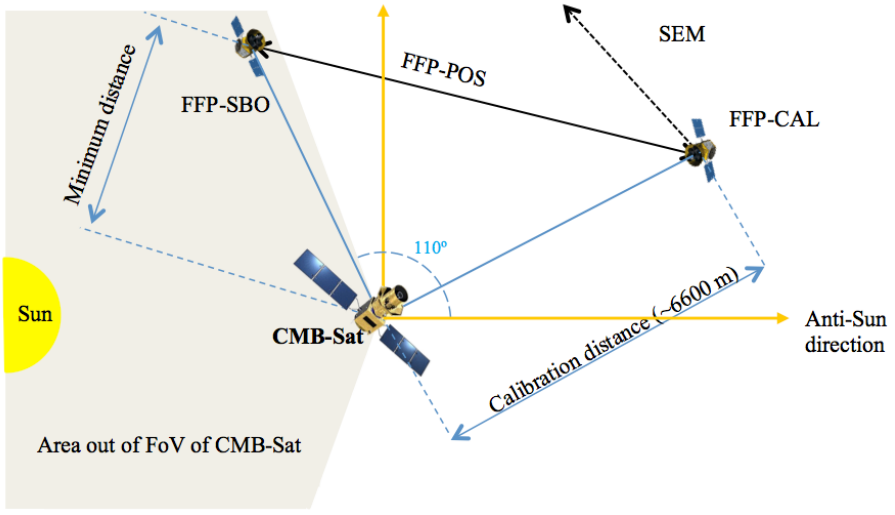


Figure 6.3: Diagram of the relative locations between the CMB satellite and CalSat during the different phases of the mission.

In this second sub-phase, CalSat is accurately placed with respect to a previously defined reference position of the CMB satellite and maintained in a relative position and orientation, enabling CalSat to periodically enter in the FOV of the CMB satellite. These periods are used to calibrate the CMB satellite instrumentation. The CalSat will ensure a proper a priori knowledge of the received signal, provided that the calibration payload continuously measures its output power. These measurements, properly time-stamped, together with GNC system and housekeeping information, will be transmitted to the CMB satellite, which will send them to the ground for postprocessing and calibration of the scientific data.

The last Formation Flying subphase is the Positioning (FFP-POS). This is a transition phase in which CalSat either enters FFP-CAL from FFP-SBO, or abandons FFP-CAL returning to FFP-SBO. The maneuvers needed to permit transfer from the FFP-SBO point to the FFP-POS point and vice versa will be optimized taking into account the specific L_2 environment.

In addition to FFP, in every phase of the mission, a Safe Escape Manoeuvre (SEM) will be available. The design of Fault Detection, Isolation and Recovery (FDIR) of CalSat will enable constant monitoring of the ranging sensors and the health status of the communications. In case of failure of any of them or whenever a close approach to the CMB satellite is detected, a SEM will be triggered by making use of the remaining active positioning systems. The propulsion module will be commanded by the on-board computer (OBC) in order to provide a predetermined thrust in a safe direction, thus avoiding collision with the CMB satellite or interference with its measurements. This maneuver will also be accessible by ground command.

Finally, the Disposal phase will ensure reaching a final orbit diverging from the one of the CMB satellite, so that avoidance of collision is ensured even beyond the lifetime of the satellites. This phase will be reached by ground command, either following the end of the useful life of the satellite, or upon determination of a nonrecoverable failure.

6.2.1 Modes of operation

Based on the mission phases defined above, the following operational modes are defined for CalSat:

- **Deployment mode**: used once, during the initial deployment of CS from the CMB satellite.
- **Stand-by mode**: activated during the FFP-SBO sub-phase.
- **Calibration mode**: activated during the FFP-CAL sub-phase.
- **Reconfiguration mode**: activated during the FFP-POS sub-phase.
- **Safe mode**: secure mode activated in case of error.
- **SEM mode**: performs evasion maneuver and transitions to safe mode.
- **Disposal mode**: activated once, when the mission is finished.

In this work, only the stand-by, calibration, and reconfiguration modes are studied in detail. In Figure 6.4, the transitions between the operational modes are illustrated.

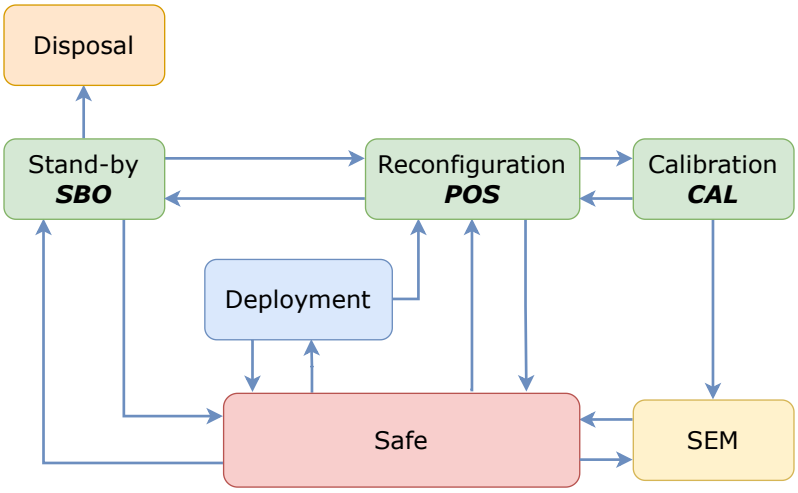


Figure 6.4: Diagram of the operational modes and their transitions. The mission subphase associated to the operational mode is indicated in bold.

6.2.2 Nominal orbit

The chosen nominal orbit around L_2 for the CMB satellite is a Lissajous orbit, similar to that of other CMB missions such as WMAP and Planck [108, 109]; the parameters that characterize this nominal orbit are collected in Table 6.11.

Table 6.11: Parameters of the nominal orbit chosen for the CMB satellite.

Parameter	Value
A_x [km]	$350 \cdot 10^3$
A_z [km]	$300 \cdot 10^3$
ψ [°]	0
ϕ [°]	180

As explained in Section 2.2, Lissajous orbits are similar to Halo orbits but the motion in the *xy*-plane and the *z*-plane does not have the same frequency, making this orbit quasi-periodic. The selection process of the type of orbit and its characteristics is out of the scope of this thesis, being assumed that it would be driven by the CMB satellite requirements and having a low impact on the ancillary satellite design and operation. In any case, nominal orbits [55] in L_2 are usually designed to follow the natural dynamics of the libration point while remaining bounded within the region, thus minimizing the required ΔV for the station keeping maneuvers. Thus, the Lissajous orbit defined in Table 6.11 is refined using differential corrections and the ephemeris model, obtaining a 3-year long trajectory with no maneuvers required

(the ΔV resulting is negligible), which is shown in Figure 6.5. Nevertheless, station keeping would be necessary on the real trajectory due to additional perturbations and thrust errors, although the amount of ΔV would be low and amounts to roughly $\sim$1 m/s per year in similar missions [59].

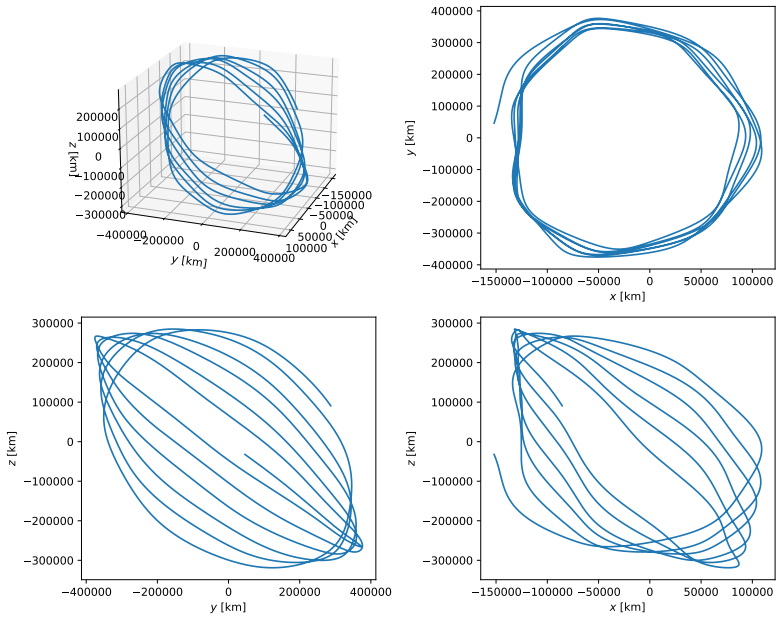


Figure 6.5: Representation of the nominal Lissajous orbit around L_2.

The transference to the nominal orbit depends on the launch date and the injection point in the target orbit. As it would be performed by the CMB satellite and its launcher, with CalSat still attached, it is not considered here.

6.3 Environment

The following sections briefly describe the different environmental conditions that CalSat will encounter at L_2 in terms of radiation, meteoroids, and thermal conditions [110]. L_2 point is located at 1.5 million km from Earth in the anti-Sun direction, where most of the interferences of Earth can be considered negligible. This includes atmosphere, magnetic field, albedo, infrared radiation, most of the plasmas and energetic radiation belts, etc. Nevertheless, the magnetosphere does influence the environment in this region, as will be described below.

The magnetosphere (see Figure 6.6) is the region of space where the properties of the plasma are controlled by the Earth's magnetic field. This magnetic field resembles a dipole, and its shape is conditioned by the solar wind, which compresses the daytime part of the magnetic field and extends the nighttime part (magnetic tail). The magnetic field is limited by the magnetopause, from which the magnetic envelope extends (magnetosheath) until it reaches the magnetic arc, a zone analogous to a shock wave where the solar wind abruptly stops.

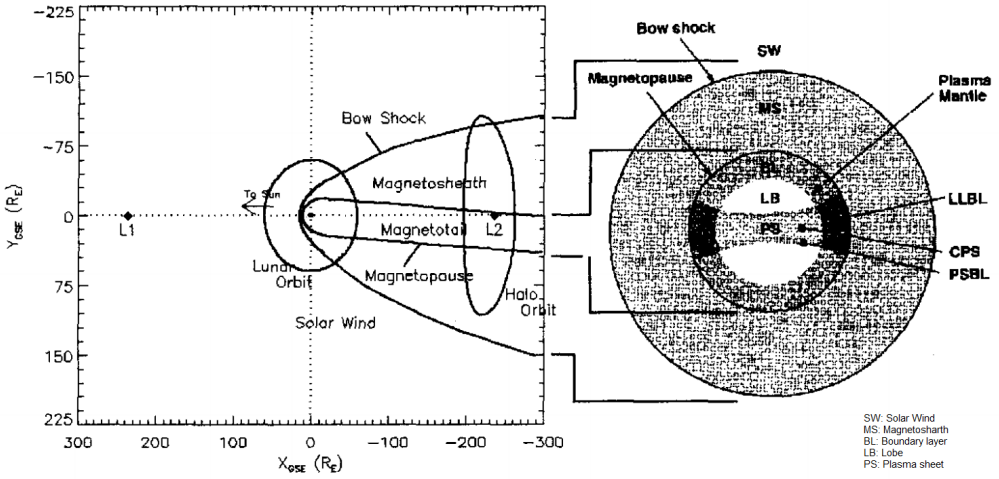


Figure 6.6: Simplified structure of the magnetosphere and its position relative to Earth and L_2 (left) and cross section (right). The magnetic tail is deflected with respect to the anti-Sun direction due to the solar wind. Extracted from [111].

Radiation

With regard to radiation, at L_2 there are high energy particle flux phenomena, noise in radio signals, solar wind, and plasma. The ECSS standard relative to spatial environment [112] states that the only regions of the Earth magnetosphere that have influence in L_2 are the magnetotail and the distant magnetosheath. In a Lissajous orbit, the spacecraft can expect to encounter all regions of the magnetotail but also the free solar wind when the orbit is out of the tail. This can happen due to variations in the magnetotail size and direction, which are determined by fluctuations of the solar wind and the season. During its immersion in the magnetotail, the spacecraft will be afforded some protection from energetic particles emitted by the Sun, e.g., by solar proton events, but it may be subjected to bombardment by energetic particles such as heavy ions and relativistic electrons during magnetospheric storms and substorms (from energies of a few tens of eV through tens of keV).

In general, the plasma present in the magnetic tail does not present a problem for the components inside the satellite since its particles will not be able to pass through its surface. However, they will cause degradation of coatings and accumulation of static charge.

Conversely, high-energy particles are capable of passing through spacecraft shielding and affecting internal spacecraft components, especially electrical ones. Depending on the type of particle, its energy and the geometry and materials selected for the vehicle, the attenuation of the particle will be greater or lesser. The particles that make up high-energy radiation can come from a variety of sources: extreme solar activity, radiation trapped in the Earth's magnetic belts or from beyond the Solar System.

Apart from the trapped plasma of the magnetotail, and due to the small influence of

the Earth, L_2 can be considered as interplanetary space; therefore exposed to cosmic rays and Solar Energetic Particles, SEP, (from 10 to 1000 keV). This high-energy particle environment is driven by the solar cycle and will largely be determined by the launch and operation time in relation to the solar cycle, as well as the mass properties of the spacecraft. Since it is a cumulative effect, the level of radiation hardness will be established by the mission duration, in Figure 6.7 the integral influence of both types of radiation for a ten-year mission is presented.

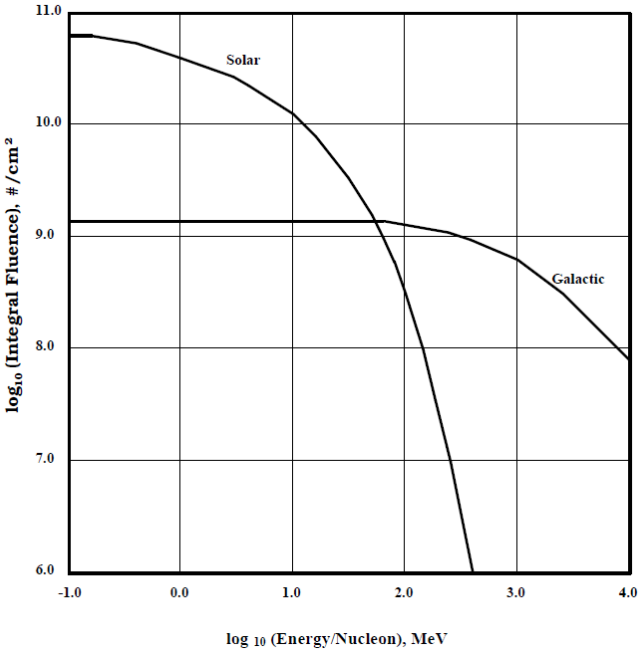


Figure 6.7: Ion spectra for 10 years at L_2 for solar and galactic sources. Extracted from [110].

The higher level of solar wind turbulence during solar events produces a dispersion of the galactic contribution, such that variations in the intensity of the galactic particle fluxes and solar flares have opposite phases. This behavior was verified by the Gaia mission [113].

Maximizing the amount of mass shielding between the electronic components and the external environment will reduce total ionizing dose damage. However, the shielding is less effective against single error events produced by galactic cosmic rays, and some consideration to be given to the selection of parts and software during the design process is recommended.

In summary, the radiation environment in L_2 is not negligible. The total dose of radiation will depend mainly on solar activity and mission duration (the next solar maximum is expected to occur around 2025). The final trajectory and spacecraft mass should also be considered. Taking this into account, the materials and components to be used must be selected with a view to their ability to minimize or withstand the effects of ionizing radiation. Nevertheless, the L_2 natural environment is relatively benign, with a comparatively low ionizing radiation environment with respect to orbits that pass through Earth's radiation belts (such as GEO orbits). Therefore, radiation is not expected to be a critical problem for the mission.

Meteoroids

The presence of meteoroids in a region of space is characterized by the micrometeorite flux and its velocity, parameters that are estimated by models based on experimental data collected by previous missions. In general, two sources of meteoroids are considered: deep space and comets.

Micrometeorites from deep space can be considered to come uniformly from all directions. In more recent models, it has been estimated, based on more current data, that there are 6 main directions of micrometeorite origin. In these models, an additional parameter, the directionality of the meteoroid, is taken into account.

In the case of meteoroids coming from comets, these are presented as debris near the orbit of the comet from which they come. Thus, encounters with these meteoroids occur periodically when crossing the wake of the comet, with peaks of greater presence of meteoroids when the comet has approached the orbit of the satellite.

L_2 is exposed to both sources of meteoroids. After two years of data collection in an orbit around L_2, the Gaia mission confirmed that the micrometeorite activity from deep space corresponded to the expected one, mainly following the interplanetary model of [114]. This model does not include meteoroids from comets and that contribution must be analyzed separately. The current and planned missions in L_2 will allow confirmation or refinement of the available models.

The impact of meteoroid can affect attitude control (generating disturbances in angular momentum), optical elements (damaging lenses, sensors, etc.), or even the integrity of the satellite itself. The study of impact probabilities makes it possible to estimate whether it is necessary to protect some of the satellite components with shielding and to estimate their useful life (or the degradation they will experience).

Thermal environment

The thermal environment in the vicinity of L_2 is conditioned primarily by the Sun. Unlike orbits around Earth, the albedo and radiation emitted by Earth itself have negligible effects on a satellite at L_2, being of the order of mW. This is due to the distance from Earth and the fact that the daytime area visible from L_2 is minimal.

The incident solar flux is slightly lower than the one that reaches the Earth because it is farther away. This flux suffers variations due to the eccentricity of the Earth's orbit (L_2 approaches and moves away from the Sun as Earth does) and to the solar activity. The radiation spectrum is similar to that of a black body at solar surface temperature. Regarding the irradiation, being the distance to the Sun very similar to the Earth's, it is enough to assume that the irradiance is 99 % the same than on Earth: 1345 W/m^2.

In the case of eclipses, due to the position of L_2 and the orbit, there is a way of avoid the eclipse by properly defining the orbit or maneuvering. From L_2, the angular size of the Sun is 0.526°, while those of the Earth and Moon are 0.487° and 0.133° respectively. Thus, in no case will a total eclipse occur, but partial eclipses of up to 80 % can happen, which, due to the long period of the orbits around L_2, can last for days.

6.4 Visibility analysis

The scanning strategy of the CMB satellite and CalSat relative position define the total access time and the number of viewed detectors. The number of detectors illuminated by the calibration signal has been determined by simulation, considering different relative positions between both satellites. The parameters of the scan law selected for the CMB satellite are $\alpha = 45°$, $\beta = 50°$, $T_{spin} = 11\,\mathrm{min}$, and $T_{prec} = 105\,\mathrm{min}$ while the detectors layout has been modeled as 7 hexagons arranged in a circular pattern (see Figure 6.8), totaling 406 detectors. The FOV of the instrument and of the detectors is set to 30° and 0.5°, respectively.

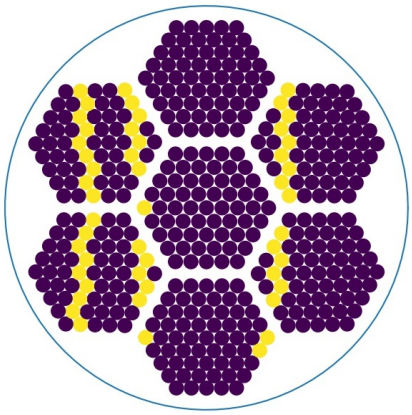
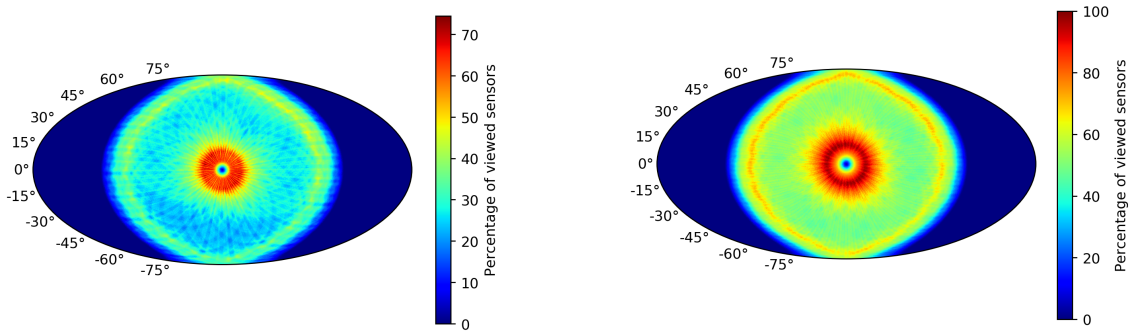


Figure 6.8: Detectors layout used for the simulations showing and example of detectors illuminated by the reference signal after the CS crosses 3 times the instrument FOV during calibration. The blue line indicates the limit of the FOV.

As shown in chapter 5, the best option to place CalSat is close to the anti-Sun axis, about 10 to 15° from it. Figure 6.9 shows the percentage of viewed detectors according to the relative position between the two satellites for a period of 6 h (a) and 12 h (b).

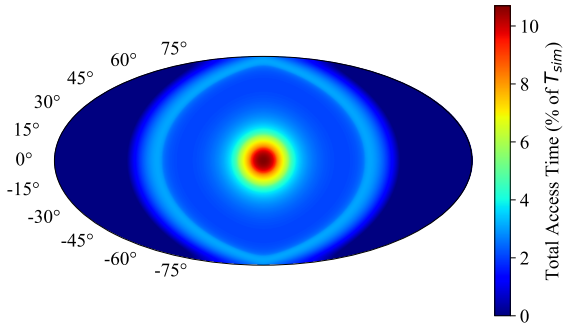


(a) 6 h **(b)** 12 h

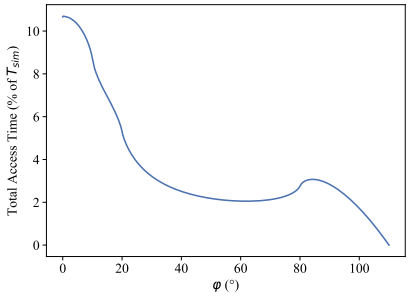
Figure 6.9: Percentage of viewed detectors for different periods of time according to the position of CalSat relative to the CMB satellite.

The percentage of viewed sensors (or detectors) is around 70 % for 6 h (red region of Figure 6.9a) but it approaches 100 % in that region for 12 h even when CalSat is kept at the same position. For longer periods of time, this percentage could be achieved from many more different positions; however, a calibration session of only 12 h has been assumed as the baseline option, since this calibration time would allow, among others, the polar angle calibration of almost the complete set of detectors.

As explained in chapter 5, the total access time only depends on the angular separation from the anti-Sun direction, α, β, and the FOV. Thus, having fixed those parameters, the total access time can be represented as a percentage of the total time (see Figure 6.10). From these figures it can be observed that in the positions with maximum percentage of viewed sensors, about 8 % of the period is available for calibration, i.e., 60 min for a 12 h calibration period.



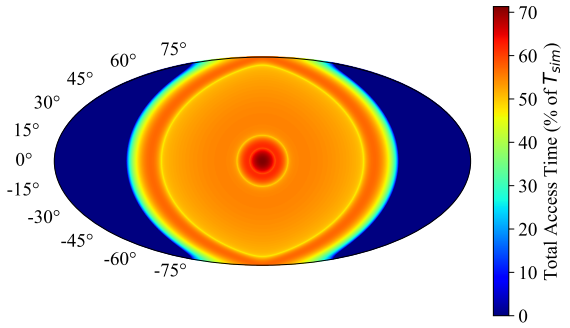
(a) Value in each relative position.



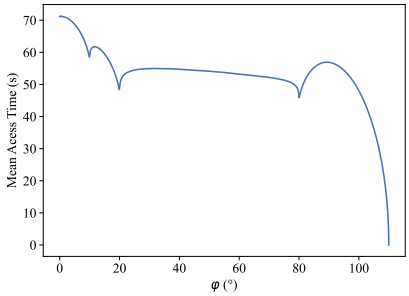
(b) Variation with the angle regarding the anti-Sun direction.

Figure 6.10: Total access time according to the position of CalSat relative to the CMB satellite.

The amount of time between two consecutive accesses also varies, and if CalSat has a separation from the precession axis greater than roughly 15°, the waiting time between accesses would be equal to one precession period, which would reduce the total access time, as can be observed in Figure 6.10b, where the % is reduced to roughly 3 %. Note also that the mean access time is uniform and around 50 s (see Figure 6.11), regardless of the calibration satellite position.



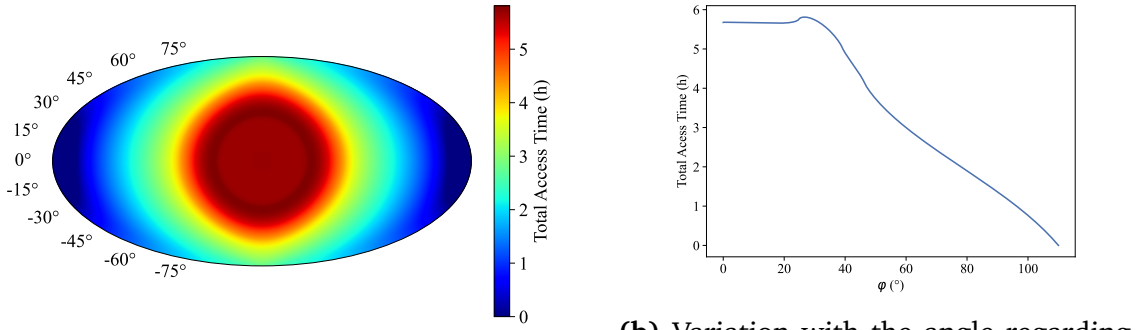
(a) Value in each relative position.



(b) Variation with the angle regarding the anti-Sun direction.

Figure 6.11: Mean access time according to the position of CalSat relative to the CMB satellite.

Furthermore, an expanded FOV of 120° has also been considered to calculate the access time available for the characterization of the near- and far-side lobes of the beams. Figure 6.12 shows that in a calibration period of 12 h, a total access time of more than 5.5 h will be available for this task. Due to the large angular values of the far-side lobes, most of the sensors can be characterized with the calibration signal simultaneously, so the required time to calibrate all of them will be much lower than the available total access time.



(a) Value in each relative position.

(b) Variation with the angle regarding the anti-Sun direction.

Figure 6.12: Total access time according to the position of CalSat relative to the CMB satellite and with a FOV of 120°.

Taking into account that over a 3-year period of CMB mission, the total observation time of Jupiter (the most powerful celestial intensity calibrator) is of about one hour, CS can provide many more opportunities of calibration. Additionally, given the high signal-to-noise ratio (SNR) provided by the calibration sources of CalSat, similar periods of time should be enough for both intensity (beam pattern, non-linearity, bandwidth...) and polarization (beam pattern, polar angle...) in-flight calibration. More details about the quality of the calibration can be found in [14].

6.5 CS Support System

The CalSat Support System main purpose is to store CalSat during the transference to L_2 and to provide support during operation once it has been deployed. It consists of the following main components:

- **BaseCalSat**: 2U electronic box.
- **Deployable Panel**: solar panel to power supply BaseCalSat.
- **Auxiliary Payload Carrier (APC)**: auxilliary platform for mechanical and electrical interface with the main satellite.
- **CS Deployer**: 6U CubeSat deployer.
- **Other minor components**: electrical harness, connectors, screws and bolts, and MLIs.

6.5.1 BaseCalsat

This BaseCalSat has the equivalent size of a 2U Cubesat ($10 \times 10 \times 20$ cm) and it contains mainly an On-Board Computer (OBC) [115], the relative positioning system (similar to RelNav) [116] and a battery [117]. These components provide navigation and communications support for CS. In Table 6.12 the main specifications of the proposed components are summarized.

Table 6.12: Specifications of the components of BaseCalSat.

Component	Parameter	Value
OBC	Size	$60 \times 40 \times 6.5$ mm
	Mass	80 g
	Power Consumption	2.3 W
RealNav	Size	$10 \times 10 \times 3.5$ mm
	Mass	400 g
	Power Consumption	2.5 W
Battery	Size	$10 \times 10 \times 2.8$ mm
	Mass	335 g
	Capacity	40 W h

6.5.2 Deployable solar panel

In order to operate autonomously, the CS Support System requires a power supply. A small deployable solar panel can cover the power needs of BaseCalSat. The solar panel would be mounted on the CS deployer with an area of 20×30 cm. Patch antennas will be installed on both sides of the deployed area (see Figure 6.13 and Figure 6.14).

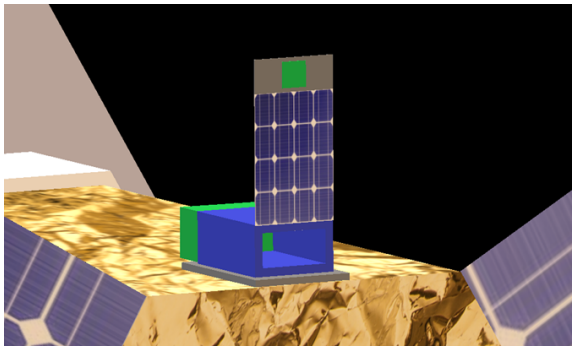


Figure 6.13: Front view of the deployable solar panel.

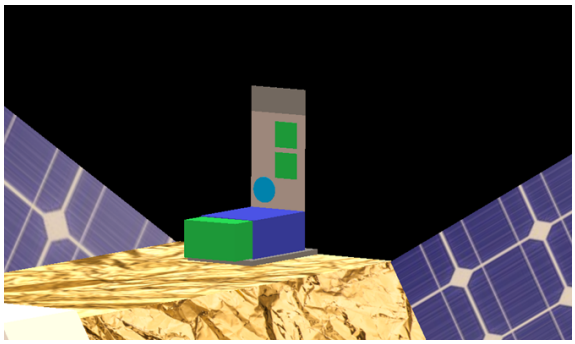


Figure 6.14: Rear view of the deployable solar panel with the patch antennas used for communications and relative positioning.

6.5.3 Mechanical interface with the CMB satellite

The whole Calibration System will be contained in two boxes which will be attached either directly to the CMB satellite or through a mechanical adapter (Auxiliary Payload Carrier or APC), similar to that employed in the MarCO mission (see Figure 6.15) [118, 119]. CalSat will be stored in its own 6U CubeSat deployer. BaseCalSat can be contained in a box with dimensions of 2U specifically designed for that purpose. Alternatively, it can also be designed as a 2U CubeSat and contained in a deactivated 2U deployer. The advantage of this second approach is that the container would be standardized and already tested in flight. This means that the only structural unions between the Calibration System and the CMB satellite will be two on-flight-tested deployers with well-defined interfaces.

APC

The APC is an auxiliary platform that, if necessary, serves as physical support of all the other components and acts as a mechanical interface with the CMB satellite. It shall be located at one of the CMB satellite laterals, allowing a safe deployment of CS towards the opposite side of the CMB satellite instrumentation location. The APC has a composite sandwich structure made of CFRP and aluminum alloys. In Table 6.13, the APC specifications are listed.

Table 6.13: APC specifications.

Parameter	Value
Size	$100 \times 50 \times 2\,\text{cm}$
Mass	0.5 kg

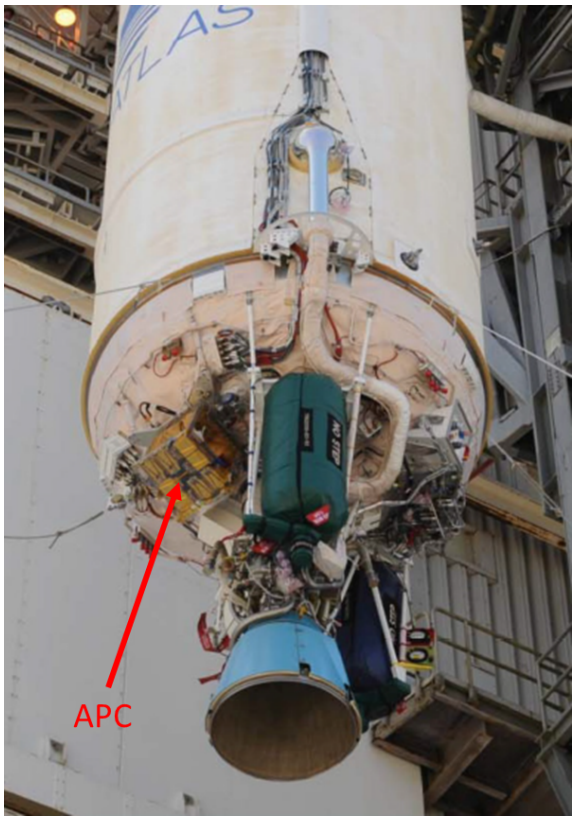


Figure 6.15: Auxiliary Payload Carrier attached to Centaur launcher. Extracted from [119].

CS Deployer

A 6U standard on-flight-tested deployer as the one provided by ISIS [120] (see Figure 6.16) will be mounted directly on the APC and will store the CS during the transference to L_2. The container does not require continuous power supply, only a power pulse for deployment that can be provided by CS. For safety reasons, pyrotechnics are not allowed in the CubeSat standard. Deployment is achieved by a pusher plate and spring ejection system. In Table 6.14, the specifications of the deployer are listed.

Table 6.14: ISIS 6U DuoPack Deployer specifications.

Parameter	Value
Size	6U
Mass	4.5 kg
Power consumption	1.75 A (28 V/250 ms)



Figure 6.16: ISIS 6U DuoPack Deployer.

After the CS deployment this box will remain attached to the CMB satellite and will serve as a support for the solar panel.

BaseCalSat

All elements of BaseCalSat will be contained in a box with the 2U CubeSat standard. Although BCS will not be deployed, in order to facilitate integration and standardize physical unions with CS, it is proposed that BCS also be contained in an on-flight tested deployer, in this case a 2U one, as the one provided by ISIS [120] (see Figure 6.17).



Figure 6.17: ISIS 2U ISIPOD Deployer.

6.5.4 Power

The CS Support system attached to the CMB satellite requires a minimum of electrical supply before and after the deployment of CS. There are two alternatives for obtaining this power. First, the CMB satellite can provide it through a connection between the power bus and BCS. If this is not possible, the second option contemplated is the self-supply using a small solar panel (see Figure 6.13).

Before deployment, the system is in stand-by, requiring a minimum of available power. A good thermal design is desirable so that active thermal control is not required. During this phase, the power needs are expected to be less than 1 W.

After deployment, BCS remains attached to the CMB satellite and continues to perform communications and distance measurement tasks. These tasks will require a power supply of 1 to 2 W.

6.5.5 Communications

The CS is designed to operate almost autonomously from the CMB satellite. However, due to its small size and small power available, CS will not be able to contact directly with ground. For this reason, communications between the ground and CS will be made through the CMB satellite communication system, but always using BCS as an intermediate node.

Communications CMB satellite – BCS

The CMB satellite does not communicate directly with CS. All communications will be through BCS. The communication between the CMB satellite and BCS will be thought of as a data bus. This line of communication will be used to forward ground orders (such as the start of a calibration phase) or for obtaining telemetry data (position and orientation) from CS that will be downloaded to ground.

Communications BCS – CS

The Calibration Systems includes a S-Band range measurement system that can also be used for communication. The same patch antennas and instruments will be used for both tasks. The antennas are located on the rear of the deployable solar panel to interfere as little as possible (see Figure 6.13 and Figure 6.14).

6.5.6 Mass budget

In Table 6.15 is summarized the mass of each element of the CS Support System and also the estimate of the total mass before and after the CS deployment.

Table 6.15: Breakdown of CS Support System mass.

Element	**Mass [kg]**
APC	0.5
CS	7.23
Deployer	4.5
Electronic Units	4
Deployable solar panel	0.4
Others	0.5
Total (10% margin)	18.84
Total after CS Deployement (10% margin)	10.89

6.6 CalSat

This section presents the preliminary design of CalSat subsystems. These results are the outcome of an iterative process that involved the redefinition and refinement of the mission concept and its requirements.

6.6.1 Payload

The payload of CalSat consists on a series of RF sources that emit the calibration signal for the CMB satellite instrument. Its design has been carried out by the Institute of Physics of Cantabria (IFCA). The payload characteristics (see Table 6.16) and the mission main objective have been the cornerstone of CalSat preliminary design process.

Table 6.16: Summary of characteristics of the Payload.

Property	Values
Mass	1.3 kg
Power Consumption	50 W
Dimensions	$20 \times 10 \times 10$ cm
Temperature Range	0 to 50 °C

Focusing in a frequency band from about 40 to 400 GHz and trying to optimise volume, cost and power consumption, it is proposed to cover six bands determined by the corresponding wave-guide standards: 33–50 GHz (WR22), 60–90 GHz (WR12), 90–120 GHz (WR8), 140–220 GHz (WR5), 220–325 GHz (WR3) and 325–500 GHz (WR2). Note that the 50–60 GHz and 120–140 GHz bands are not covered by the sources. For simplicity, it has been assumed that they can be omitted in this first study but, if necessary, an alternative frequency coverage could be considered in a future analysis. It is critical to include the higher (WR2) frequency band since at these frequencies it is not possible to use the orbital dipole (a Doppler effect generated by the orbital motion of the CMB mission) to calibrate the intensity, as was done by the Planck mission for lower frequencies.

In order to generate calibration signals covering all these frequency bands, it is proposed the use of two common low-frequency sources (monochromatic frequency-variable and broadband) that can be used to generate variable signals. Then, the required bandwidth coverage will be achieved by means of power splitters and Frequency Multipliers (FM). Figure 6.18 shows a schematic of this kind of source implementation.

The calibration source consists of a variable low-frequency Continuous Wave (CW) source, which is able to cover a given bandwidth BWLF, and a broadband noise source (NS) covering the same bandwidth, feeding both of them a common frequency multiplying system that translates the signals to the required frequency bands.

The broadband NS can be implemented by means of a noisy diode or a 50 Ω termination connected to a Power Amplification (PA) chain with the same bandwidth BWLF that will provide the required level of signal power. A PIN (P-type, Intrinsic semiconductor, N-type) switch diode is used to select the kind of signal to be used, as a function of the particular systematic to be calibrated. A variable attenuator (VA) is used to change the power level for linearity and beam calibrations. VA applied directly to the common low-frequency signals will reduce the cost and complexity of the overall source. The signal is then divided to feed the sub-band transmitters and the frequency of the signal is multiplied using FM to get the required frequency coverage in each of them. A Band-Pass Filter (BPF) rejects undesired harmonics of the signal and a Directional Coupler (DC) is used to measure the emitted power level by connecting a Zero-Bias-Detector (ZBD) to the coupled output. The direct output is connected to a feed-horn providing the calibration signal of each sub-band.

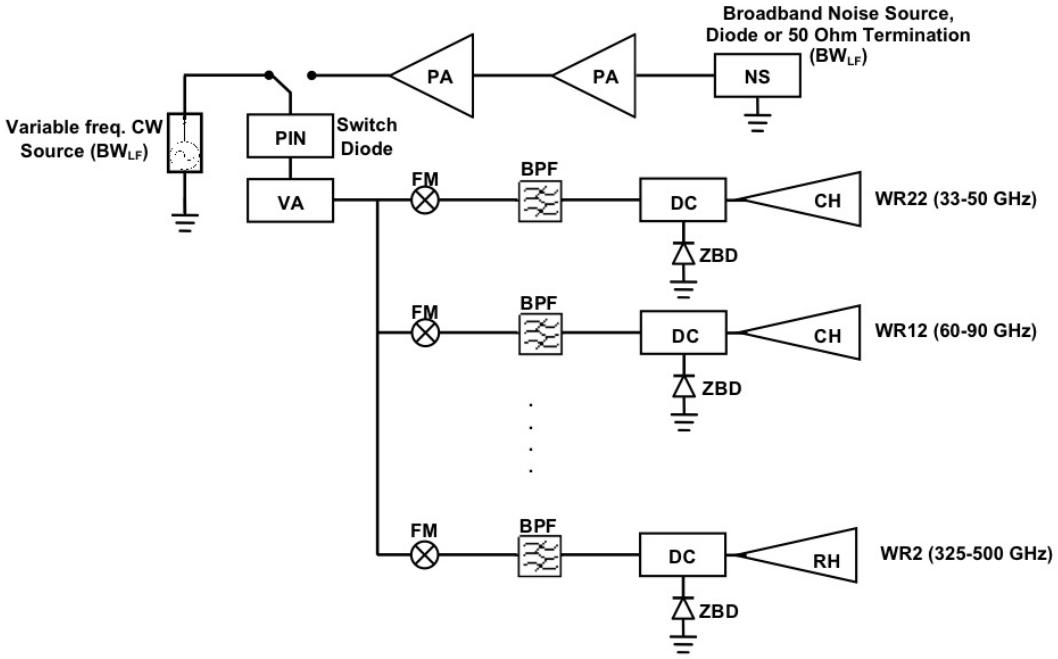


Figure 6.18: Calibration source diagram.

Due to the difficulties to generate microwave power at the highest frequencies, it has been proposed the use of conical horns (CH), with 20 dB gain, for the two lower frequency bands and rectangular horns (RH), with 26 dB gain, for the rest of bands.

Figure 6.19 shows a sketch of the frontal view of the calibration source. Another requirement of the calibration source is to provide a very pure linearly polarized signal, presenting a cross-polarization degree of the order of 60 dB. This can be also achieved by means of the use of Wire-Grid Polarisers (WGP) placed in front of the source's horns and accurately aligned with their polarization axes [12, 121].

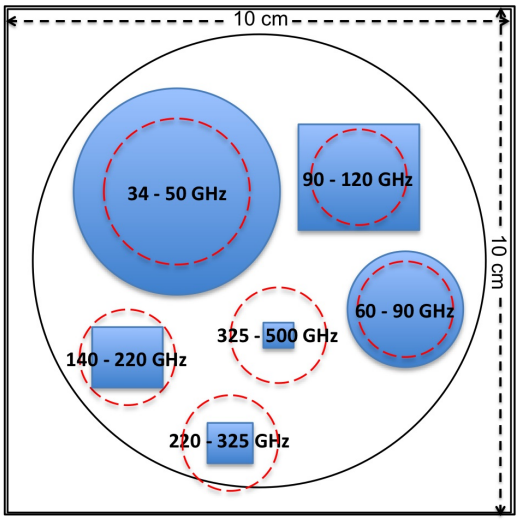


Figure 6.19: Calibration source front view.

6.6.2 ADCS

This subsystem must be capable of steering the spacecraft fulfilling the established ADCS requirements without any magnetic elements nor GNSS support, as they cannot be used in libration points. For this subsystem, the components shown in Table 6.17 are considered:

Table 6.17: ADCS components and their specifications. From [122].

Component	Mass [g]	Power [W]	Accuracy [°]	Number
OBC	56	0.12	-	1
Star tracker	47	0.165	0.021/0.061	1
Fine Sun Sensor	20	0.1	0.2	1
Coarse Sun Sensor	2	0.005	10	6
Reaction wheels	150	0.19	-	3

The star tracker has an accuracy (3σ) of 0.021° and 0.061° for each axis (cross-axis and roll-axis, respectively) and is the key element for attitude control. It will provide the required accuracy for the calibration phase. However, its low operational threshold for the angular velocity of the satellite (<0.3 °/s) makes it unsuitable for maneuvering. For this purpose, the fine sun sensor is included. It has a lower accuracy (3σ) of 0.2°, but it is operational for higher angular velocities (<70 °/s). Finally, the reaction wheels provide three-axis control. All these components possess flight heritage. Initial simulations indicate that the specified level of precision (as detailed in section 6.1.2) can be achieved using a PID controller. This controller is expected to be tested on the upcoming ANSER mission, launched in 2023.

The on-board computer shown in Table 6.17 is specifically intended for attitude control, and it is in charge of carrying out all necessary operations to keep control of the spacecraft attitude. This computer is independent from the main computer

of the OBDH subsystem (although it operates in coordination with it), which is specifically devoted to the payload operations.

6.6.3 GNC

The guidance, navigation, and control system of CalSat is responsible for controlling the orbital motion of it, enabling the control of the formation in all the different operational modes. In Figure 6.20, the scheme of the GNC system for the CS is displayed. Based on the developments presented in chapter 3, a KF scheme is implemented as a navigation algorithm and a MPC as control algorithm. The guidance function is established by defining the target states for each operational mode. In Table 6.18 the position and velocity achieved by the GNC during the Calibration phase is shown while in Table 6.19, the ΔV consumed by the GNC during the life mission is included.

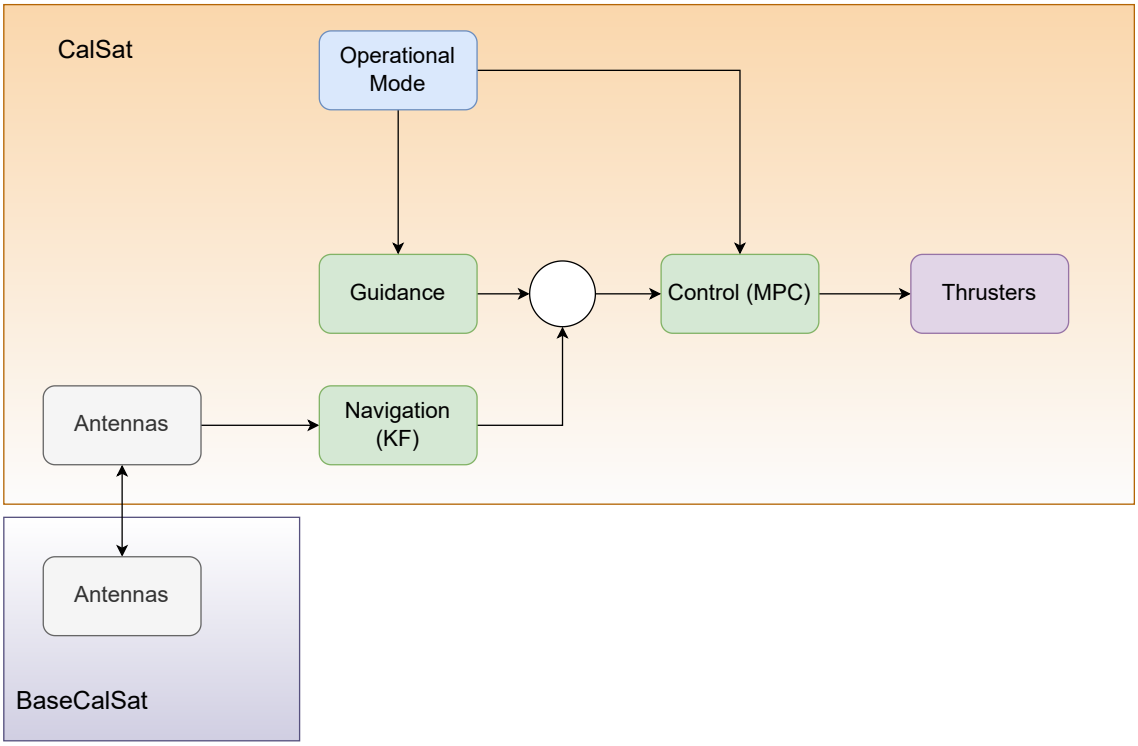


Figure 6.20: Scheme of the GNC system of CalSat.

Table 6.18: Achieved position and velocity accuracy for the calibration phase. Spherical components.

Position [m]			**Velocity [m/s]**		
e_ρ	e_θ	e_ϕ	e_{v_ρ}	e_{v_θ}	e_{v_ϕ}
0.19	0.22	0.20	4.11e-04	1.47e-03	1.68e-03

Table 6.19: ΔV in each phase for the whole mission (6 calibrations).

Phase	ΔV [m/s]
Calibration	0.12
Stand-by	2.4
Reconfiguration	5.38
Total	7.9

ΔV budget

The ΔV budget is divided in several parts. The first component takes into account all orbital maneuvers that ought to be made in order to maintain the Lissajous orbit, removing non-stable terms that make the spacecraft drift away. Taking into account similar missions, such as Planck, which also possesses a Lissajous orbit, the ΔV can be extrapolated from this mission to 1 m/s per year [55, 59].

In order to separate the deputy from the chief spacecraft, a deployment ΔV must be added. For this case, the PROBA-3 mission has been considered as a reference for this calculation. As shown in [123], the ΔV necessary for the deployment is 0.2 m/s. Adding the ΔV consumption of the operational modes, the budget is completed. The results are summarized in 6.20, where the total ΔV is included, with a 10% safety margin.

Table 6.20: Total ΔV budget.

Action	ΔV [m/s]
Maintenance at L_2	3.0
Deployment	0.2
Calibration maneuvers	7.9
Total budget + 10% margin	**12.21**

Knowing the final ΔV necessary for the whole mission, the propellant mass can be determined using the Tsiolkovsky equation. The specific impulse of the thrusters can be found in the propulsion module datasheet [78]. The total propellant mass that is needed is:

$$\Delta V = I_{sp} \ln\left(\frac{m_D + m_P}{m_D}\right) \rightarrow m_P = 89.5\,\mathrm{g} \tag{6.1}$$

6.6.4 OBDH

The On-Board Data Handling (OBDH) subsystem is responsible for collecting, processing, routing, storing, and downlinking on-board generated data and for routing and storing uplinked data. A COTS on-board computer with flight heritage

designed by GomSpace is selected for this purpose. Main features of the NanoMind Z7000 GOMSpace on-board computer are summarized in 6.21 [124].

Table 6.21: NanoMind Z7000 GomSpace on-board computer main specifications.

Characteristic	Value
Processor	Dual ARM Cortex A9 MPCore 800 MHz
RAM	1 GB (DDR3)
Storage	32 GB
Power consumption	2.3 W
Mass	77 g

6.6.5 Propulsion

High accuracy is needed throughout the calibration process. For that reason, very low ΔV (near $10 \cdot 10^{-6}$ m/s) are needed. Therefore, it is required a propulsion system which generates a very low thrust. In order to carry out the propulsion tasks of the satellite, a commercial propulsion module manufactured by Nano Space is selected, see [78]. With a minimum thrust of 10 μN the minimum ΔV that it is capable of giving is enough to meet the positioning requirements during the calibration process.

Table 6.22: NanoProp GP3 GomSpace propulsion module.

Characteristic	Value
Nominal thrust	1 mN
Thrust resolution	10 μN
I_{sp}	100 s
Power consumption	2 W
Mass	350 g

Two commercial propulsion modules have been selected, given that each of them can carry 50 g of propellant of butane, and several thrusters have been placed on one of the satellite faces, as shown in Figure 6.21. This distribution permits to obtain force on the directions $+X$, $-X$, $+Y$, $-Y$, $-Z$. In order to obtain thrust along $+Z$, it is necessary to perform a manoeuvre which rotates 180° the vehicle around the axis X or Y. It must be taken in account that whenever the thrust is given along Z there is no disturbance on the momentum balance, however whenever the loaded direction is X or Y, a non-compensated momentum appears which must be stabilized by means of the reaction wheels.

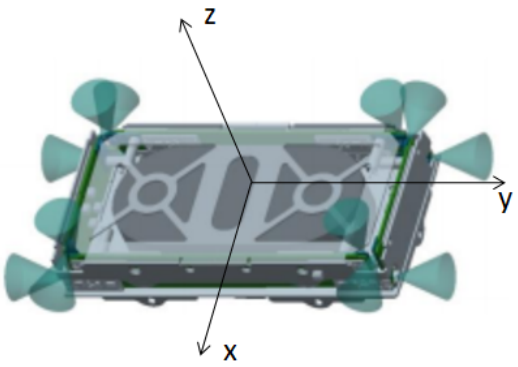


Figure 6.21: Representation of an analogous thrusters distribution. Extracted from [78].

6.6.6 Power

The electrical power system (EPS) generates, stores, conditions, controls, and distributes power within the specified voltage band to all bus and payload equipment. In CalSat, the EPS is a photovoltaic-battery system, in which the power is generated by a solar array (SA) and the excess of power is stored in a battery. As there will not be eclipses during the mission, most of the time the SA will provide enough power to the system and the battery will only be required in certain scenarios: the deployment, the peak of power consumption during calibration phase, and whenever the SA are not pointing to the Sun (maneuvers).

In order to generate power during for the satellite, a couple of 6U deployable panels composed of triple-junction solar cells [125] are proposed. Additionally, 2/3 of the central section of CalSat would also be occupied by solar cells. The layout of solar cells is shown in Figure 6.22.

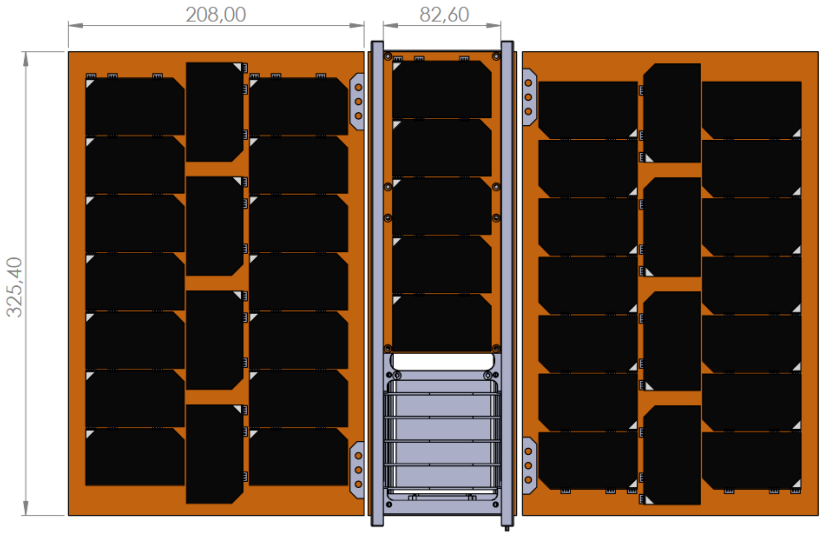


Figure 6.22: Solar panels view. The solar cells are arranged to maximize the occupation factor.

The solar array power is estimated at the beginning and at the end of the mission as a result of multiplying the total power generated by the solar arrays by a lifetime degradation index (L_d):

$$P_{EOL} = P_{BOL}(1 - EOL \cdot L_d) \tag{6.2}$$

The total power generated by the solar panels at the beginning of the mission can be determined from:

$$P_{BOL} = \eta_{cell} n_{cell} A_{cell} E \tag{6.3}$$

where η_{cell} is the efficiency of the solar cells, n_{cell} the number of cells, A_{cell} the area of each cell, and E the solar irrandiance. All these parameters are shown in Table 6.23. The total power generated by the solar panels at the beginning and at the end of the mission is shown in Table 6.24 as a result of the previous calculations. The power consumption for the different operational modes is detailed in Table 6.25. As can be observed in this table, the power consumption during the calibration phase exceeds the power generation (22.15 W extra consumption). Based on the battery characteristics (Table 6.26), the available calibration time would be:

$$t_{on} = \frac{C_{batt}}{P_{tot}} = \frac{80\,\mathrm{W\,h}}{22.15\,\mathrm{W}} = 216.7\,\mathrm{min} \tag{6.4}$$

where C_{batt} is the battery capacity and P_{tot} the excess of power consumed in Calibration mode. If the payload is turned off, there would be an excess of 29.15 W. Based on this, it would take approximately 164.6 minutes to charge the battery completely. This means that for each minute of calibration it is necessary around 0.75 min of charging, i.e., the payload can be turned on roughly 75 % of the time. As this proportion of time is higher than the percent of total access time available for calibration (roughly 8 %), the power supply is ensured.

Table 6.23: Power generation parameters.

Parameter	**Value**
Cell efficiency (η_{cell})	30 %
Solar irradiance (E)	1367 W/m^2
Number of solar cells (n_{cell})	41
Solar cell area (A_{cell})	26.06 cm^2
Lifetime degradation index (L_d)	0.5 %
End of Life (EOL)	3 years

Table 6.24: Power generated at the beginning and at the end of the mission.

Time	**Power [W]**
Beginning of mission	44.73
End of mission	44.05

Table 6.25: Power consumption for different operational modes.

Subsystem	Power consumption [W]		
	Stand-by	Reconfiguration	Calibration
Payload	0	0	50
ADCS	1	1	2.3
OBDH	2.3	2.3	2.3
GNC	0.2	0.2	0.2
Propulsion	2	2	2
Communications	5	5	5
Power	4.4	4.4	4.4
Thermal	0	0	0
Total	**14.9**	**14.9**	**66.2**

Table 6.26: Battery specifications [117].

Parameter	Value
Capacity	80 W h
Mass	670 g
Peak power output	32.2 W

6.6.7 Thermal control

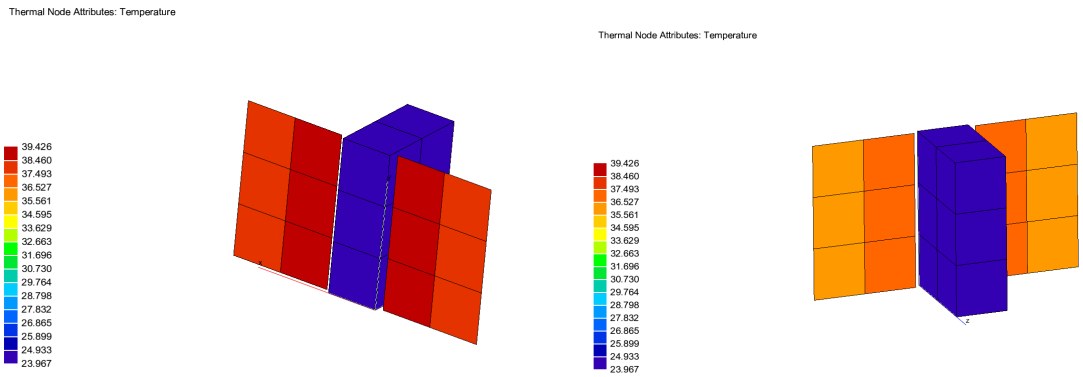
In this section, the results of a preliminary thermal analysis of the CS are presented. These results are the starting point to study the thermal influence from CalSat to the microwave detector situated in the telescope of the CMB satellite. In order to achieve that goal, the maximum external temperature of the calibration satellite and the heat flow exchanged between it and the detector have been computed.

The preliminary deputy design has been implemented in ESATAN® software, as shown in Figure 6.23. The orbital parameters of the spacecraft have been established according to the mission requirements shown in Section 6.1.2. The properties of the structure as well as the solar panels are shown in Table 6.27.

Table 6.27: Thermal and optical properties of the model.

Parameter	**Value**	
Component	Structure	Solar cells
Material	Aluminium	GaAs
Density [kg/m^3]	2700	5300
Specific Heat [J/(kg K)]	900	1000
Conductivity [W/(m K)]	135	55
α	0.95	0.91
ε	0.87	0.84

As shown in Figure 6.23, the maximum temperature is around $\approx 39\,^{\circ}\mathrm{C}$ and corresponds to the frontal side of the solar arrays. The rear side of the solar panels is slightly colder ($\approx 36\,^{\circ}\mathrm{C}$) as it does not receive direct solar flux and can radiate to deep space more efficiently. The structure of the satellite, made of aluminum, presents a lower and more uniform temperature ($\approx 25\,^{\circ}\mathrm{C}$) as most of its surface is in shadow.



(a) Front side. **(b)** Rear side.

Figure 6.23: Rear side.

Based on the solar panels surface, a thermal impact analysis of CalSat over the main satellite was carried out. This study helped establish the nominal distance of calibration so the sensors of the CMB satellite would not get saturated by thermal radiation.

6.6.8 Communications

To achieve the accuracy definite by the requirements, an RF-based relative navigation system has been defined using the principles defined in [126]. One possible hardware proposed is the "Swift RelNav" by Testhers Unlimited (Figure 19). It allows to measure the distance using RF technology in S-Band with the precision required.

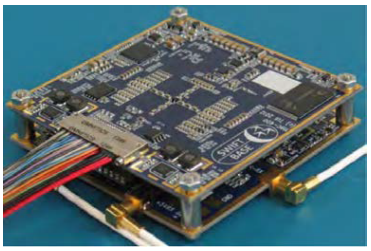


Figure 6.24: Relative position hardware “Swift RelNav” by Testhers Unlimited.

The navigation system utilizes totally generated RF ranging signals. The transceiver terminal is suggested to consist of one transceiver and several antennas. This systems allows to calculate an estimation of the relative line-of-sight (LOS) and the relative distance using carrier phases differences arriving at multiple antennas.

An additional advantage of this technology is that it can be used for communications between the two spacecraft, the double functionality helps to reduce the total mass and volume of the CubeSat.

6.6.9 Structure and configuration

This section describes the structure and configuration of the spacecraft. Due to mission constraints, the configuration is fixed to a standard 6U CubeSat.

Structure

Different standard commercial options have been taken into account. The proposed structure is made of Aluminum 6061 with a total weight of 0.9 kg and manufactured by Endurosat [127]. The 3D model of the mentioned structure is shown in Figure 6.25.

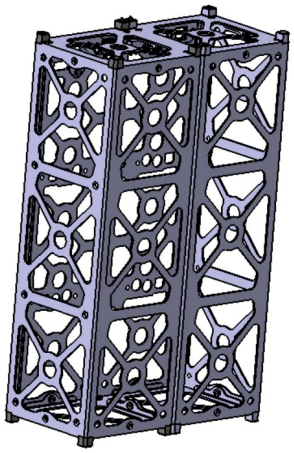
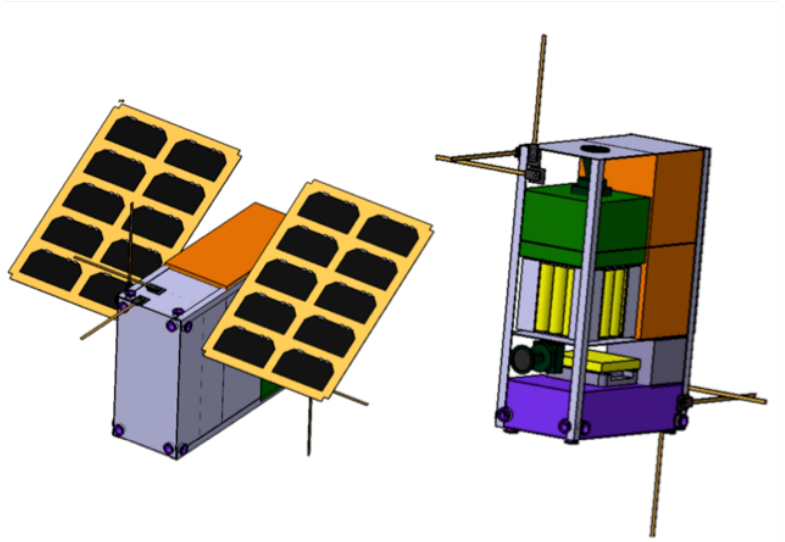


Figure 6.25: 3D model of the 6U structure from Endurosat.

Configuration

The preliminary proposed CubeSat configuration is shown in Figure 6.26; Figure 6.27 shows an exploded view drawing of this configuration.



(a)

Figure 6.26: Preliminary design configuration.

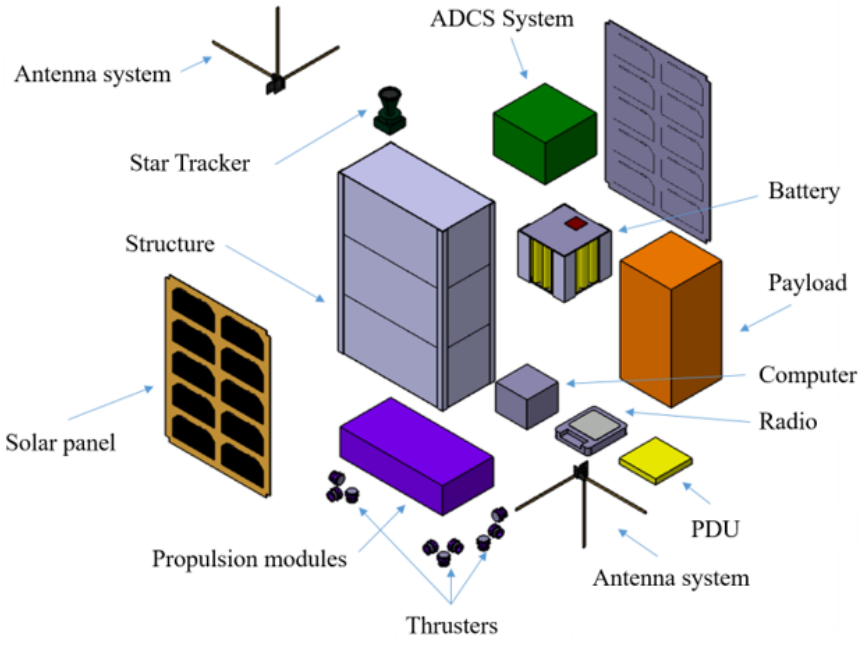


Figure 6.27: Exploded view of CalSat subsystems.

Dimensions of each subsystem are shown in 6.28, and their masses in 6.29. The total dry mass of the spacecraft adds up to 7.14 kg.

Table 6.28: Subsystem dimensions

Subsystem	Height [mm]	Length [mm]	Width [mm]
Antenna	3	140	16
Radio	13	67	79
Structure	300	100	100
Propulsion (engine + tank)	50	98	198
Solar panel	280	202	1
Battery	76	90	90
Radiators	50	50	2
Sensors (ADCS)	55	30	30
Actuators	10	15	15
Payload	98	98	198

Table 6.29: Subsystem masses.

Subsystem	Mass [kg]
Communication	0.48
Propulsion	0.95
Power	2.25
ADCS	1.11
Payload	1.30
Structure	0.90
Thermal	0.15
Total (dry mass)	7.14

The inertia of the complete spacecraft and subsystems with respect to the global axis system centered at the spacecraft center of mass is shown in 6.30.

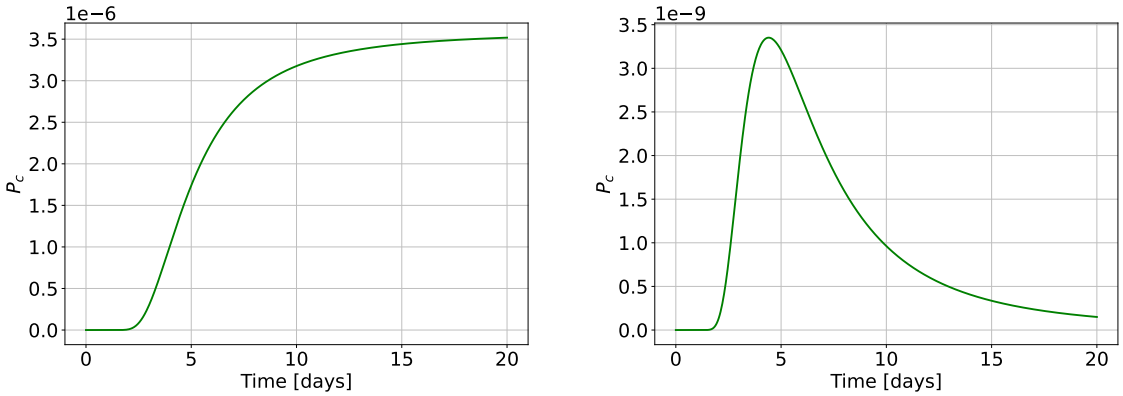
Table 6.30: Subsystem masses.

Axis	Inertia [kg m^2]
XX	0.079
YY	0.060
ZZ	0.036
XY	-0.002
XZ	0.002
YZ	0.004

6.7 Collision risk assessment

The nominal distance during the calibration phase has been set to 6600 m in the requirements. Given this considerable distance, it is reasonable to expect that the collision risk during the calibration is low. Furthermore, the collision avoidance restriction imposed in the MPC control will prevent CalSat of getting closer than the safe distance established during the reconfiguration phase and the stand-by phase. Nevertheless, the collision risk during the calibration has been computed using the approach presented in chapter 4 in order to rigorously assess that the collision risk is in fact low or negligible. Furthermore, it is presented the evolution of the collision risk for distances closer than 6600 m, as this distance is set to avoid the saturation of the 400 GHz detectors and other distances (as low as 300 m) were considered in this study for cases in which these detectors were not included.

In Figure 6.28, the results of this collision risk assessment are shown. A safety sphere centered in the CMB satellite and with a radius of 5 m has been considered to define the collision. In the Figure 6.28a, the evolution of the cumulative probability over time is shown. Although it reaches $3.5 \cdot 10^{-6}$ over time, it must be noted that the collision risk is zero for at least two days, which leaves enough margin to maneuver the CMB satellite away if it considered necessary. The low probability of a collision in this scenarios can be confirmed by looking at Figure 6.28b, in which the instantaneous probability of collision is shown, marking a maximum probability of $3.5 \cdot 10^{-9}$. These low values of the probabilities and the long periods of time involved indicate that the collision risk can be considered negligible.



(a) Cumulative probability.

(b) Instantaneous probability.

Figure 6.28: Evolution of the collision risk for a nominal distance of 6600 m and a safety sphere with a radius of 5 m.

Although it has been proven that the collision risk is low for the nominal calibration distance, it must be noted that the risk of getting closer to the CMB satellite without colliding is considerable higher. In Figure 6.29 the maximum instantaneous probability of collision for different nominal distances and safety radius sphere is shown. For the same formation control performance, the risk CalSat getting closer than 50 m is one thousand higher than the collision risk. This shall be taking into account to assess the risk of interfere with the nominal operation of the CMB satellite.

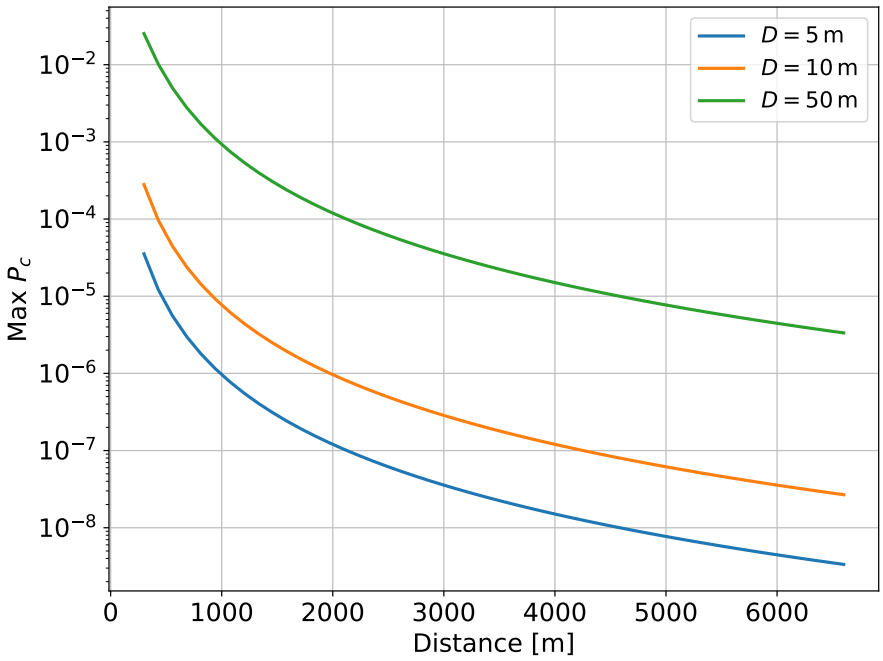


Figure 6.29: Maximum probability of collision for different formation distances and safety spheres sizes.

6.8 Cost budget

The cost analysis for CalSat mission has been done using a similar approach as the one presented in [128]. However, in this case the CS cost has been estimated by collecting prices of each of the main hardware components instead of using a mass-related equation to calculate the overall cost and then fractioning the cost by subsystems.

The first step has been the development of the Cost Breakdown Structure, shown in Figure 6.30, where the main element costs are identified. For the Space Segment Costs (see Table 6.31), the CS Bus and the CS Support System are divided in subsystems and the cost of each subsystem is calculated by aggregating the cost of their components.

The total estimated cost of the space segment is roughly 450 k€, which is similar to the estimations made by [129] for a 6U CubeSat mission to the Moon, comparable in complexity to CalSat.

The project level cost estimations (see Table 6.32) have been done based on cost fractions retrieved from [130] which are applied to the total space segment cost. As CalSat would operate as part of the LiteBird mission, some of the project level costs would be already covered and can be removed from the estimation for CalSat. The elements not considered are mission operations, science, launch services and ground data system. This makes a total cost for the project level of approximately 1.4 M€.

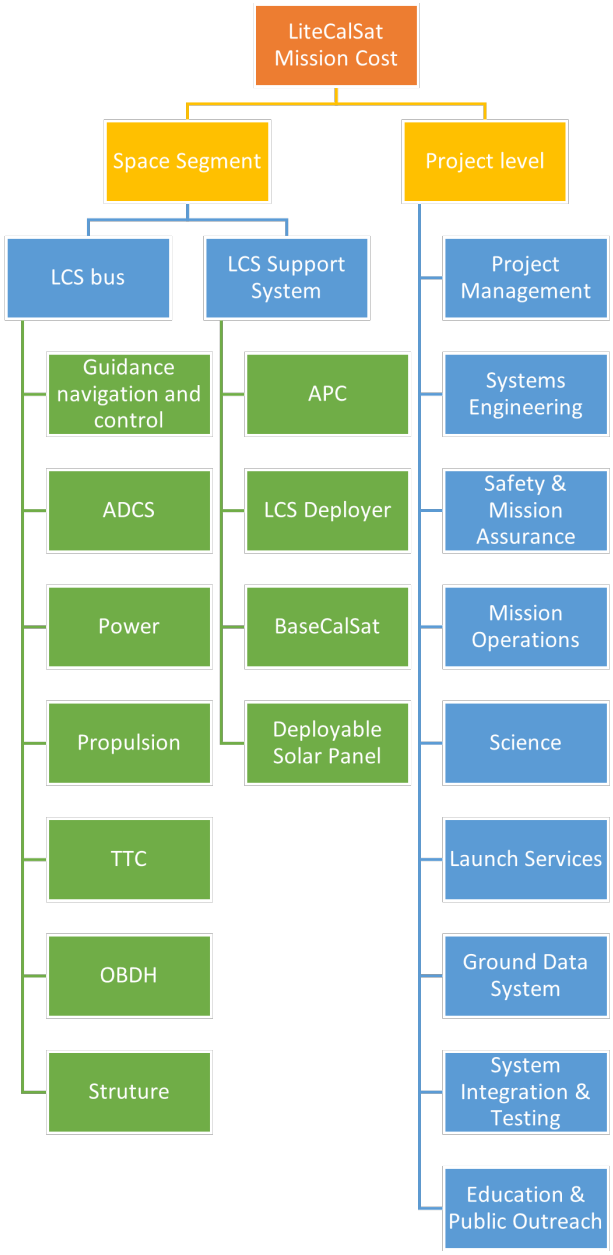


Figure 6.30: Cost Breakdown Structure for CalSat Mission.

Table 6.31: Space Segment Costs.

System	Subsystem			Estimated cost
CS	Guidance, Navigation & Control	2%	65%	10 000 €
	ADCS	16%		70 000 €
	Power	15%		67 500 €
	Propulsion	29%		130 000 €
	TTC	1%		2 500 €
	OBDH	1%		4 400 €
	Structure	2%		7 850 €
CS Support System	APC	2%	35%	10 000 €
	CS deployer	18%		80 000 €
	BaseCalsat	12%		52 400 €
	Deployable solar panel	3%		13 500 €
Total		100%		**445 550** €

Table 6.32: Project level costs. Element costs in italics are not considered for the computation of the Total project Level without global mission costs.

Project level	% of total S/C Bus cost	Estimated cost
Project Management	73.26%	328 608 €
System Engineer	76.36%	342 513 €
Safety & Mission Assurance	78.37%	351 529 €
Mission Ops	65.13%	292 141 €
Science	72.25%	324 077 €
Launch Services	78.37 %	351 529 €
Ground Data System	73.26%	328 608 €
System Integration & Testing	73.26%	328 608 €
Education % Public Outreach	7.54%	33 821 €
Total Project Level	597.80%	**2 681 532** €
Total Project Level w/o global mission costs	308.79%	**1 385 078** €

In Table 6.33 are presented the mission overall costs. As it can be observed, just over 75% of the total cost would be assumed by the project organization and activities while roughly 25% would be used for the acquisition of hardware.

Table 6.33: Mission overall costs.

Cost Element		**Estimated cost**
Space segment	24.5%	448 550 €
Project level	75.5%	1 385 078 €
Total		**1 833 628** €

Finally, the distribution of the cost throughout the mission phases has been performed using beta curves [130]. As can be seen in Table 6.34, half of the total cost concentrates in the last two phases (C and D), when most of the hardware would be acquired, integrated and tested.

Table 6.34: Distribution of costs among the development phases of the project.

Phase		**Estimated cost**
Phase A	1.6%	28 650 €
Phase B1	17.2%	315 155 €
Phase B2	27.3%	501 324 €
Phase C	34.3%	628 659 €
Phase D	19.6%	359 840 €

CHAPTER 7

Conclusions

The work presented in this doctoral dissertation aimed to assess the feasibility of a formation flying mission at Sun-Earth L_2. The formation under study is composed of a CMB observation satellite (chief) and a calibration ancillary satellite (deputy). In particular, three aspects have been analyzed in detail for this chief-deputy formation at such location: the control of the formation, its collision risk, and the visibility between the satellites. Finally, a preliminary design for the deputy, based on CubeSat architecture, has been presented.

In chapter 2, the theoretical background on the libration point dynamics has been presented, as a foundation for the developments presented in the following chapters.

In chapter 3, a proposal for the GNC subsystem of the deputy has been defined and analyzed. Three different modes are proposed for the control and guidance configuration (calibration, stand-by, and reconfiguration), defined according to the operational mission needs, while a Kalman Filter is employed for the navigation tasks. A Model Predictive Controller (MPC) has been proposed for the control of the formation. This controller is based on the linearized relative dynamics of the formation at L_2. This model has been applied both in the controller and in the Kalman Filter used for navigation. Although the MPC requires an optimization process with each controller action, the proper problem formulation and limitation of the horizon size enable faster computation, rendering it feasible as the formation controller.

The proposed GNC system has proved to be a feasible option for a chief-deputy mission on L_2. The MPC has been able to meet the objective of each control mode. To assess the control performance, the MPC controller has been compared through

numerical simulations with two well-known control laws (LQR and ETM) that serve as a baseline reference. The MPC controller has achieved similar precision to the baseline reference, with a lower ΔV cost in the Calibration mode. However, this reduction is not achieved in the Reconfiguration mode, in which the MPC requires a higher ΔV than the baseline reference.

An additional advantage of the MPC lies in its capability to easily incorporate control signal limits and a constraint to avoid collision between both satellites into the optimization problem. Furthermore, it combines the benefits of LQR (optimal solution) and ETM (discrete control with maneuvers separated by arbitrary time intervals). This adaptability allows its use it across all three control modes, with only the need to adjust the controller configuration. Its main limitations are its omission of the Solar Radiation Pressure (SRP) perturbation, which could potentially be included in the future, and the restriction on the horizon size, as previously discussed.

In chapter 4, the potential collision risk within the formation has been assessed in the event of critical failure of the deputy, which would leave it at the expense of the natural forces of the dynamic environment and with a residual relative velocity which depends on the formation control accuracy. To that end, and based on the assumption that the relative velocity dominates the system's dynamics during the initial time period, a semi-analytical method to compute the probability of collision has been proposed. This method, based on the formation configuration (size and minimum safe distance) and the formation control performance, allows to obtain the instantaneous probability of collision and the cumulative probability collision as a function of time.

This approach has been validated using the Monte Carlo method, yielding favorable results. Then, it has been employed in a case study to assess the impact of formation characteristics (size and minimum distance) and control accuracy on collision probabilities.

The presented method has proven to be much faster than the numerical alternative. This facilitates an evaluation of the interaction between formation parameters and control performance in order to select them while keeping the collision risk below a predefined threshold.

The primary limitation of this method is that, due to the exclusion of the SRP disturbance in the dynamic model on which it is based, the results tend to diverge (the error increases) over time when the satellites in the formation present different area-to-mass ratios.

In chapter 5, the visibility of the formation has been studied. A typical spin and precession scan strategy has been assumed for the main satellite acting as the chief. For the deputy, its visibility and access availability depend on its relative position, the chief's scanning strategy parameters and the FoV of the instrument to be calibrated.

In order to study the visibility and obtain a tool to evaluate and locate the best position for the deputy, three different time parameters have been analyzed: total access time, mean access time, and maximum access time. For each of these parameters and depending on the scanning strategy, an analytical calculation

method has been presented. These analytical solutions have been validated against the results from numerical simulations of the problem, obtaining satisfactory results. As in the case of the probability of collision, the advantage of the analytical formulation is that it allows for the evaluation of the performance of different scanning strategies quickly and easily compared to the numerical approach. It also allows for sensitivity analysis to be carried out by providing a clear view of the effect that the scan strategy and relative position have in the parameter variation.

In the same regard, a second level of analysis has been carried out to test other characteristics of the calibration not directly related to the access time: the percentage of calibrated instrument detectors and the variety of relative polarization orientations with which they observe the calibration source. This analysis was not well suited for analytical methods, but a numerical approach based on an instrument sensor distribution model has been proposed instead. Such a model allows us to evaluate the performance of a given calibration process at detector level and could be easily adapted to obtain other quantities and their distribution over the detectors array.

Finally, a case study based on different scanning strategy options for future scientific missions has been studied in order to test the proposed tools. Results show that the region around the precession axis presents the most favorable properties for all the parameters. Nevertheless, the final decision will be subject to a trade-off analysis according to the requirements of the particular calibration process. The results of this study provide tools to do so both rapidly and systematically.

In chapter 6 a first preliminary design has been carried out for the deputy, a calibration satellite for CMB space missions at the second Lagrange point of the Sun–Earth system. This design is in compliance with the requirements and objectives of a small-aperture CMB polarization mission, but can also be adapted to others, both in the microwave or in a different frequency range (optical, IR, etc.). The initial design of the calibration satellite was developed using a CDF, following the CubeSat conceptual framework of implementation, and then different subsystems and aspects of the missions have been iterated, increasing its level of detail. The calibration sources have been described and a simple but efficient and secure calibration strategy has been proposed.

The possibility of employing the CalSat concept to calibrate CMB telescopes in the L_2 libration point has been analyzed in the present work and the main conclusion drawn is that it is feasible. Furthermore, this work provides a set of tools that could help to design and develop such a mission. The CalSat can offer a unique source of calibration and opens the possibility of extending the concept to mitigate other systematic errors or even calibrate other telescopes in the same region. The use of formation flying in space missions at the libration points has not yet been carried out but this study demonstrates that the concept is feasible and the technology level is mature enough for a demonstration mission.

Future work

During the development of this doctoral dissertation, some future research lines have been identified:

- **MPC control with SRP**. The inclusion of SRP in the dynamics model of the MPC would further improve the performance of the controller and allow to expand the time between maneuvers without increasing the bias.
- **Extend the analytical methods for the collision risk analysis**. The presented method could be enhanced by including the SRP in the covariance propagation. This feature and the generalization of the method to not aligned error ellipsoids and safety spheres would allow its use for formations with different values of area-to-mass ratio.
- **Expanding the analytical methods for the visibility study**. The orbital motion of the satellite around the Sun could be incorporated and thus consider an annual period of time. Additionally, the methods could be adapted to study the same quantities at detector level.
- **Predesign**. Explore the alternative of using a microsatellite, which would allow to further reduce the impact on the main satellite architecture and could be deployed on its own capabilities into the nominal orbit at L_2.

Finally, regarding the code developed for this doctoral dissertation and in particular the astrodynamic library mubody, it has proven to be not only a valuable tool for studying advanced mission concepts but also a bridge to openly collaborate between students and with other research institutions. It is a reservoir of the acquired knowledge during the development of this dissertation, and if properly governed, it could serve as a stepping stone to reach further into more advanced research. All the code is available under the open source MIT license, with the aim of facilitating the replicability of these results and the use of the methods presented.

Appendices

APPENDIX A

Code repositories

The following libraries have been developed during this thesis:

- **mubody**: an astrodynamics library focused on libration point dynamics. It allows to propagate the motion of the satellites in this location, adding thrusting forces, and generate halo and Lissajous orbits. It provides simplified models of motion in the libration points (CRTBP) and also a high-fidelity model based on the N-body problem and the SRP perturbations. The theoretical fundamentals are explained in chapter 2.
- **ffnavpy**: this library implements the GNC simulator described in chapter 3. It allows to define simulation cases, with an arbitrary number of satellites, each one featuring an OBC. Such an OBC implements the GNC main functions, and is able to switch between different control and estimation modes and configurations, all by setting predefined commands. It uses mubody (or SEMpy) to propagate the motion of the satellites.
- **ffriskpy**: this library implements the analytical method presented in chapter 4 to compute the probability of collision in the formation. Furthermore, it also implements the Monte Carlo analysis required to compute numerically the same probability, based on the formation characteristics. For the Monte Carlo analysis, this library uses mubody to propagate the satellite trajectories.
- **nutpy**: this library gathers all the analytical and numerical methods presented in chapter 5 to perform the formation visibility analysis.

All the code is released under the MIT license with the aim of facilitating the replicability of these results and the use of the methods presented. It can be accessed in GitLab:

- mubody: `https://gitlab.com/mubody/mubody`
- ffnavpy, ffriskpy, and nutpy: `https://gitlab.com/phd-jb`

APPENDIX B

Libration points location

B.1 Collinear points

Substituting Equations (2.11) and (2.12) into (2.19), Equation (B.1) is obtained.

$$x - (1-\mu)\frac{x-x_1}{|x-x_1|^3} - \mu\frac{x-x_2}{|x-x_2|^3} = 0 \tag{B.1}$$

Equations for the location of the collinear libration points:

- L_1: $x_1 < x < x_2$
  In this case $x - x_1 > 0$ and $x - x_2 < 0$

$$x - \frac{1-\mu}{(x+\mu)^2} + \frac{\mu}{(x-1+\mu)^2} = 0 \tag{B.2}$$

- L_2: $x > x_2 > x_1$
  In this case $x - x_1 > 0$ and $x - x_2 > 0$

$$x - \frac{1-\mu}{(x+\mu)^2} - \frac{\mu}{(x-1+\mu)^2} = 0 \tag{B.3}$$

- L_3: $x < x_1 < x_2$
  In this case $x - x_1 < 0$ and $x - x_2 < 0$

$$x + \frac{1-\mu}{(x+\mu)^2} + \frac{\mu}{(x-1+\mu)^2} = 0 \tag{B.4}$$

These equations can be also expressed as polynomials in its canonical form:

$$a_5x^5 + a_4x^4 + a_3x^3 + a_2x^2 + a_1x + a_0 = 0 \tag{B.5}$$

with different coefficients for each case:

- L_1: $x_1 < x < x_2$

$$a_5 = 1 \tag{B.6}$$
$$a_4 = 4\mu - 2 \tag{B.7}$$
$$a_3 = 6\mu^2 - 6\mu + 1 \tag{B.8}$$
$$a_2 = 4\mu^3 - 6\mu^2 + 4\mu - 1 \tag{B.9}$$
$$a_1 = \mu^4 - 2\mu^3 + 5\mu^2 - 4\mu + 2 \tag{B.10}$$
$$a_0 = 2\mu^3 - 3\mu^2 + 3\mu - 1 \tag{B.11}$$

- L_2: $x_2 < x$

$$a_5 = 1 \tag{B.12}$$
$$a_4 = 4\mu - 2 \tag{B.13}$$
$$a_3 = 6\mu^2 - 6\mu + 1 \tag{B.14}$$
$$a_2 = 4\mu^3 - 6\mu^2 + 2\mu - 1 \tag{B.15}$$
$$a_1 = \mu^4 - 2\mu^3 + \mu^2 - 4\mu + 2 \tag{B.16}$$
$$a_0 = -3\mu^2 + 3\mu - 1 \tag{B.17}$$

- L_3: $x < x_1$

$$a_5 = 1 \tag{B.18}$$
$$a_4 = 4\mu - 2 \tag{B.19}$$
$$a_3 = 6\mu^2 - 6\mu + 1 \tag{B.20}$$
$$a_2 = 4\mu^3 - 6\mu^2 + 2\mu + 1 \tag{B.21}$$
$$a_1 = 4\mu^4 - 2\mu^3 + \mu^2 + 4\mu - 2 \tag{B.22}$$
$$a_0 = 3\mu^2 - 3\mu + 1 \tag{B.23}$$

These polynomials of fifth order does not present analytical solution and must be solved numerically. For the case of Sun-Earth system ($\mu = 3.0404235 \cdot 10^{-6}$), the location of the collinear libration points is:

$$L_1 = 0.989986 \tag{B.24}$$
$$L_2 = 1.0100752 \tag{B.25}$$
$$L_3 = -1.0000013 \tag{B.26}$$

Instead of finding the position of the collinear libration points in the synodic frame, it is possible to modify the previous equations in order to obtain the distance from the libration point to the closest primary γ_i (see Figure B.1).

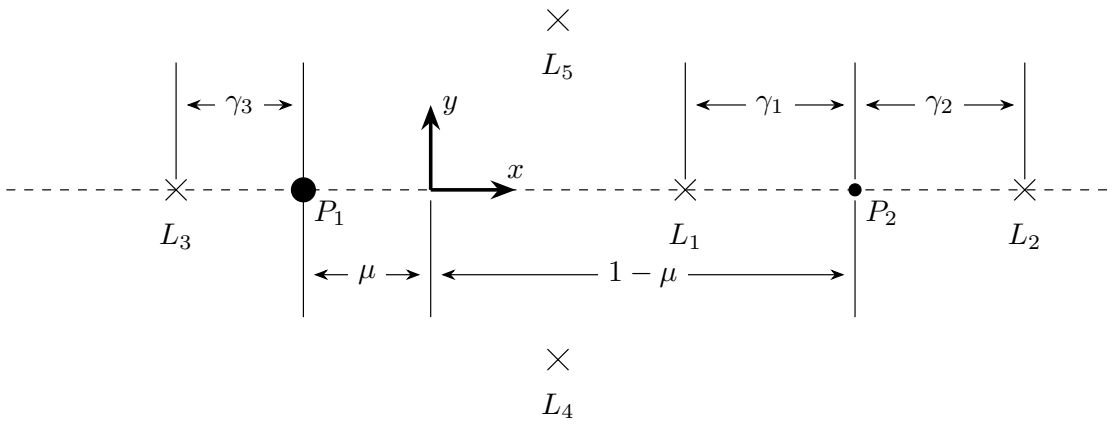


Figure B.1: Location of the collinear libration points regarding the closest primary.

Substituting x by its corresponding equivalence with γ_i according to the libration point, the following expressions are obtained:

- L_1: $x = 1 - \mu - \gamma_1$

$$\gamma_1^5 - (3-\mu)\gamma_1^4 + (3-2\mu)\gamma_1^3 - \mu\gamma_1^2 + 2\mu\gamma_1 - \mu = 0 \tag{B.27}$$

- L_2: $x = 1 - \mu + \gamma_2$

$$\gamma_2^5 + (3-\mu)\gamma_2^4 + (3-2\mu)\gamma_2^3 - \mu\gamma_2^2 - 2\mu\gamma_2 - \mu = 0 \tag{B.28}$$

- L_3: $x = -\mu - \gamma_2$

$$\gamma_3^5 + (2+\mu)\gamma_3^4 + (1+2\mu)\gamma_3^3 - (1-\mu)\gamma_3^2 - (2-2\mu)\gamma_3 - (1-\mu) = 0 \tag{B.29}$$

which, for the case of Sun-Earth system gives:

$$\gamma_1 = 0.010010977 \tag{B.30}$$
$$\gamma_2 = 0.01007824 \tag{B.31}$$
$$\gamma_3 = 0.9999982 \tag{B.32}$$

B.2 Triangular points

The location of the triangular points is significantly easier to find compared to that of collinear points. The triangular libration points are located at the same distance from both primaries, i.e. at the vertex of an equilateral triangle whose base is the line between the two primaries (see Figure 2.2). As the length of this line is one under the normalized units, the distance from the primaries to either L_4 or L_5 must be one. Therefore, the coordinates of the triangular points are:

$$L_4 = \begin{pmatrix} 1/2 - \mu \\ \sqrt{3/2} \\ 0 \end{pmatrix} \tag{B.33}$$

$$L_5 = \begin{pmatrix} 1/2 - \mu \\ -\sqrt{3/2} \\ 0 \end{pmatrix} \tag{B.34}$$

which, for the case of Sun-Earth system ($\mu = 3.0404235 \cdot 10^{-6}$) gives:

$$L_4 = \begin{pmatrix} 0.49999696 \\ 0.8660254 \\ 0 \end{pmatrix} \tag{B.35}$$

$$L_5 = \begin{pmatrix} 0.49999696 \\ -0.8660254 \\ 0 \end{pmatrix} \tag{B.36}$$

APPENDIX C

Linearization of CRTBP equations

The equations of motion of the Circular Restricted Three Body Problem (CRTBP) are in Eq. (2.13). These equations can be expressed in matrix form, with $\boldsymbol{r} = \begin{pmatrix} x & y & z \end{pmatrix}^\top$:

$$\ddot{\boldsymbol{r}} = \underbrace{\begin{pmatrix} 1 & 0 & 0 \\ 0 & 1 & 0 \\ 0 & 0 & 0 \end{pmatrix}}_{\mathrm{M}_1} \boldsymbol{r} + \underbrace{\begin{pmatrix} 0 & 2 & 0 \\ -2 & 0 & 0 \\ 0 & 0 & 0 \end{pmatrix}}_{\mathrm{M}_2} \dot{\boldsymbol{r}} \underbrace{-\frac{1-\mu}{\rho_1^3}(\boldsymbol{r}-\boldsymbol{r}_1) - \frac{\mu}{\rho_2^3}(\boldsymbol{r}-\boldsymbol{r}_2)}_{\boldsymbol{f}(\boldsymbol{r})} \tag{C.1}$$

with $\boldsymbol{r}_1 = \begin{pmatrix} -\mu & 0 & 0 \end{pmatrix}^\top$ and $\boldsymbol{r}_2 = \begin{pmatrix} 1-\mu & 0 & 0 \end{pmatrix}^\top$ being the position of the primaries.

Let $\boldsymbol{r}_{L_2} = \begin{pmatrix} x_L & 0 & 0 \end{pmatrix}^\top$ denote the coordinates of L_2. The linearization of $\boldsymbol{f}(\boldsymbol{r})$ around $\boldsymbol{r}_{L_2}$ yields:

$$\boldsymbol{f}(\boldsymbol{r}) \approx \boldsymbol{f}(\boldsymbol{r}) + \left.\frac{\partial \boldsymbol{f}}{\partial \boldsymbol{r}}\right|_{\boldsymbol{r}_{L_2}} (\boldsymbol{r} - \boldsymbol{r}_{L_2}) \tag{C.2}$$

$$\frac{\partial \boldsymbol{f}}{\partial \boldsymbol{r}} = \underbrace{\frac{\partial}{\partial \boldsymbol{r}}\left[-\frac{1-\mu}{\rho_1^3}(\boldsymbol{r}-\boldsymbol{r}_1)\right]}_{\mathrm{B}} + \underbrace{\frac{\partial}{\partial \boldsymbol{r}}\left[-\frac{\mu}{\rho_2^3}(\boldsymbol{r}-\boldsymbol{r}_2)\right]}_{\mathrm{C}} \tag{C.3}$$

$$\mathrm{B} = -(1-\mu)\left[\underbrace{\frac{\partial(1/\rho_1^3)}{\partial \boldsymbol{r}}(\boldsymbol{r}-\boldsymbol{r}_1)}_{\mathrm{B}_1} + \underbrace{\frac{1}{\rho_1^3}\frac{\partial(\boldsymbol{r}-\boldsymbol{r}_1)}{\partial \boldsymbol{r}}}_{\mathrm{B}_2}\right] \tag{C.4}$$

$$\mathrm{B}_1 = \frac{-3}{\rho_1^4}\frac{\partial \rho_1}{\partial \boldsymbol{r}}(\boldsymbol{r}-\boldsymbol{r}_1) = \frac{-3}{\rho_1^4}\frac{(\boldsymbol{r}-\boldsymbol{r}_1)^\top}{\rho_1}(\boldsymbol{r}-\boldsymbol{r}_1) \tag{C.5a}$$

$$\mathrm{B}_2 = \frac{1}{\rho_1^3}\mathrm{I}_{3\times 3} \tag{C.5b}$$

$$\mathrm{B}_1|_{\boldsymbol{r}_{L_2}} = \frac{-3}{|x_L+\mu|^5}\begin{pmatrix} |x_L+\mu|^2 & 0 & 0 \\ 0 & 0 & 0 \\ 0 & 0 & 0 \end{pmatrix} \tag{C.6a}$$

$$\mathrm{B}_2|_{\boldsymbol{r}_{L_2}} = \frac{1}{|x_L+\mu|^3}\mathrm{I}_{3\times 3} \tag{C.6b}$$

$$\mathrm{B}|_{\boldsymbol{r}_{L_2}} = \frac{1-\mu}{|x_L+\mu|^3}\begin{pmatrix} 2 & 0 & 0 \\ 0 & -1 & 0 \\ 0 & 0 & -1 \end{pmatrix} \tag{C.7}$$

$$\mathrm{C} = -\mu\left[\underbrace{\frac{\partial(1/\rho_2^3)}{\partial \boldsymbol{r}}(\boldsymbol{r}-\boldsymbol{r}_2)}_{\mathrm{C}_1} + \underbrace{\frac{1}{\rho_2^3}\frac{\partial(\boldsymbol{r}-\boldsymbol{r}_2)}{\partial \boldsymbol{r}}}_{\mathrm{C}_2}\right] \tag{C.8}$$

$$\mathrm{C}_1 = \frac{-3}{\rho_2^4}\frac{\partial \rho_2}{\partial \boldsymbol{r}}(\boldsymbol{r}-\boldsymbol{r}_2) = \frac{-3}{\rho_2^4}\frac{(\boldsymbol{r}-\boldsymbol{r}_1)^\top}{\rho_2}(\boldsymbol{r}-\boldsymbol{r}_2) \tag{C.9a}$$

$$\mathrm{C}_2 = \frac{1}{\rho_2^3}\mathrm{I}_{3\times 3} \tag{C.9b}$$

$$\mathrm{C}_1|_{\boldsymbol{r}_{L_2}} = \frac{-3}{|x_L-(1-\mu)|^3}\begin{pmatrix} |x_L-(1-\mu)|^2 & 0 & 0 \\ 0 & 0 & 0 \\ 0 & 0 & 0 \end{pmatrix} \tag{C.10a}$$

$$\mathrm{C}_2|_{\boldsymbol{r}_{L_2}} = \frac{1}{|x_L-(1-\mu)|^2}\mathrm{I}_{3\times 3} \tag{C.10b}$$

$$\mathrm{C}|_{\boldsymbol{r}_{L_2}} = \frac{\mu}{|x_L-(1-\mu)|^3}\begin{pmatrix} 2 & 0 & 0 \\ 0 & -1 & 0 \\ 0 & 0 & -1 \end{pmatrix} \tag{C.11}$$

$$\left.\frac{\partial \boldsymbol{f}}{\partial \boldsymbol{r}}\right|_{\boldsymbol{r}_{L_2}} = \left(\frac{1-\mu}{|x_L+\mu|^3} + \frac{\mu}{|x_L-(1-\mu)|^3}\right) \begin{pmatrix} 2 & 0 & 0 \\ 0 & -1 & 0 \\ 0 & 0 & -1 \end{pmatrix} = \begin{pmatrix} 2\alpha & 0 & 0 \\ 0 & -\alpha & 0 \\ 0 & 0 & -\alpha \end{pmatrix} \tag{C.12}$$

Useful expressions:

$$\frac{\partial(\boldsymbol{r}-\boldsymbol{r}_i)}{\partial \boldsymbol{r}} = \mathrm{I}_{3\times 3}, \quad \boldsymbol{r}_i \in cte \tag{C.13}$$

$$|\boldsymbol{f}(x)|' = \frac{\boldsymbol{f}(x)^\top}{|\boldsymbol{f}(x)|}\boldsymbol{f}'(x) \tag{C.14}$$

$$\rho_i = |\boldsymbol{r}-\boldsymbol{r}_i| \tag{C.15a}$$
$$\rho_1|_{\boldsymbol{r}_{L_2}} = |x_L+\mu| \tag{C.15b}$$
$$\rho_2|_{\boldsymbol{r}_{L_2}} = |x_L-(1-\mu)| \tag{C.15c}$$

$$\frac{\partial \rho_i}{\partial \boldsymbol{r}} = \frac{\partial|\boldsymbol{r}-\boldsymbol{r}_i|}{\partial \boldsymbol{r}} = \frac{(\boldsymbol{r}-\boldsymbol{r}_i)^\top}{|\boldsymbol{r}-\boldsymbol{r}_i|} = \frac{(\boldsymbol{r}-\boldsymbol{r}_i)^\top}{\rho_i}\mathrm{I}_{3\times 3} = \frac{(\boldsymbol{r}-\boldsymbol{r}_i)^\top}{\rho_i} \tag{C.16}$$

$$(\boldsymbol{r}-\boldsymbol{r}_i)(\boldsymbol{r}-\boldsymbol{r}_i)^\top\big|_{\boldsymbol{r}_{L_2}} = \begin{pmatrix} |x_L-x_i|^2 & 0 & 0 \\ 0 & 0 & 0 \\ 0 & 0 & 0 \end{pmatrix} \tag{C.17}$$

APPENDIX D

Multiple-shooting scheme

The formulation presented here was first applied to LPO by Howell [54] and only reduces the ΔV of each interior patchpoint. The method is first presented for the case of three patchpoints (see Figure D.1, 'o', 'p' and 'f', with a ΔV maneuver applied in 'p'. The goal is to express ΔV as a function of the change in positions of 'o', 'p', and 'f' and changes in the segment times and compute those changes to drive ΔV to zero.

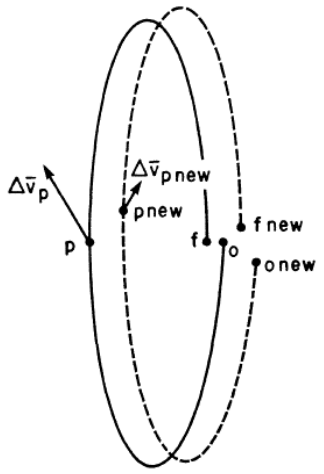


Figure D.1: Multiple-shooting scheme.

First, it is considered the propagation backwards from 'f' to 'p' and expressed using the STM and the variation of the time segment:

$$\delta \boldsymbol{X} = \Phi(t_p, t_f)\delta \boldsymbol{X}_f + \left.\frac{\partial X}{\partial t}\right|_{p^+} (\delta t_{p^+} - \delta t_f) \tag{D.1}$$

where the symbol p^+ indicate conditions at 'p' on segment two and p^- on segment one. Also, the STM is divided into four submatrices of 3×3:

$$\Phi(t_p, t_f) = \begin{bmatrix} \mathrm{A}_{pf} & \mathrm{B}_{pf} \\ \mathrm{C}_{pf} & \mathrm{D}_{pf} \end{bmatrix} \tag{D.2}$$

Then, the Eq. (D.1) can be rewritten:

$$\begin{pmatrix} \delta \boldsymbol{r}_{p^+} \\ \delta \boldsymbol{v}_{p^+} \end{pmatrix} = \begin{bmatrix} \mathrm{A}_{pf} & \mathrm{B}_{pf} \\ \mathrm{C}_{pf} & \mathrm{D}_{pf} \end{bmatrix} \begin{pmatrix} \delta \boldsymbol{r}_f \\ \delta \boldsymbol{v}_f \end{pmatrix} + \begin{pmatrix} \boldsymbol{v}_{p^+} \\ \boldsymbol{a}_{p^+} \end{pmatrix} (\delta t_{p^+} - \delta t_f) \tag{D.3}$$

where $\boldsymbol{a}$ is the acceleration vector. Solving the previous equation for $\delta \boldsymbol{v}_f$:

$$\delta \boldsymbol{v}_f = \mathrm{B}_{pf}^{-1}\delta \boldsymbol{r}_{p^+} - \mathrm{B}_{pf}^{-1}\mathrm{A}_{pf}\delta \boldsymbol{r}_f - \mathrm{B}_{pf}^{-1}\boldsymbol{v}_{p^+}(\delta t_{p^+} - \delta t_f) \tag{D.4}$$

Substituting this equation into the second vector equation of Eq. (D.3) yields

$$\delta \boldsymbol{v}_{p^+} = (\mathrm{C}_{pf} - \mathrm{D}_{pf}\mathrm{B}_{pf}^{-1}\mathrm{A}_{pf})\delta \boldsymbol{r}_f + \mathrm{D}_{pf}\mathrm{B}_{pf}^{-1}\delta \boldsymbol{r}_{p^+} - (\mathrm{D}_{pf}\mathrm{B}_{pf}^{-1}\boldsymbol{v}_{p^+} - \boldsymbol{a}_{p^+})(\delta t_{p^+} - \delta t_f) \tag{D.5}$$

Analogously, the equation for the first segment (from 'o' to 'p') is:

$$\delta \boldsymbol{v}_{p^-} = (\mathrm{C}_{p0} - \mathrm{D}_{p0}\mathrm{B}_{p0}^{-1}\mathrm{A}_{p0})\delta \boldsymbol{r}_0 + \mathrm{D}_{p0}\mathrm{B}_{p0}^{-1}\delta \boldsymbol{r}_{p^-} - (\mathrm{D}_{p0}\mathrm{B}_{p0}^{-1}\boldsymbol{v}_{p^-} - \boldsymbol{a}_{p^-})(\delta t_{p^-} - \delta t_0) \tag{D.6}$$

Subtracting Eq. (D.6) from Eq. (D.5) and constraining position and time at point 'p' to be the same for both segments, i.e., $\boldsymbol{r}_{p^+} = \boldsymbol{r}_{p^-}$ and $t_{p^+} = t_{p^-}$, produces:

$$\delta \Delta \boldsymbol{v}_p = \begin{bmatrix} \mathrm{M}_0 & \mathrm{M}_{t_0} & \mathrm{M}_p & \mathrm{M}_{t_p} & \mathrm{M}_f & \mathrm{M}_{t_f} \end{bmatrix} \begin{bmatrix} \delta \boldsymbol{r}_0 \\ \delta t_0 \\ \delta \boldsymbol{r}_p \\ \delta t_p \\ \delta \boldsymbol{r}_f \\ \delta t_f \end{bmatrix} \tag{D.7}$$

where the M matrices are defined as:

$$\mathrm{M}_0 = \mathrm{D}_{p0}\mathrm{B}_{p0}^{-1}\mathrm{A}_{p0} - \mathrm{C}_{p0} \tag{D.8}$$

$$\mathrm{M}_{t_0} = \boldsymbol{a}_{p^-} - \mathrm{D}_{p0}\mathrm{B}_{p0}^{-1}\boldsymbol{v}_{p^-} \tag{D.9}$$

$$\mathrm{M}_p = \mathrm{D}_{pf}\mathrm{B}_{pf}^{-1} - \mathrm{D}_{p0}\mathrm{B}_{p0}^{-1} \tag{D.10}$$

$$\mathrm{M}_{t_p} = \mathrm{D}_{p0}\mathrm{B}_{p0}^{-1}\boldsymbol{v}_{p^-} - \mathrm{D}_{pf}\mathrm{B}_{pf}^{-1}\boldsymbol{v}_{p^+} + \boldsymbol{a}_{p^+} - \boldsymbol{a}_{p^-} \tag{D.11}$$

$$\mathrm{M}_f = \mathrm{C}_{pf} - \mathrm{D}_{pf}\mathrm{B}_{pf}^{-1}\mathrm{A}_{pf} \tag{D.12}$$

$$\mathrm{M}_{t_f} = \mathrm{D}_{pf}\mathrm{B}_{pf}^{-1}\boldsymbol{v}_{p^+} - \boldsymbol{a}_{p^+} \tag{D.13}$$

$$\tag{D.14}$$

As it is desired to drive $\Delta \boldsymbol{v}_p$ to zero, $\delta \Delta \boldsymbol{v}_p = -\Delta \boldsymbol{v}_p$. The system of Eq. (D.7) has three equations and twelve unknowns so the chosen solution is the one with the

smallest norm. Now, if n segments are considered ($n+1$ points), the Eq. (D.7) can be generalizes as:

$$[\mathrm{M}]\delta\boldsymbol{r} = \Delta\boldsymbol{v} \tag{D.15}$$

where

$$\delta\boldsymbol{r} = \begin{Bmatrix} \delta\boldsymbol{r}_0 \\ \delta t_0 \\ \delta\boldsymbol{r}_1 \\ \delta t_1 \\ \delta\boldsymbol{r}_2 \\ \delta t_2 \\ \delta\boldsymbol{r}_3 \\ \delta t_3 \\ \vdots \\ \delta\boldsymbol{r}_0 \\ \delta t_n \end{Bmatrix}; \quad -\Delta\boldsymbol{v} = \begin{Bmatrix} -\Delta\boldsymbol{v}_1 \\ -\Delta\boldsymbol{v}_2 \\ -\Delta\boldsymbol{v}_3 \\ \vdots \\ -\Delta\boldsymbol{v}_{n-1} \end{Bmatrix} \tag{D.16}$$

and

$$[\mathrm{M}] = \begin{bmatrix} \mathrm{M}_{0_1} & \mathrm{M}_{t_{0_1}} & \mathrm{M}_{p_1} & \mathrm{M}_{t_{p_1}} & \mathrm{M}_{f_1} & \mathrm{M}_{t_{f_1}} & 0 & 0 & 0 & 0 & \dots & 0 \\ 0 & 0 & \mathrm{M}_{0_2} & \mathrm{M}_{t_{0_2}} & \mathrm{M}_{p_2} & \mathrm{M}_{t_{p_2}} & \mathrm{M}_{f_2} & \mathrm{M}_{t_{f_2}} & 0 & 0 & \dots & 0 \\ 0 & 0 & 0 & 0 & \mathrm{M}_{0_3} & \mathrm{M}_{t_{0_3}} & \mathrm{M}_{p_3} & \mathrm{M}_{t_{p_3}} & \mathrm{M}_{f_3} & \mathrm{M}_{t_{f_3}} & \dots & 0 \\ & . & & & & & . & & . & & & \\ & & . & & & & & . & & . & & \\ & & & . & & & & & . & & . & \\ 0 & 0 & 0 & 0 & \dots & 0 & \mathrm{M}_{0_{n-1}} & \mathrm{M}_{t_{0_{n-1}}} & \mathrm{M}_{p_{n-1}} & \mathrm{M}_{t_{p_{n-1}}} & \mathrm{M}_{f_{n-1}} & \mathrm{M}_{t_{f_{n-1}}} \end{bmatrix} \tag{D.17}$$

M is of dimension $(3n-3)\times(4n+4)$, $\delta\boldsymbol{r}$ is a column vector of length $(4n+4)$ and $\Delta\boldsymbol{v}$ is a column vector with $(3n-3)$ elements for $n \geq 2$. The solution that minimizes $||\delta\boldsymbol{r}||$ is:

$$\delta\boldsymbol{r} = -\mathrm{M}^\top(\mathrm{M}\mathrm{M}^\top)^{-1}\Delta\boldsymbol{v} \tag{D.18}$$

An advanced version of the second level that incorporates constraints can be found in [57].

APPENDIX E

Coordinate systems

E.1 Spherical coordinate system

Spherical coordinates are often more convenient when dealing with problems that involve spherical symmetry. In the spherical coordinate system (see Figure E.1), a point is represented as (r, θ, ϕ), where:

- r is the radial distance from the origin to the point.
- θ is the polar angle, which is the angle between the positive z-axis and the line connecting the origin to the point. It ranges from 0° to 180°.
- ϕ is the azimuthal angle, which is the angle between the positive x-axis and the projection of the line connecting the origin to the point onto the xy-plane. It ranges from 0° to 360°.

The transformation between Cartesian and spherical coordinates is made through the following equations:

$$r = \sqrt{x^2 + y^2 + z^2} \tag{E.1}$$

$$\theta = \arctan\left(\frac{y}{x}\right) \tag{E.2}$$

$$\phi = \arccos\left(\frac{z}{r}\right) \tag{E.3}$$

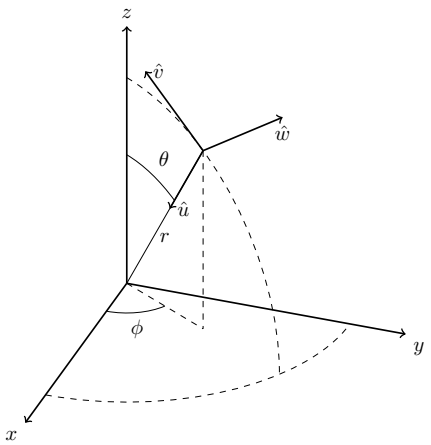


Figure E.1: Spherical coordinates and the local coordinate frame asociated.

In the context of spherical coordinates, a local coordinate system can be established at a given point in a three-dimensional space. Its basis vectors are essential to describe directions and vectors associated with spherical coordinates (r, θ, ϕ) at that specific location. These basis vectors are defined as follows:

- The downward unit vector, denoted as $\hat{\boldsymbol{u}}$, points from the specific point in space to the origin.

$$\hat{\boldsymbol{u}} = \begin{pmatrix} -\sin(\theta)\cos(\phi) & -\sin(\theta)\sin(\phi) & -\cos(\theta) \end{pmatrix}^\top \tag{E.4}$$

- The polar unit vector, denoted as $\hat{\boldsymbol{v}}$, is orthogonal to the downward direction and indicates the direction of decreasing θ. It can be expressed as:

$$\hat{\boldsymbol{v}} = \begin{pmatrix} -\cos(\theta)\cos(\phi) & -\cos(\theta)\sin(\phi) & \sin(\theta) \end{pmatrix}^\top \tag{E.5}$$

- The azimuthal unit vector, denoted as $\hat{\boldsymbol{w}}$, is orthogonal to both the downward and polar directions, indicating the direction of increasing ϕ. It is defined as:

$$\hat{\boldsymbol{w}} = \begin{pmatrix} -\sin(\phi) & \cos(\phi) & 0 \end{pmatrix}^\top \tag{E.6}$$

The rotation matrix to transform coordinates from this local coordinate frame to Cartesian is:

$$\mathrm{R} = \begin{pmatrix} -\sin(\theta)\cos(\phi) & -\cos(\theta)\cos(\phi) & -\sin(\phi) \\ -\sin(\theta)\sin(\phi) & -\cos(\theta)\sin(\phi) & \cos(\phi) \\ -\cos(\theta) & -\sin(\theta) & 0 \end{pmatrix} \tag{E.7}$$

The transpose of this matrix provides the inverse transformation.

Bibliography

[1] Johannes STHOENMAEKERS, Rüdiger Jehn, Markus Landgraf, and Michael Khan. Mission analysis towards a european harmonisation. *ESA bulletin*, 134:10–19, 2008.

[2] James R Wertz, David F Everett, and Jeffery J Puschell. *Space mission engineering: the new SMAD*. Microcosm Press, 2011.

[3] STScI. Historical sensitivity estimates. URL `https://www.stsci.edu/jwst/about-jwst/history/historical-sensitivity-estimates`.

[4] Tommaso Ghigna, Tomotake Matsumura, Guillaume Patanchon, Hirokazu Ishino, and Masashi Hazumi. Requirements for future cmb satellite missions: photometric and band-pass response calibration. *Journal of Cosmology and Astroparticle Physics*, 2020(11):030, 2020.

[5] Marc Kamionkowski and Ely D Kovetz. The quest for b modes from inflationary gravitational waves. *Annual Review of Astronomy and Astrophysics*, 54:227–269, 2016.

[6] Antje Ludewig, Quintus Kleipool, Rolf Bartstra, Robin Landzaat, Jonatan Leloux, Erwin Loots, Peter Meijering, Emiel van der Plas, Nico Rozemeijer, Frank Vonk, et al. In-flight calibration results of the tropomi payload on board the sentinel-5 precursor satellite. *Atmospheric Measurement Techniques*, 13(7):3561–3580, 2020.

[7] Xin Jing, Larry Leigh, Dennis Helder, Cibele Teixeira Pinto, and David Aaron. Lifetime absolute calibration of the eo-1 hyperion sensor and its validation. *IEEE Transactions on Geoscience and Remote Sensing*, 57(11):9466–9475, 2019. doi: 10.1109/TGRS.2019.2926663.

[8] J. Aumont, J. F. Macías-Pérez, A. Ritacco, N. Ponthieu, and A. Mangilli. Absolute calibration of the polarisation angle for future cmb b-mode experiments from current and future measurements of the crab nebula. *Astronomy & Astrophysics*, 634, 2020. doi: 10.1051/0004-6361/201833504.

[9] Jacques Delabrouille, Maximilian H Abitbol, Nabila Aghanim, Yacine Ali-Haïmoud, David Alonso, Marcelo Alvarez, Anthony J Banday, James G Bartlett, Jochem Baselmans, Kaustuv Basu, et al. Microwave spectro-polarimetry of matter and radiation across space and time. *arXiv preprint arXiv:1909.01591*, 2019.

[10] Masashi Hazumi, Peter AR Ade, Alexandre Adler, Erwan Allys, David Alonso, Kam Arnold, Didier Auguste, Jonathan Aumont, Ragnhild Aurlien, Jason Austermann, et al. LiteBIRD satellite: JAXA's new strategic L-class mission for all-sky surveys of cosmic microwave background polarization. In *Space Telescopes and Instrumentation 2020: Optical, Infrared, and Millimeter Wave*, volume 11443, page 114432F. International Society for Optics and Photonics, 2020.

[11] Brian M Sutin, Marcelo Alvarez, Nicholas Battaglia, Jamie Bock, Matteo Bonato, Jullian Borrill, David T Chuss, Joelle Cooperrider, Brendan Crill, Jacques Delabrouille, et al. PICO-the probe of inflation and cosmic origins. In *Space Telescopes and Instrumentation 2018: Optical, Infrared, and Millimeter Wave*, volume 10698, page 106984F. International Society for Optics and Photonics, 2018.

[12] Bradley R Johnson, Clement J Vourch, Timothy D Drysdale, Andrew Kalman, Steve Fujikawa, Brian Keating, and Jon Kaufman. A CubeSat for calibrating ground-based and sub-orbital millimeter-wave polarimeters (CalSat). *Journal of Astronomical Instrumentation*, 4(03n04):1550007, 2015.

[13] Juan BERMEJO-BALLESTEROS, Sergio GARCIA-GONZALEZ, Javier CUBAS, Francisco Javier Casas REINARES, and Enrique Martinez GONZALEZ. Development of a calibration satellite for a cmb telescope flying in formation about l2 libration point. In *8th European Conference for Aeronautics and Space Sciences*, 2019. doi: 10.13009/eucass2019-697.

[14] Francisco J Casas, Enrique Martínez-González, Juan Bermejo-Ballesteros, Sergio García, Javier Cubas, Patricio Vielva, Rita B Barreiro, and Angel Sanz. L2-calsat: A calibration satellite for ultra-sensitive cmb polarization space missions. *Sensors*, 21(10):3361, 2021.

[15] J Delabrouille, P De Bernardis, FR Bouchet, A Achúcarro, PAR Ade, R Allison, F Arroja, E Artal, M Ashdown, C Baccigalupi, et al. Exploring cosmic origins with CORE: Survey requirements and mission design. *Journal of Cosmology and Astroparticle Physics*, 2018(04):014, 2018.

[16] James Bock, Asantha Cooray, Shaul Hanany, Brian Keating, Adrian Lee, Tomotake Matsumura, Michael Milligan, Nicolas Ponthieu, Tom Renbarger, and Huan Tran. The Experimental Probe of Inflationary Cosmology (EPIC): a mission concept study for NASA's Einstein inflation probe. *arXiv preprint arXiv:0805.4207*, 2008.

[17] Xavier Dupac and Jan Tauber. Scanning strategy for mapping the Cosmic Microwave Background anisotropies with Planck. *Astronomy & Astrophysics*, 430(1):363–371, 2005.

[18] Saptarshi Bandyopadhyay, Rebecca Foust, Giri P. Subramanian, Soon-Jo

Chung, and Fred Y. Hadaegh. Review of formation flying and constellation missions using nanosatellites. *Journal of Spacecraft and Rockets*, 53(3): 567–578, 2016. doi: 10.2514/1.A33291. URL https://doi.org/10.2514/1.A33291.

[19] Ewan S Douglas, Jared R Males, James Clark, Olivier Guyon, J Lumbres, W Marlow, and Kerri L Cahoy. Laser guide star for large segmented-aperture space telescopes. i. implications for terrestrial exoplanet detection and observatory stability. *The Astronomical Journal*, 157(1):36, 2019.

[20] Kenneth G Carpenter, Carolus J Schrijver, Margarita Karovska, and SI Mission Concept Development Team. The stellar imager (si) project: a deep space uv/optical interferometer (uvoi) to observe the universe at 0.1 milli-arcsec angular resolution. *Astrophysics and Space Science*, 320:217–223, 2009.

[21] Shufan Wu, Wen Chen, Yonghe Zhang, Willem Baan, and Tao An. Sulfro: a swarm of nano-/micro-satellite at se l2 for space ultra-low frequency radio observatory. In *28th Annual AIAA/USU Conference on Small Satellites*, 2014.

[22] Sara Seager, Margaret Turnbull, William Sparks, Mark Thomson, Stuart B Shaklan, Aki Roberge, Marc Kuchner, N Jeremy Kasdin, Shawn Domagal-Goldman, Webster Cash, et al. The exo-s probe class starshade mission. In *Techniques and Instrumentation for Detection of Exoplanets VII*, volume 9605, pages 273–290. SPIE, 2015.

[23] Daria Malyh, Sergey Vaulin, Victor Fedorov, Ruslan Peshkov, and Mikhail Shalashov. A brief review on in-orbit refueling projects and critical techniques. *Aerospace Systems*, 5(2):185–196, 2022.

[24] Wei-Jie Li, Da-Yi Cheng, Xi-Gang Liu, Yao-Bing Wang, Wen-Hua Shi, Zi-Xin Tang, Feng Gao, Fu-Ming Zeng, Hong-You Chai, Wen-Bo Luo, et al. On-orbit service (oos) of spacecraft: A review of engineering developments. *Progress in Aerospace Sciences*, 108:32–120, 2019.

[25] Martin N Sweeting. Modern small satellites-changing the economics of space. *Proceedings of the IEEE*, 106(3):343–361, 2018.

[26] Robyn M. Millan, Rudolf von Steiger, Meir Ariel, Sergey Bartalev, Maurice Borgeaud, Stefano Campagnola, Julie C. Castillo-Rogez, René Fléron, Volker Gass, Anna Gregorio, David M. Klumpar, Bhavya Lal, Malcolm Macdonald, Jong Uk Park, V. Sambasiva Rao, Klaus Schilling, Graeme Stephens, Alan M. Title, and Ji Wu. Small satellites for space science: A cospar scientific roadmap. *Advances in Space Research*, 64(8):1466–1517, 2019. ISSN 0273-1177. doi: https://doi.org/10.1016/j.asr.2019.07.035. URL https://www.sciencedirect.com/science/article/pii/S0273117719305411.

[27] Stephen Serjeant, Martin Elvis, and Giovanna Tinetti. The future of astronomy with small satellites. *Nature Astronomy*, 4(11):1031–1038, 2020.

[28] Andrew Klesh, Brian Clement, Cody Colley, John Essmiller, Daniel Forgette, Joel Krajewski, Anne Marinan, and Tomas Martin-Mur. Marco: Early operations of the first cubesats to mars. 2018.

[29] Elisabetta Dotto, Vincenzo Della Corte, Marilena Amoroso, I Bertini, JR Brucato, A Capannolo, B Cotugno, G Cremonese, V Di Tana, I Gai, et al. Liciacube-the light italian cubesat for imaging of asteroids in support of the nasa dart mission towards asteroid (65803) didymos. *Planetary and Space Science*, 199:105185, 2021.

[30] Ryu Funase, Shintaro Nakajima, Yosuke Kawabata, Ryota Fuse, Hokuto Sekine, and Hiroyuki Koizumi. Equuleus: Initial operation results of an artemis-1 cubesat to the earth—moon lagrange point. 2023.

[31] Adam Koenig, Simone D'Amico, and E Glenn Lightsey. Formation flying orbit and control concept for the visors mission. In *AIAA Scitech 2021 Forum*, page 0423, 2021.

[32] Tomas J Martin-Mur, Eric D Gustafson, and Brian T Young. Interplanetary cubesat navigational challenges. In *25th International Symposium on Space Flight Dynamics (ISSFD), Munich, Germany*, 2015.

[33] Anna Gregorio and Federico Alimenti. Cubesats for future science and internet of space: Challenges and opportunities. In *2018 25th IEEE International Conference on Electronics, Circuits and Systems (ICECS)*, pages 169–172. IEEE, 2018.

[34] Stefano Speretta, T Pérez Soriano, Jasper Bouwmeester, Mr Johan Carvajal-Godinez, Alessandra Menicucci, Mr Trevor Watts, Mr Prem Sundaramoorthy, Jian Guo, and Eberhard Gill. Cubesats to pocketqubes: Opportunities and challenges. In *Proceedings of the 67th International Astronautical Congress (IAC)*. IAF, 2016.

[35] Giuseppe Di Mauro, Margaret Lawn, and Riccardo Bevilacqua. Survey on guidance navigation and control requirements for spacecraft formation-flying missions. *Journal of Guidance, Control, and Dynamics*, 41(3):581–602, 2018.

[36] Celine Beugnon, Bertrand Calvel, Sebastien Boulade, and Finn Ankersen. Design and modeling of the formation-flying gnc system for the darwin interferometer. In *Modeling and Systems Engineering for Astronomy*, volume 5497, pages 28–38. SPIE, 2004.

[37] Cassandra M Webster and David C Folta. Understanding the sun-earth libration point orbit formation flying challenges for wfirst and starshade. In *International Workshop on Satellite Constellations and Formation Flying (IWSCFF) 2017*, number IWSCFF 17-74, 2017.

[38] J.S. Llorente, A. Agenjo, C. Carrascosa, C. de Negueruela, A. Mestreau-Garreau, A. Cropp, and A. Santovincenzo. Proba-3: Precise formation flying demonstration mission. *Acta Astronautica*, 82(1):38–46, 2013. ISSN 0094-5765. doi: https://doi.org/10.1016/j.actaastro.2012.05.029. URL `https://www.sciencedirect.com/science/article/pii/S0094576512002202`. 6th International Workshop on Satellite Constellation and Formation Flying.

[39] Guo-Ping Liu and Shijie Zhang. A survey on formation control of small satellites. *Proceedings of the IEEE*, 106(3):440–457, 2018.

[40] Grant Bonin, Niels Roth, Scott Armitage, Josh Newman, Ben Risi, and Robert E Zee. Canx–4 and canx–5 precision formation flight: Mission accomplished! 2015.

[41] JS Ardaens and S D'Amico. Control of formation flying spacecraft at a lagrange point. Technical report, DLR/GSOC, 2008.

[42] Diane C Davis, Kenza K Boudad, Sean M Phillips, and Kathleen C Howell. Disposal, deployment, and debris in near rectilinear halo orbits. In *AAS/AIAA Space Flight Mechanics Meeting*, number JSC-E-DAA-TN64520, 2019.

[43] Marissa K Reynolds and Dawn P Moessner. Preliminary design and analysis for the imap sun-earth l1 libration point disposal maneuver. In *AIAA SCITECH 2022 Forum*, page 1626, 2022.

[44] Christopher GR Wallis, Michael L Brown, Richard A Battye, and Jacques Delabrouille. Optimal scan strategies for future CMB satellite experiments. *Monthly Notices of the Royal Astronomical Society*, 466(1):425–442, 2017.

[45] Juan Bermejo-Ballesteros, Javier Cubas, Francisco Casas, and Enrique Martínez-González. Visibility study in a chief-deputy formation for cmb polarization missions. *The Journal of the Astronautical Sciences*, 69(3): 651–691, 2022.

[46] ECSS Secretariat. Ecss-m-st-10c space project management—project planning and implementation. *ESA-ESTEC Requirements & Standards Division, Noordwijk, Netherlands*, 2009.

[47] Bruce Yost, Sasha Weston, Gabriel Benavides, Frederic Krage, John Hines, Stephanie Mauro, Selasi Etchey, Kiara O'Neill, and Barbra Braun. State-of-the-art small spacecraft technology. 2021.

[48] Wang Sang Koon, Martin W Lo, Jerrold E Marsden, and Shane D Ross. *Dynamical Systems, the Three-Body Problem and Space Mission Design*. Marsden Books, 2011.

[49] Timothy Gowers, June Barrow-Green, and Imre Leader. *The Princeton companion to mathematics*, pages "493–494". Princeton University Press, 2010.

[50] Zdzislaw E Musielak and Billy Quarles. The three-body problem. *Reports on Progress in Physics*, 77(6):065901, 2014.

[51] Victory Szebehely. *Theory of orbit: The restricted problem of three Bodies*. New York: Academic Press, 1967.

[52] Hanspeter Schaub and John L Junkins. *Analytical mechanics of space systems*. AIAA, 2003.

[53] David Vallado. *Fundamentals of astrodynamics and applications*, volume 12. Springer Science & Business Media, 2001.

[54] Kathleen C Howell and Henry J Pernicka. Numerical determination of lissajous trajectories in the restricted three-body problem. *Celestial mechanics*, 41(1-4):107–124, 1987.

[55] Martin Hechler and Jordi Cobos. Herschel, planck and gaia orbit design. In *Libration Point Orbits and Applications*, pages 115–135. World Scientific, 2003.

[56] Kathleen Connor Howell. Three-dimensional, periodic,'halo'orbits. *Celestial mechanics*, 32(1):53–71, 1984.

[57] Jeffrey S Parker and Rodney L Anderson. *Low-energy lunar trajectory design*, volume 12. John Wiley & Sons, 2014.

[58] D Scheeres and N Vinh. Dynamics and control of relative motion in an unstable orbit. In *Astrodynamics Specialist Conference*, page 4135, 2000.

[59] Maksim Shirobokov, Sergey Trofimov, and Mikhail Ovchinnikov. Survey of station-keeping techniques for libration point orbits. *Journal of Guidance, Control, and Dynamics*, 40(5):1085–1105, 2017.

[60] LOUIS A D'AMARIO and Theodore N Edelbaum. Minimum impulse three-body trajectories. *AIAA Journal*, 12(4):455–462, 1974.

[61] Robert W Farquhar, Daniel P Muhonen, Charles R Newman, and Howard S . Heubergerg. Trajectories and orbital maneuvers for the first libration-point satellite. *Journal of Guidance and Control*, 3(6):549–554, 1980.

[62] GERARD GOMEZ, ANGEL JORBA, JOSEP MASDEMONT, and C Simó. A dynamical systems approach for the analysis of the soho mission. *ESA, Spacecraft Flight Dynamics p 449-454(SEE N 92-24719 15-12)*, 1991.

[63] Kathleen C Howell and MW Lo. Trajectory design using a dynamical systems approach with application to genesis. In *AAS/AIAA Astrodynamics Specialist Conference*, 1997.

[64] Charles H Acton Jr. Ancillary data services of nasa's navigation and ancillary information facility. *Planetary and Space Science*, 44(1):65–70, 1996.

[65] Juan Bermejo Ballesteros, José María Vergara Pérez, Alejandro Fernández Soler, and Javier Cubas Cano. Mubody, an astrodynamics open-source python library focused on libration points. In *4th Symposium on Space Educational Activities*. Universitat Politècnica de Catalunya, 2022.

[66] Charles Acton, Nathaniel Bachman, Boris Semenov, and Edward Wright. A look towards the future in the handling of space science mission geometry. *Planetary and Space Science*, 150:9–12, 2018.

[67] David Folta, Natasha Bosanac, Ian Elliott, Laurie Mann, Rebecca Mesarch, and Jose Rosales. Astrodynamics convention and modeling reference for lunar, cislunar, and libration point orbits. Technical report, 2022.

[68] IA Out. Formation flying in the sun-earth/moon perturbed restricted three-body problem.[master's thesis]. *Netherlands: Delft University of Technology Faculty of Aerospace Engineering*, 2017.

[69] Kenza K Boudad. *Trajectory Design Between Cislunar Space and Sun-Earth Libration Points in a Four-Body Model*. PhD thesis, Purdue University Graduate School, 2022.

[70] Tomás Elices Concha. *Introducción a la dinámica espacial*. Instituto Nacional de Técnica Aeroespacial, 1991.

[71] JD Mireles James. Celestial mechanics notes set 4: The circular restricted three body problem, 2006.

[72] Zdzislaw Musielak and Billy Quarles. *Three body dynamics and its applications to exoplanets*. Springer, 2017.

[73] Jesse Leitner. Formation flying-the future of remote sensing from space. In *18th International Symposium on Space Flight Dynamics*, volume 548, page 621, 2004.

[74] Kyle T Alfriend, Srinivas R Vadali, Pini Gurfil, Jonathan P How, and Louis Breger. Chapter 1. In *Spacecraft formation flying: Dynamics, control and navigation*. Elsevier, 2009.

[75] Vincenzo Pesce, Andrea Colagrossi, and Stefano Silvestrini. Chapter 10. In *Modern Spacecraft Guidance, Navigation, and Control: From System Modeling to AI and Innovative Applications*. Elsevier, 2022.

[76] BG Marchand and KC Howell. Control strategies for formation flight in the vicinity of the libration points. *Journal of guidance, control, and dynamics*, 28(6):1210–1219, 2005.

[77] Rui Qi, Shijie Xu, and Ming Xu. Impulsive control for formation flight about libration points. *Journal of Guidance, Control, and Dynamics*, 35(2):484–496, 2012.

[78] *NanoProp GP3*. Gomspace, 2017. URL `https://gomspace.com/UserFiles/Subsystems/flyer/gomspace_nanoprop_cgp3.pdf`.

[79] Michel Delpech, Pierre-Yves Guidotti, Thomas Grelier, and Jon Harr. Rf based navigation for prisma and other formation flying missions in earth orbits. *Advances in the Astronautical Sciences*, 135(2):1533–1551, 2009.

[80] Michel Delpech, Jean-Claude Berges, Thomas Karlsson, and Fabien Malbet. Results of prisma/ffiord extended mission and applicability to future formation flying and active debris removal missions. *International Journal of Space Science and Engineering 5*, 1(4):382–409, 2013.

[81] Dan Simon. Chapter 5. In *Optimal state estimation: Kalman, H infinity, and nonlinear approaches*. John Wiley & Sons, 2006.

[82] Nicholas Hamilton, David Folta, and Russell Carpenter. Formation flying satellite control around the l2 sun-earth libration point. In *AIAA/AAS Astrodynamics Specialist Conference and Exhibit*, page 4528, 2002.

[83] Andrea Capannolo, Giovanni Zanotti, Michèle Lavagna, and Giuseppe Cataldo. Model predictive control for formation reconfiguration exploiting quasi-periodic tori in the cislunar environment. *Nonlinear Dynamics*, pages 1–19, 2023.

[84] Daniel Morgan, Soon-Jo Chung, and Fred Y Hadaegh. Model predictive con-

trol of swarms of spacecraft using sequential convex programming. *Journal of Guidance, Control, and Dynamics*, 37(6):1725–1740, 2014.

[85] David Folta and Mark Beckman. Libration orbit mission design: applications of numerical and dynamical methods. In *Libration Point Orbits and Applications*, pages 85–113. World Scientific, 2003.

[86] Giuseppe D Racca, René Laureijs, Luca Stagnaro, Jean-Christophe Salvignol, José Lorenzo Alvarez, Gonzalo Saavedra Criado, Luis Gaspar Venancio, Alex Short, Paolo Strada, Tobias Bönke, et al. The euclid mission design. In *Space telescopes and instrumentation 2016: optical, infrared, and millimeter wave*, volume 9904, pages 235–257. SPIE, 2016.

[87] Florian Renk and Markus Landgraf. Gaia: Trajectory design with tightening constraints. In *24th International Symposium on Space Flight Mechanics-ISSFD*, 2014.

[88] E Blazquez, T Gateau, and S Lizy-Destrez. Sempy: a python open-source toolbox for non-keplerian astrodynamics. In *International Conference on Astrodynamics Tools and Techniques (ICATT)*, 2021.

[89] GL Slater, Sharyl Marie Byram, and TW Williams. Collision avoidance for satellites in formation flight. *Journal of guidance, control, and dynamics*, 29 (5):1140–1146, 2006.

[90] Laura Garcia-Taberner and Josep J Masdemont. Feff methodology for spacecraft formations reconfiguration in the vicinity of libration points. *Acta Astronautica*, 67(7-8):810–817, 2010.

[91] Mingwu Li, Haijun Peng, and Wanxie Zhong. Optimal control of loose spacecraft formations near libration points with collision avoidance. *Nonlinear Dynamics*, 83:2241–2261, 2016.

[92] Jia-Sheng Li, Zhen Yang, and Ya-Zhong Luo. A review of space-object collision probability computation methods. *Astrodynamics*, 6(2):95–120, 2022.

[93] Ken Chan. Short-term vs. long-term spacecraft encounters. In *AIAA/AAS astrodynamics specialist conference and exhibit*, page 5460, 2004.

[94] Salvatore Alfano. Eliminating assumptions regarding satellite conjunction analysis. *The Journal of the Astronautical Sciences*, 59(4):676–705, 2012.

[95] JC Dolado, P Legendre, R Garmier, B Reveling, and X Pena. Satellite collision probability computation for long term encounters. *Adv. Astronaut. Sci*, 142, 2011.

[96] Vincent T Coppola et al. Including velocity uncertainty in the probability of collision between space objects. In *AAS/AIAA Spaceflight Mechanics Meeting*, pages 2012–2247. American Astronautical Soc, 2012.

[97] Russell P Patera. General method for calculating satellite collision probability. *Journal of Guidance, Control, and Dynamics*, 24(4):716–722, 2001.

[98] Fabio Santoni, Fabrizio Piergentili, and Rei Kawashima. Global university space debris observation network (gusdon). In *title JAXA Special Publication: Proceedings of the 8th Space Debris Workshop*, page 183, 2019.

[99] James Diebel. Representing attitude: Euler angles, unit quaternions, and rotation vectors. *Matrix*, 58(15-16):1–35, 2006.

[100] Shaul Hanany, Marcelo Alvarez, Emmanuel Artis, Peter Ashton, Jonathan Aumont, Ragnhild Aurlien, Ranajoy Banerji, R Belen Barreiro, James G Bartlett, Soumen Basak, et al. PICO: probe of inflation and cosmic origins. *arXiv preprint arXiv:1902.10541*, 2019.

[101] JA Tauber, PH Nielsen, A Martín-Polegre, B Crill, FRANCESCO Cuttaia, K Ganga, Jón Gudmundsson, W Jones, C Lawrence, P Meinhold, et al. Characterization of the in-flight properties of the Planck telescope. *Astronomy & Astrophysics*, 622:A55, 2019.

[102] Duc Thuong Hoang, Guillaume Patanchon, Martin Bucher, Tomotake Matsumura, Ranajoy Banerji, Hirokazu Ishino, Masashi Hazumi, and Jacques Delabrouille. Bandpass mismatch error for satellite CMB experiments I: estimating the spurious signal. *Journal of Cosmology and Astroparticle Physics*, 2017(12):015, 2017.

[103] Krzysztof M Gorski, Eric Hivon, Anthony J Banday, Benjamin D Wandelt, Frode K Hansen, Mstvos Reinecke, and Matthia Bartelmann. Healpix: A framework for high-resolution discretization and fast analysis of data distributed on the sphere. *The Astrophysical Journal*, 622(2):759, 2005.

[104] Adrian M Price-Whelan, BM Sipőcz, HM Günther, PL Lim, SM Crawford, S Conseil, DL Shupe, MW Craig, N Dencheva, A Ginsburg, et al. The Astropy project: Building an open-science project and status of the v2.0 core package. *The Astronomical Journal*, 156(3):123, 2018.

[105] Pauli Virtanen, Ralf Gommers, Travis E Oliphant, Matt Haberland, Tyler Reddy, David Cournapeau, Evgeni Burovski, Pearu Peterson, Warren Weckesser, Jonathan Bright, et al. SciPy 1.0: fundamental algorithms for scientific computing in Python. *Nature methods*, 17(3):261–272, 2020.

[106] John Parr Snyder and Philip M Voxland. *An album of map projections*. 1453. US Government Printing Office, 1989.

[107] Peter AR Ade, RW Aikin, D Barkats, SJ Benton, Colin A Bischoff, JJ Bock, KJ Bradford, JA Brevik, I Buder, E Bullock, et al. Bicep2/keck array. iv. optical characterization and performance of the bicep2 and keck array experiments. *The Astrophysical Journal*, 806(2):206, 2015.

[108] Charles L Bennett, M Bay, M Halpern, G Hinshaw, C Jackson, N Jarosik, A Kogut, M Limon, SS Meyer, L Page, et al. The microwave anisotropy probe* mission. *The Astrophysical Journal*, 583(1):1, 2003.

[109] Jan Alexander Tauber, Nazzareno Mandolesi, J-L Puget, T Banos, Marco Bersanelli, François R Bouchet, Reginald Christopher Butler, J Charra, Gerald Crone, John Dodsworth, et al. Planck pre-launch status: The planck mission. *Astronomy & Astrophysics*, 520:A1, 2010.

[110] Steven W Evans et al. Natural environment near the sun/earth-moon l2 libration point. *Next Generation Space Telescope Program, NASA Marshall Space Flight Center, MSFC, AL, http://sail. msfc. nasa. gov/nse/sgst. html*, 2002.

[111] Joseph Minow, William Blackwell, and Anne Diekmann. Plasma environment and models for l2. In *42nd AIAA Aerospace Sciences Meeting and Exhibit*, page 1079, 2004.

[112] ECSS Secretariat. Space environment. Technical report, ECSS-E-10-04A, ESA Publications Division [Internet], 2000. Available from . . . , 2008.

[113] Gaia Collaboration et al. The gaia mission. *arXiv preprint arXiv:1609.04153*, 2016.

[114] E Grün, HA Zook, H Fechtig, and RH Giese. Collisional balance of the meteoritic complex. *Icarus*, 62(2):244–272, 1985.

[115] *NanoMind*. Gomspace, 2 2021. URL `https://gomspace.com/shop/subsystems/command-and-data-handling/nanomind-a3200.aspx`.

[116] Tethers Unlimited. Swift-relnav brochure.

[117] *Battery Optimus*. Clyde Space, 7 2020. URL `https://www.aac-clyde.space/wp-content/uploads/2021/10/AAC_DataSheet_Optimus.pdf`.

[118] Andrew Klesh and Joel Krajewski. Marco: Cubesats to mars in 2016. 2015.

[119] United Launch Alliance. Aft bulkhead carrier auxiliary payload user's guide. *ULA, Centennial*, 2014.

[120] ISIS. Isis cubesat deployers brochure, 2020. URL `https://www.isispace.nl/wp-content/uploads/2016/02/CubeSat-deployers-Brochure-web-compressed.pdf`.

[121] Federico Nati, Mark J Devlin, Martina Gerbino, Bradley R Johnson, Brian Keating, Luca Pagano, and Grant Teply. Polocalc: a novel method to measure the absolute polarization orientation of the cosmic microwave background. *Journal of Astronomical Instrumentation*, 6(02):1740008, 2017. doi: 10.1142/S2251171717400086.

[122] *CubeADCS ICD*. CubeSpace, 11 2022. URL `https://www.cubespace.co.za/downloads/cubeadcs_-_icd_v7.4_.pdf`.

[123] Thomas V Peters, João Branco, Diego Escorial, Lorenzo Tarabini Castellani, and Alex Cropp. Mission analysis for proba-3 nominal operations. *Acta Astronautica*, 102:296–310, 2014.

[124] *NanoMind Z7000*. Gomspace, 2019. URL `https://gomspace.com/UserFiles/Subsystems/datasheet/gs-ds-nanomind-z7000-15.pdf`.

[125] *Solar Cell*. Azur Space, 8 2016. URL `https://www.azurspace.com/images/products/0003401-01-01_DB_3G30A.pdf`.

[126] R Sun. Relative navigation for satellite formation flying based on radio frequency metrology. 2014.

[127] *6U structure*. Endurosat, 6 2019. URL `https://satcatalog.s3.amazonaws.com/components/477/SatCatalog_-_EnduroSat_-_6U_CubeSat_Structure_-_Datasheet.pdf?lastmod=20210715031953`.

[128] Gianluca Benedetti, Nicoletta Bloise, Davide Boi, Francesco Caruso, Andrea Civita, Sabrina Corpino, Erik Garofalo, Giuseppe Governale, Luigi Mascolo, Gianluca Mazzella, et al. Interplanetary cubesats for asteroid exploration: Mission analysis and design. *Acta Astronautica*, 154:238–255, 2019.

[129] Mick Wijnen, Nereida Agüera-Lopez, Sara Correyero-Plaza, and Daniel Perez-Grande. Cubesat lunar positioning system enabled by novel on-board electric propulsion. *IEEE Transactions on Plasma Science*, 46(2):319–329, 2018.

[130] Lisa Guerra. Cost estimating module, space systems engineering, version 1.0. *Lecture, Space Systems Engineering*, 2008.